

**Quantifying and Modelling Adaptive Astronaut
Movement: Motion Strategies for Long-Duration
Spaceflight Missions**

by

Philip Andrew Ferguson

Master of Science - MIT, January 2003

Submitted to the Department of Aeronautics and Astronautics
in partial fulfillment of the requirements for the degree of

Doctor of Philosophy

at the

MASSACHUSETTS INSTITUTE OF TECHNOLOGY

May 2006

[June 2006]

© Massachusetts Institute of Technology 2006. All rights reserved.

Philip A. Ferguson

Author

Department of Aeronautics and Astronautics

May 26, 2006

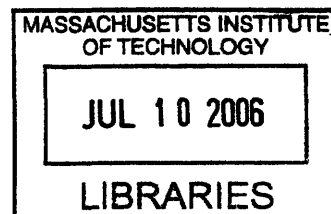
Jaime Peraire

Accepted by

Jaime Peraire

Professor of Aeronautics and Astronautics

Chair, Committee on Graduate Students



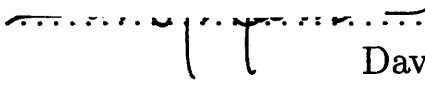
ARCHIVES

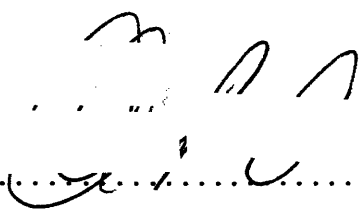
Quantifying and Modelling Adaptive Astronaut Movement: Motion Strategies for Long-Duration Spaceflight Missions

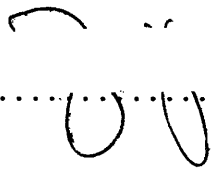
by


Philip Andrew Ferguson

MASSACHUSETTS INSTITUTE OF TECHNOLOGY

Certified by

Dava J. Newman
Professor of Aeronautics and Astronautics
and Engineering Systems
Thesis Supervisor

Accepted by

Charles C. Coleman
Assistant Professor of Aeronautics and Astronautics

Accepted by

Steve G. Massaquoi
Assistant Professor
Department of Electrical Engineering
Division of Health Sciences and Technology

Accepted by

Jean-Jacques Slotine
Professor of Mechanical Engineering and Information Sciences
Professor of Brain and Cognitive Sciences

Quantifying and Modelling Adaptive Astronaut Movement: Motion Strategies for Long-Duration Spaceflight Missions

by

Philip Andrew Ferguson

Submitted to the Department of Aeronautics and Astronautics
on May 26, 2006, in partial fulfillment of the
requirements for the degree of
Doctor of Philosophy

Abstract

Past spaceflight experience has shown that astronauts adapt their motor control strategies to microgravity movements after approximately four weeks of microgravity exposure. A similar (but typically shorter) re-adaptation period is required upon return to Earth or partial gravity environment such as the Moon or Mars. During these adaptation periods, astronaut performance is considerably degraded and can lead to falls and mission-threatening injuries.

This dissertation describes a research program to quantitatively study the dynamics and control aspects of human motor control adaptation to a spectrum of gravity environments. The key hypotheses of this research were that a) locomotor control adaptation could be observed following short exposure (on the order of hours) to a different dynamic environment and b) the observed adaptation could be predicted using a single model that applied to a spectrum of gravitational environments.

Experiments were conducted on a 1-G air-bearing floor microgravity simulator and underwater to provide contrasting dynamic and gravitational environments. Subjects performed leg push-offs and hand landings to demonstrate their control strategies as they adapted. Forces and moments from the push-offs and landings were recorded using 6-axis force-moment sensors. Joint angles were measured using a kinematic video analysis system. A suite of dynamic estimation filters was written to combine the kinetic and kinematic data. Experimental results showed significant motor control adaptation to the air-bearing floor experiments, evidenced by reduced peak push-off forces and increased sensor contact times. A model based on Golgi tendon organ (GTO) force feedback was proposed to predict the observed adaptation. Comparisons between the experimental data and the model predictions indicate that the GTO adaptation model can adequately predict the observed adaptation.

Thesis Supervisor: Dava J. Newman
Title: Professor

Acknowledgments

Completing my PhD has been one of the most difficult and most rewarding tasks I've ever done, second only to being a dad. Over the course of my research, I quickly realized that the magnitude and scope of my project required the help from a great many people. In this section, I try to recognize all of those people who made a difference in helping me graduate.

Firstly, I want to thank Professor Dava Newman, for her unending support and guidance throughout my work. Dava's passion for her work and consideration for her students made her a pleasure and an honour to work for. I also want to pass on a huge thank you to the rest of my thesis and defense committee: Steve Massaquoi, Charles Coleman, Jean-Jacques Slotine, Jeff Hoffman and Chuck Oman. While not on my official committee, I would also like to thank Larry Young for his guidance and support throughout this work. Their input, feedback and individual perspectives gave me the backing I needed to complete a well-rounded and comprehensive research program. Thanks to all!

Throughout my research, I was fortunate enough to be able to work with a tiger-team of savvy engineers and technicians from Payload Systems Inc. from Cambridge, MA. Chris Krebs, John Merk and Joanne Vining in particular helped me on a daily basis by assembling the most high-tech, waterproof, jam-packed, smallest, shiniest, heaviest, coolest and generally the most well-thought out force-moment sensors in the world. I can only hope that my future endeavours put me in contact with people half as qualified as everyone at Payload Systems Inc.

I was extremely fortunate to have ended up in a lab full of fantastic students and staff that were always willing to lend a helping hand. Every member of the Man-Vehicle Lab (MVL) helped me out in enormous ways. People helped by lifting ridiculously heavy equipment, building frames and crates, moving air pallets and even guarding video cameras in the building 37 lobby. While everyone helped out an extraordinary amount, in particular, I want to acknowledge Leia Stirling for her video analysis and help during all phases of the experiments, Liang Sim and Kevin Duda

for their help in the pool and packing things up for the Houston trip, Chris Carr for introducing me to the MVL and always being available to discuss my research, Jessica Edmonds, Jessica Marquez, Kristen Bethke and Erika Wagner for their technical moral and babysitting support and Dan Buckland, Paul Elias and Hiro Aoki for their ongoing donation of good old fashioned elbow grease.

A lot of my work involved interacting with folks from NASA Johnson Space Center while we prepared our MICRO-G ISS flight experiment. Lindsay Kirshner, Cathy Watson, Catherine Hughes, Sherry Carter and Cory Meander all served at one time or another on our experiment support team and consistently provided us with technical support from years of accumulated experience in the spaceflight industry. I especially want to thank Lindsay Kirshner for her help and attention to detail in making sure that our C-9 flights went smoothly.

Administratively, the Aero/Astro department at MIT has been second to none, providing me constant support in the form of office supplies, equipment purchasing, reimbursement forms and even tracking down faculty. Thanks especially to Sally Chapman, Liz Zotos, Kathryn Fisher and Ping Lee. In the academic programs office, Barbara Lechner, Marie Stuppard and Beth Marois have guided me through the countless hoops (some of which were on fire) that one needs to jump through in order to graduate. For that, I am forever grateful.

There is a handful of guys at MIT who tirelessly work to ensure that both graduate and undergraduate students get all of their equipment built and functioning properly. Dave Robertson, Todd Billings, Dick Perdichizzi, Paul Bauer and Pete Young all provided technical support (often in the form of telling me I was crazy for trying to build what I was building) that I could not have made do without. Thanks guys!

During my research, many undergraduate students helped me along the way as part of the Undergraduate Research Opportunity Program (UROP). Among these UROP's who provided valuable help with everything from sensor testing and calibration to building underwater structures were Rachel Ellman, Conor Lenahan, Shambhavi Kadam, Katherine Ingle, Andrew Pinkham and Scott Lazarus. However, one UROP, Rebecca Sampson, stood out, providing technical and research contributions

that went well above and beyond what was expected of her. Her willingness to tackle new problems made her an absolute pleasure to work with.

I, of course, want to thank my family: Mom, Dad, Mia, Alan, Matthew and Catherine – LYP! You listened to me complain about the bad things and brag about the good things, just like you did for the last two degrees, and this was no exception. I also appreciate nobody making any cracks (at least to my face) about how I was the first kid to start school and the last one to leave!

And finally, I have the most important people to thank: my beautiful, loving wife Ally and my favourite, cutest and funniest daughter, Wendy. This thesis, and everything I do professionally and in my spare time would not have been fathomable without the support I receive at home. The worst day in the lab is made better the second I open the door to my apartment and get a kiss from Ally, a goofy smile from Wendy, and a couple of soggy Cheerios thrown at my feet (along with a nice rendition of DAH DAH DAH DAHHHHH!!!). Ally and Wendy gave me love, support and general life perspective that I needed on a daily basis to get through this and all of life's challenges. Thank you, thank you, thank you. I Love you both so much.

For my princesses, Ally and Wendy.

As I cross the great divide and join the thundering crowd ...

Contents

1	Introduction	23
1.1	Hypotheses	25
1.2	Background	27
1.3	Thesis Outline	29
2	Body Motion Sensor Design	31
2.1	Introduction	31
2.2	Sensor System	33
2.2.1	Force-Moment Sensors	34
2.2.2	Kinematic Video System	43
2.3	The MICRO-G Experiment	46
2.4	Sample Data	47
2.5	Summary	48
3	Dynamic Modelling and Analysis Techniques	51
3.1	Body Center of Mass Tracking	53
3.1.1	Estimator Development	53
3.1.2	Simulations and Results	59
3.2	Joint Torque Estimation	61
3.2.1	Multi-Link Limb Statics and Dynamics	62
3.2.2	Estimator Development	65
3.2.3	Simulations and Results	69
3.2.4	Discussion	77

3.3	Conclusions and Recommendations	79
4	Dynamic Human Adaptation Experiments	81
4.1	Testing Environments	82
4.1.1	Air-Bearing Floor	82
4.1.2	Underwater	83
4.2	Pilot Studies	84
4.2.1	Lessons Learned from the Pilot Studies	85
4.3	Experiment 1 - Simulated Microgravity Push-Offs and Landings . . .	87
4.3.1	Subjects	87
4.3.2	Methods	87
4.3.3	Measurements	91
4.4	Experiment 2 - Hoop Game	92
4.4.1	Subjects	93
4.4.2	Methods	93
4.4.3	Measurements	95
4.5	Experiment 3 - Underwater Push-Offs and Landings	96
4.5.1	Subjects	96
4.5.2	Methods	96
4.5.3	Measurements	98
4.6	Results	98
4.6.1	Maximum Push-Off Force	99
4.6.2	Push-off Contact Time	103
4.6.3	Force Profiles	104
4.6.4	Astronaut Data	108
4.6.5	Relative Force Magnitudes	109
4.7	Experiment Summary	111
5	Adaptation Modelling and Discussions	113
5.1	Push-off Control using Springs	114
5.2	Muscle Dynamics, Force Feedback and Transportation Delays	121

5.2.1	Long-loop, Cerebellar Tracking Control	122
5.2.2	Golgi Tendon Organ Feedback	125
5.2.3	Excitation / Contraction Coupling	126
5.3	Adaptation Model	127
5.4	Discussion	129
5.4.1	Hybrid Feedforward / Feedback Model Performance	129
5.4.2	Limitations of the Proposed Model	131
5.4.3	Other Feedback Loops to Consider	133
6	Conclusions and Recommendations	135
6.1	Thesis Summary	135
6.2	Contributions	139
6.3	Recommendations	140
6.4	Future Work	142
A	Individual Subject Data	145
B	Nonlinear Least Squares Algorithm Development	151
C	Unscented Kalman Filter Development	155
D	Sensor Calibration	157
D.1	Introduction	157
D.2	The EDLS Calibration Procedures	158
D.2.1	EDLS Calibration Fixture	158
D.2.2	EDLS Calibration Algorithm	159
D.3	The MICR0-G Calibration Procedure	160
D.3.1	The MICR0-G Calibration Fixture	160
D.3.2	MICR0-G Calibration Algorithm	164
D.4	Calibration Results	167
D.5	Recommended MICR0-G Design Modifications	169
D.5.1	Wiring modifications	170

D.5.2	Flexure interfaces	170
D.6	Calibration Matrices	170
D.6.1	Prototype Sensor #001	171
D.6.2	Prototype Sensor #002	171
D.6.3	Prototype Sensor #003	171
D.6.4	Prototype Sensor #004	174
E	Hoop Game Design	177
F	Sensor Operating Procedures	179
F.1	Theory of Operation	179
F.1.1	Overview	179
F.1.2	Electrical	179
F.1.3	Software	180
F.2	Detailed Instructions	184
F.2.1	Setup	184
F.2.2	Sensor Software Startup	185
F.2.3	Restarting Sensor Software for a New Subject	186
F.2.4	Powering Down the Sensors	186
G	Data Analysis Software	187
H	Human Subject Use Documentation	203
H.1	Informed Consent Form	203
H.2	Underwater Subject Selection Questionnaire	210

List of Figures

2-1	EDLS Hardware	33
2-2	MICR0-G Force-Moment Sensor	35
2-3	MICR0-G Sensor Strain Gauges	36
2-4	MICR0-G Flight Sensors	36
2-5	MICR0-G Sensor Electronics	37
2-6	MICR0-G Sensor Software Flowchart	39
2-7	Wireless Ethernet Adapter	40
2-8	Realtime feedback features of the MICR0-G sensors	42
2-9	MICR0-G Sensor Underwater	42
2-10	Camera configurations for the ground-based experiments.	44
2-11	Schematic of the kinematic video analysis.	45
2-12	Prescribed Motion Illustration	46
2-13	Regular Daily Activities Illustration	47
2-14	Subject Performing a Push-off	48
2-15	Sample Sensor Data	49
3-1	Kinematic / Kinetic Information Synthesis	53
3-2	N-link Planar Limb	55
3-3	Body Center of Mass Estimation Errors	71
3-4	Body COM Position Comparisons	72
3-5	Conventional Filter Flow	72
3-6	Updated Control Input Filter Flow	73
3-7	Three-Joint Angle-Only Torque Estimation Results	73

3-8	Three-Joint Torque Estimation: Forces, Moments, Angles	74
3-9	UKF Three-link Estimation: Forces, Moments, Angles	74
3-10	Four-Joint Torque Estimation: Forces, Moments, Angles	75
3-11	UKF Four-link Estimation: Forces, Moments, Angles	75
3-12	Real Torque Estimation Data	76
3-13	Three-Joint Torque Estimation: Forces, Angles	78
3-14	Three-Joint Torque Estimation: Forces, Angles, Accelerations	79
4-1	Air-Bearing Floor Setup	83
4-2	Sensor Mounting Frame Underwater	84
4-3	Tactile Cue for Center of Sensor	85
4-4	Subject Motion Paths	88
4-5	Air-Bearing Floor Configurations	89
4-6	Hoop Game Setup	94
4-7	Phase / Trial Descriptions	97
4-8	Underwater Video Housing	98
4-9	Adaptation and Dual-Adaptation Result	100
4-10	Maximum Push-off Force Across Break	102
4-11	Maximum Push-off Force Underwater	103
4-12	Experiment 1 Contact Time	104
4-13	Underwater Contact Time	105
4-14	Force shape profiles	107
4-15	Sample Astronaut Data	109
4-16	Relative Force Magnitudes	110
5-1	Force Profile Contrast	114
5-2	Rigid Body Model	115
5-3	Torsional Springs and Dampers	116
5-4	Joint Control Block Diagram	117
5-5	Step Reference Trajectory Simulation Results	118
5-6	Ramp Reference Trajectory Simulation Results	119

5-7	Delayed Activation Simulation Results	120
5-8	Long-Loop Control	123
5-9	GTO Feedback	126
5-10	Excitation / Contraction Dynamics	127
5-11	Fully Integrated Control Block Diagram	128
5-12	Data vs. Model Comparison	129
5-13	Model Error Performance	130
5-14	Spinal vs. Cerebellar Control	132
A-1	All Subjects Max Force Data, Exp. 1, 2	146
A-2	All Subjects Max Force Data Across Break	147
A-3	All Subjects Contact Time Data, Exp. 1	148
A-4	All UW Subjects Max Force Data, Exp. 1, 3	149
A-5	All UW Subjects Contact Time Data, Exp. 1, 3	150
D-1	Photo showing the calibration fixture used for the EDLS calibration.	159
D-2	MICR0-G calibration fixture	162
D-3	MICR0-G sensor axis convention	163
D-4	Calibration Curves for Sensor 001	168
D-5	Calibration Curvers for Sensor 002	172
D-6	Calibration Curvers for Sensor 002	173
D-7	Calibration Curvers for Sensor 004	175
E-1	Hoop Game	178
E-2	Hoop Game Electronic Schematic	178
F-1	The MICR0-G Sensor	180
F-2	MICR0-G Power Supply	181
F-3	Wireless Router	182

List of Tables

2.1	Views Captured by Each Camera	45
3.1	Simulated Mass Properties	69
4.1	Experiment 1 Motions	90
4.2	Directly Measured Quantities	92
4.3	Derived Quantities	93
4.4	Experiment 2 Motions	95
4.5	Statistical Results Summary	106
D.1	MICR0-G calibration fixture loading offsets	164
D.2	A/D settings.	171

Chapter 1

Introduction

Future space missions will require astronauts spend months to years in reduced gravity environments. Such missions include extended visits to the International Space Station (ISS) and exploration missions to the Moon and eventually to Mars [Bush, 2004]. However, before humans will be able to optimally perform during these long trips in space, a substantial amount of research is required. During spaceflight, astronauts lose 1-2% of bone mass, 20-30% of muscle mass and 40% of their overall strength per month. Ongoing research into the skeletal [Beck et al., 1990, Schaffner, 1999, Newman and Schaffner, 2003], muscular [Fitts et al., 2000], vestibular [Oman, 1988, Young et al., 1993, Lathan and Clément, 1997, Newman et al., 2003] and cardiovascular [Heldt et al., 2002] changes that occur during spaceflight is providing new countermeasures. Other research programs are focussing on the human factors of spaceflight. For example, several scholars are studying the effects of humans operating in extreme environments such as a cramped spacecraft [Brubakk, 2000, Stuster, 2000, Newman and Lathan, 1999], while others are studying ways to prevent astronauts from becoming disoriented in convoluted space station modules [Oman, 2001, Young et al., 1993].

While all of the above mentioned challenges are important to the success of future long duration spaceflights, this research focuses on an equally important and challenging aspect: understanding the mechanisms by which astronauts develop motor strategies for differing gravity environments. This research examines astronaut mo-

tion and how it changes over time. The overall goal of the proposed research is to improve astronaut performance and efficiency through the use of rigorous quantitative dynamic analysis, simulation and experimentation.

One of the key challenges to living in space is locomotor function in a microgravity environment. Moving from place to place within the spacecraft requires an altered set of control strategies than are applicable for 1-G. Fortunately, astronauts have demonstrated their ability to adapt their locomotor control strategies to fit the needs of microgravity operations [Newman and Jackson, 2000]. However, during the period of time before astronauts completely adapt to this new environment ($\approx 2 - 4$ weeks) the productivity of the astronauts is severely limited (as evidenced by recent research using instrumented hand and foot restraints [Newman et al., 2001, 1999]). Furthermore, while the newly adapted movement strategies are typically appropriate for the microgravity environment, they are not suitable for partial gravity environments, possibly forcing a re-adaptation period upon return to Earth or arrival at another planet [Baroni et al., 2001a]. For planetary exploration missions, where astronauts are expected to explore a gravity environment immediately after a lengthy (> 6 months) microgravity spaceflight, this re-adaptation phase could significantly affect the astronauts' ability to perform their mission and science duties. Understanding and modelling the characteristics of the locomotor control strategies adopted by veteran astronauts as well as the adaptation or skill selection process used to arrive at them could provide insight into new training techniques and countermeasures intended to accelerate the adaptation and re-adaptation. A single model that can predict locomotor control adaptation to a spectrum of gravitational and dynamic environments would permit detailed studies of astronaut exploration activities prior to the actual flight and could lead to improved operations planning, spacesuit and/or tool design and in-flight countermeasures to aid in the locomotor adaptation.

In order to optimize astronaut performance, this research studies the locomotor adaptation process that permits astronauts to efficiently perform motor tasks across a *spectrum* of gravitational environments (*i.e.*, Earth, Moon, Mars and microgravity). In the research presented herein, I quantitatively characterize the skills and motor

control strategies that veteran astronauts use to move their bodies through differing gravity environments and how the control strategies develop over time. A key hypothesis in this work was that a single adaptation process will be found responsible for the adaptation seen across the entire gravity spectrum.

During this research, emphasis is placed on the *locomotor*¹ skills required to move one's entire body from place to place while on orbit. Understanding this process requires a highly accurate data acquisition system such as the one being used for the Microgravity Investigations and Crew Reactions in 0-G (MICRO-G) flight experiment slated for the International Space Station (ISS) [Ferguson et al., 2004b]. The MICRO-G sensors and accompanying kinematic video system will provide a complete picture of the astronauts' control strategy since joint torques can be computed from the coupled kinetics and kinematics. Knowledge of the joint torques will permit a detailed analysis of the joints and muscle groups being employed to execute the motions as well as provide clues suggesting a neural adaptation process.

This thesis presents the results of human motion experiments performed both underwater and on a two-dimensional frictionless air-bearing floor to observe the development of motor control strategies for multiple environments.

1.1 Hypotheses

Prior to studying human motion adaptation, a sensing system must be created that can observe adaptation while it happens. In addition to creating the sensor, algorithms and dynamic filters must be created that can effectively reduce the data into manageable and meaningful metrics. Hypothesis #1 explores the ability to combine kinetic and kinematic data for adaptation monitoring purposes.

Hypothesis #1: Kinetic data from a force / moment sensor and kinematic joint angle data can be combined in a dynamic filter to produce accurate, reliable estimates of whole body motions during adaptation ex-

¹The term "locomotor" was coined by Jacob Bloomberg in his work [Bloomberg et al., 2001], and is defined as the skills required to move one's body mass in any gravitational environment.

periments. Using the combined kinetic and kinematic data, metrics can be defined that illustrate control strategy adaptation to different gravitational and dynamic environments.

Hypothesis #2: Given exposure to a particular gravity environment, humans will retain the adapted locomotor control strategies for multiple weeks of constant exposure to a different gravity environment, providing evidence of *multi-adaptation*.

Studying dual adaptation requires exposing subjects to different environments and looking for the amount of control adaptation retained over a period of time. If subjects who have had prior exposure to a given environment show improved performance after exposure to a different environment, it could provide evidence of *multi-adaptation*.

In addition to developing sensing systems for quantifying human motion, this thesis explores the ability of several different control models of human body motions to describe the adaptation observed during the human experiments. While classical adaptive control structures [Slotine and Li, 1991, Niemeyer and Slotine, 1991] have demonstrated the ability to adapt to different model parameters, they have difficulty in altering the entire control strategies. A Bayesian optimization approach [Ferguson et al., 2004a, Tryfonidis, 1999] to control strategy adaptation may be applicable, however, it often requires internal dynamic models that some argue are not practical for humans to implement [Flash, 1987, Flash et al., 2003, Bizzi et al., 1994]. The traditional equilibrium trajectory control model avoids the requirement that internal models exist in the human brain, but has difficulty predicting adaptation to different environments.

Hypothesis #3: A single adaptation mechanism governs human locomotor control strategies across a spectrum of gravity environments in a manner similar to that predicted by either Bayesian optimization; or the virtual trajectory hypotheses or a combination of the two.

1.2 Background

Sensor technology for quantifying human motion has been growing for many years. Recent developments in video analysis [DeCarlo and Metaxas, 2000, Metaxas, 1996, Zhang et al., 2003, Barron et al., 1992, Ferrigno et al., 1999] have enabled detailed kinematic analysis of human motion. However, these video analysis techniques lack acceleration information important to understanding the *control* of human motion. While force / moment sensor technology is not new, researchers have been implementing them more and more into human applications [Amir, 1998, Ferguson and Newman, 2006]. Some have studied using force / moment sensors to aid in robot torque control [Liu et al., 1998, Morel and Dubowsky, 1996] and human joint work estimation [Nagano et al., 1998], but none have combined the kinetic force / moment information with kinematic measurements to enable more reliable motion tracking without the need for acceleration estimation.

A substantial amount of research has also been conducted on the development of simulators for exposing humans to gravity environments other than the 1-G environment found on Earth. Engineering and operational concerns during underwater operations and training have also been studied [Akin, 1986, Wickman and Luna, 1996], however both studies lacked accurate kinetic measurements underwater. [Newman and Wu, 2000] developed a partial weight suspension system known as the “moon-walker” for simulating partial gravity environments. A similar, but actively controlled partial weight suspension system called POGO was also developed at the Johnson Space Center (JSC) for astronaut training purposes [Ray, 1993].

The problem of human motor control adaptation to spaceflight has been studied by several researchers in the past. Drawing upon the vast amounts of literature on human arm control [Atkeson and Hollerbach, 1985, Feldman, 1994, Flash, 1987, Flash and Hogan, 1985, Flash et al., 2003, Hasan, 1986, Katayama and Kawato, 1993, Mussa-Ivaldi et al., 1985], several have attempted to understand the control changes of the human 2-link arm. Lackner and DiZio from Brandeis University have also studied the effect of coriolis forces on arm control using a large rotating room

[Lackner and DiZio, 1994, 1998]. These studies showed that humans are capable of rapidly (over the course of only about 10 trials in less than one hour) adapting their arm control strategies to altered gravity environments. This work extended to arm, posture and vestibulo-oculo reflex (VOR) control adaptation in weightlessness [Lackner and DiZio, 1996, 1999], using data collected during parabolic flight. [Bock et al., 1992] have also studied arm adaptation to differing gravitational environments, measuring how quickly subjects learn the new gravitational dynamics.

Tryfonidis' doctoral work augmented some of the work done by Lackner and DiZio and added some data taken from actual spaceflights [Tryfonidis, 1999]. In his thesis, Tryfonidis developed a theory for arm control adaptation to varying gravitational environments that follows directly from conventional adaptive sliding control theory for robots. Tryfonidis compared his theory to data taken on the Russian space station *Mir* of astronauts throwing small balls to illustrate the new control strategies astronauts adopt during spaceflight [Tryfonidis et al., 2004]. In this work, Bayesian optimization was used to develop an arm adaptive control strategy that accounted for observations taken in both 1-G and microgravity.

Other research has focussed on postural control of the head and trunk in space. Baroni, Pedrocchi and Pedotti, along with Massion and Clément have performed numerous studies using data from *Mir* and parabolic flights [Baroni et al., 2001b, 1999, Massion et al., 1997, 1998, Clément and Lestienne, 1988]. These studies used kinematic data collected by specially designed video capture systems. These systems use body reflectors that are picked up by carefully calibrated video cameras and then video processing algorithms are used to compute the body joint angles and rates.

Research in the mid 1990's used rats to demonstrate sensorimotor adaptation of posture to altered gravity environments as a result of vestibular alterations [Fox et al., 1998]. In these experiments, rats were dropped into pools of water in normal (Earth) and hyper-gravity. Fox et al. monitored the rats posture in free fall and while swimming and watched as they adapted to their new gravity environments. Fox's research concluded that the observed adaptation was a result of gain reductions in the gravity-sensitive portion of the vestibular system.

The concept of *dual adaptation* (also known as *plasticity* or *context-specific adaptation*) has also been studied in the context of motor adaptation to spaceflight. These theories state that humans have the capability of retaining several different control sets for different environments. Baroni et al. explored dual adaptation of postural control during long-term microgravity exposure in 2001 [Baroni et al., 2001a]. Shelhamer has also provided evidence of dual adaptation, this time with respect to neurovestibular adaptation to differing gravitational environments, including microgravity on the KC-135 microgravity aircraft [Shelhamer and Clendaniel, 2002, Shelhamer et al., 2002, 2003]. Finally, Bloomberg has performed several experiments that demonstrate visuo-motor plasticity [Roller et al., 2002, 2001]. Bloomberg's results were recently extended to astronaut locomotor problems following spaceflight through a series of pre- and post-flight walking experiments [Bloomberg and Mulavara, 2003, Layne et al., 2001].

Other researchers have focused on the plausibility of the cerebellum for use in adaptive control [Houk et al., 1996] and signal delay compensation [Massaquoi and Slotine, 1996, Miall et al., 1993]. Kawato and Gomi have studied the role of the cerebellum in the adaptation of the Vestibulo-Occular Reflex (VOR) [Kawato and Gomi, 1992]. Later, Schweighofer and colleagues proposed a model of the cerebellum that accounted for motor learning in arm reaching experiments and was physically possible given the neuronal structure of the cerebellum [Schweighofer et al., 1998a,b].

There is a large body of literature that covers how humans learn motor tasks. [Shadmehr and Holcomb, 1997] show the effect of breaks on motor learning (known as consolidation). Others have studied the ability for humans to apply arm motor skills learned in one environment to different environments [Seidler, 2004].

1.3 Thesis Outline

This thesis presents the results of a research program designed to study the adaptive control strategies of humans in different gravitational and dynamic environments. The next chapter (Chapter 2) describes the design of a custom 6-axis force/moment

sensor designed in parallel for this thesis research and for an International Space Station experiment known as the Microgravity Investigation of Crew Reactions in 0-G (MICRO-G). Chapter 2 also contains a summary of the MICRO-G flight experiment and how its objectives relate to this work.

In order to clearly understand the control strategies being used by astronauts and experiment subjects, algorithms needed to be developed to track the subjects' body motions and to estimate joint control torques given the interaction forces and moments and the subjects' joint angles. Chapter 3 describes the development of a Kalman filter based body motion estimator and a non-linear control torque estimator that were developed as part of this research program to aid in the analysis of experimental data.

Chapter 4 describes the three different experiments conducted for this research program: air-bearing floor experiments and the underwater experiments. Along with detailing the experiment protocols, results are presented that illustrate locomotor control adaptation.

Chapter 5 describes the development of a single model that describes the locomotor adaptation observed in Chapter 4. Simulation results from the model are compared to the actual human experiments to illustrate a good match.

Finally, Chapter 6 summarizes this thesis by discussing the results and their relevance not only in the fields of bioastronautics and human space exploration, but also in the fields of dynamics, control and estimation.

Chapter 2

Body Motion Sensor Design

The work presented in this thesis represents the ground studies of the Microgravity Investigations of Crew Reactions in 0-G (MICR0-G) research program. This chapter presents the hardware and software design for the MICR0-G flight experiment. In addition, a preliminary experimental protocol for the MICR0-G International Space Station experiment. Since the research presented in this thesis was completed as part of the MICR0-G research program, most of the hardware and software developed for the spaceflight experiment is identical to that used for the experiments presented later in this thesis. Differences between the flight experiment and the ground studies are noted below.

2.1 Introduction

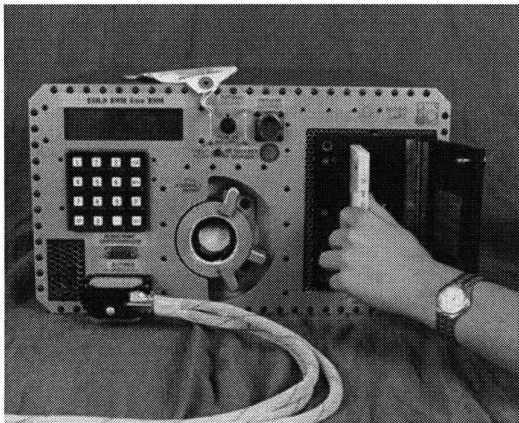
The development of countermeasures that enable astronauts to withstand extended stays in changing gravitational environments has been identified as an enabling technology for future human space exploration missions [Kieza et al., 2004]. As such, there is a need for a human factors, technology-based bioastronautics research effort to develop an integrated system that reduces risk and provides scientific knowledge of astronaut-induced loads and adaptation mechanisms during long-duration missions on the International Space Station (ISS), which will lead to appropriate countermeasures and diagnostic tools.

The primary objectives of the Microgravity Investigations of Crew Reactions in 0-G (MICRO-G) research effort (known to NASA as simply “Adapt”) are to quantify astronaut adaptation and movement as well as to model motor strategies for differing gravity environments [Ferguson et al., 2004b]. The overall goal of this research program is to improve astronaut performance and efficiency through the use of rigorous quantitative dynamic analysis, simulation and experimentation. The MICRO-G research effort provides a modular, kinetic and kinematic capability for the ISS. The collection and evaluation of kinematics (whole-body motion) and dynamics (reaction forces and torques) of astronauts within the ISS will allow for quantification of human motion and performance in weightlessness, gathering fundamental human factors information for design, scientific investigation in the fields of dynamics and motor control, technological assessment of microgravity disturbances, and the design of miniaturized space electronics.

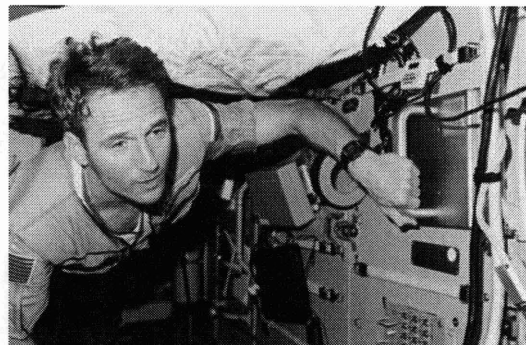
A key hypothesis of the MICRO-G research program is that a single model can be identified that predicts human control strategies across a spectrum of gravitational environments. Evaluating the ability of a particular dynamic model of human motion requires a comprehensive sensing system, able to monitor the motion and control strategies of humans in different gravitational environments. Four dynamic load sensors/restraints have been developed to measure astronaut forces and torques. Standard ISS video cameras record typical astronaut operations and prescribed IVA motions for 3-D kinematics. Forces and kinematics are combined for dynamic analysis of astronaut motion, exploiting the results of the detailed dynamic modeling effort for the quantitative verification of astronaut IVA performance, induced-loads, and adaptive control strategies for crewmember whole-body motion in microgravity. This comprehensive effort, provides an enhanced human factors approach based on physics-based modeling to identify adaptive performance during long- duration spaceflight, which is critically important for astronaut training as well as providing a spaceflight database to drive countermeasure design. This chapter describes the entire MICRO-G experiment in detail, including hardware, software and experimental protocol development.

2.2 Sensor System

The MICRO-G force-moment sensor design is based on that used for the Enhanced Dynamic Load Sensors (EDLS) experiment (pictured in Figure 2-1). The EDLS sensors were designed to measure 3-axis forces and 3-axis moments at 250 Hz in order to measure the crew-induced loads to the *Mir* space station structure [Newman et al., 2001]. The experiment was successful, however, it became apparent that the sensing



(a) Photo of the Experiment Support Module (ESM) that the three EDLS sensors plugged into.



(b) Photo of an astronaut using one of the sensors in the EDLS experiment.

Figure 2-1: Sensor hardware from the Enhanced Dynamic Load Sensors (EDLS) flight experiment.

system had some drawbacks, namely:

- The sensors required umbilicals to connect to a separate, bulky support module (seen in Figure 2-1(a)), limiting the positions with the space station where the sensors could be located.
- The sensors only provided kinetic (force-moment) data without any kinematics (body and joint positions).
- No feedback was provided to the astronauts as to the magnitudes of forces being imparted on the sensors (a feature that many astronauts have requested).

The EDLS experiment served its purpose well - to quantify the types of load disturbances astronauts impart to the space station. However, to quantify and model

astronaut whole-body adaptation, a more comprehensive and modular sensing system was required.

The MICR0-G sensing system was designed to address the drawbacks of the EDLS system and is comprised of two parts: (A) Wireless, modular force-moment sensors with visual feedback and (B) A kinematic video system. My contribution to the development of the new MICR0-G sensors involved the design concepts, electrical design (except the load cell design that was replicated from the EDLS design) and software design and implementation.

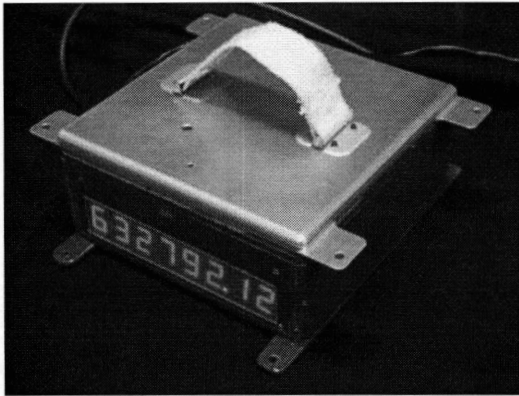
2.2.1 Force-Moment Sensors

I developed the concept for the MICR0-G sensors to follow the basic functionality of the EDLS sensors, but featuring entirely self-contained electronics. To test the concept, I assembled a working prototype using a backup EDLS sensor and a Commercial Off The Shelf (COTS) electronics backplane. A custom clock board was also designed, built and integrated into the concept prototype¹. Payload Systems Inc. (PSI) of Cambridge, MA then took the MICR0-G sensor concept prototype I designed and built and professionally manufactured the prototype MICR0-G sensors. Figure 2-2(a) shows a photo of the first “concept” prototype that was passed on to PSI. Figure 2-2(b) shows a photo of one of four prototype MICR0-G sensors assembled by PSI.

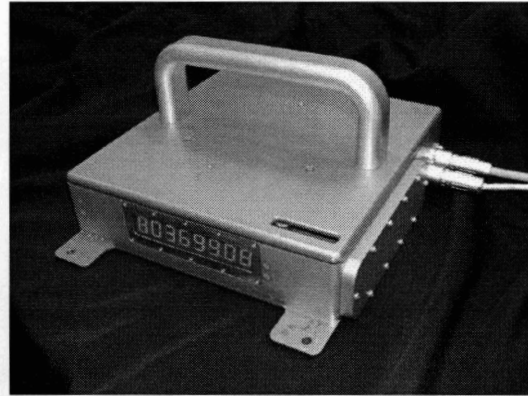
The load cell design and layout for the MICR0-G sensors is identical to that used on the EDLS sensors. The design employs three aluminum flexures, each instrumented with two full strain-bridges for a total of six load cells per sensor. Six independent strain measurements arranged in the geometry illustrated in Figure 2-3 can adequately observe three orthogonal forces and three orthogonal moments. The sensor top plate attaches directly to the three flexures.

In addition to using the flight-tested flexure design of the EDLS sensors, the MICR0-G force-moment sensors are equipped with several new features that make them better suited to adaptation research on the ISS. The new features include:

¹Thanks to Andrew Pinkham, a UROP that aided in the clock board design



(a) A photo of the concept prototype I built, configured as a foot restraint.



(b) A photo of one of the 4 prototype MICR0-G sensors (configured as a hand hold), assembled by PSI.

Figure 2-2: Early versions of the MICR0-G force-moment sensor prototype.

- **Standard ISS Restraint Accommodation**
- **On-board Data Acquisition**
- **Custom Software**
- **Video Synchronization**
- **Wireless Communication**
- **Realtime Feedback**
- **Waterproofing**
- **Easy Data Backup System**

Many of the new features have already been developed and are incorporated into 4 prototype sensors. Other features will be implemented in the flight version of the MICR0-G sensors to be manufactured immediately following the experiment Critical Design Review (CDR). The following sections describe the key features of the MICR0-G sensors.

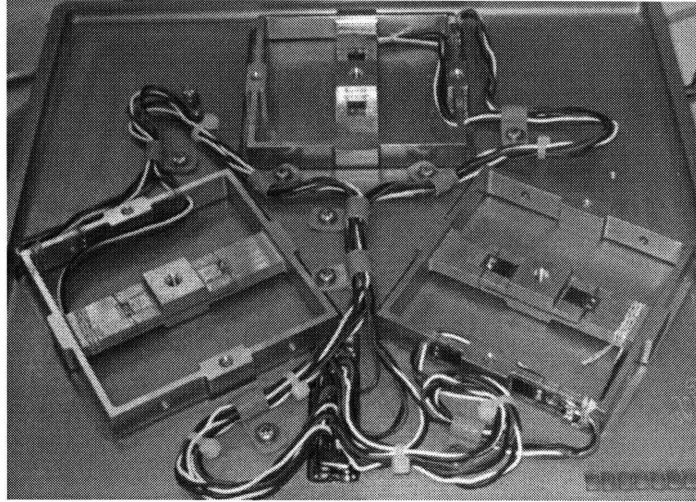
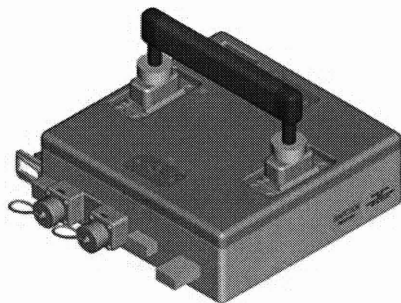


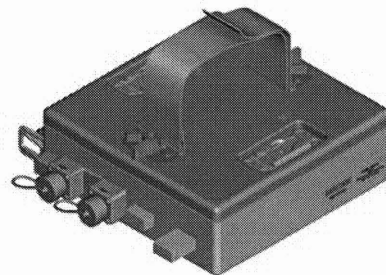
Figure 2-3: A photo of the strain gauge flexures underneath the top plate of the new MICR0-G prototype sensor. The flexure design is unchanged from the original EDLS design.

Standard ISS Restraint Accommodation

In order to measure natural astronaut motions, the MICR0-G sensors need to look and feel similar to the restraints astronauts currently use on the ISS. While the prototype sensors accommodate generic hand holds (as seen in Figure 2-2(b)) and fabric foot restraints, the flight sensors will be able to accommodate the actual hand hold and foot restraints used by the astronauts. Figure 2-4 illustrates what the flight sensors will look like when configured as either a hand hold (Figure 2-4(a)) or a foot restraint (Figure 2-4(b)).



(a) MICR0-G sensor configured as a hand-hold.



(b) MICR0-G sensor configured as a foot restraint.

Figure 2-4: CAD images of the MICR0-G sensors for use on the ISS.

One of the key features of the new MICR0-G sensors is their modularity. Each

sensor can be configured as either a hand hold or a foot restraint depending on the requirements of the given task. The MICR0-G sensors also come with multiple attachment options, making it easy for astronauts to relocate the sensors if an extra restraint is needed in another part of the space station.

On-board Data Acquisition

A small PC/104-based CPU, data acquisition system and 60 GB hard drive are built into the sensors to make them entirely self-contained. As such, they no longer require a separate experiment support module for data acquisition. Figure 2-5 shows the electronics inside one of the prototype MICR0-G sensors.

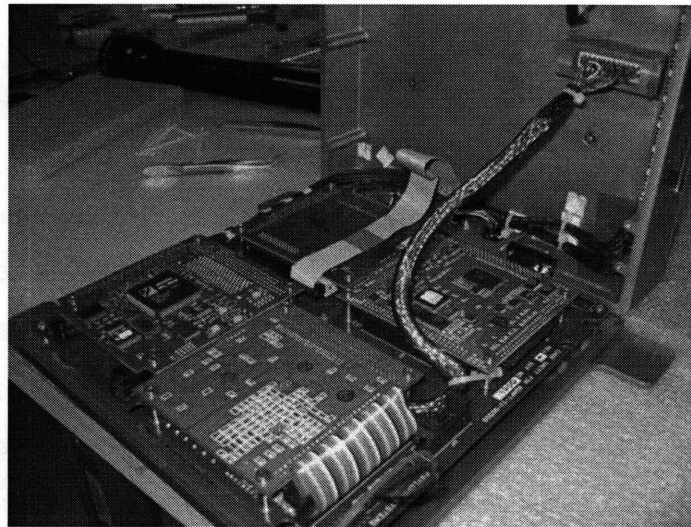


Figure 2-5: A photo showing the electronics inside the prototype MICR0-G sensors. Starting from the board at the far left, the boards are: PCMCIA card interface, VGA module, CPU and the Analog to Digital Board.

The MICR0-G sensors are driven by the Prometheus CPU by Diamond Systems (part number PR-Z32-EA-ST). The Prometheus employs a 486-class processor chip with on-board analog to digital circuitry and several programmable digital I/O ports. A dedicated analog to digital card, the DMM-16-AT board by Diamond Systems, enables high frequency differential measurement of up to 8 strain gauge signals (although each sensor only requires six differential measurements).

A PC/104 VGA card by Arcom (part number AIM104-VGA-CRT) provides easy

debugging access through a standard VGA monitor. The PCMCIA module (also a PC/104 card) is manufactured by Ampro (part number MM2-PCC-Q-71).

The MICR0-G sensor backplane was custom designed to house the four PC/104 modules side-by-side to conserve space inside the sensor². The sensor backplane also houses a custom filtering and gain circuit that preconditions the analog sensor voltages prior to the analog to digital conversion done by the DMM-16-AT board.

Custom Software

To maximize flexibility, each sensor has a full installation of Slackware Linux, complete with device drivers, C compilers, multi-threading constructs and disk and network utilities. Linux provides an easy environment for developing software for the MICR0-G sensors as well as eliminates the need to develop basic capabilities such as remote login shells and file transfer protocols.

The MICR0-G sensor software was designed to be as autonomous as possible. Upon start-up, the sensor software initializes the data acquisitions boards and begins sampling the strain gauges. If the forces or moments raise above a settable threshold for a specified period of time, the sensors identify that as a contact event and begin writing data to the hard drive at a rate of 250 Hz. To ensure that no data is lost, a buffer of two seconds on either side of every detected event is also saved to the hard drive.

In a separate execution thread, a network server waits for a connection from the MICR0-G client software (described in Section 2.2.1). When connected, the MICR0-G sensor transmits live data to the client software at a rate of 10 Hz for realtime display purposes.

Other threads control the clock display and the force-level indicator (also described in Section 2.2.1). All interactions with the sensor software are executed via a telnet connection. A flowchart depicting the basic operation of the MICR0-G sensor software can be seen in Figure 2-6.

²The typical mounting configuration of PC/104 modules is one on top of the other.

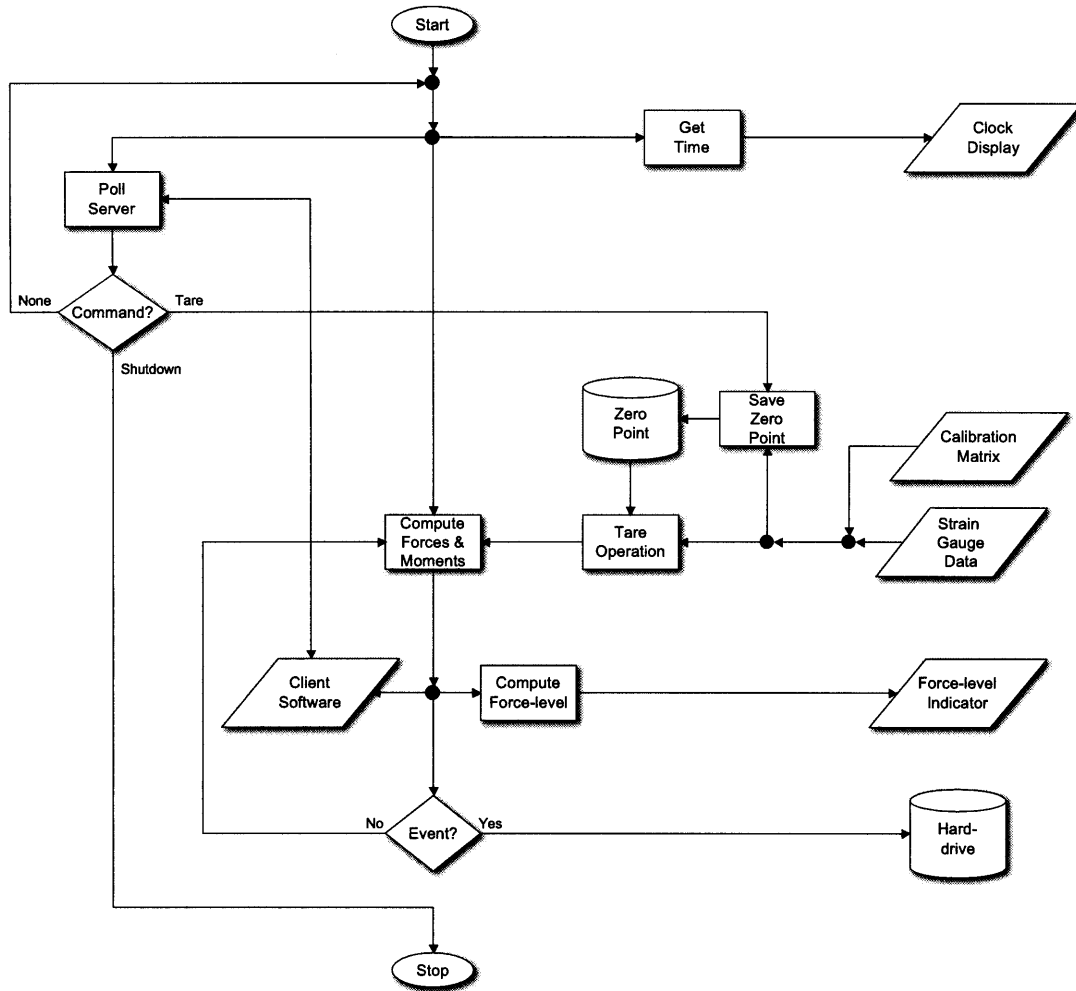


Figure 2-6: MICR0-G Sensor Software Flowchart.

Video Synchronization

A digital clock window (seen in Figure 2-2(b)) displays the six least significant digits of the Linux system time (including two digits past the decimal point). The Linux system time is stored as a double precision number representing the number of seconds since the Epoch (defined somewhat arbitrarily by the Linux community as 00:00:00 UTC, January 1, 1970). The time displayed in the sensor clock window is precisely the time saved with the force data. Thus, as long as the camera can see the clock window, the kinematic data from the video camera can be easily synchronized with the force data by simply reading the time from one of the video frames.

In order to synchronize the sensors to one another, Linux's Network Time Protocol

(NTP) is used. NTP allows Linux machines to synchronize their clocks with various publicly available atomic clock servers. However, users can identify any Linux machine running the NTP daemon as the source for their time synchronization. In the case of the MICRO-G sensors, all are setup to be peers of one another on the same stratum.³ Upon startup, the sensors poll each other and self-organize to agree upon a common time with which to synchronize. Within two or three minutes, the sensor clocks are synchronized typically to within 10 milliseconds of one another (or about two or three frames of force-moment data).

Wireless Communication

The new sensors communicate wirelessly to each other and to a central laptop, providing time synchronization, easy sensor commanding and real-time data plots. Wireless communication enables the sensors to be easily relocated anywhere within range of the wireless network. An optional battery back-up in the flight version of the MICRO-G sensors will allow the sensors to be operated for up to two hours without requiring a power hookup. Figure 2-7 shows the USB wireless ethernet adapter used in the prototype MICRO-G sensors.



Figure 2-7: The DWL-122 wireless ethernet adapter (802.11). In the prototype sensors, this adapter is attached on the bottom of the sensor backplane. In the flight version of the MICRO-G sensors, the wireless adapter will be located in an indentation on the exterior of the sensor housing to improve signal quality.

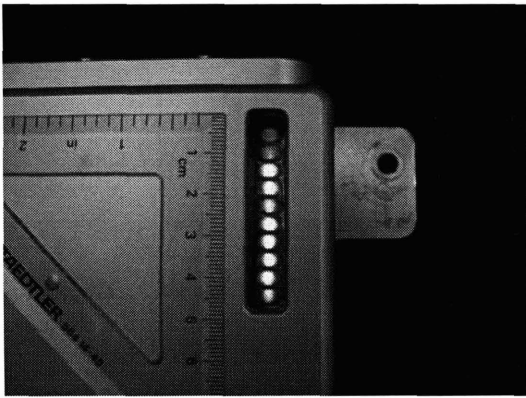
³All NTP servers must be identified with a particular stratum number. The lower the stratum number, the higher fidelity the clock source is (the few publicly available atomic clocks in the world are denoted stratum 1). Identifying different strata within local networks reduces the NTP polling delay and hence provides better time synchronization across a given network.

Realtime Feedback

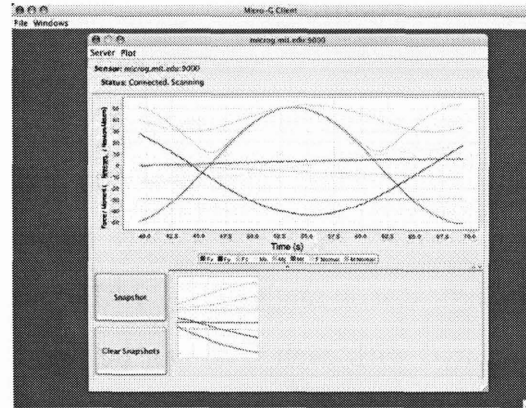
A small force-level indicator on top of the sensor provides programmable feedback to the astronauts as to the relative force magnitudes they are applying to the sensor. The indicator is made of ten LEDs, six green, two yellow and two red. The forces associated with each level can be programmed via the onboard sensor software. This kind of display not only provides feedback that the sensor is operating normally, but it can aid the astronauts in their adaptation with appropriate selection of the green, yellow and red zones. For example, astronauts could be instructed to keep their interaction forces below the red zone in order to maximize their motion accuracy. Figure 2-8(a) shows a photo of the force-level display on one of the prototype MICRO-G sensors.

In addition to the force-level indicator on the surface of the sensor, astronauts can also use the MICRO-G client software for viewing force and moment traces from a given maneuver. The MICRO-G client software connects to the sensors wirelessly and receives force and moment data at a reduced rate of 10 Hz (recall that the data saved to the on-board sensor hard drive is collected at 250 Hz). Astronauts can view the forces and moments either as a strip-chart recorder or in a moving bar-chart format. In addition to viewing data, astronauts can send commands to the sensors that either enable or disable data collection, upload new calibration matrices or zero the sensors.

One full window of data can be saved as a “snapshot” for viewing later either in the client itself or in Matlab. When snapshots are taken, the MICRO-G client software reports summary statistics of the event, including maximum and minimum forces and moments, means, medians and standard deviations. Future versions of the MICRO-G client will be able to track the astronauts’ adaptation as the experiment progresses. It is anticipated that astronauts may use the MICRO-G client as a diagnostic tool for evaluating their level of adaptation to their new environment. Figure 2-8(b) shows a screenshot of the MICRO-G client software.



(a) The force-level indicator on the surface of the MICR0-G sensors.



(b) A screenshot of the MICR0-G client software.

Figure 2-8: Realtime feedback features of the MICR0-G sensors.

Waterproofing

The new MICR0-G sensors are waterproof, permitting simulated weightlessness studies to be carried out in pools up to 10 meters deep. While operating underwater, the wireless ethernet signals are not viable due to attenuation by the water. Thus, a wired ethernet cable and the power cable are routed through waterproof connectors. All other connectors (*i.e.*, serial, VGA and keyboard) as well as the PCMCIA card slots are sealed prior to submersion underwater. Figure 2-9 illustrates a SCUBA diver installing a MICR0-G sensor at the bottom of MIT's Alumni Pool.



Figure 2-9: A photo of the new MICR0-G prototype sensor (configured as a hand-hold) being mounted during an underwater experiment. The digital display is for video synchronization.

Easy Data Backup System

The prototype MICR0-G sensors employ two standard PCMCIA card slots for additional data backup. Astronauts and/or experiment operators can easily backup the data saved on the sensor hard drives by plugging small PCMCIA drives into one of the card slots.

On the flight MICR0-G sensors, the PCMCIA card slots have been replaced by an external USB port to save space and power. More compact and higher capacity USB memory sticks can then be inserted and removed easily for data backup purposes. As with the PCMCIA card solution, the Linux operating system supports hot-swapping of USB devices, making implementation easy. The USB memory stick can be seen as a small protruding box in Figure 2-4. The larger protruding box represents the USB wireless network adapter described in Section 2.2.1.

2.2.2 Kinematic Video System

The kinematic video system provides relevant joint angle trajectories of the subjects interacting with the MICR0-G force-moment sensors. These data are then used as input into the dynamic modeling code developed by Ferguson [Ferguson and Newman, 2006]. In order to obtain the joint angles over time, the ability to track the moving joint must exist. Not only must the joint be fully visible in the field of view of the camera, but the motion must be observable from this same view. It is therefore important to arrange the cameras such that all potential movements can be captured. The camera set-up for the ground-based experiments is shown in Fig. 2-10 with the given coordinate system. The views captured by each camera are shown in Table 2.1.

The 3-D motion of the subject can be reconstructed by applying the principles of articulated movements of deformable models [Metaxas, 1996]. The use of optical flow measurements provides an added constraint to the determination of the limb movements [DeCarlo and Metaxas, 2000] and thus the joint angles. Upon experiment completion, the videos were analyzed with this knowledge using the following methodology (shown as a schematic in Fig. 2-11). The videos were first separated

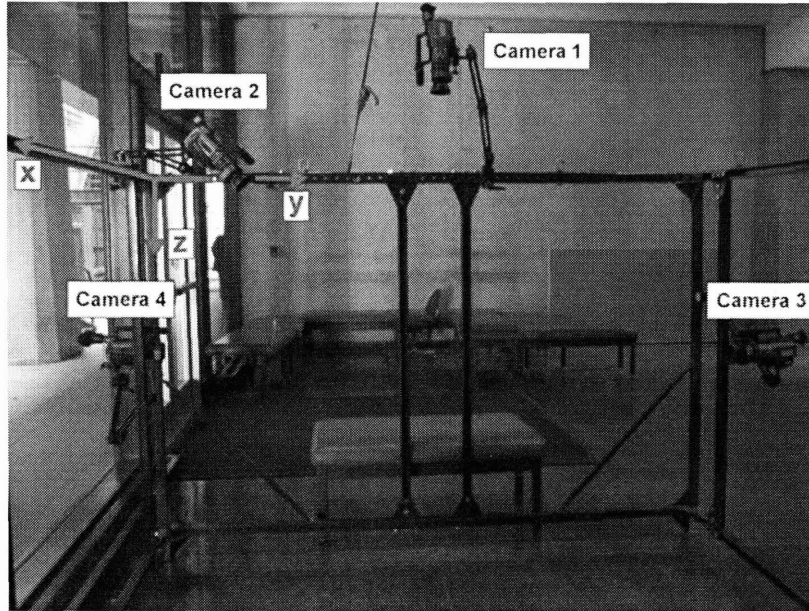
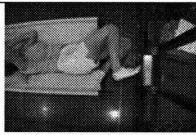





Figure 2-10: Camera configurations for the ground-based experiments.

into individual frames. The pixels in each frame were tracked using the ideas of visual and motion consistency through the optical flow code. The visual grouping is done according to color similarity and intensity. Since the optical flow problem is underconstrained, a constraint is added in order to determine the pixel movement direction and velocity [Barron et al., 1992]. The added constraint maintains motion consistency by limiting velocities of neighboring pixels. Thus the distance one pixel can move with respect to a neighboring pixel is implicitly limited. Once this is completed, custom software that implements the principles of articulated motion is used to track the movement of the limbs based on the user-selected joint locations and the optical flow information. The use of optical flow as a constraint to the articulated movement assumes that the color does not change significantly between frames. In order to account for changes in intensity and color due to shadows and variations in the object depth, the user is queried every few frames to select the location of the desired joints. The number of frames between queries can be modified by the user. With the knowledge of each camera orientation and location, data from multiple cameras enable the 3-D reconstruction of the joint angles. The task of reconstruction is made simpler when a calibration procedure is performed such that the exact position

Table 2.1: Views Captured by Each Camera

Camera Number	Coordinate Plane	Description	Image
1	xy	Top View	
2	xyz cross-plane	Perspective View	
3	xz	Side View	
4	xz	Close-up on the Sensor, Side View	

and orientation of the camera with respect to the subject is not necessary [Zhang, 1999]. However, the analyses presented here were performed using one camera view with motions visible purely in the corresponding plain.

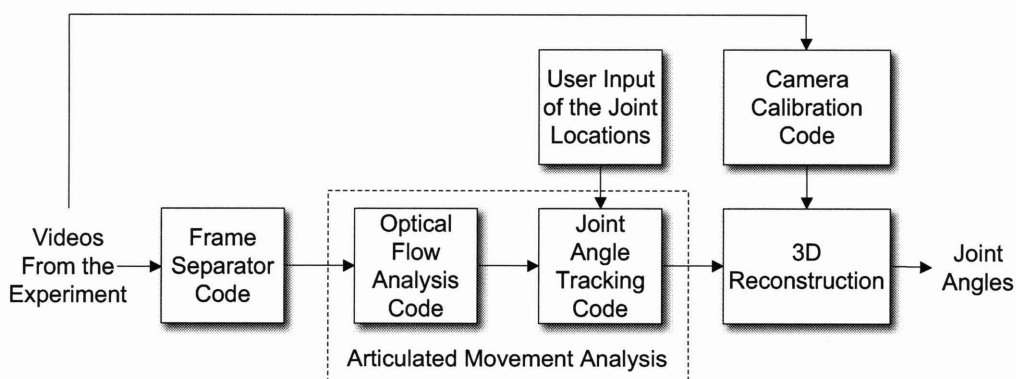


Figure 2-11: Schematic of the kinematic video analysis.

2.3 The MICR0-G Experiment

The MICR0-G flight experiment consists of two classes of experiment sessions, each repeated approximately 12 times over a single ISS increment (typically lasting six months). The first class of experiment sessions is known as the *Prescribed Motion* sessions. In these sessions, each participating crewmember will perform several body motions designed to demonstrate their locomotor control strategies. These motions will include push-offs and landings using both feet and hands, as well as several torso, leg and other body motions. Figure 2-12 illustrates a crewmember carrying out some prescribed motions.

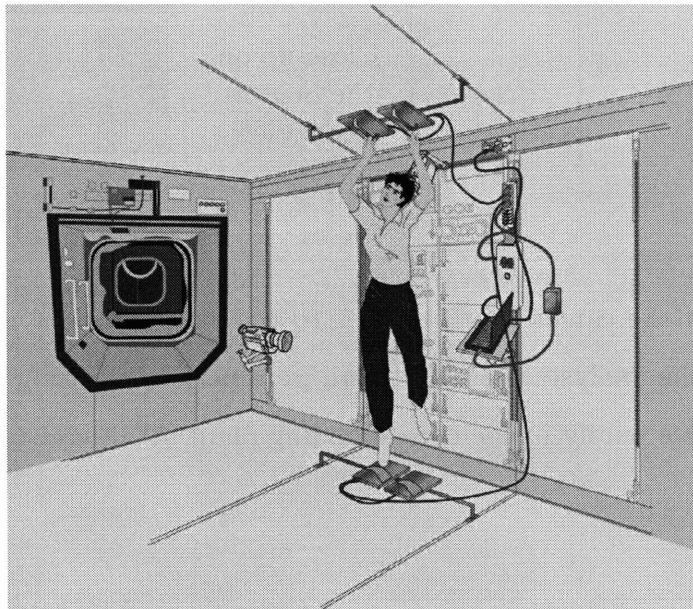


Figure 2-12: Illustration showing a crewmember using the MICR0-G foot and hand-hold sensors during a *Prescribed motion* experiment session.

Notice how in Figure 2-12, video cameras have been positioned to capture the joint angle kinematics of the prescribed body motions. One of the requirements for the prescribed motion sessions is that at least two video cameras are positioned in such a manner to capture the three-dimensional motion and permit accurate joint angle determination. The *Prescribed Motion* sessions supply controlled data at regularly-spaced intervals which will show the crew's locomotor adaptation to microgravity.

In between the *Prescribed Motion* sessions are the *Regular Daily Activity* sessions.

During these sessions, the MICR0-G sensors are powered and will record any interactions the crewmembers have with them during other science or ISS maintenance activities in close proximity to the sensors. The crewmembers will be asked to position cameras in the work area while interacting with the MICR0-G sensors to provide limited kinematic measurements, however this is not a hard requirement. The purpose of the *Regular Daily Activity* sessions is to supplement the *Prescribed Motion* data with natural crew motions.

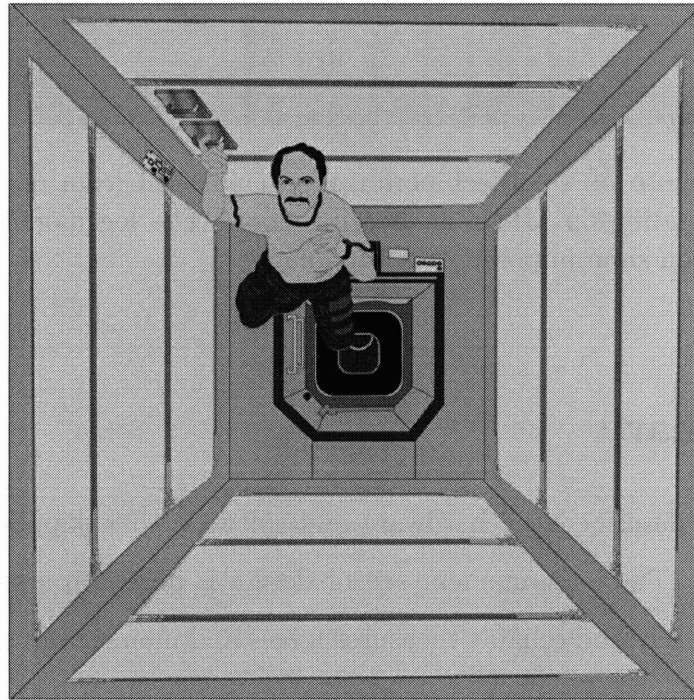


Figure 2-13: Illustration showing a crewmember using a MICR0-G handhold sensor to pull himself through an ISS module.

Details of the MICR0-G flight experiment can be found in the Experiment Document (ED) [Newman, 2005] and in [Ferguson et al., 2004b].

2.4 Sample Data

Figure 2-15 shows some typical data (forces, moments and angles) collected using the MICR0-G sensing system while a subject was performing a leg push-off (the leg model is pictured in Figure 2-14). In the following analysis, out of plane forces and

moments are ignored since they are entirely reacted by the air-bearing cart and floor and do not lead to subject motion.

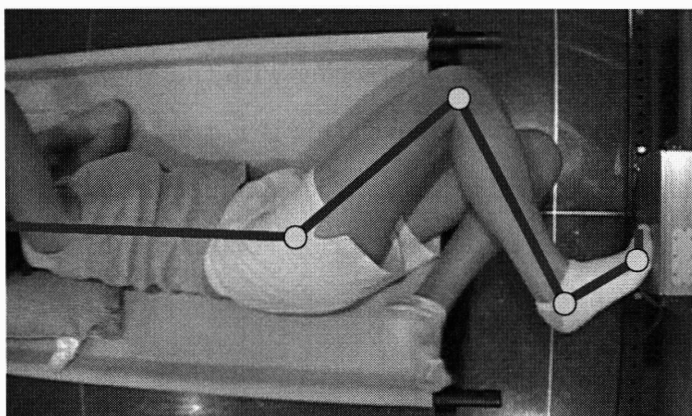
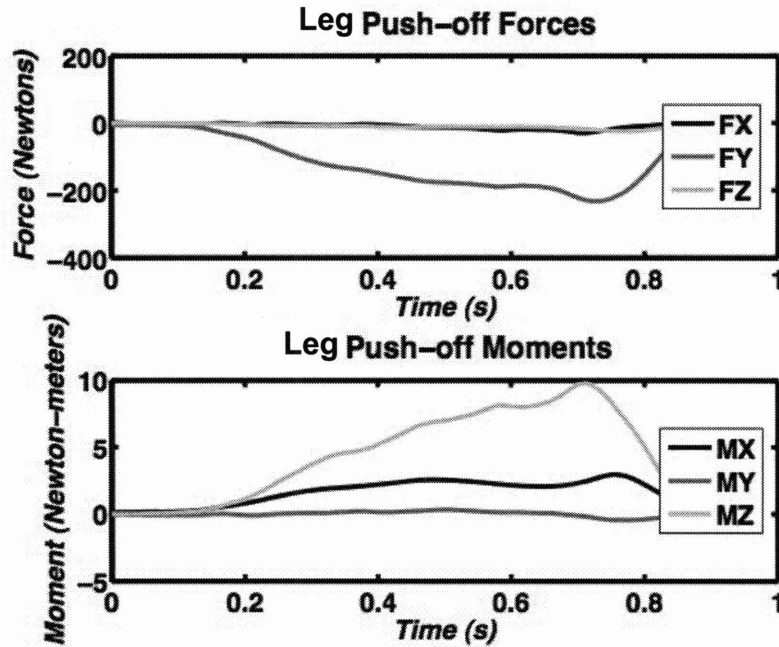


Figure 2-14: A photo of a subject performing a push-off from one of the MICR0-G sensors while gliding on MIT's air-bearing floor. The leg model used for torque estimation has been superimposed over the image.

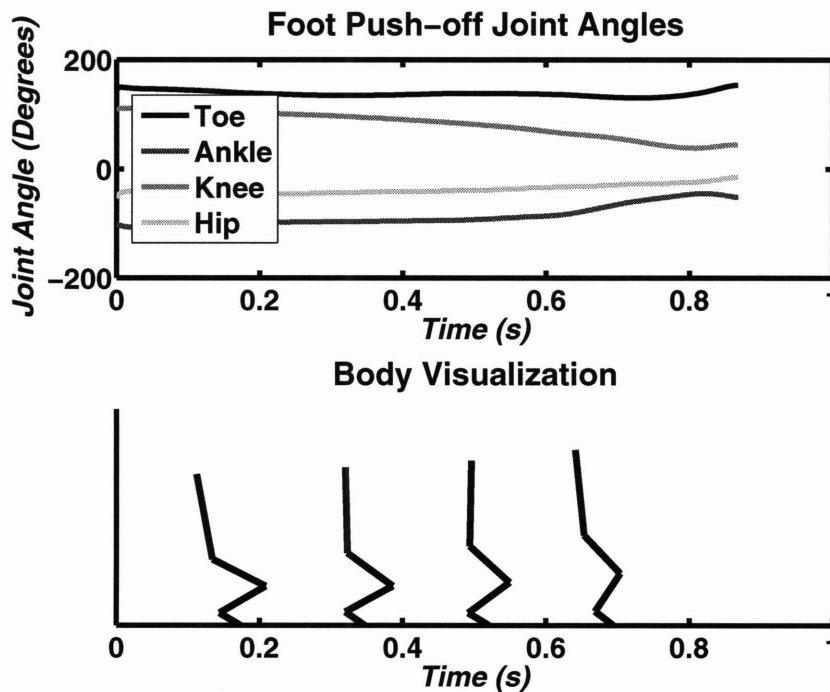
2.5 Summary

This chapter has described the hardware and software that support the MICR0-G research program. The force-moment sensor design is based on a spaceflight-proven design that accurately and reliably measures forces and moments in changing gravitational environments. New on-board electronics make the MICR0-G sensors modular, self-contained and easy to relocate, thus minimizing the crew time required to use them on-orbit. Enhanced real-time feedback features of the MICR0-G sensors engage the astronauts in the experiment and can lead to improved adaptation performance.

The next chapter presents a suite of tools developed to interpret the raw MICR0-G data. These tools include a joint control torque estimator as well as a body motion estimator.



(a) Plot of force-moment data collected using the MICR0-G force-moment sensors. Data is collected at 250 Hz only when the sensors are touched.



(b) Arm joint angles measured using the kinematic video system. The bottom plot shows the body position using the model depicted as an overlay in Figure 2-14.

Figure 2-15: Sample data resulting from a simple one-handed push-off on MIT's custom air-bearing floor.

Chapter 3

Dynamic Modelling and Analysis

Techniques

The work presented in this thesis involves the analysis and processing of vast quantities of data. Three dimensional forces and moments are collected at 250 Hz and joint angle kinematics are collected at 30 Hz. The design of the force-moment sensors and the kinematic video analysis system was described in Chapter 2. One of my hypotheses is that by analyzing the data collected from the force-moment sensors and the video system, I would be able to observe, identify and quantify the key metrics that define the control adaptation to a given environment.

In order to observe control adaptation during simple motions (*e.g.*, push-offs and landings in a microgravity environment), certainly basic metrics such as maximum force application, force application direction and net joint angle deflection from each joint can provide a great deal of insight. Since these metrics are directly derived from the force-moment and joint angle measurements, very little processing is required to extract these metrics, aside from simple low-pass filtering to remove high-frequency noise. However, other metrics such as body center of mass motion and joint control torques require a substantial amount of processing in order to arrive at the final metric.

Of course, all metrics could be derived from the joint angle measurements alone, provided they could be differentiated twice to yield joint rates and joint accelerations.

The angles, rates and accelerations together with reasonable estimates of the dynamic parameters of the subjects' bodies would, in theory, provide all of the kinematic and dynamic information about a given movement. However, given that the joint angle measurements are imperfect and often tainted with noise, reliable differentiation once is difficult and differentiation twice often leads to meaningless, noisy accelerations. Estimation by differentiation in this manner is explored further in this section to demonstrate the associated difficulties.

The basic problem associated with observing and analyzing dynamic motions using position measurements alone is the lack of true acceleration information. Fortunately, the force-moment measurements collected by the MICRO-G force-moment sensors provide this missing acceleration information. However, whereas the kinematic joint angle measurements lack acceleration information, the force-moment measurements provide position information. In theory, if the initial joint angles of a subject were known and the degrees of freedom of the model were sufficiently small compared to the richness of the motion (see Section 3.2.4 for more details), the forces and moments could be integrated to yield a complete picture of the body motion and dynamics and thence the desired metrics. Due to the double integration, however, errors continually accrue and the reliability of the resulting position information degrades over time. Figure 3-1 illustrates the information content of kinematic and kinetic measurements graphically.

An obvious solution to the problem described above is to *combine* both the kinematic and kinetic measurements together to yield more accurate estimates of the adaptation metrics than would have been achieved using one or the other measurements alone. Furthermore, knowing something about the system dynamics should also provide more insight into obtaining more reliable metrics. The question, however, is how to do this effectively. This chapter describes the modelling and analysis algorithms that were developed as part of this research program to reduce and interpret the kinetic and kinematic data. Custom filters, derived from non-linear Kalman filters, were developed that assimilate the force, moment and joint angle information along with knowledge of the system dynamics into reliable body position and joint torque estimates.

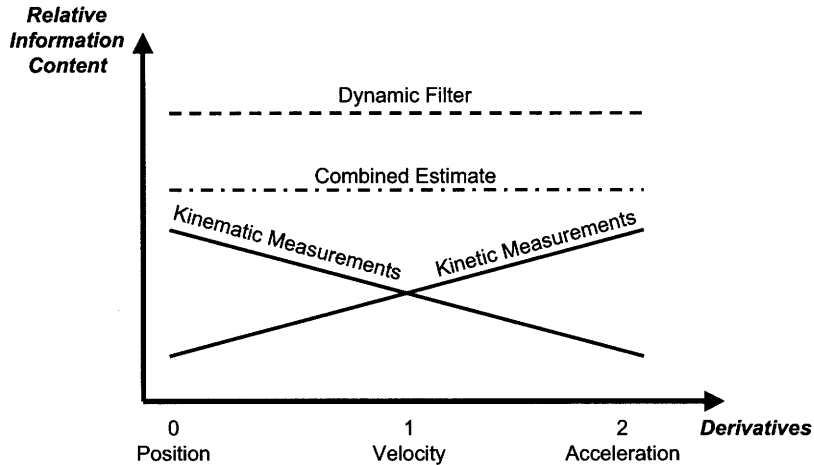


Figure 3-1: The relative information content in kinematic (joint angle) and kinetic (force & moments) measurements. The bottom two lines show the information gained by assimilating the data and then introducing a filter cognizant of the system dynamics respectively.

3.1 Body Center of Mass Tracking

When observing the motion of a human, it is often useful to answer the question, where is the location of a subject’s center of mass (COM)? In a gravity-based environment, the primary means of human locomotion is some form of walking, loping, hopping or otherwise, depending on the acceleration due to gravity [Carr, 2005]. With each step on the ground, humans apply forces to their body and their center of mass accelerates. The resulting motion of the center of mass position is a wave that repeats with each step. In microgravity, Newton’s laws dictate that the motion of the body center of mass follow a perfect straight line after the subject loses contact with the surface used to push-off from. During the push-off, however, the center of mass position and velocity can change as the push-off force varies.

3.1.1 Estimator Development

A Kalman filter is proposed to estimate the position and velocity of the center of mass of the subject during a push-off maneuver. By combining the force and joint angle measurements with the joint angle data from the kinematic video system, along with knowledge of the system dynamics, it is anticipated that a better estimate of

the COM motion will result.

As with any estimator development, the first step is defining the quantity to be estimated, followed by the measurements and finally the dynamics, if known. In the case of estimating body center of mass motion, the state vector is defined as:

$$\mathbf{X}_{com} = \begin{bmatrix} \mathbf{x}_{com} \\ \dot{\mathbf{x}}_{com} \end{bmatrix} \quad (3.1)$$

where \mathbf{x}_{com} is the cartesian position of the center of mass of the subject and $\dot{\mathbf{x}}_{com}$ denotes the time derivative of \mathbf{x}_{com} .

As described earlier, the measurements available to estimate our state vector \mathbf{X}_{com} are the kinematic joint angles (from the video system) and the kinetic force and moment measurements (from the force-moment sensors). However, only the joint angles can be used as true measurements in the estimator since the forces and moments can not be expressed as functions of the state vector. The force - moment “measurements” will be used to describe the control inputs to the plant dynamics.

Figure 3-2 illustrates the configuration of the rigid body model assumed for estimation purposes. Each link of the limb represents a given segment of the body. For instance, a 4-link model used to describe leg push-offs could include a toe, ankle, knee and hip joint. Figure 2-14 from Chapter 2 illustrates such a model overlaid on top of an image of a subject.

Figure 3-2 depicts a planar model, only capable of motion in the xy plane. Given the degrees of freedom of the human leg and the natural tendencies of subjects during motions, a planar leg model is usually adequate. The following analysis will assume planar motion. It should be noted, however, that extension of these models and methods to three dimensions would require only minor changes to the descriptions of the measurements and dynamics.

The forward kinematics of a simple, two-link model are described by the trigonometric relations below:

$$x = l_1 \cos(\theta_1) + l_2 \cos(\theta_1 + \theta_2) \quad (3.2)$$

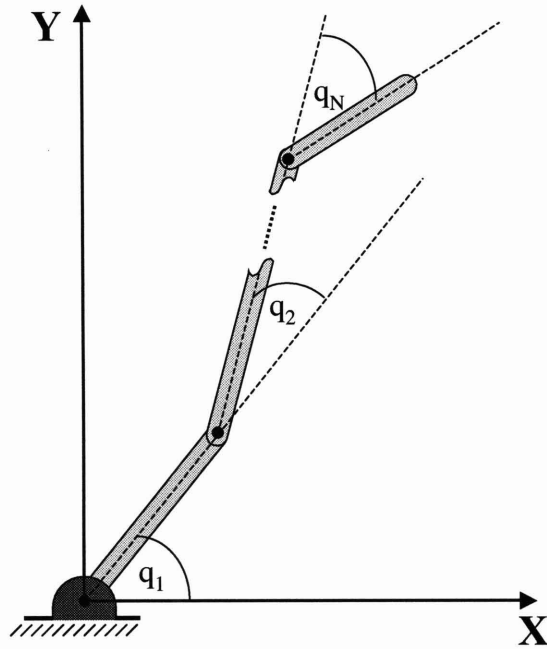


Figure 3-2: An N-link limb in one plane. The joint angles are represented as θ_i where i is the joint number.

$$y = l_1 \sin(\theta_1) + l_2 \sin(\theta_1 + \theta_2) \quad (3.3)$$

where l_i is the length of the i^{th} link.

The position of the body center of mass is a function of the body joint angles. It should be noted that the position of the center of mass may not necessarily lie on the body itself. Equation 3.4 describes the cartesian coordinates of the body center of mass location.

$$\mathbf{x}_{com} = \left(\sum_{i=1}^n \mathbf{x}_{ci} m_i \right) / \left(\sum_{i=1}^n m_i \right) \quad (3.4)$$

where \mathbf{x}_{ci} represents the cartesian position vector of the center of mass of the i^{th} link and m_i represents the mass of the i^{th} link. The center of mass positions of each link are simple trigonometric functions of the joint angles that take very similar forms to the forward kinematics equations described in Equations 3.2 and 3.3.

In order to implement a dynamic filter, it is necessary to express the measurements as a function of the state vector. For a two-link model, it is possible (for most

configurations) to invert Equations 3.2, 3.3 and 3.4 to obtain:

$$\boldsymbol{\theta} = \mathbf{h}(\mathbf{x}_{com}) \quad (3.5)$$

where $\mathbf{h}(\mathbf{x}_{com})$ is a non-linear combination of inverse trigonometric functions. However, in general, for greater than two links, forming Equation 3.5 is not possible.

In order to get around this difficulty, Equation 3.4 can be used to generate a “pseudo-measurement” of the body COM directly. The only complication with this technique is that now, the measurement variance matrix, R , is no longer constant, but now depends on the joint angles, $\boldsymbol{\theta}$.

To determine R from $\boldsymbol{\theta}$, one must go back to the basic definition of the measurement variance matrix. From first principles,

$$R = E\langle(\delta\mathbf{y}_{com})(\delta\mathbf{y}_{com}^T)\rangle \quad (3.6)$$

where \mathbf{y}_{com} is the measurement vector. If each element of \mathbf{y}_{com} is independent, R from Equation 3.6 is simply a diagonal matrix with the individual variances of each measurement located on the diagonal. When creating “pseudo-measurements”, however, each element is no longer independent and one would expect off-diagonal entries in R .

Taking the first variation of Equation 3.4 results in:

$$\delta\mathbf{x}_{com} = \delta\mathbf{y}_{com} = f(\delta\boldsymbol{\theta}) \quad (3.7)$$

where $f(\delta\boldsymbol{\theta})$ is, in general, a linear function of $\delta\boldsymbol{\theta}$. Substituting Equation 3.7 into Equation 3.6 and taking the expectation provides an expression for R , which is now a function of $\boldsymbol{\theta}$.

While the above technique provides a good estimate for how R will change with $\boldsymbol{\theta}$, it runs into difficulties when the body position nears singularities. If any body angles are (or near) an integer multiple of $\pi/2$, certain diagonal elements of R may reduce to zero. Clearly, this cannot be the case, since simply transforming one measurement

vector into another cannot reduce the measurement error down to zero. The reason why this occurs is because the covariance matrix by definition only considers the expected value of the first variation squared of a function and this first variation can go to zero while the second and higher order terms do not. In other words, looking at a Taylor series expansion, the covariance matrix assumes terms that are second order and beyond are negligible. In fact, if the measurements were tainted with true Gaussian noise (an assumption that is always made prior to constructing a Kalman filter), all but the first and second central moments (*i.e.*, standard deviation and variance) would be identically zero. In constructing the “pseudo-measurements” of Equation 3.4, however, non-Gaussian measurements have been created and appropriate actions must be taken to ensure that R does not become singular for any values of θ .

To remedy this problem, a small diagonal factor is added to R to ensure it is always positive definite. The term needs to be big enough to ensure numerical stability when inverting R , but not so big that it causes the Kalman filter to essentially ignore the measurements. Since the need for this extra term stems from ignored second order terms, it seems appropriate that the additional term take the form of the variance squared. Thus, the expression for the measurement covariance matrix is:

$$R = R(\theta) + \xi_R \quad (3.8)$$

where $R(\theta)$ is computed from Equations 3.7 and 3.6 and

$$\xi_R = \begin{bmatrix} \sum_{i=1}^n l_i^2 \sigma_{\theta_i}^4 & 0 \\ 0 & \sum_{i=1}^n l_i^2 \sigma_{\theta_i}^4 \end{bmatrix} \quad (3.9)$$

With the measurements, \mathbf{y}_{com} and their associated covariance estimates, R defined as above, the measurement equation can be expressed as:

$$\mathbf{y}_{com} = H\mathbf{X}_{com} \quad (3.10)$$

where

$$H = \begin{bmatrix} 1 & 0 & 0 & 0 \\ 0 & 1 & 0 & 0 \end{bmatrix} \quad (3.11)$$

Continuing with the Kalman filter development, the dynamics and process noise must now be defined. The dynamics of motion of the body COM follow Newton's laws of motion. The force inputs are simply the measured forces from the force-moment sensor. In the absence of gravity or other friction forces, the dynamics can be written as:

$$\dot{\mathbf{X}}_{com} = A\mathbf{X}_{com} + B\mathbf{F} \quad (3.12)$$

where

$$A = \begin{bmatrix} 0 & 0 & 1 & 0 \\ 0 & 0 & 0 & 1 \\ 0 & 0 & 0 & 0 \\ 0 & 0 & 0 & 0 \end{bmatrix} \quad (3.13)$$

$$B = \begin{bmatrix} 0 & 0 \\ 0 & 0 \\ \sum_{i=1}^n m_i & 0 \\ 0 & \sum_{i=1}^n m_i \end{bmatrix} \quad (3.14)$$

and \mathbf{F} is the vector of two-dimensional forces measured from the force-moment sensor.

The continuous process noise matrix, Q comes from the measurement noise variance of the force-moment sensor. Thus,

$$Q = \begin{bmatrix} 0 & 0 & 0 & 0 \\ 0 & 0 & 0 & 0 \\ 0 & 0 & (\sigma_{\mathbf{F}} / (\sum_{i=1}^n m_i))^2 & 0 \\ 0 & 0 & 0 & (\sigma_{\mathbf{F}} / (\sum_{i=1}^n m_i))^2 \end{bmatrix} \quad (3.15)$$

All of the pieces are now in place to execute a traditional Kalman filter. The equations for a generic Kalman filter are found below:

Kalman Measurement Update

$$K_k = P_k^- H^T (H P_k^- H^T + R_k)^{-1} \quad (3.16)$$

$$\hat{\mathbf{X}}_k^+ = \hat{\mathbf{X}}_k^- + K_k (\mathbf{y}_k - H \hat{\mathbf{X}}_k^-) \quad (3.17)$$

$$P_k^+ = (I - K_k H) P_k^- \quad (3.18)$$

Kalman Time Update

$$\hat{\mathbf{X}}_{k+1}^- = \Phi_k \hat{\mathbf{X}}_k^+ + B_k \mathbf{u}_k \quad (3.19)$$

$$P_{k+1}^- = \Phi_k P_k^+ \Phi_k^T + Q_k \quad (3.20)$$

where k denotes the current time-step, $(\cdot)^-$ indicates a quantity before the measurement update, $(\cdot)^+$ indicates a quantity after the measurement update and Φ is the state transition matrix.

3.1.2 Simulations and Results

A simulation of a 4-link model performing a simple “extension” maneuver was created to test the estimator described in the previous section. First, the truth was simulated and the resulting joint angles were recorded. Next, artificial Gaussian white measurement noise was added to the joint angles ($\sigma_\theta = 1^\circ$) and the body COM position was computed at each time-step. The resulting reaction force trace was computed from the truth angles and artificial Gaussian white measurement noise was added ($\sigma_F = 1N$).

The filter was initiated using an initial estimate of the body COM position that had an error consistent with the joint angle measurement errors. The estimated position and velocity were recorded and compared with the truth. Figure 3-3 illustrates the position and velocity errors as well as the $1 - \sigma$ covariance bounds as a function of time during the extension maneuver.

It is interesting to note in Figure 3-3 that the error (and indeed the error covariance bounds) decreases over time. This improvement is expected since the filter is able

to glean more and more dynamic information about the system as the richness of the motion increases. Since the extension maneuver contained primarily y motion with very little x component, the filter was able to obtain a higher accuracy in the y direction than in the x direction.

Figure 3-4 illustrates the body COM motion as seen in the cartesian plane. Figure 3-4 shows the benefit of the dynamic filter by plotting the results obtained by using just the forces or the joint angles alone.

While the joint angle measurements alone always have traceability back to the approximate position of the body COM, the noise greatly obscures the result. Furthermore, it is clear that differentiating the noisy joint angle measurements would not yield any useful velocity estimates.

The forces, on the other hand, produce a relatively smooth estimate, but it is greatly affected by the initial starting point. Without joint angles to aid in the starting location, a conservative initial error estimate of less than 10 centimeters was assumed. In reality, this error could easily be much worse. Notice how the estimate using the force measurements alone is never able to come close to the true body COM position because it contains no direct position information.

The estimate obtained using the Kalman filter is able to effectively extract the best parts of each signal to obtain a useful and reliable estimate. The covariance bounds associated with the Kalman filter estimate conveys the degree to which these estimates can be trusted.

The previous section has described the design of a dynamic filter to combine kinetic force measurements with kinematic joint angles to arrive at an accurate estimate of the body COM motion (position and velocity). The next section explores how the same measurements can be used to estimate the joint control torques that were used to affect the observed motion.

3.2 Joint Torque Estimation

For years, researchers have been developing theories regarding how humans control their limb and body motions [Gribble et al., 1998, Gomi and Kawato, 1996, Flash and Hogan, 1985, Bizzi et al., 1994]. Many researchers develop models to predict human motion under a variety of conditions. To verify the models, simulation results are often compared to actual human motion experiments. While simple joint angle trajectory comparisons may provide a cursory performance comparison, alone they do not provide insight into the dynamics being controlled. Since many widely accepted limb control strategies rely on control torques being applied to joints (resulting either through explicitly computed torques [Gribble et al., 1998] or those generated naturally by the spring-like properties of muscles [Bizzi et al., 1982]), one means of characterizing human motion controllers is to study the joint control torques.

[Bergmann et al., 1995] have measured joint control torques directly by instrumenting hip joints with strain gauges. While these techniques can provide relatively high accuracy joint control torque information, they come at the price of invasive surgical procedures, garments or prostheses that can impede the natural motion of the human subjects.

Without measuring joint torques directly, the only other option is to non-invasively measure several indirect quantities and use them to estimate the joint torques. Estimating joint torques for multi-link limbs is complicated by several factors, including:

- The strong non-linearity of the system dynamics
- Their dependence on joint accelerations, which are difficult to measure
- The unpredictability of joint torques
- The fact that joint torques need not be continuous

Many studies measure joint angles using either a manipulandum [Flash, 1987, Gomi and Kawato, 1996] or a video-kinematic tracking system [Amir et al., 2001]. To obtain the joint torques, the angles are differentiated twice to obtain rates and accelerations. Inverse dynamics are then used to compute the dynamic joint torques. This

technique can work well, provided the joint angles can be effectively differentiated. Often, however, the joint angle data is noisy, leading to even noisier rate estimates and often useless acceleration information.

Other studies have employed the use of force-plates to measure ground reaction forces and moments during a particular body motion [Newman et al., 2001]. Ground reaction forces and moments can be useful for computing joint control torques since both joint torques and reaction forces/moments are related to joint accelerations. Several other researchers have attempted to back out robot joint control torques from reaction forces and torques measured at the base of the robot arm [DeVita and Hortobagyi, 2003, Morel et al., 2000, Nagano et al., 1998]. However, all have relied on estimates of joint acceleration¹ that can be extremely difficult to estimate from noisy joint angle measurements (as described above).

This chapter provides a novel dynamic estimation algorithm that effectively combines joint angle measurements (kinematics) with force-plate reaction forces (kinetics) without requiring accurate acceleration information to estimate the joint control torques in addition to the joint angle and rate states of a multi-link limb. Before developing the estimator, the next section presents a brief background on the statics and dynamics of multi-link limbs.

3.2.1 Multi-Link Limb Statics and Dynamics

Figure 3-2 illustrates the generic limb configuration considered in this chapter.² Joint angles are denoted as θ_i where i is the joint number. The (x, y) position in space of the tip of the limb can be represented as a function of the joint angles, θ_i . For a 2-link limb, these tip position coordinates are computed as in Equations 3.2 and 3.3 above. Differentiating Equations 3.2 and 3.3 and rearranging, one can define the *Jacobian* matrix $J(\boldsymbol{\theta})$ as:

¹With the exception of Morel [Morel et al., 2000] who assumes that for fine motion tasks, acceleration terms can be ignored.

²For simplicity, the examples presented throughout this thesis will address only planar motion. A simple extension of these methods permits application to motion in three dimensions.

$$d\mathbf{x} = J(\boldsymbol{\theta}) d\boldsymbol{\theta} \quad (3.21)$$

where

$$\mathbf{x} = \begin{bmatrix} x \\ y \end{bmatrix} \quad (3.22)$$

and

$$\boldsymbol{\theta} = \begin{bmatrix} \theta_1 \\ \theta_2 \end{bmatrix} \quad (3.23)$$

If we apply a constant force, \mathbf{F}_t to the tip of the limb and assume that the limb is not in motion, the principle of virtual work states that:

$$\mathbf{F}_t d\mathbf{x} = \tau d\boldsymbol{\theta} \quad (3.24)$$

where τ is the vector of joint torques. Substituting Equation 3.21 into Equation 3.24 and rearranging results in:

$$\tau = J(\boldsymbol{\theta})^T \mathbf{F}_t \quad (3.25)$$

Equation 3.25 illustrates how static forces translate into joint torques. Equation 3.25 does not account for any inertial, centripetal, Coriolis or frictional torques that are present when a limb is in motion.

To account for all dynamic torques, one must consider the full dynamic equations of motion of a multi-link limb. [Asada and Slotine, 1986] discuss several different ways to derive these equations. The resulting dynamic equations can be expressed as:

$$\tau = H(\boldsymbol{\theta}) \ddot{\boldsymbol{\theta}} + C(\boldsymbol{\theta}, \dot{\boldsymbol{\theta}}) \dot{\boldsymbol{\theta}} + D(\boldsymbol{\theta}, \dot{\boldsymbol{\theta}}) \dot{\boldsymbol{\theta}} + G(\boldsymbol{\theta}) \quad (3.26)$$

where $H(\boldsymbol{\theta})$ is the configuration dependent inertia matrix, $C(\boldsymbol{\theta}, \dot{\boldsymbol{\theta}})$ is the centrifugal/Coriolis matrix, $D(\boldsymbol{\theta}, \dot{\boldsymbol{\theta}})$ is the joint friction (or damping) matrix and G is the vector of torques due to gravity.

Equation 3.26 illustrates the non-linear dependence of joint angles, rates and accelerations on the joint control torques. Thus, estimating dynamic control torques requires developing some knowledge of angles, rates and accelerations. Fortunately, angle and (noisy) rate information can be determined from a video tracking system [Pedrocchi et al., 2003, Amir et al., 2001, Pedrocchi et al., 2005, Goldenstein et al., 2003] and accelerations can be inferred from the force-plate information. Assuming the limb remains in contact with the force-moment sensor, the force vector, \mathbf{F}_b , can be expressed as:

$$\mathbf{F}_b = \sum_{i=1}^{i=N} m_i \ddot{\mathbf{r}}_i + \mathbf{F}_G \quad (3.27)$$

where m_i and $\ddot{\mathbf{r}}_i$ is the mass and acceleration, of the i^{th} link respectively, \mathbf{F}_G is the total gravity weight (if applicable) and N is the total number of links. Similarly, the moments measured by the force-moment sensor, \mathbf{M}_b , can be expressed as:

$$\mathbf{M}_b = \sum_{i=1}^N \mathbf{r}_i \times m_i \ddot{\mathbf{r}}_i + I_i \dot{\boldsymbol{\omega}}_i + \boldsymbol{\omega}_i \times (I_i \boldsymbol{\omega}_i) \quad (3.28)$$

where I_i , $\boldsymbol{\omega}_i$, $\dot{\boldsymbol{\omega}}_i$ are the moment of inertia, angular velocity and angular acceleration respectively of the i^{th} joint as expressed in reference frames attached to the center of mass of each joint.

Since Equations 3.27 and 3.28 depend on the cartesian acceleration of each link in the limb, they also depend on the joint angle accelerations. This relationship is found by twice differentiating N-link versions of Equations 3.2 and 3.3 and combining with Equation 3.27. As such, combining Equations 3.26, 3.27 and 3.28 with measurements of joint angles and force-moment data should provide enough information to compute the joint control torques. The following section develops a dynamic estimator that effectively combines both angle and force-moment measurements to arrive at a better estimate than would be computed from angle measurements alone.

3.2.2 Estimator Development

Classical dynamic state estimators (such as the one developed in Section 3.1.1) follow the flow pictured in Figure 3-5. Assuming the control inputs are known, the state for the next time-step is predicted. Measurements from this new time-step are then incorporated to correct the predicted estimate and the iteration continues.

In the case of estimating joint control torques, while the dynamics are known (Equation 3.26), the control inputs pictured in Figure 3-5 are not immediately available since they are the quantity being estimated. Furthermore, since control torques are chosen by the subject, they cannot be predicted by any dynamic equation. Thus, conventional predictor-corrector estimators (*e.g.*, Kalman filters) are not appropriate for solving this problem and other single-step methods³ must be explored.

When designing an estimator of any kind, one must first decide on the state vector to be estimated. A logical choice for the state vector would be joint control torques; however, this choice provides a substantial mathematical difficulty since the measurements must be expressed as a function of the state vector. Given the nonlinearities of Equations 3.26, 3.27 and 3.28, it is not possible to find an expression for the joint angles or reaction forces as a function of joint torques alone. To simplify the mathematics, a state vector containing joint angles, rates and accelerations will be used. Then, with a good estimate of joint angles, rates and accelerations, Equation 3.26 can be used to compute the joint control torques (*i.e.*, inverse dynamics). The state vector, \mathbf{X} , for this filter is thus defined as:

$$\mathbf{X} = \begin{bmatrix} \boldsymbol{\theta} \\ \dot{\boldsymbol{\theta}} \\ \ddot{\boldsymbol{\theta}} \end{bmatrix} \quad (3.29)$$

The measurements available for estimation from the kinematic video system and

³Single step estimators only perform the “correction” step of the predictor-corrector estimator depicted in Figure 3-5.

a force-moment plate are:

$$\mathbf{y} = \begin{bmatrix} \boldsymbol{\theta} \\ \mathbf{F}_b \\ \mathbf{M}_b \end{bmatrix} + \boldsymbol{\nu} = \mathbf{h}(\mathbf{X}) + \boldsymbol{\nu} \quad (3.30)$$

where $\mathbf{h}(\mathbf{X})$ represents the nonlinear measurements as a function of the state vector, \mathbf{X} and $\boldsymbol{\nu}$ is a vector of normally distributed Gaussian white noise with zero mean and standard deviation of R (denoted $N(0, R)$). R is a diagonal matrix that defines the expected noise or reliability of each measurement (expressed as the *variance* (σ^2) of the signal); the higher the diagonal entry in R , the more uncertain the associated measurement.

The optimal single-step estimator for a linear system with measurements tainted by Gaussian white noise is known as a “least squares” estimator. However, given the nonlinear measurements in Equation 3.30, the linear least squares estimator cannot be used. Instead, an iterated nonlinear least squares estimator must be used. While not optimal, the nonlinear least squares estimator (NLSE) can provide a good one-step estimate of a state vector with noisy nonlinear measurements [How, 2002]. The development of the nonlinear least squares estimator can be found in Appendix B.

As seen in Appendix B, the nonlinear least squares algorithm requires a guess of the full state vector at each time step. The guess state is required because the full state is not completely observable given the measurements for any limb larger than two links. The observability of the state given a particular set of measurements can be found by computing the rank of the *information content* of the measurements. The information content, Y , is defined as:

$$Y = H^T R^{-1} H \quad (3.31)$$

where H is the linearized measurement matrix such that

$$\mathbf{h}(\mathbf{X}) \approx H\mathbf{X} \quad (3.32)$$

If the rank of Y is less than the length of the state vector \mathbf{X} , then the full state is not observable. Unless the measurement vector contains repeated measurements of the same quantity, the rank of Y is usually equal to the number of measurements. For a planar manipulator, only two forces and one moment are non-zero. Incorporating the joint angle measurements to the force and moment measurements provides:

$$\text{rank}(Y) = N + 3 \quad (3.33)$$

Equation 3.33 indicates that in order to estimate all angles, rates and accelerations of each joint (*i.e.*, $3N$ elements) a good prior estimate must exist since the rank of Y is always less than the length of X for any limb with more than one joint.

The measured joint angles can form the position portion of the NLSE guess state. Guess joint rates can be found via filtered differentiation of the measured joint angles. However, as stated earlier, differentiating a second time to obtain an estimate of the joint accelerations is often not practical. To obtain an appropriate guess of the joint accelerations, a preliminary NLSE step can be taken to estimate the joint accelerations using the force and moment measurements alone. For a limb with 3 or fewer joints, the joint accelerations are completely observable and an appropriate initial joint acceleration guess would be zero for all joints. If $N > 3$ or if no moment measurements are available⁴, a rough estimate of the joint accelerations may be required, however in most cases, an initial estimate of zero for all joint accelerations is sufficient.

The acceleration estimates from the preliminary NLSE step described above along with the measured joint angles and differentiated joint angles can now form the complete guess state for the full NLSE step, which is further described in Appendix B.

The NLSE results in an estimate of the joint torques, based partially upon differentiated angle measurements to obtain rate and acceleration information. With knowledge of the joint torques, the full system dynamics are known and a dynamic (two-step) estimator can be used with the original measurements to obtain a more ac-

⁴See Section 3.2.4 for a more detailed discussion of torque estimation without moment measurements.

curate estimate of the joint angles, rates and accelerations. The estimate computed using a dynamic estimator will be better than the differentiation of noisy angles because a dynamic estimator can make use of the plant dynamics to observe the changing state and aide in the estimation. The only remaining question is what kind of dynamic estimator should be used?

Given the non-linear dynamics (Equation 3.26) and measurements (Equations 3.27 and 3.28), a regular Kalman filter cannot be used. One option would be to use an Extended Kalman Filter (EKF) [Gelb et al., 1999]. However, while the EKF handles some of the linearization errors associated with a traditional Kalman Filter, it still requires linearization of the state dynamics to propagate the covariance matrix. Linearizing Equations 3.27 and 3.28 is manageable, however, linearizing Equation 3.26 is extremely tedious and prone to error, especially for limbs with greater than two joints.

The Unscented Kalman Filter (UKF) is a filter designed to remove the burden and error-inducing effects of linearizing the measurement and dynamic equations [Julier and Uhlmann, 2004, Wan and van der Merwe, 2001]. The UKF works by generating a selection of solution points with an associated mean and covariance and then propagating each one nonlinearly through the dynamics. The mean and covariance of the newly propagated points is then evaluated to determine the new estimate and covariance. Appendix C outlines the equations used in the UKF. For a detailed development of the UKF, see [Julier and Uhlmann, 2004] and [Wan and van der Merwe, 2001].

It should be noted here that while the UKF state vector contains the joint accelerations, the UKF cannot actually estimate the accelerations since they are not *true* state variables.⁵ However, since the force and moment measurements depend on joint accelerations, the accelerations are required to execute the UKF. Knowing the joint angles, rates and control torques, the joint accelerations can be computed by

⁵A state variable is one that is required to completely describe a dynamical system at any point in time. Typically, a state vector contains only position and velocity states. Accelerations can change instantaneously and do not hold any “memory” in the same way that position and velocity states do, so they are not considered state variables.

re-arranging Equation 3.26 as:

$$\ddot{\boldsymbol{\theta}} = H^{-1}(\boldsymbol{\theta}) \left[\tau_c - C(\boldsymbol{\theta}, \dot{\boldsymbol{\theta}}) \dot{\boldsymbol{\theta}} - D(\boldsymbol{\theta}, \dot{\boldsymbol{\theta}}) \dot{\boldsymbol{\theta}} - G(\boldsymbol{\theta}) \right] \quad (3.34)$$

Figure 3-6 illustrates how the UKF and the NLSE are combined to form the new torque estimation technique.

3.2.3 Simulations and Results

Simulations were developed to test the estimator described in the previous section. The simulations represent human subjects performing a standing maneuver taking one second to complete. The motions are controlled by a simple proportional-derivative (PD) joint controller. The resulting control torques, joint angles, rates and accelerations are saved and denoted the “truth”. From the truth, noisy measurements are generated and used to estimate the actual joint torques, angles and rates.

Two models of a human were developed: one represents a human with three joints and the other represents a human with four joints. The three-joint configuration models the ankle, knee and hip joints. With these joints, the segments between the joints represent the lower leg, upper leg and torso. The four-joint configuration models the toe, ankle, knee and hip joints. The corresponding segments represent the foot (behind the toes), lower leg, upper leg and torso. Table 3.2.3 describes the mass properties of the body parts used for the simulations.

Table 3.1: Mass properties for the limb models.

Link	Length (m)	Mass (kg)
Foot	0.12	0.3
Lower Leg	0.40	5.0
Upper Leg	0.40	10.0
Torso	0.80	45.0

The inertias of each limb segment were computed assuming they were uniform

density rods as:

$$I = m \frac{l^2}{12} \quad (3.35)$$

where m is the mass of the limb segment and l is the length of the limb segment. The joint friction of each joint was assumed to be zero. Section 3.2.4 provides a brief discussion on why joint friction values were not included in the models.

Random noise was added to all measurements to ensure appropriate realism. The angle measurements used in the simulations were assumed to be accurate to within $\pm 1^\circ$, force measurements to within $\pm 0.2 N$ and the moment measurements to within $\pm 0.5 Nm$.

When propagating the truth states, process noise was added to simulate unmodeled effects. At every time step, random noise was added to the velocities ($0.1^\circ/s$) and joint accelerations ($0.2^\circ/s^2$).

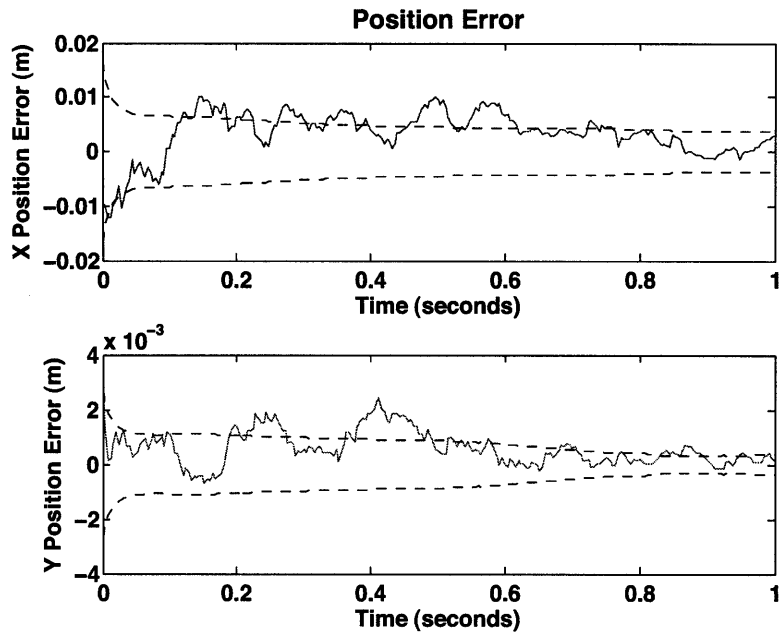
Finally, all simulations assume no gravitational forces (since the original intent for this work was the analysis of astronaut motions in space).

Prior to implementing the new estimator developed above, an initial simulation was conducted to illustrate the performance of a torque estimator that does not include force or moment measurements. Figure 3-7 illustrates the torque estimation results for the 3-link model. Clearly the torque estimates bear no resemblance to the actual joint torques.

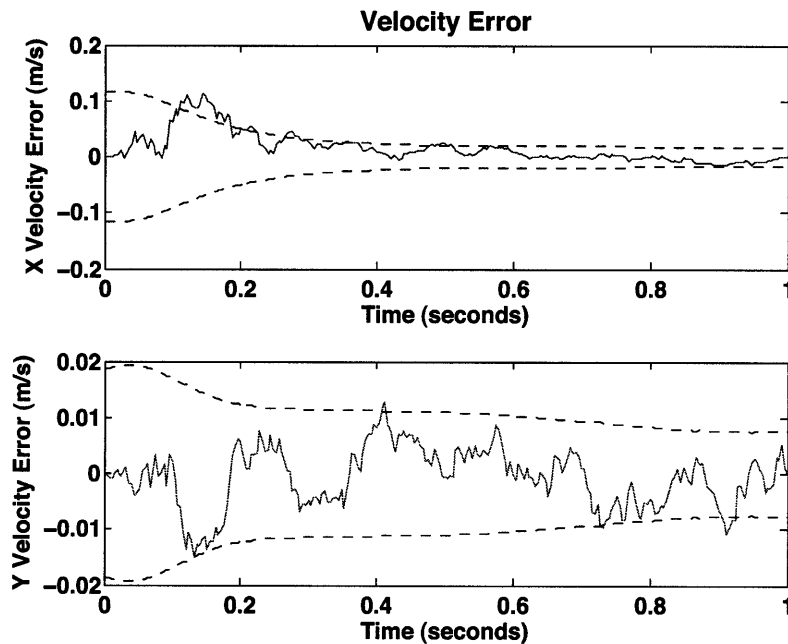
Figure 3-8 illustrates the torque estimation results using the new estimator. Figure 3-9 shows the angle and rate estimates resulting from the UKF. The force and moment measurements provide sufficient acceleration information to fully estimate the joint accelerations and thus the joint control torques.

Figure 3-10 shows joint control torques utilizing the new estimator for the 4-link model. Figure 3-11 illustrates joint angles and rates for the 4-link model. Notice again how well the torques, angles and rates track the truth.

Using the force, moment and joint angle data presented in Figure 2-15 in Chapter 2, Figure 3-12 illustrates the torques computed using the algorithms described in this chapter.



(a) Simulated COM position estimation errors.



(b) Simulated COM velocity estimation errors.

Figure 3-3: Position and velocity errors during the simulated motion. The dashed lines above and below the error trace indicate the covariance (1σ) bounds.

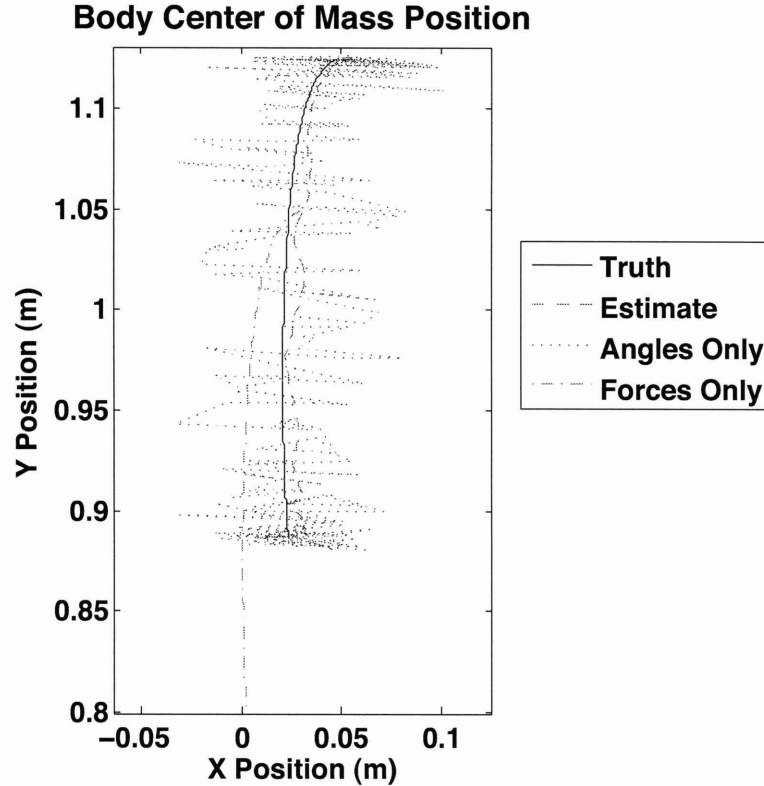


Figure 3-4: The true and estimated position of the body COM during a simulated motion. The solid line represents the truth and the dashed line represents the result from the body COM motion estimator. The dotted and dash-dotted lines represent the results that would have been obtained if only the angle measurements or the force measurements respectively were used on their own to estimate the body COM position.

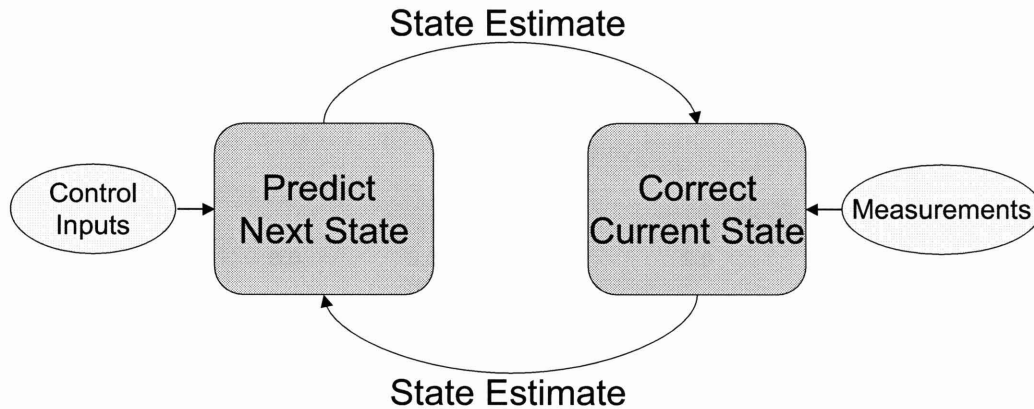


Figure 3-5: The information flow of a conventional predictor-corrector filter.

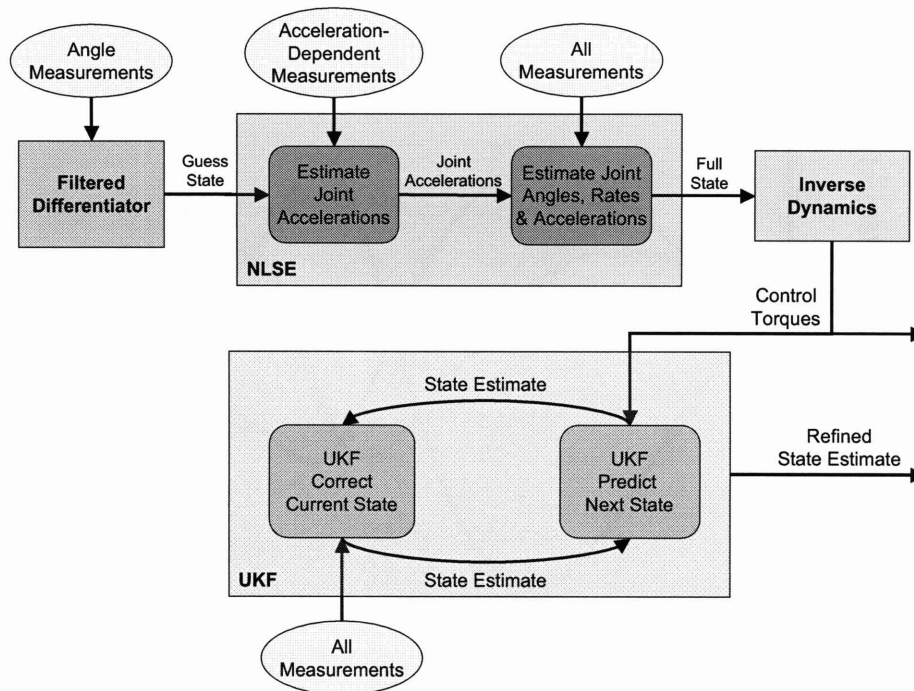


Figure 3-6: The information flow of the newly-developed joint torque and state estimation technique using an Unscented Kalman Filter (UKF) and the Nonlinear Least Squares Estimator (NLSE).

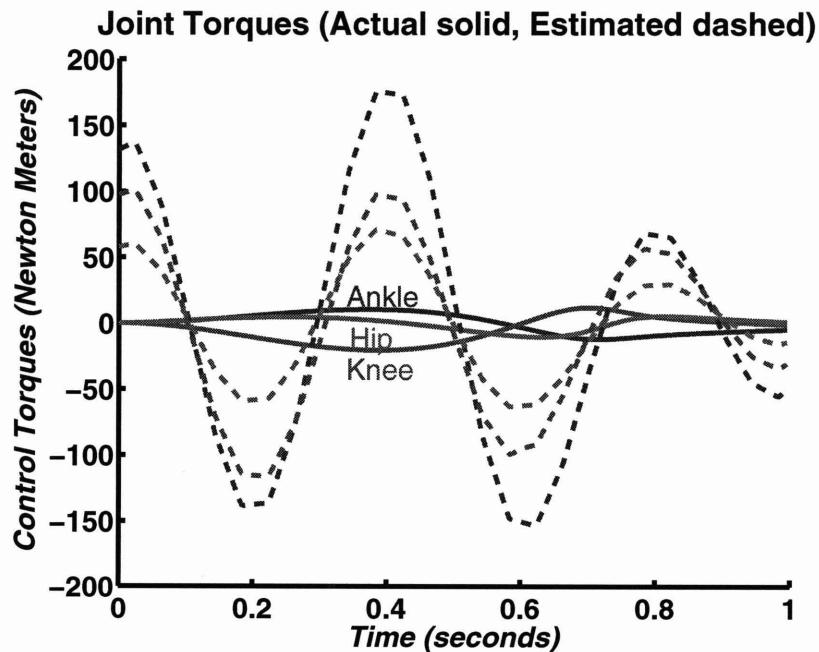


Figure 3-7: Actual (solid) and estimated (dashed) joint control torques for a 3-link model using only differentiated joint angles.

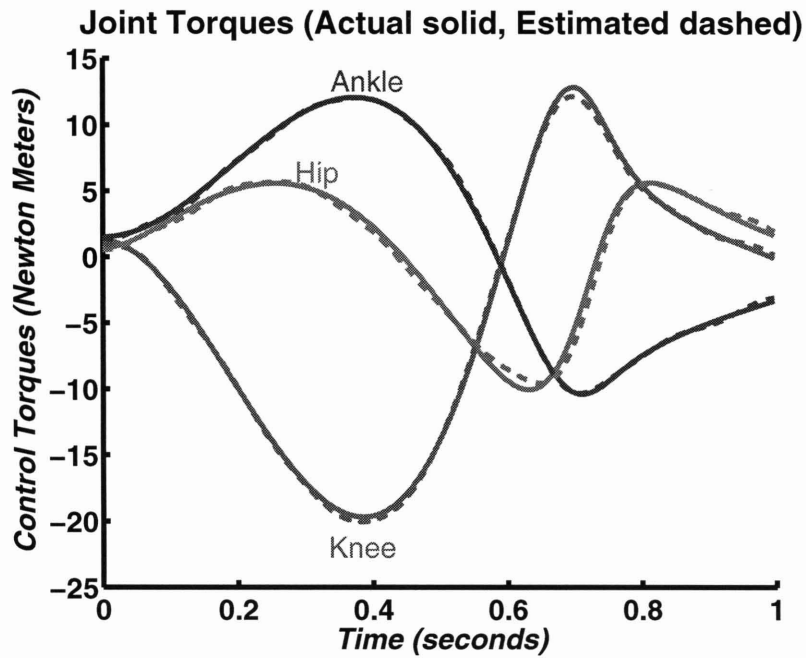
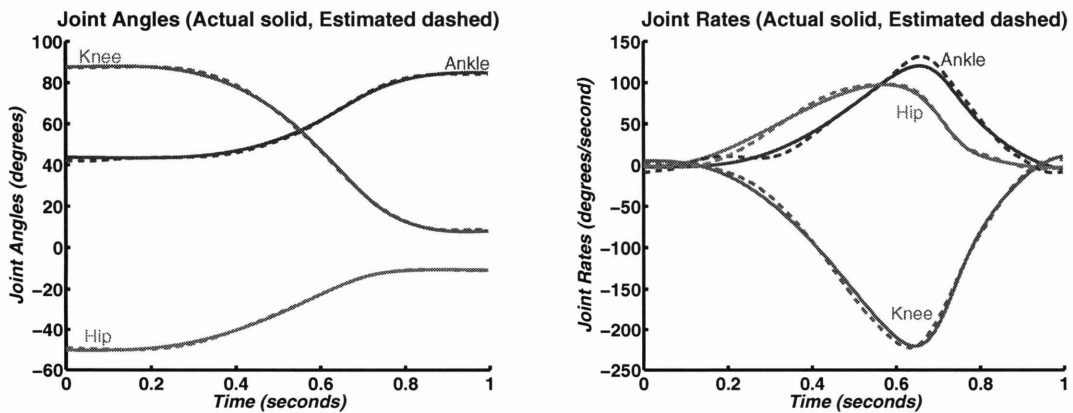


Figure 3-8: Actual (solid) and estimated (dashed) joint control torques for a 3-link model using force, moment and angle measurements.



(a) Actual (solid) and estimated (dashed) joint angles. (b) Actual (solid) and estimated (dashed) joint rates.

Figure 3-9: State estimation results from the UKF for a 3-link model using force, moment and angle measurements.

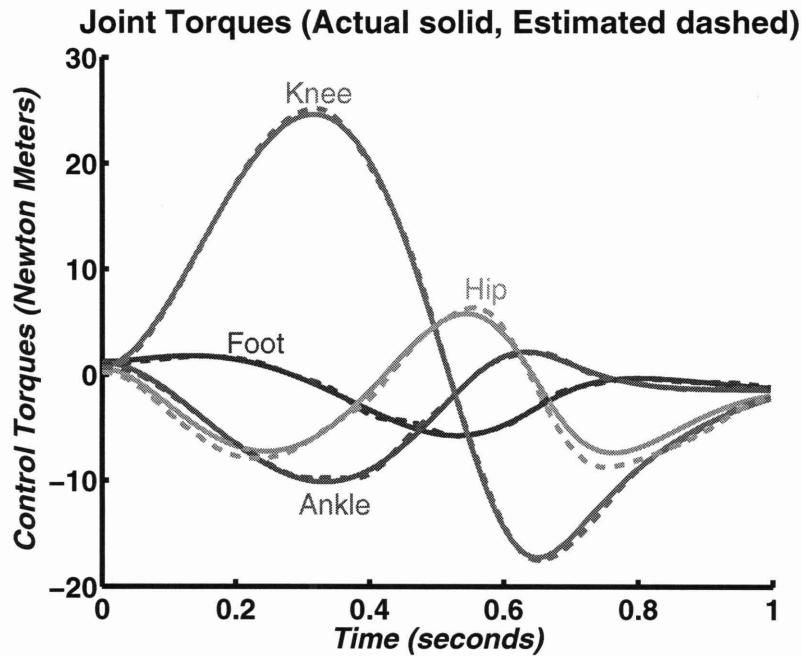
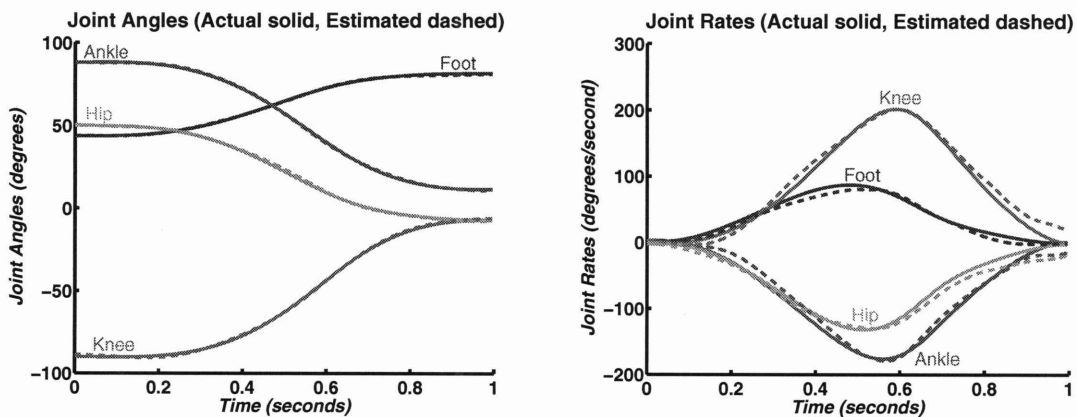


Figure 3-10: Actual (solid) and estimated (dashed) joint control torques for a 4-link model using force, moment and angle measurements.



(a) Actual (solid) and estimated (dashed) joint angles. (b) Actual (solid) and estimated (dashed) joint rates.

Figure 3-11: State estimation results from the UKF for a 4-link model using force, moment and angle measurements.

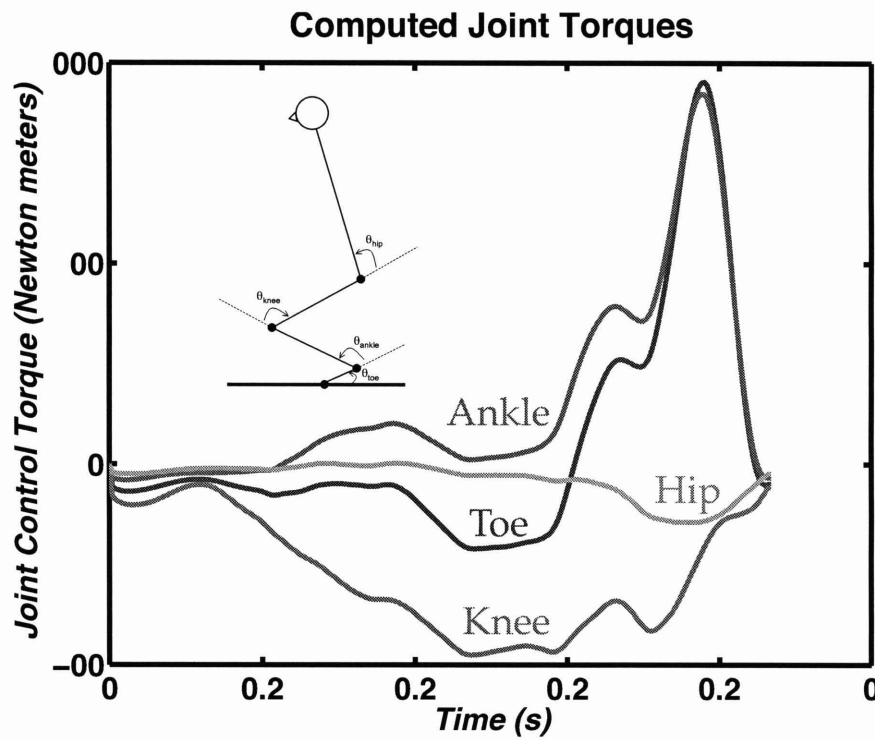


Figure 3-12: Torque data estimated using actual forces, moments and joint angles collected during a push-off motion. The inset shows the joint angle convention used to further define the joint torques.

3.2.4 Discussion

The results presented in Section 3.2.3 clearly illustrate the benefit of incorporating force and moment measurements to estimate joint control torques. However, an important step of the estimation process is the computation of the inverse dynamics via Equation 3.26. For any manipulator with more than 2 links, developing the details of Equation 3.26 can be extremely tedious. Fortunately, [Corke, 1996] presents a robotics control toolbox for MATLAB that computes the dynamics of Equation 3.26, which have been implemented in the simulations herein.

Since the computed joint torques depend on the quality of the model parameters in Equation 3.26, reliable techniques must be in place to determine them for any human subject. Fortunately, the inertia matrix and segment masses for a human limb can be accurately determined using several body measurements, as described in [Yeadon, 1990].

The above analysis assumed that the joint friction (damping) was zero for each joint. While others have measured the actual joint frictions for various joints [Zhang et al., 1998] and found true, non-zero values for the joint frictions, this does not invalidate these results. Since joint friction is dissipative, the joint torques due to joint friction are not observable in force plate measurements. Thus, if appropriate estimates of joint friction were known, they could be added to the estimated joint torques after the estimation.

The results presented in this chapter assume planar motion only to provide a worst case observability. As mentioned in Section 3.2.2, only one moment and two forces are non-zero for a planar limb. If any joint were to move out of plane, it would add at least one more non-zero force measurement and one more (possibly two) non-zero moment measurement, thus, increasing the rank of the information content.

All simulations presented in this chapter assumed that no prior joint acceleration was known. In reality, it may be possible to filter the joint angles sufficiently such that a rough joint acceleration estimate can be made through differentiation alone. In such a case, the prior acceleration estimate can aid in the estimation process and

permit a greater number of joints in a given model.

A common difficulty in using force-moment sensors with human subjects arises when the subjects' feet or hands slip across the force plate. In this case, the assumption that the limb remains firmly attached to the plate is no longer true. The most sensitive measurements to such slipping are the moments. Estimating joint torques using only forces and joint angles (*i.e.*, no moment measurements) is much more difficult due to the observability issue described in Section 3.2.2. Figure 3-13 illustrates the torque estimation results for the three-link model without moment measurements.

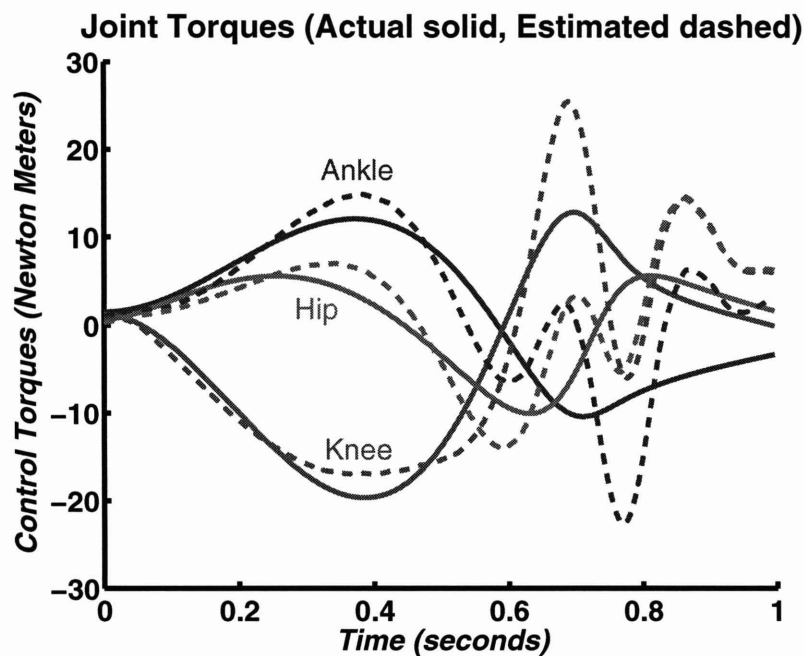


Figure 3-13: Actual (solid) and estimated (dashed) joint control torques for the 3-link model using force and angle measurements (no moments).

Since the estimator used in Figure 3-13 is rank deficient (see Section 3.2.2), a very rough acceleration estimate was obtained by double differentiation to start the estimator. While the first half of Figure 3-13 tracks reasonably well, the second half of the simulation is degraded. In such a case, a better prior estimate of the joint accelerations could be sought (as described above), or different measurements could be added. One such measurement could be the addition of a common 2-axis accelerometer. Figure 3-14 shows the same simulation presented in Figure 3-13, but with accelerometer measurements added to the center of mass of the subject's torso.

Figure 3-14 shows a noticeable improvement over the force and angle measurements alone in Figure 3-13.

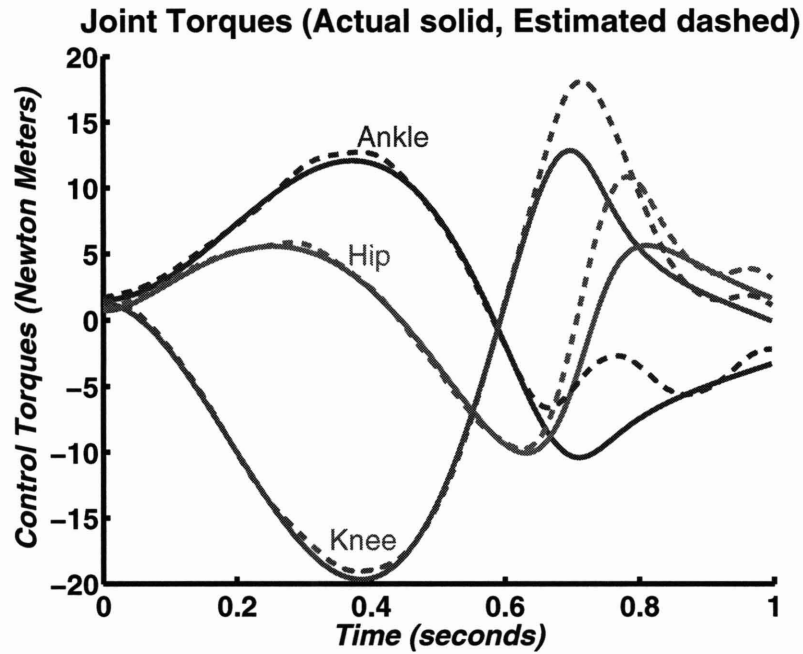


Figure 3-14: Actual (solid) and estimated (dashed) joint control torques for the 3-link model using force and angle and accelerometer measurements.

3.3 Conclusions and Recommendations

This chapter has presented a nonlinear estimator for computing joint control torques, joint angles and joint rates, using force, moment and angle measurements. The estimator is based on a novel combination of the nonlinear least squares estimator and the unscented Kalman filter. Dynamic models of the human body were presented that propagate the state estimates from time step to time step and enable the estimator to function even when incomplete measurement information is available.

Simulation results show the remarkable improvement that force and moment measurements can add to joint torque and whole body motion estimation. At the heart of dynamic motion is acceleration, and forces and moments are rich with acceleration information that the new torque estimator uses to enhance the estimation. Not only do the resulting joint control torques offer a glimpse into the human movement

control strategy, but the knowledge of joint torques permits further refinement of the angle and rate estimates through dynamic estimation.

The results of this study strongly suggest that the addition of a force-moment sensor into whole body motion studies can remarkably improve the quality of the observed motion data with minimal effort. A simple, commercial force-moment sensor can easily be placed into most experimental environments with minimal cost. Furthermore, the algorithms presented in this chapter can be easily modified to incorporate other measurements. Section 3.2.4 provides an example of adding accelerometer measurements, but other measurements from devices such as laser range finders or joint rate encoders could be added with minimal modification. In fact, if subjects were instrumented with in vivo strain gauges to measure joint torques (as is the case with [Hodge et al., 1989]), the measured joint torques could be added as an additional measurement. In this case, information from the force-moment data and the directly measured joint torques would be combined by the dynamic estimator to arrive at an estimate that is much more accurate than one computed from the force-moment or torque measurements alone.

The algorithms presented in this chapter could also be used in the design and control of robotic manipulators. [Morel et al., 2000] describe a novel control approach that uses a force-moment sensor mounted at the base of the manipulator and joint acceleration measurements to estimate the joint torques and feeds them back into the controller. However, the joint torque estimator presented in this chapter does not require joint acceleration information in order to compute the joint torques, making the controller presented in [Morel et al., 2000] more widely applicable.

Chapter 4

Dynamic Human Adaptation Experiments

This chapter describes the human adaptation experiments that were conducted to test the experimental hypotheses (outlined in Chapter 1). All human studies adhered to the guidelines issued by MIT's Committee On the Use of Human Experimental Subjects (COUHES). Please refer to Appendix H for the COUHES documentation supporting this research.

As outlined in Chapter 1, the purposes of the human experiments were to a) Observe human locomotor adaptation to different gravitational environments, b) Test whether dual adaptation could be observed over short periods of time (*i.e.*, after several weeks of exposure to a different gravitational environment) and c) Define metrics that clearly show the observed adaptation. The hypotheses directly tested by these experiments were:

Hypothesis #1: Kinetic data from a force / moment sensor and kinematic joint angle data can be combined in a dynamic filter to produce accurate, reliable estimates of whole body motions during adaptation experiments. Using the combined kinetic and kinematic data, metrics can be defined that illustrate control strategy adaptation to different gravitational and dynamic environments.

Hypothesis #2: A single adaptation mechanism governs human locomotor control strategies across a spectrum of gravity environments in a manner similar to that predicted by either Bayesian optimization; or the virtual trajectory hypotheses or a combination of the two.

Human adaptation experiments were conducted on a 1-G microgravity simulator (air-bearing floor) and underwater to attempt to measure contrasting locomotor control adaptation. Subjects were instructed to perform a series of repeated push-offs and landings using both hands and feet to demonstrate their control strategy during whole-body motion and adaptation to the new environment. These experiments serve as the ground-based studies for the MICR0-G ISS experiment described in Chapter 2. While the MICR0-G ISS experiment aims to quantify and model long-term (on the order of months) adaptation, it was expected that short-term adaptation would be evident after minimal exposure to particular dynamic environments. The following section describes each of the two testing environments employed for this study.

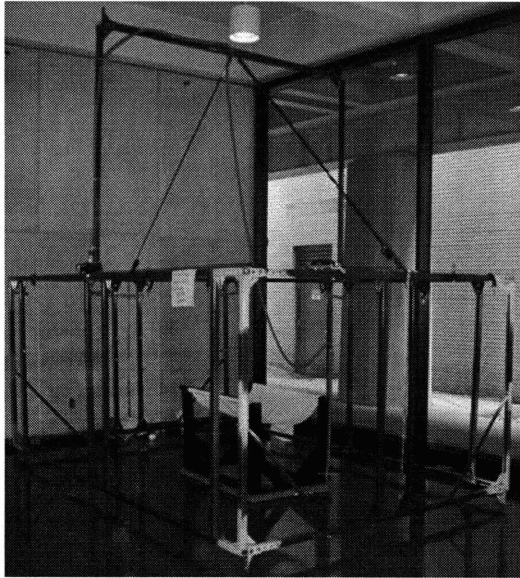
4.1 Testing Environments

To simulate different gravitational and dynamic environments on Earth, two different testing scenarios have been developed: (A) On a near frictionless air-bearing floor and (B) Underwater.

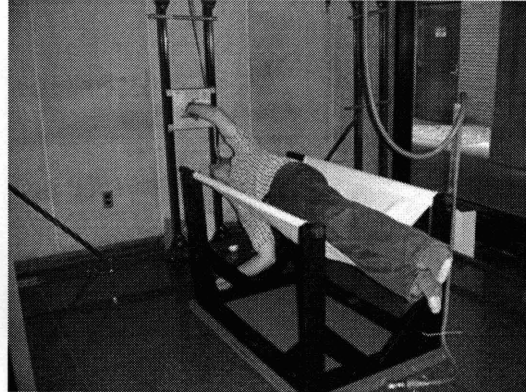
4.1.1 Air-Bearing Floor

To easily simulate microgravity in one plane, a custom-made air-bearing floor was designed and built as part of this research program (see Figure 4-1). The air-bearing cart is made of a four-bearing air palette by AeroGo Inc. from Seattle, WA. The coefficient of dynamic friction of the air cart was empirically determined to be approximately 0.005 (or about that of a speed skater [de Koning et al., 1992]).

Subjects either lie on their side in the sling mounted on top of the air palette or sit upright in a chair atop the palette. The sling was constructed to allow free motion



(a) A photo of the sensor mounting frame, complete with the hose mast.



(b) An EDLS force / moment sensor is mounted to the mounting frame to test sensor placement options. Subjects lying in the sling can easily interact with the sensors with both their arms and legs.

Figure 4-1: Photos illustrating the setup of the sensor mounting frame around the air-bearing floor.

of the subjects' arms and legs while cradling their torso comfortably. A headrest was offered to subjects to minimize neck strain, however, all subjects opted not to use the headrest.

The MICRO-G sensors (force moment sensors) were mounted on a steel mounting frame in positions easy for the subjects to reach while they were in both the horizontal (lying in the sling) and vertical (sitting in the chair) positions. The mounting frame also featured a 4 meter tall mast for holding the air hose to prevent it from dragging on the floor. Please see Figure 4-1 for photos of the mounting frame surrounding the air-bearing floor.

4.1.2 Underwater

Testing subjects underwater provides simulated weightlessness in three degrees of freedom. Using the same mounting frame as used in the air-bearing floor experiments, waterproof force moment sensors and underwater video cameras collect force

/ moment and 3-D motion data. Figure 4-2 shows the MICRO-G sensor mounting frame assembled at the bottom of MIT's Alumni Pool.



Figure 4-2: A photo of the sensor mounting frame (the same frame used on the air-bearing floor) assembled at the bottom of MIT's Alumni pool. Using SCUBA gear, subjects perform push-offs and landings in a neutral buoyancy environment, simulating weightlessness while introducing the added dynamics of water viscosity.

Performing motion experiments underwater introduces the added dynamics of water viscosity. While the effects of water viscosity are certainly not present during spaceflight, it is important to study the effect of water viscosity on human motion since the vast majority of astronaut training occurs in underwater environments.

4.2 Pilot Studies

Prior to conducting the studies presented in this thesis, a short series of pilot studies were conducted to verify the data collection system and hone the subject instructions to evoke repeatable measures. The pilot studies were loosely structured intentionally to enable efficient and often real-time modifications of the experiment protocol based on the subjects' verbal input during the experiment.

In total, 7 consenting female subjects completed the pilot study. Each subject performed between 10 and 30 push-offs and landings using both hands and legs in both the sling and chair configurations of the air-bearing floor. Instructions varied per subject, but the overall goal of the instructions was to give the subject as much freedom as possible to choose the strategy that she wanted to employ while retaining

subject repeatability. Instructions were also modified to ensure that proper measurements could be attained from the force / moment sensors as well as the kinematic video system. After each subject completed the pilot study, they were debriefed in a short interview to get information about what parts of the experiment were clear or unclear and what aspects could be improved upon. The following section lists the primary lessons learned from the pilot studies that were incorporated into the final experimental protocol for the experiments presented in this thesis.

4.2.1 Lessons Learned from the Pilot Studies

1. Subjects needed some direction so that their hands and feet pushed off from the middle of the sensor. Early pilot studies were difficult to analyze because of false off-axis loads due to push-offs being executed off the side of the sensor. To remedy this, a small, vinyl bump (pictured in Figure 4-3) was added to the top plate of each sensor. Subjects were then instructed to feel for the bump with their hands or feet prior to starting their motion.

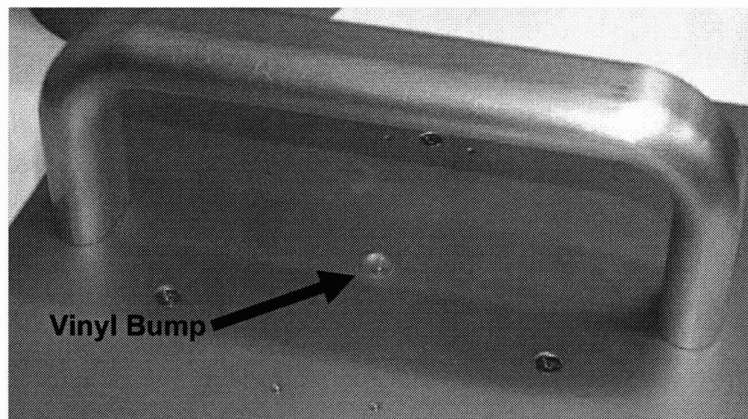


Figure 4-3: Vinyl bump added to the sensor top plates to encourage subjects to push off from the center of the sensor.

2. After approximately 15 trials, most subjects began to experience hip fatigue due to the need to cantilever their leg off of the edge of the air-bearing cart. Some subjects reported this fatigue while others did not; however, in all cases, fatigue was manifested by inaccurate or “sloppy” motions at approximately the

15th trial. To alleviate the fatigue and to ensure that the data is not adversely affected, subjects will be asked to take a short (1-2 minute) break following trial number 15. In most cases, the subjects will not even need to sit up - they can simply rest their top leg on their supported bottom leg.

3. Originally, subjects were instructed to conduct the push-offs and landings at a comfortable speed and to attempt to complete them as accurately as possible. While all subjects interpreted this to mean they needed to hit the target sensor in the middle, some subjects felt that it was okay if after they hit the target sensor, they spun out of control. Clearly, the instructions were too vague, and needed clarification. It was observed that the subjects that spun out of control after their landing always expected the experiment operator to physically move them back to the push-off sensor prior to the next motion. Subjects that continued to adapt to the point where they did not spin out of control upon landing were those who always attempted to move themselves back to the push-off sensor by pushing off of the landing sensor. This resulted in a new instruction aimed at fixing this discrepancy. All subjects are now instructed to push themselves back to the starting point from the landing sensor under their own power. This should cause the subjects to continue their adaptation to a point where their landing is accurate *and* does not spin out of control.
4. Procedures for the early pilot studies had the experiment operator setting up the initial conditions and asking the subject if they felt they needed the initial position to be adjusted. It was then observed that many subjects were able to move themselves around, using their hands on the floor and their feet on the sensor or on the mounting frame. Now, all subjects are instructed to set up their own starting position to ensure that the test director in no way affects the strategy that they choose.
5. In order to ensure the force traces can be understood properly, subjects are now instructed to pause motionless for approximately one second prior to the start of their motion. Often, as subjects become well-adapted to the motions, they need

to be reminded of this because there is a tendency for them to start “bouncing” back and forth between the push-off and landing sensor. This has the effect of combining the landing force signature with the push-off force signature.

6. Subjects tend to restrict their limb motions to one plane, thus justifying only planar models for analysis.

4.3 Experiment 1 - Simulated Microgravity Push-Offs and Landings

The first experiment of this study took place on the air-bearing floor. The purpose was to initially expose each subject to the dynamics of being “weightless” in one plane and observe how they develop locomotor control strategies applicable for this environment.

4.3.1 Subjects

12 (6 male, 6 female). All subjects consented to participate in this experiment and, as such, signed the informed consent form found in Appendix H. Since all subjects were also being considered for the underwater study (described later in this chapter), all subjects were required to be SCUBA certified.

4.3.2 Methods

Each subject performed a series of push-offs and landings that were designed to illustrate the locomotor control strategy for each task. Subjects performed the motions in two different orientations. The first orientation was with their body parallel to the direction of travel, known as horizontal. The second orientation was when the subjects oriented their body perpendicular to the direction of motion, known as vertical. Given the location of the sensors within the mounting frame (see Figure 4-4), subjects were able to use their hands or feet while horizontal, but could only use

hands while vertical. Figure 4-5 illustrates the vertical and horizontal configurations of the air-bearing floor pictorially.

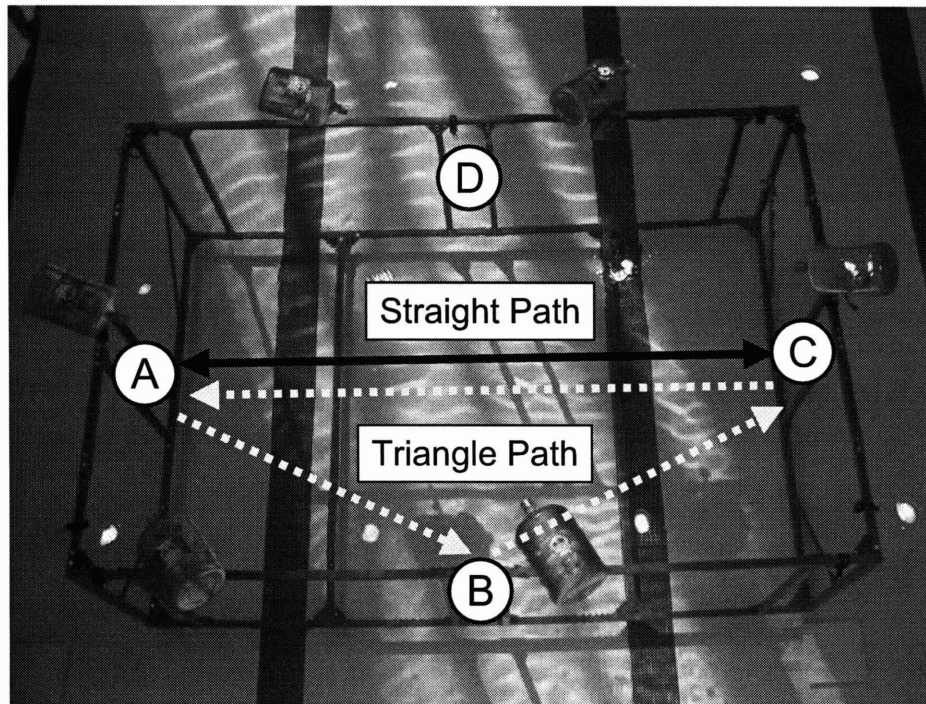


Figure 4-4: The sensor mounting frame with overlay arrows indicating the paths subjects were to take during the experiments.

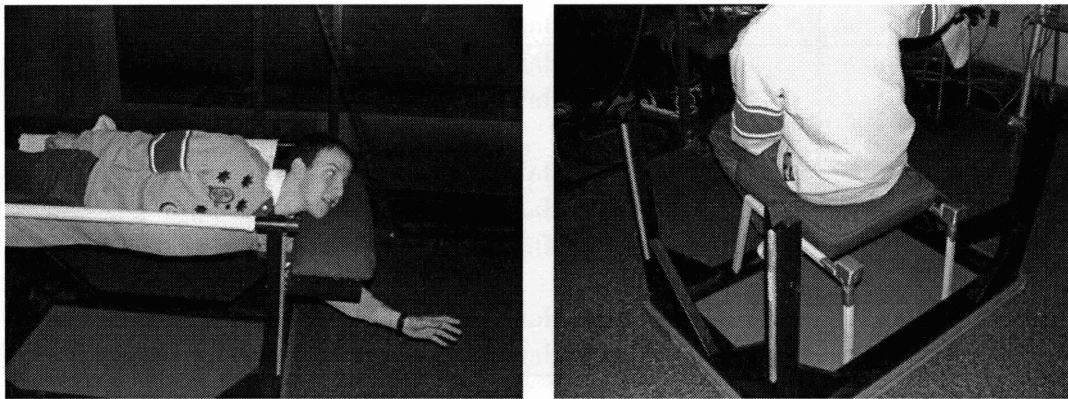
Subjects first completed a set of motions known as course traverses. In these motions, subjects move from one sensor to another along a pre-defined path. Using the letter designations in Figure 4-4, the different course traverses were:

1. **Triangle, Horizontal:**

- (a) Foot push-off A
- (b) Hand landing B
- (c) Hand push-off B
- (d) Hand landing C
- (e) Hand push-off C
- (f) Foot landing A

2. **Triangle, Vertical:**

- (a) Hand push-off A
- (b) Hand landing B
- (c) Hand push-off B
- (d) Hand landing C
- (e) Hand push-off C
- (f) Hand landing A



(a) A subject using the air-bearing floor in the horizontal configuration. (b) A subject using the air-bearing floor in the vertical configuration.

Figure 4-5: Photos of the air-bearing floor in each of the horizontal and vertical configurations. While horizontal, both hand and feet are free to use. In the vertical position, only the hands can be used.

After the triangular course traverse, the subjects performed straight push-offs and landings from sensor A to C, illustrated in Figure 4-4 as the black arrow. After 30 repeated trials of straight push-offs and landings, the triangle course was repeated for 5 trials, followed by another set of 30 straight push-offs and landings between sensors and finally another set of triangular course traverses. Once these motions were complete, the subject then re-configured to the vertical position and conducted the same motions using only hands. Figure 4-7 illustrates the the phase / trial break down for all experimental data analyzed for this research program. Data collected from the vertical configuration was collected but not analyzed herein. The vertical configuration data could potentially support future studies. Table 4.1 summarizes the motions the subjects took for Experiment 1.

Table 4.1: Motions carried out by each subject for Experiment 1. The triangle courses are depicted in Figure 4-4.

Motion	Push Limb	Land Limb	Body Orientation	Trials
Triangle Course	Foot	Hand	Horizontal	5
Push-off	Foot	Hand	Horizontal	15
Break				
Push-off	Foot	Hand	Horizontal	15
Triangle Course	Foot	Hand	Horizontal	5
Push-off	Foot	Hand	Horizontal	15
Break				
Push-off	Foot	Hand	Horizontal	15
Triangle Course	Foot	Hand	Horizontal	5
Triangle Course	Hand	Hand	Vertical	5
Push-off	Hand	Hand	Vertical	15
Break				
Push-off	Hand	Hand	Vertical	15
Triangle Course	Hand	Hand	Vertical	5
Push-off	Hand	Hand	Vertical	15
Break				
Push-off	Hand	Hand	Vertical	15
Triangle Course	Hand	Hand	Vertical	5

Subject Instructions

Prior to beginning the motions, the subjects were briefed as to the experimental and individual goals they should strive towards. The goals were described as follows:

Your goal is to push off from the indicated sensor with your right hand/foot (depending on the motion) and land with your right hand/foot (again, depending on the motion). You should strive to be as accurate as possible when pushing off, such that your landing is as close to the center of the sensor as possible. Upon arriving at the landing sensor, you will be required to push yourself back to the initial push-off sensor. You may choose any speed you feel comfortable with.

As previously stated, to ensure that the subjects had complete control over the initial conditions, subjects were initially positioned at a nominal distance away from the push-off sensor (approximately 60 cm from the sensor surface to the edge of

the air-bearing cart). Subjects were encouraged to use their hands on the floor to reposition themselves prior to the motion.

To ensure that subjects always performed their push-offs from the center of the sensor (to enable accurate force and moment readings), a small acrylic bump was placed at the center of each force-moment sensor (see Figure 4-3). Prior to each motion, the subjects were instructed to place their hand or foot in the center of the sensor so that they could feel the bump at the center of the sensor's top plate.

Once the subject was satisfied with their initial conditions, they were asked to pause motionless for one second to provide a recognizable point in the force signature that signified the start of the motion. The exact instructions for positioning the subjects prior to each motion were as follows:

Prior to each motion, you will determine the starting orientation that best suits the motion. You will be placed close to the sensor and then will be permitted to use your hands on the floor to reposition yourself. Feel free to use your feet on the sensor or on the side of the mounting frame to aid in your repositioning. When satisfied with your starting position, please feel for the bump on the sensor and ensure that you will be pushing on the sensor at this location. If need be, use your hands and/or feet to reposition yourself. Once you are satisfied with your starting position, remove your hands from the floor and pause motionless for approximately 1 second before beginning the motion.

4.3.3 Measurements

Force, moment and video data were collected during the experiments. The forces are analyzed herein and video analysis of the joint angles (outside the scope of this thesis) will be analyzed in the future. Table 4.2 summarizes the directly measured quantities and their attributes.

One of the goals of this research program was to identify the key metrics that define adaptation to different gravity environments. As such, a comprehensive set of

Table 4.2: Directly measured quantities. Forces, moments and video were all recorded during the experiments. Only a subset of the measurements were used in this study (see Section 4.6).

Measurement	Symbol	Units	Data Rate	Comments
X Force	F_x	Newtons	250 Hz	Per sensor
Y Force	F_y	Newtons	250 Hz	Per sensor
Z Force	F_z	Newtons	250 Hz	Per sensor
X Moment	M_x	Newton-meters	250 Hz	Per sensor
Y Moment	M_y	Newton-meters	250 Hz	Per sensor
Z Moment	M_z	Newton-meters	250 Hz	Per sensor
Toe Joint Angle	θ_t	radians	30 Hz	
Ankle Joint Angle	θ_a	radians	30 Hz	
Knee Joint Angle	θ_k	radians	30 Hz	
Hip Joint Angle	θ_h	radians	30 Hz	
Finger Joint Angle	θ_f	radians	30 Hz	
Wrist Joint Angle	θ_w	radians	30 Hz	
Elbow Joint Angle	θ_e	radians	30 Hz	
Shoulder Joint Angle	θ_s	radians	30 Hz	

metrics were defined and computed¹. Table 4.3 lists all metrics derived from the raw measurements listed in Table 4.2.

4.4 Experiment 2 - Hoop Game

During Experiment 1, some subjects did not need to change their control strategy very much due to the fact that the task they were required to do was quite simple. The primary purpose of the second experiment was to provide a much more difficult task for the subjects to complete such that all subjects needed to make distinct changes to their control strategies to be successful. In this second experiment, subjects were instructed to place a copper hoop on a copper post located mid-way while soaring from one sensor to the next.

The secondary purpose of the second experiment was to test the dual-adaptation hypothesis. Approximately two to three weeks elapsed between the time when each

¹For most of the trials, joint angle data was not immediately available from the kinematic video analysis system. As such, metrics based on joint angle estimates were not used for most trials.

Table 4.3: Derived Quantities. For each derived metric, the required inputs are listed. In the “Units” column, n denotes the number of time-steps the subject is in contact with the sensor during the push-off or landing (which ever is being analyzed).

Measurement	Symbol	Units	Dim.	Req. Inputs	Comments
Filtered Forces	F_{filt}	Newtons	$[n \times 3]$	F	$f_c = 30 \text{ Hz}$
Filtered Moments	M_{filt}	Newton-meters	$[n \times 3]$	M	$f_c = 30 \text{ Hz}$
Normal Force Direction Vector	F_{dir}	unitless	$[n \times 3]$	F	
Normal Force	F_{norm}	Newtons	$[n \times 1]$	F	Mean-square
Max. Normal Force	F_{max}	Newtons	scalar	F_{norm}	
Contact Time	$t_{contact}$	seconds	scalar	F, M	Push-off only
Filtered Angles	θ_{filt}	radians	$[n \times 4]$	θ	$f_c = 5 \text{ Hz}$
Joint Torques	τ	Newton-meters	$[n \times 4]$	F, M, θ	From torque est.
Estimated Joint Angles	θ_{est}	radians	$[n \times 4]$	F, M, θ	From torque est.
Estimated Joint Rates	$\dot{\theta}_{est}$	radians/second	$[n \times 4]$	F, M, θ	From torque est.
Estimated Joint Acc.	$\ddot{\theta}_{est}$	radians/second ²	$[n \times 4]$	F, M, θ	From torque est.
Body COM Position	X_{body}	meters	$[n \times 3]$	$F, \theta_{est}, \dot{\theta}_{est}, \tau$	Estimated
Body COM Velocity	\dot{X}_{body}	meters/second	$[n \times 3]$	$F, \theta_{est}, \dot{\theta}_{est}, \tau$	Estimated
Body Rotation Angle	θ_{body}	radians	$[n \times 3]$	ω_{body}	Estimated
Body Rotation Rate	ω_{body}	radians/second	$[n \times 3]$	$F, \theta_{est}, \dot{\theta}_{est}, \tau$	Estimated
Departure Velocity	v_{depart}	meters/second	$[3 \times 1]$	\dot{X}_{body}	Push-off only
Departure Speed	V_{depart}	meters/second	scalar	v_{depart}	Push-off only
Departure Rotation Rate	$\omega_{departure}$	radians/second	$[3 \times 1]$	ω_{body}	Push-off only
Estimated Landing Error	ΔL	meters	scalar	X_{body}, \dot{X}_{body}	Push-off only
Body Major Inertia	I_{body}	kilograms/meter ²	$[n \times 1]$	θ_{est}	
Body Inertia Change	ΔI_{body}	percent	scalar	I_{body}	
Linear Body Energy	E_{lin}	Joules	scalar	\dot{X}_{body}	At departure
Rotational Body Energy	E_{rot}	Joules	scalar	ω_{body}, I_{body}	At departure
Differential Joint Work	dW	Joules	$[n \times 4]$	τ, θ_{est}	
Total Joint Work	W	Joules	$[1 \times 4]$	τ, θ_{est}	
Internal Limb Energy	E_{limb}	Joules	$[n \times 1]$	$\theta_{est}, \dot{\theta}_{est}$	

subject conducted Experiment 1 and Experiment 2. If subjects exhibit similar control strategies at the beginning of experiment 2 as the end of experiment 1, it would suggest that the subjects retained their adaptation even after being subjected to a 1-G environment for 2 - 3 weeks.

4.4.1 Subjects

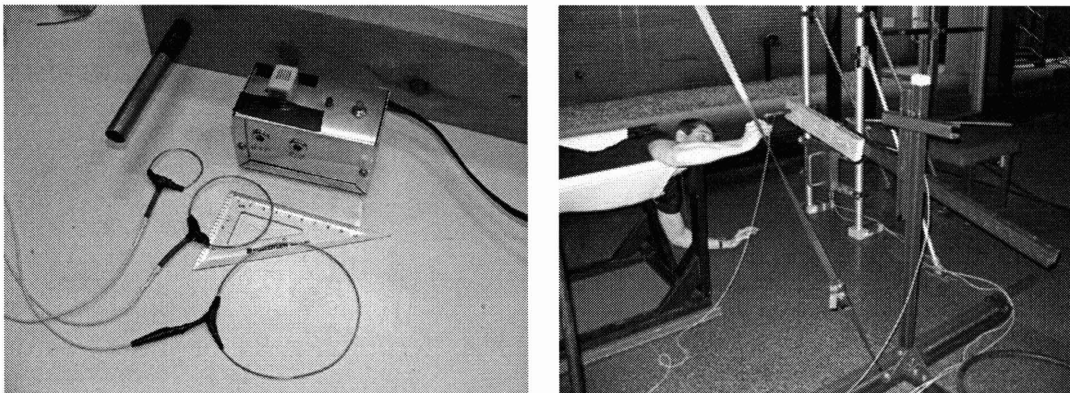
To enable repeated measures statistical analysis techniques, 11 of the 12 subjects that performed Experiment 1 returned to participate in Experiment 2. In total, 6 consenting males and 5 consenting females participated in the hoop experiment. All subjects signed the informed consent form found in Appendix H.

4.4.2 Methods

The second experiment was carried out on the same air-bearing floor described in Section 4.3. To provide a direct comparison with Experiment 1, the first 15 trials and the last 15 trials of Experiment 2 were designed to be identical to the horizontal

trials in Experiment 1 (*i.e.*, straight leg push-offs and hand landings).

After the first 15 trials, the hoop game commenced. Subjects were instructed to place a copper hoop on a copper post with electrical tape at the far end. The goal was to place the hoop on the taped portion of the post without touching the copper hoop to the copper post. If, at any time, the hoop contacted the copper portion of the post, a buzzer sounded and an LED lit up to indicate to the test director and to the subject that their attempt had failed. As the experiment progressed, subjects were presented with a large (10 cm in diameter), medium (6 cm in diameter) and small (4 cm in diameter) hoop. See Figure 4-7 for a detailed description of the phase / trial break down. Figure 4-6(a) illustrates the hoop game system with the three different sizes of hoops present for relative size comparison. Figure 4-6(b) shows a subject attempting to place the hoop on the post during Experiment 2. Appendix E outlines the design and electrical schematic for the hoop game.



(a) The largest hoop measured 10 cm in diameter, the medium-sized hoop was 6 cm in diameter and the smallest hoop was 4 cm in diameter. The post (made of standard copper plumbing pipe) was 1.27 cm in diameter. (b) A subject attempting to place one of the hoops on the post during Experiment 2. Subjects used their right hand to place the hoop on the post and their left hand to land on the landing sensor.

Figure 4-6: The hoop game designed for Experiment 2.

Subjects were instructed to repeat the game trials 15 times for each of the three hoop sizes. Table 4.4 describes the various phases of Experiment 2.

Table 4.4: Motions carried out by each subject for experiment 2.

Motion	Push Limb	Land Limb	Body Orientation	Trials
Push-off	Foot	Hand	Horizontal	15
Game (Big Hoop)	Foot	Hand	Horizontal	15
Game (Medium Hoop)	Foot	Hand	Horizontal	15
Game (Small Hoop)	Foot	Hand	Horizontal	15
Push-off	Foot	Hand	Horizontal	15

Subject Instructions

Since the first 15 and the last 15 trials of Experiment 2 were identical to the horizontal trials in Experiment 1, the subject instructions for those phases were identical. During the phases where the hoop game was conducted, the following instructions were provided:

These next push-offs and landings will be conducted in exactly the same way as the previous ones in that you will push off with your right foot after positioning yourself using your hands on the floor and your feet on the sensor and / or the mounting frame. However, before you arrive at the landing sensor, during the gliding motion, you will be required to place the given hoop over the post and place it on the black tape area without touching the hoop on the copper part of the post. When returning, you will be required to lift the hoop off of the post and carry it back to the starting point of your motion. If you are not successful and the copper hoop contacts the copper post, a buzzer will sound. If you are successful, you will hear nothing. Your goal is be successful as often as possible.

4.4.3 Measurements

The measurements for Experiment 2 are the same as in Experiment 1 with the addition of the binary succeed / fail variable associated with the hoop game. If the hoop contacted the post while it was being placed on the hoop or if it bounced to contact the post after being placed, the trial was considered to be a failure.

4.5 Experiment 3 - Underwater Push-Offs and Landings

The near-frictionless, air-bearing floor used in Experiments 1 and 2 provides an easy and effective means of simulating weightlessness in two dimensions. One way to simulate weightlessness in three dimensions is to use an underwater environment, just as NASA often does when training astronauts.

Experiment 3 reproduces the first half of Experiment 1, but underwater instead of on an air-bearing floor.

4.5.1 Subjects

Four of the twelve subjects (1 female, 3 male) that completed Experiment 1 participated in Experiment 3. All subjects consented and thus signed the informed consent form located in Appendix H. In addition to signing the consent form, all subjects were required to answer a brief questionnaire to ensure they were able to safely participate in the underwater portion of the study. The underwater subject questionnaire can also be found in Appendix H.

4.5.2 Methods

All subjects used a SCUBA regulator at the end of a 7.6 meter long hose, connected to a SCUBA tank situated on the pool deck. This type of SCUBA equipment is frequently referred to as a “hookah”. Subjects wore a soft weight belt containing bags of lead shot to provide neutral buoyancy. Each subject required different amounts of mass in order to achieve neutral buoyancy, but on average, subjects tended to use between 1 and 2 kg of extra mass. In addition to the hookah and the weight belt, subjects wore a SCUBA mask to aid in their breathing and to provide as much visual feedback as possible. No other equipment other than a bathing suit was worn by the subjects (*e.g.*, no buoyancy compensators, fins, snorkels or wet-suits).

Subjects performed two sets of 15 push-offs and landings in the same manner as

the first two phases of Experiment 1. Figure 4-7 illustrates the phase / trial breakdown for all three experiments. The sensor spacing used in Experiment 3 was identical to that used in Experiment 1 on account of the same mounting frame being used in both experiments.

Subjects were instructed to take as much time as they required to set themselves up in front of the sensors, using their hands and legs as they see fit. The push-offs were conducted from sensor A, to C and back to A again, as denoted in Figure 4-4. Subjects used their right leg to push-off from sensor A and the left hand to land to land on sensor C. When returning, subjects pushed off with their left hand from sensor C and landed on sensor A with their right leg.

Exp. 1	Phases	1A			1B			Break	1C			1D				
	Trials	5	5	5	5	5	5		5	5	5	5	5	5		
Exp. 2	Phases	2A			Big Hoop			Medium Hoop			Small Hoop			2B		
	Trials	5	5	5	5	5	5	5	5	5	5	5	5	5	5	5
Exp. 3	Phases	3A						3B								
	Trials	5	5	5	5	5	5									

Figure 4-7: Figure depicting the phase designations and trials for each of the three experiments. Each experiment was broken down into phases. A single phase consists of three sub-phases and each sub-phase consists of five trials. Experiment 1 contains 4 phases, Experiment 2 contains 5 phases and Experiment 3 contains 2 phases.

Subject Instructions

The instructions for Experiment 3 were identical to Experiment 1 in all respects, except that instructions needed to be given to the underwater subjects regarding the temptation for them to “swim” to the target sensor. The additional instruction was

During the motions, you will be tempted to use your hands and feet in

swimming motions. Please resist these temptations. Unless you are reaching for a sensor, please do not move your arms or legs during the portion of the motion while you are not in contact with any sensor.

4.5.3 Measurements

The same measurements and metrics were recorded for Experiment 3 as were recorded for Experiment 1. Special underwater housings for the video cameras (pictured in Figure 4-8) were used to enable high-resolution, underwater video.

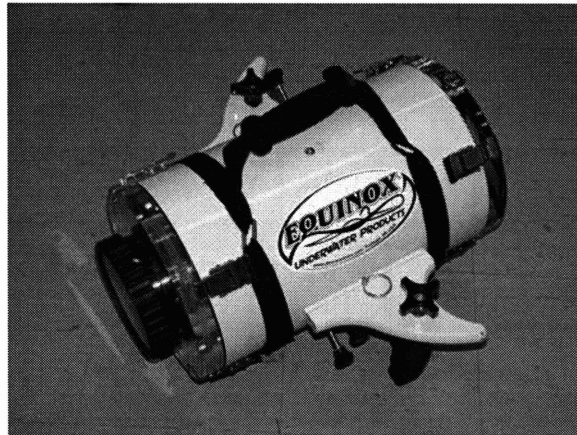


Figure 4-8: Underwater video camera housing by Equinox Underwater Products.

4.6 Results

One of the purposes of this research program was to identify the signature metrics that clearly show adaptation trends. While Table 4.3 lists all of the metrics considered as possible candidates, only a subset of them showed any significant change over the course of the experiment. Of those that showed significant change, most of the relevant behavior could be reduced down to and captured in two basic metrics: the maximum push-off force and the amount of time the subject is in contact with the sensor during the push-off. Most other metrics were strong functions of these two primitive metrics. The following subsections present the basic observations and statistical analyses of

the three experiments described above. Please see Table 4.5 for a complete summary of the statistical results of all three experiments.

During the two air-bearing floor experiments (Experiments 1 and 2), it became evident that two of the female subjects were not following instructions appropriately. After several repeated instructions, subjects continued to use their hands on the floor during their motions, thus tainting their results. As a consequence of this, data from both subjects that did not follow the instructions were omitted from the analysis that follows. One of the two subjects that did not follow instructions during Experiment 1 was the same subject that did not participate in Experiment 2. Thus, the following analysis for Experiments 1 and 2 considers only the complete set of 10 subjects who completed both experiments and followed the instructions correctly.

In the analysis that follows, both male and female subjects have been grouped together. This decision was justified by choosing 11 metrics from Table 4.3 and using a general linear model (GLM) to test for a gender effect. Only one of the 11 metrics tested showed a significant gender effect (*i.e.*, the computed landing error metric showed a significant gender effect with $p = 0.031$ and $F = 7.235$)². Table 4.5 summarizes the results from all 11 metrics used to test for a gender effect. With only 10 subjects being tested and 11 different metrics, it is not unreasonable that one metric could show a significant gender effect by chance (since significance was defined as $p < 0.05$). Thus, the one significant gender result was considered an anomaly and both males and females were grouped together for the remaining analysis.

The following sections present data averaged across all subjects to illustrate adaptation. Please see Appendix A for individual subject data.

4.6.1 Maximum Push-Off Force

A common observation by astronauts and others who have experienced true weightlessness during parabolic flight or microgravity is that most control problems encountered when exposed to the weightless environment are due to excessively high forces during push-offs and hence, landings. As such, the maximum force vector magnitude

²A significant effect was claimed when $p < 0.05$.

of each push-off was recorded and analyzed to find evidence of adaptation.

Each experiment was split into phases, each phase consisted of three sub-phases, and each sub-phase consisted of five repetitions of the particular push-off or landing (thus, each phase consisted of 15 trials; see Figure 4-7). Considering all phases of the first two experiments (four phases in Experiment 1 and five phases in Experiment 2), a significant difference between phases was found among subjects using a repeated measures general linear model ($p = 0.017$, $F = 5.892$, $n = 10$)³. Figure 4-9 illustrates the average maximum force vector magnitude for each phase across all subjects.

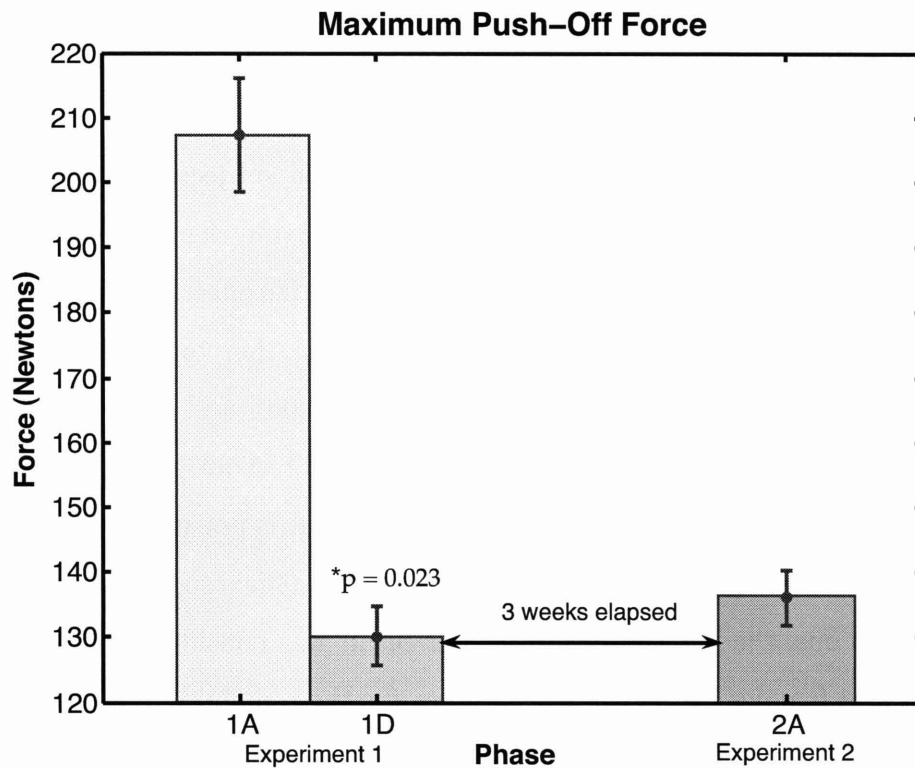


Figure 4-9: Proof of adaptation ($p = 0.023$, $F = 6.822$, $n = 10$), and dual-adaptation ($p = 0.996$, $F = 0.004$, $n = 10$) when comparing the maximum force application during push-offs across phases in Experiments 1 and 2.

Using the general linear model, contrast hypothesis tests were performed to test for significant adaptation effects. Comparing the first phase of Experiment 1 (*i.e.*, phase 1A) with the last phase of Experiment 1 (*i.e.*, phase 1D), a significant reduction in the average maximum push-off force ($p = 0.023$, $F = 6.822$, $n = 10$) was found, indicating

³All statistical results found using SYSTAT.

the presence of adaptation to this particular simulated gravitational environment (*i.e.*, the frictionless air-bearing floor, providing free movement in two dimensions). Thus, referring back to the hypotheses in Chapter 1, this significant adaptation result in combination with the sensor development in Chapter 2 and the data analysis methods presented in Chapter 3 verifies that Hypothesis #1 (that adaptation can be observed by defining metrics that clearly show the adaptation) is true.

Figure 4-9 also illustrates the average maximum push-off force for all subjects in the first phase of Experiment 2. From the time that Experiment 1 concluded and Experiment 2 commenced, approximately three weeks had elapsed. During that time, subjects were in constant exposure to the 1-G gravitational pull of Earth. If the subjects did not have the ability to retain the adaptation gained during Experiment 1, one would expect to see a significant difference between the maximum force application at the end of Experiment 1 and the beginning of Experiment 2. However, a contrast hypothesis test comparing phase four (the final phase) of Experiment 1 to phase 1 of Experiment 2 showed no significant difference in maximum force application ($p = 0.996$, $F = 0.004$, $n = 10$). This result supports the theory that humans can at least “dual-adapt” to two different gravity environments and suggests that Hypothesis #2 may be true. One can only speculate about “multi-adaptation” (*i.e.*, the ability to adapt to more than two different environments and retain all adaptations) at this point since this experiment only tested 1-G versus microgravity.

As described in Section 4.3.2, subjects performed a short set of five course traverses between phases two and three of Experiment 1. The purpose of these course traverses was to give the subjects a break from the straight, back and forth push-offs and landings. Figure 4-10 demonstrates the possible effect this short break had on the subjects’ adaptation.

As evidenced in Figure 4-10, a significant reduction ($p = 0.008$, $F = 10.494$, $n = 10$) in the maximum force application occurred across the course traverse break. For this analysis, sub-phases were contrasted against each other, again using a repeated measures general linear model. Furthermore, Figure 4-10 shows no significant change ($p = 0.184$, $F = 2.178$, $n = 10$) when comparing the final two sub-phases prior to the

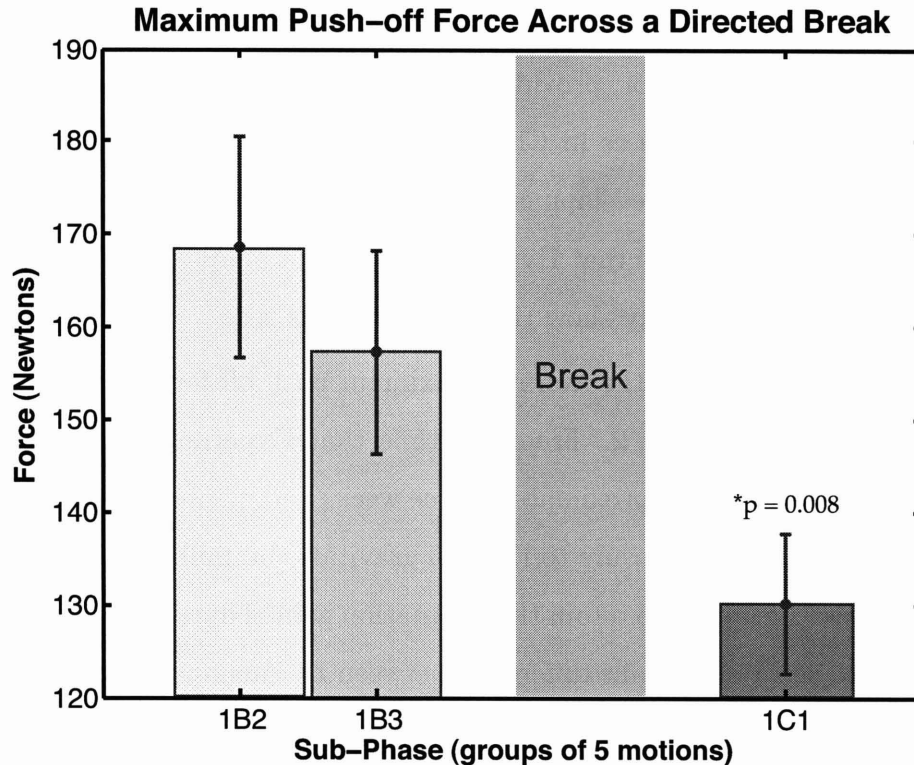


Figure 4-10: Maximum force plot illustrating the effect of a short break on the observed adaptation. No significant difference ($p = 0.184$, $F = 2.178$, $n = 10$) was detected between the two sub-phases immediately prior to the course traverse break. However, a significant reduction in the maximum force application between the two sub-phases that span the break ($p = 0.008$, $F = 10.494$, $n = 10$) was found.

break. Thus, it is reasonable to conclude that the break accelerated the adaptation, causing a small step change (reduction) in the maximum force application during push-off. A similar motor learning result (although over different time-scales) was reported in [Shadmehr and Holcomb, 1997].

Due to waterproofing difficulties, data from only two subjects (1 male and 1 female) turned out to be useful from the underwater studies. However, the dramatic trends in maximum force application illustrated by both subjects provided a significant adaptation result in Figure 4-11.

Figure 4-11 compares the maximum push-off force application from Experiment 1 (all four phases averaged) with the average of both phases from the underwater experiment (Experiment 3). A significant increase ($p = 0.015$, $F = 1913.366$, $n = 2$) using a repeated measures general linear model was detected.

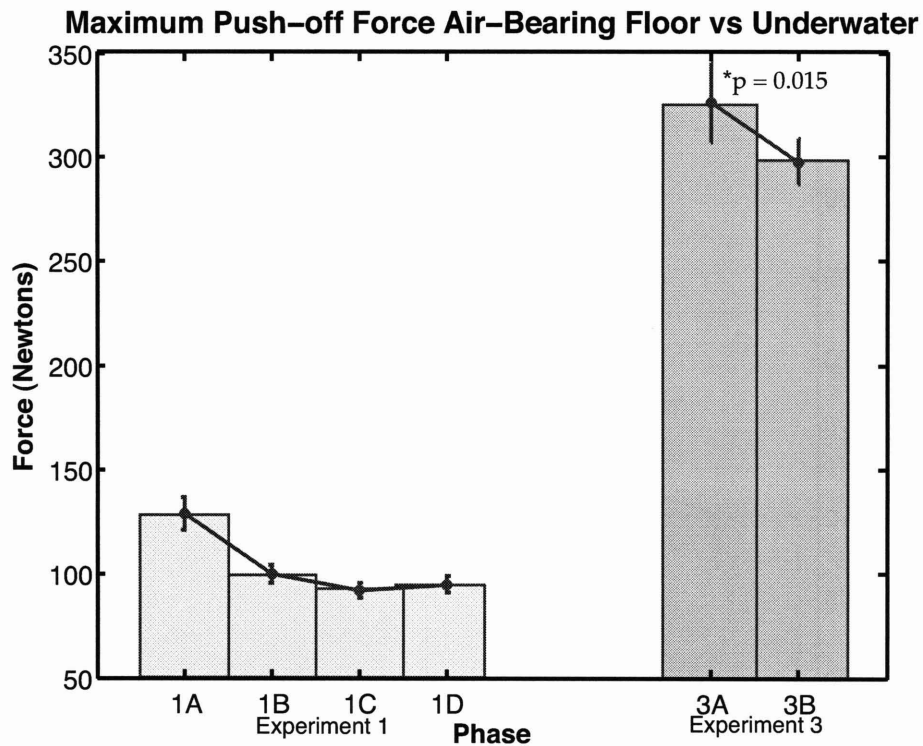


Figure 4-11: Maximum force application plot illustrating the difference between the average of phases 1-4 of Experiment 1 and the average of both underwater phases ($p = 0.015$, $F = 1913.366$, $n = 2$).

4.6.2 Push-off Contact Time

Another metric that indicated a change in the overall control strategy as the subjects adapted was the amount of time the subjects remained in contact with the push-off sensor while pushing off. Figure 4-12 illustrates the change in sensor contact time across all four phases of Experiment 1. A significant increase in contact time ($p = 0.016$, $F = 8.001$, $n = 10$) was detected between phases one and three. As in the maximum force analysis, a repeated measures general linear model was used with contrast hypothesis testing.

Figure 4-13 shows the significant reduction in contact time ($p = 0.044$, $F = 211.809$, $n = 2$) resulting from the underwater environment. This result, in combination with the increase in maximum force application in Figure 4-11 suggests that a different control strategy is being used underwater versus on the air-bearing floor due to the underwater hydrodynamics.

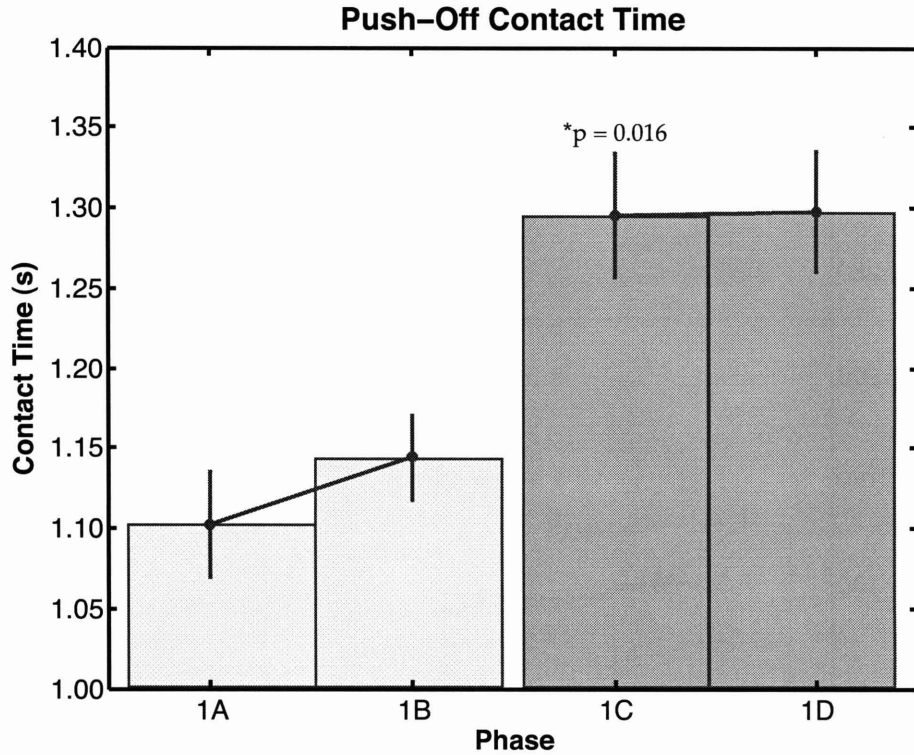


Figure 4-12: Push-off contact time plot illustrating a significant difference between phases 1 and 3 of Experiment 1 ($p = 0.016$, $F = 8.001$, $n = 10$).

4.6.3 Force Profiles

While the maximum force application and contact time metrics show significant adaptation results across the three experiments conducted in this research, they only provide a small window into the locomotor control strategies employed by the subjects. By analyzing the force profiles of representative trials from each phase, a clear, qualitative change in the force shape is evident as the subjects adapt. Figure 4-14 illustrates representative axial force profiles (*i.e.*, force in the direction pointing to the target sensor versus time for a single subject / trial) for every phase of all three experiments.

The force traces depicted in Figure 4-14 are the forces in the axial direction (*i.e.*, in the direction of the target sensor) during the push-off. At the beginning of Experiment 1, the motions are characterized by smooth, bell-shaped force profiles. As the subject adapts to the environment in Experiment 1, a pronounced second maximum develops. At the beginning of Experiment 2, the subjects indicate they have retained

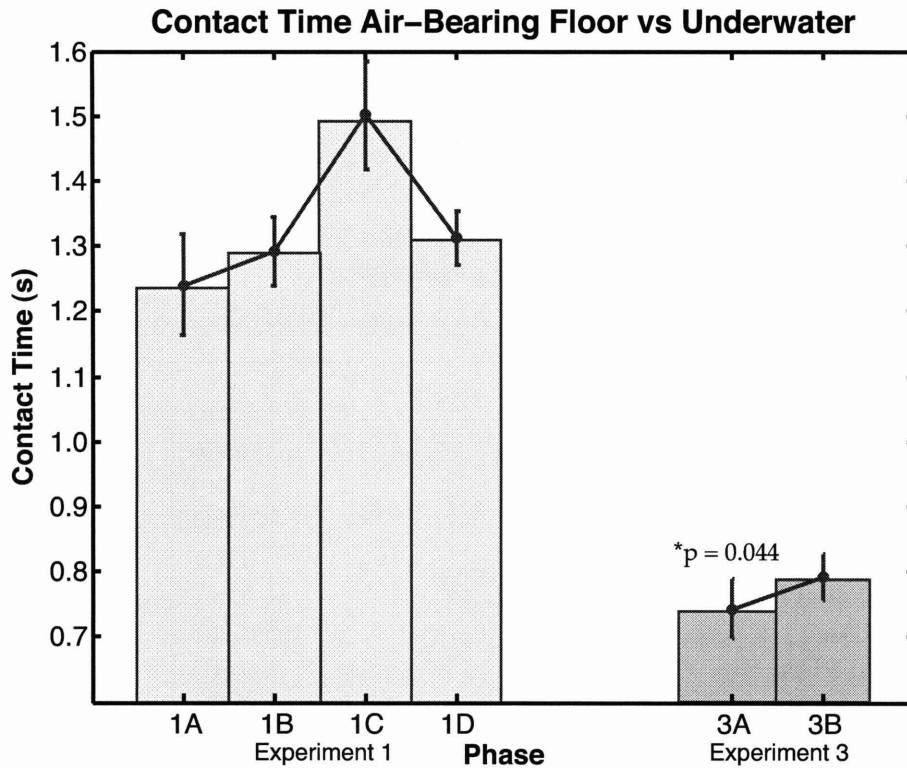


Figure 4-13: Contact time plot showing a significant difference between the average of phases 1-4 and the average of both underwater phases ($p = 0.044$, $F = 211.809$, $n = 2$).

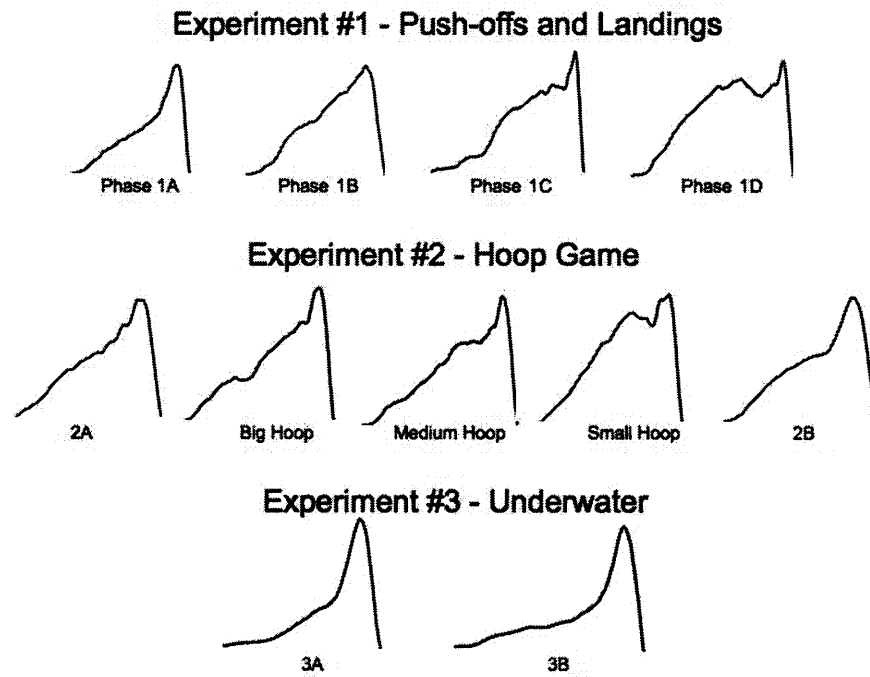
some of their adapted “bumpy” force profile, but not all of it. Once the hoops are introduced in Experiment 2, the task gets much more difficult and the prominent second maximum appears again. However, when the subject is no longer required to place the hoop (in the last phase of Experiment 2), the force profile returns to a smoother (but skewed) bell-shape. The observed changes in force profiles point to a distinct change in control strategy as the subjects adapt to their new environment.

It is interesting to point out that the force profiles from the underwater experiments show no sign of any second maximum and look very similar to the smooth, single-peaked profiles observed early in Experiment 1. This dramatic change in force profiles, in addition to the significant increase in maximum push-off force (see Figure 4-11) and significant decrease in sensor contact time (see Figure 4-13) are most likely due to the added viscosity and drag associated with underwater motions. While such dynamic differences are obvious, the important point to be made about the underwa-

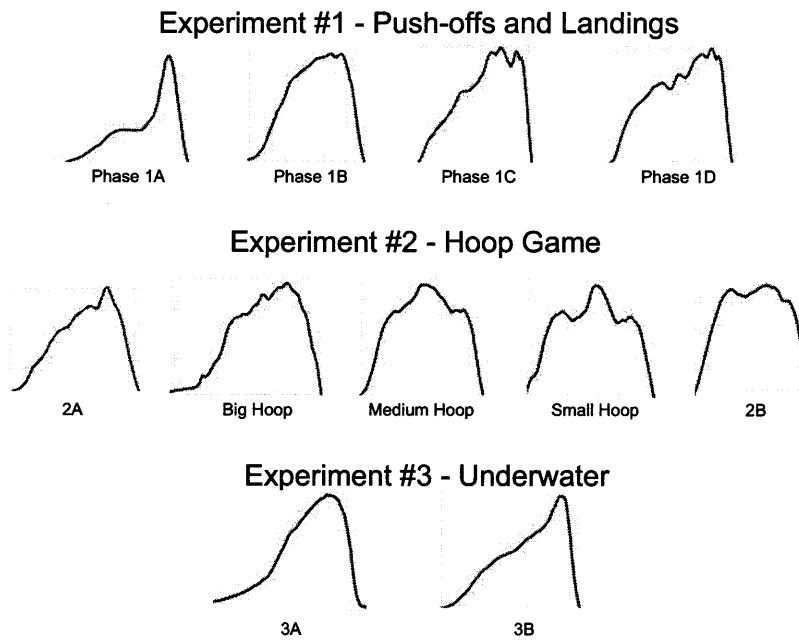
Table 4.5: Summary of all statistical results. The gender tests (to test for any gender effects) are performed across 10 subjects from all phases of Experiments 1 and 2 using a general linear model (GLM). The contrast tests are also using a GLM, contrasting phase averages and sub-phase averages (where noted below). The last three entries report contrast results comparing the average of multiple phases versus the average of other sets of multiple phases. This permits comparison of all 4 phases of Experiment 1 versus both phases of Experiment 3, for example.

Test	<i>p</i>	<i>F</i>	<i>n</i>
Gender Tests			
Max Force	0.412	0.762	10
Contact time	0.970	0.357	10
Mean Force	0.510	0.482	10
Linear Pushoff Energy	0.684	0.180	10
Sig. Landing error	0.031	7.235	10
Mean Force Direction Angle (FDA)	0.997	< 0.001	10
Max FDA	0.228	1.745	10
Integral FDA	0.805	0.065	10
Variance FDA	0.280	1.372	10
Body Angle Change (at departure)	0.433	0.692	10
Body Departure Velocity	0.325	1.123	10
Average contrast tests			
Sig. Max Force 1A - 1D	0.023	6.822	10
Max Force 1D - 2A	0.996	0.004	10
Max Force 1B2 - 1B3 (sub-phases)	0.184	2.178	10
Sig. Max Force 1B3 - 1C1 (sub-phases)	0.008	10.494	10
Sig. Max Force 1ABCD - 3AB (phase averages)	0.015	1913.366	2
Sig. Contact Time 1AB - 1CD (phase averages)	0.016	8.001	2
Sig. Contact Time 1ABCD - 3AB (phase averages)	0.044	211.809	2

ter data is that subjects appear to be developing control strategies underwater that are not consistent with those that are required for a true microgravity environment.



(a) Subject A.



(b) Subject B.

Figure 4-14: Normalized force shape progression for two subjects throughout the experiment (single trials shown). All profiles have been normalized to have the same height (maximum force) and width (contact time) to illustrate changes in the overall force profile.

4.6.4 Astronaut Data

While the above results clearly indicate that an adaptation of the subjects' control strategy took place, it is not immediately evident that the control strategies the subjects adapted to reflected those used by astronauts in a microgravity environment.

Fortunately, an astronaut who has flown on five separate Space Shuttle missions was available to perform a subset of the air-bearing floor push-off experiments presented in this chapter. Since it has been well-documented that veteran astronauts retain their locomotor control adaptation from flight to flight, it was reasonable to assume that this astronaut's control strategies exhibited while moving on the air-bearing floor would be representative of the strategies he developed during his time spent in microgravity.

Figure 4-15 is a representative push-off force profile (in the axial direction) taken from one of the push-offs the astronaut subject performed. The astronaut subject was given the same instructions as all regular subjects were given for Experiment 1.

The data in Figure 4-15 clearly shows the same aspects that other subjects exhibited after they had adapted to the air-bearing floor experiment, but at a much more refined level. The contact time used by the astronaut subject was 1.6 seconds, compared to an average of approximately 1.3 seconds for subjects that had become experienced at the air-bearing floor experiment (*i.e.*, in phase 1D). The astronaut subject also had a maximum push-off force that was less than 70 Newtons. While the other subjects' maximum push-off force dramatically reduced as they adapted to the air-bearing floor experiments, the average push-off force from phase 1D was approximately 130 Newtons (almost twice that of the astronaut subject).

Perhaps the most telling aspect of the astronaut subject's data was the prominent multi-peaked force profile. Figure 4-14 illustrates the other experimental subjects developing a second and sometimes a third peak to their force profiles, but the astronaut data in Figure 4-15 shows several well-defined peaks.

While it is difficult to draw strong conclusions from only one astronaut subject with limited data, it is reasonable to assume that given much more time to adapt, the

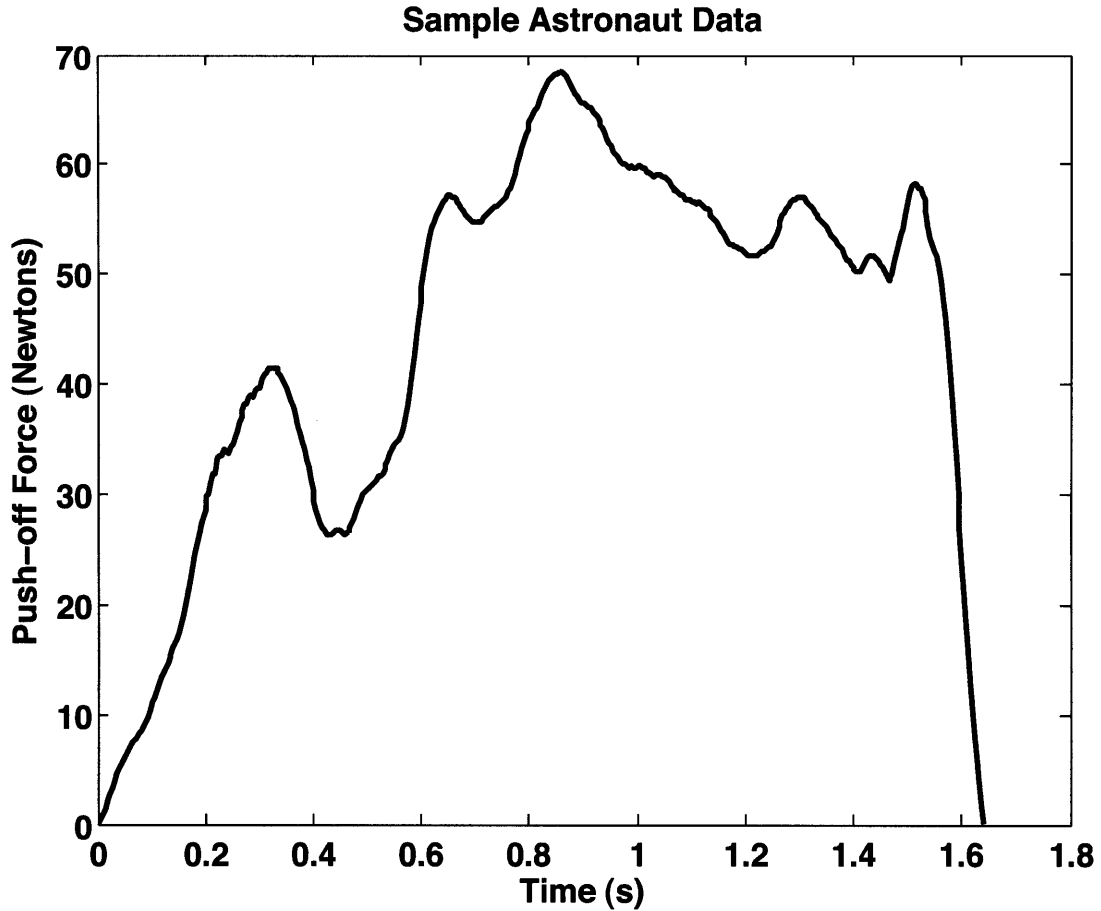


Figure 4-15: A representative push-off force profile taken from an experienced astronaut.

control strategies exhibited by the other experimental subjects would likely approach the control strategy exhibited by the astronaut subject. The data shown in Figure 4-15 can be viewed as a highly advanced version of the data collected from the other experimental subjects.

4.6.5 Relative Force Magnitudes

It is instructive to consider the orders of magnitude of the average interaction forces from the experiments presented in this dissertation in comparison with data from different gravitational environments. Figure 4-16 shows average interaction forces across a spectrum of gravitational and dynamic environments. The air-bearing floor and underwater data was collected from the experiments presented herein. The space

data is from [Amir and Newman, 2000]. The walking and running data is from 1-G and gravity extrapolated data from [McMahon, 1984].

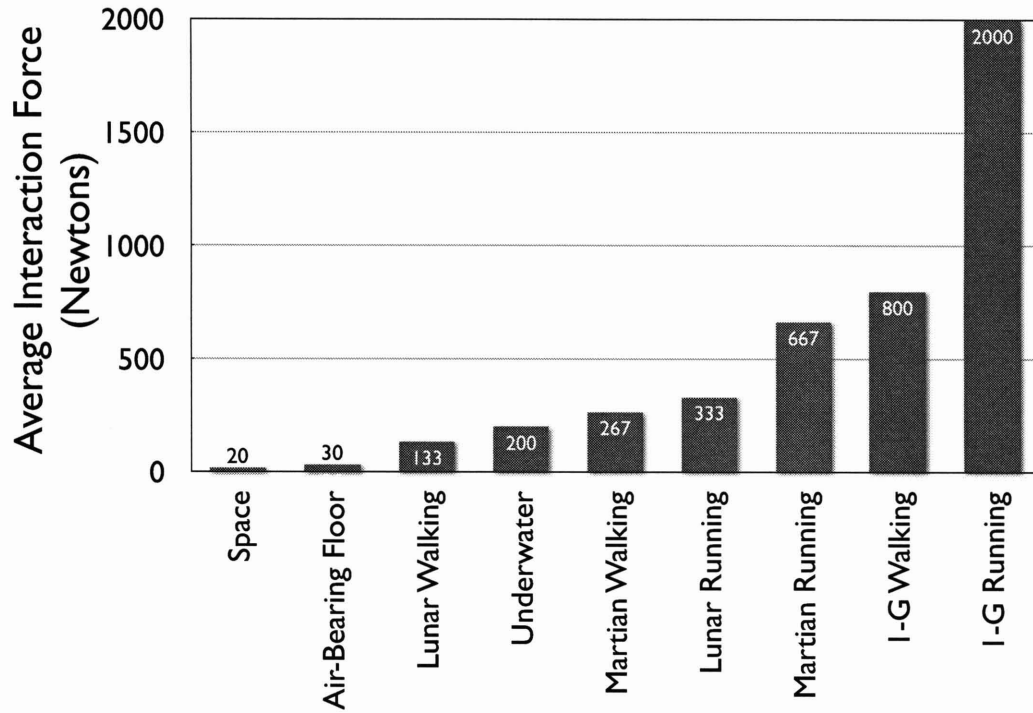


Figure 4-16: Average interaction force magnitudes from different gravitational environments for comparison [McMahon, 1984, Amir and Newman, 2000].

Notice how small the space and air-bearing floor data is compared with 1-G walking and running. Furthermore, while the underwater force data is significantly greater than the space and air-bearing floor data, it is still much less than 1-G walking and running. It is interesting to note that while the underwater environment seems to be inappropriate for developing microgravity control strategies, the relative force magnitudes seem to indicate that it may still be appropriate for simulating lunar and martian motions. Of course, the water viscosity and drag would still be present, but it is possible that the hydrodynamics would impact the walking-type motions expected for lunar and martian locomotion less than the push-off motions required for microgravity locomotion [Newman, 1992].

4.7 Experiment Summary

This chapter has presented the experimental protocols and primary observations from the dynamic human adaptation experiments conducted as part of this research program. The experimental data provides evidence of not only adaptation, but dual adaptation. Together with the simulation results of Chapter 3, these experimental results prove Hypothesis # 1 (that adaptation can be detected using kinetic and kinematic measurements during human motion experiments in different gravity environments). The results from Figure 4-9 provide evidence of dual-adaptation, suggesting that Hypothesis #2 (on dual- or multi-adaptation) could be true. In order to fully test Hypothesis #2, a more complete set of experiments would need to be conducted that exposed subjects to partial gravity environments (in addition to 1-G and micro-gravity environments) and varied the amount of time subjects were required to retain their control strategies.

The only hypothesis remaining to be tested is Hypothesis #3 - that a single adaptation mechanism could be found responsible for locomotor adaptation to a spectrum of gravitational environments. The following chapter addresses this hypothesis by exploring the capabilities of different physiologically plausible control strategies to predict the data seen in the experiments presented in this chapter.

Chapter 5

Adaptation Modelling and Discussions

The previous chapter illustrated the aspects of kinetic data (*i.e.*, forces and moments) that show locomotor adaptation of human subjects to altered gravitational environments. As such, kinetic data was found to adequately characterize the motions. In this chapter, the kinetic data characteristics observed in the previous chapter are studied further.

The experiments in Chapter 4 suggests that as subjects adapt to motions in a simulated microgravity environment, their peak forces reduce, the push-off contact times increase and the force profiles become multi-peaked. One possible reason for such control modifications could be to provide more time for the subjects to correct small errors during the push-off. In the sections that follow, different candidate control strategies are presented and evaluated in terms of their ability to reproduce the qualitative observations from the human experiments as well as the physiological plausibility.

Specifically, a model is sought that can reproduce both the smooth, skewed bell-shaped force profiles seen early in the subjects' adaptation as well as the multi-peaked force-profiles exhibited by well-adapted subjects. Ideally, the model should have a single parameter that can be adjusted to cause the observed adaptation. Figure 5-1 explicitly compares three force profiles from one subject. The first profile is from

the first few trials of Experiment 1, the second profile is from the the middle of Experiment 1 and the third profile is from the last few trials of Experiment 1. For a more detailed progression of force shapes for one subject across the entire study, please refer to Figure 4-14 in Chapter 4.

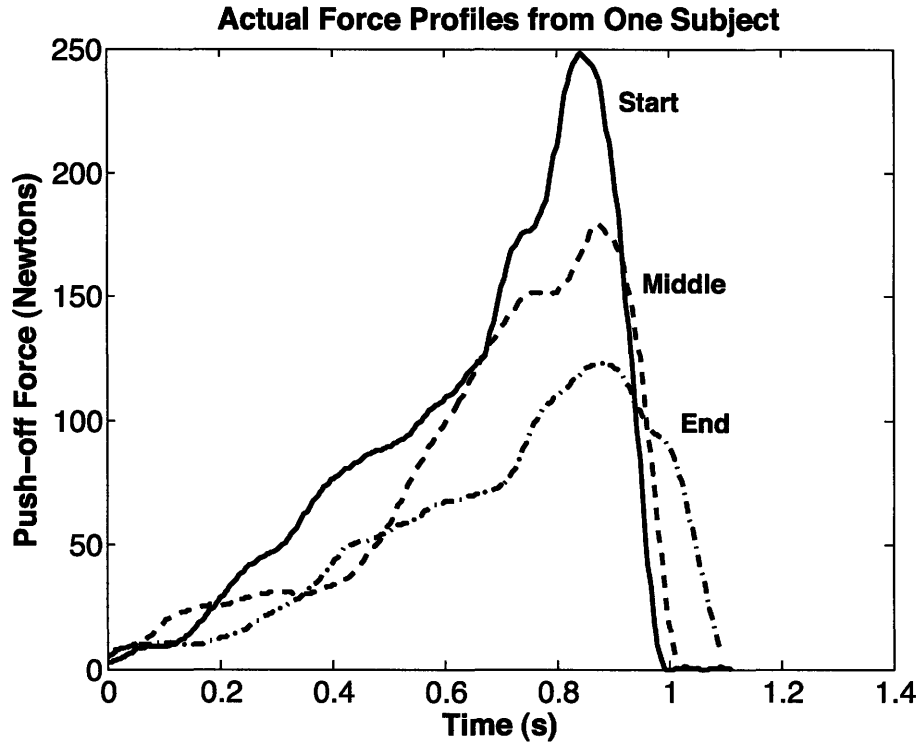


Figure 5-1: Representative force profiles for one subject plotted together to show explicit differences in maximum force, contact time and overall shape. The solid line is a representative profile from trials 1 - 5 of phase A of Experiment 1, the dashed line is a representative profile from the last 5 trials of phase B and the first 5 trials of phase C and the dash-dotted line is from the last 5 trials of phase D Experiment 1 (*i.e.*, the end of Experiment 1).

5.1 Push-off Control using Springs

A common way to model the human body during running is to represent the lower limbs as springs that repeatedly compress and then release their energy with every stride [Cavagna and Margaria, 1966, McMahon, 1984]. Naturally, an extension of this principle should lead to jumping (in 1-G) or push-offs (in microgravity). By

pre-loading the “spring” made by the lower limbs and releasing it, a jump or push-off should result. Figure 5-2 illustrates the mechanics of the push-off model being considered for this study.

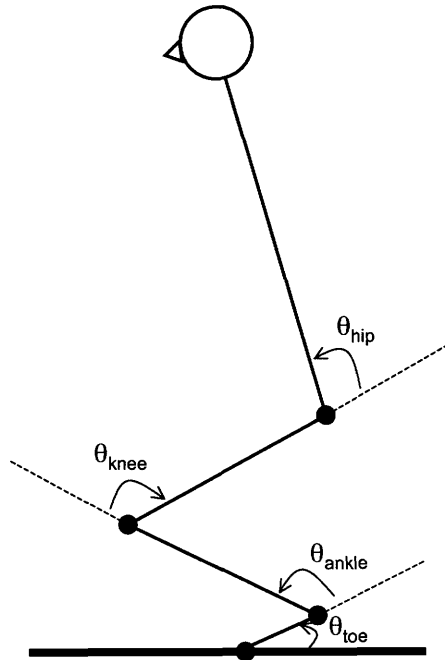


Figure 5-2: A stick-figure model representing the joints of the leg using a rigid-body model. The dynamics for this system are described in detail in Chapter 3.

Muscle pairs acting on joints are often modelled as settable torsional springs and dampers [Flash, 1987, Bizzi et al., 1994]. When the muscles connected to a particular joint are set to a particular (constant) activation level, the joint will eventually come to rest at some position that is dependent upon the force field that the joint happens to be in at the time (known as the equilibrium position, since at that point, all joint torques are in equilibrium). If the joint is exposed to gravity, it will deflect. If there’s friction of some sort, this will also alter the rest position of the joint accordingly. In a dynamic situation, where the activation levels change over time, the joint may never reach its equilibrium position. Instead, the joint “chases” the command as the torsional springs and dampers respond to the difference between their current state, the command and any external forces (*i.e.* gravity, friction, etc.).

A simple proportional-derivative (PD) controller can adequately represent the

joint control described above. Figure 5-3 illustrates the imaginary torsional springs and dampers added to each joint and Figure 5-4 depicts the control block diagram.

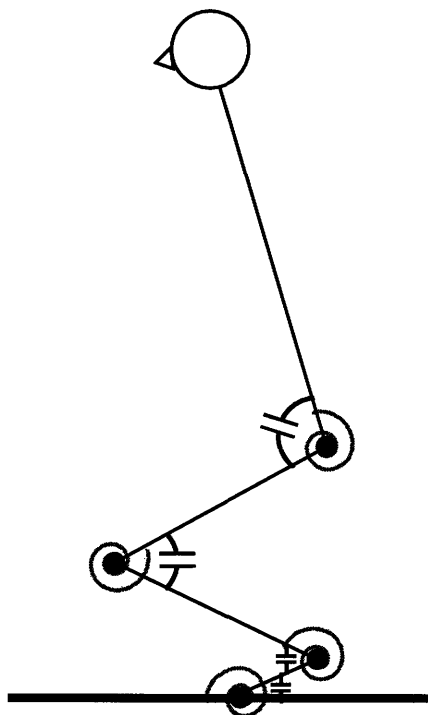


Figure 5-3: The stick figure model from Figure 5-2 with torsional springs added to the joints to illustrate the dynamic model assumed to describe muscle / joint motion.

Mathematically, this control law can be written as:

$$\tau = -(K_p(\theta - \theta_{ref}) + K_d(\dot{\theta})) \quad (5.1)$$

where τ is the joint torque for a given joint, θ is the joint angle, $\dot{\theta}$ is the joint rate, θ_{ref} is the commanded reference trajectory for the given joint and K_p and K_d are the stiffness and damping of the joint. It is important to note that the control law chosen for this study controls to zero velocity in the damping term. In other words, this control law “damps to ground”. While others [McIntyre and Bizzi, 1993] have proposed equilibrium control models that damp to the actual velocity trajectory as opposed to simply zero, the purpose of this study was to keep the models as simple as possible and still reproduce the observed behaviour. For the simulations presented

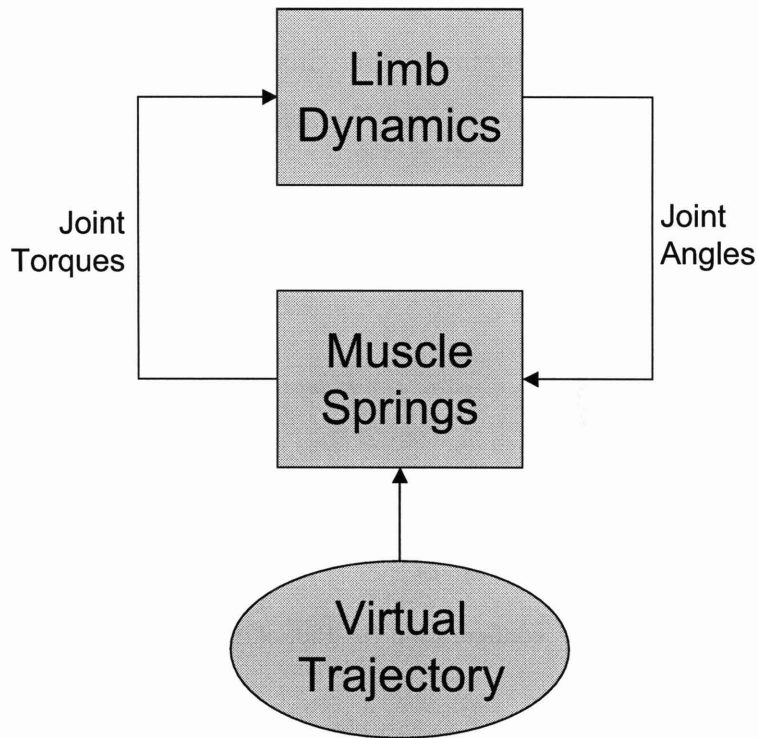


Figure 5-4: Control block diagram for the torsional spring / damper control model.

in this chapter,

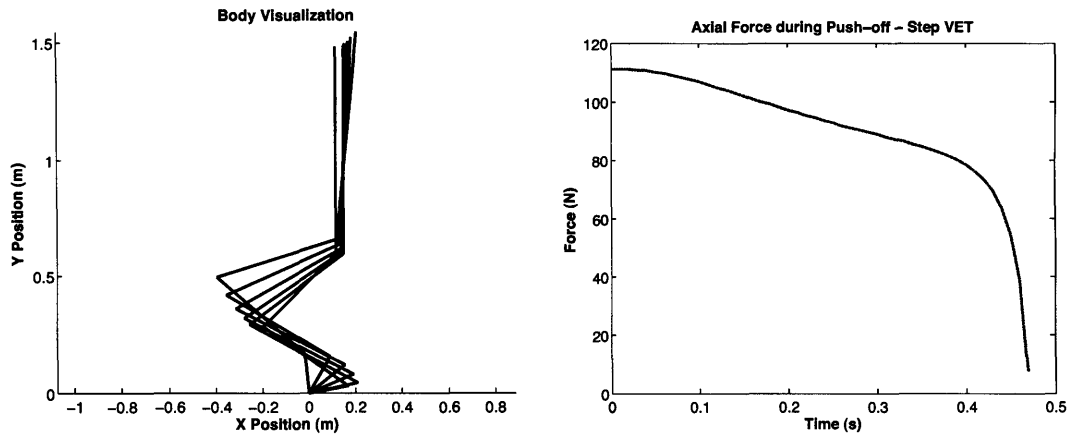
$$K_p = \begin{bmatrix} 1.00 & 0 & 0 & 0 \\ 0 & 3.75 & 0 & 0 \\ 0 & 0 & 7.50 & 0 \\ 0 & 0 & 0 & 3.75 \end{bmatrix} \quad (5.2)$$

and

$$K_d = K_p/10 \quad (5.3)$$

Before the above control can be implemented, a decision must be made about what the reference joint trajectories should look like. The simplest form of the reference trajectories would be a step change in all joint trajectories from the initial joint angles to angles that represent the fully out-stretched position (based on the joint angle notation convention in Figure 3-2, this would correspond to 90 degrees for the first joint and 0 degrees for all other joints). Lyapunov stability analysis reveals that this kind of control law will always be stable [Asada and Slotine, 1986], however, can

it reproduce the typical force profiles that were observed in Chapter 4? Figure 5-5 illustrates the push-off results obtained using this type of reference trajectory along with the model outlined in Figure 5-4 and Equation 5.1.



(a) Plot illustrating the body configuration over time. (b) Plot of the axial push-off force as a function of time.

Figure 5-5: Simulation results using a step change in the joint reference trajectories. Notice how while the body visualization seems correct, the forces are not representative of the skewed bell-shaped profile seen during the experiments.

Notice in Figure 5-5(a) that while the general body shape of the simulated subject looks approximately correct, the force trace in Figure 5-5(b) does not contain the skewed bell-shaped profile seen in Figure 5-1. The kinematics in Figure 5-5(a), however, do look correct since most of the observed motion came from the subjects' ankles and toes. The fact that the kinematics look correct while the kinetics do not underscores the importance kinetic data analysis. Since the torques start immediately following the step change, Figure 5-5(b) does not reproduce the ramp up in forces seen in the data from Chapter 4.

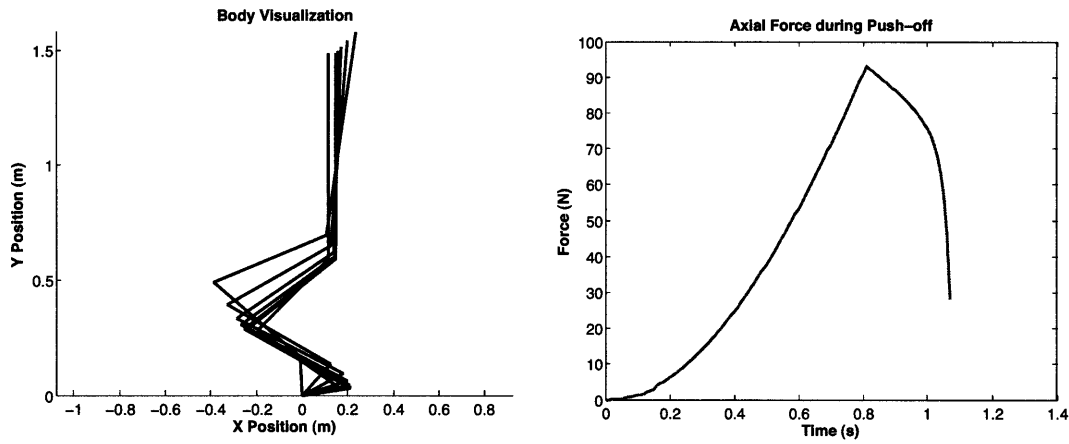
A natural change to the reference trajectory would be to make it gradually move from the starting position to the end position with the start and end points fixed and the initial slope constrained to zero. The time taken for the reference joint trajectories to reach their final destinations is a parameter that can be adjusted. Realizing such a reference trajectory requires that each joint follow a quadratic trajectory taking the form:

$$\theta_{ref}(t) = \theta_0 + \alpha t^2 \quad (5.4)$$

where

$$\alpha = \frac{\theta_f - \theta_0}{t_c} \quad (5.5)$$

In the above, θ_0 and θ_f are the initial and final joint angles respectively and t_c is the time the command takes to move from the initial joint positions to the final joint positions. Figure 5-6 illustrates the results using a gradually sliding reference trajectory.



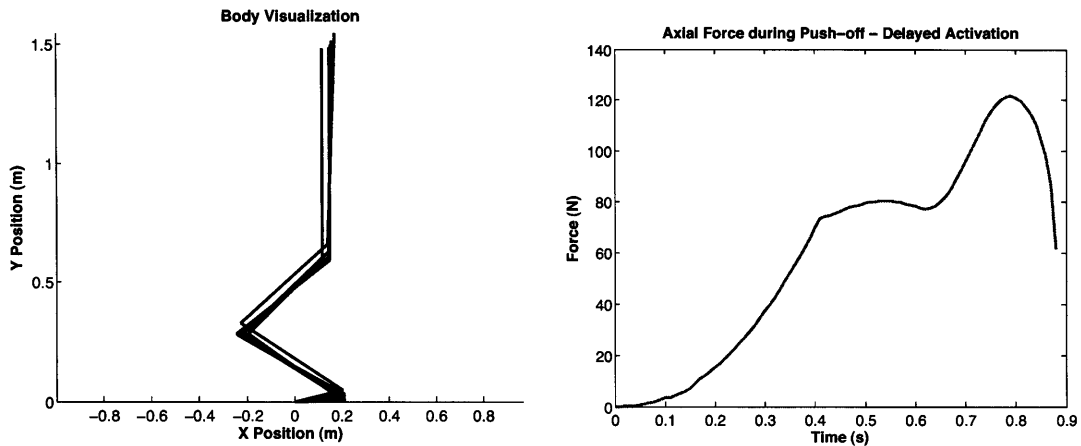
(a) Plot illustrating the body configuration over time. (b) Plot of the axial push-off force as a function of time.

Figure 5-6: Simulation results using a gradual change in the reference trajectory. While not smooth, the general skewed bell-shaped force profile is similar to the early, pre-adapted experimental results.

For the above simulation, the reference trajectory for each joint was assumed to arrive at their final destinations at the same time. The results in Figure 5-6 are certainly an improvement over Figure 5-5 in that the forces build up from zero. Furthermore, comparing the overall shape of Figure 5-6 with early, pre-adaptation trials in Figures 4-14 and 5-1, a clear similarity is noted. However, since all joints are activating at the same time and roughly the same rate, only one force peak can be predicted by this model. Furthermore, aside from adjusting the joint stiffnesses, it is not clear what part of the model could plausibly adapt to different gravitational environments.

A simple way to create multiple force peaks is to offset the muscle activations in time. This can be realized by delaying when the reference trajectory for each joint

begins to move to its target. By delaying only the toe joint, a clear second peak due to a “toe flick” can be seen just as the modelled subject leaves the sensor (see Figure 5-7).



(a) Plot illustrating the body configuration over time. (b) Plot of the axial push-off force as a function of time.

Figure 5-7: Simulation results using a gradual change in the reference trajectory with delayed muscle activation offsets. The shape of the force profile resembles the shape of adapted subjects. However, a method for choosing the offsets is not intuitive and is entirely feed forward in nature.

While the results in Figure 5-7 are promising and clearly do a reasonable job predicting the shape of the observed data from later trials in the adaptation process, it is not clear how the subjects would select these time delays. Furthermore, a completely different set of activation times and stiffnesses are required in order to predict each motion. Thus, subjects would need a completely different set of activation times and muscle stiffnesses in order to execute a fast, high-force push-off versus a slow, low-force push-off.

Finally, the above control strategy is entirely feedforward in nature. By definition, the reference trajectory is feedforward, however, the selection of activation times also need to be pre-determined prior to the motion. Anecdotal comments from subjects during the experiments revealed that subjects found themselves able to correct for small errors during the push-off if they slowed their motions sufficiently. Certainly, the fact that subjects perceived errors being compensated for during the motions suggests that some sort of feedback was present during the later trials. In general, the proposed feedforward control scheme alone is not robust enough to be considered plausible for human motion.

The next section explores some fundamental properties of the human neuro-muscular system, namely muscle activation dynamics, force feedback through the Golgi tendon organs (GTO), physical signal propagation delays in the human body and the ability for the cerebellum to close a proprioceptive feedback tracking loop. It will be shown that intrinsic properties of these neuro-muscular characteristics can help predict not only the observed force-shape trends, but also the adaptation of those trends.

5.2 Muscle Dynamics, Force Feedback and Transportation Delays

Using physiologically-relevant elements provides strength to models because they tend to remove any arbitrary components added merely to improve model performance.

It is sometimes the case that adding more complexity to a model ends up providing simpler, more meaningful results [Gribble et al., 1998].

The following sections provide some basic background for the physical elements incorporated into the proposed control model. Specifically, it will be shown how cerebellar and spinal feedback, along with representative signal transmission delays and dynamics can be used to improve the model fidelity and reproduce the observed adaptation behaviour described in Chapter 4.

5.2.1 Long-loop, Cerebellar Tracking Control

One of the observations noted in Chapter 4 was a significant increase in sensor contact time as the subjects adapted to the floor experiment. One possible reason for remaining in contact with the sensor longer could be to give the subjects more time to correct errors in the positioning of the subjects' center of mass, since a straight push-off requires the push-off force to go through the center of mass.

Using visual and / or proprioceptive feedback, it is reasonable that the subjects could close a feedback loop around the sensed center of mass angle error. This computation would need to be performed in the cerebellum, as pictured in Figure 5-8.

The round-trip signal propagation delay between the cerebellum and the lower leg is typically on the order of 100 ms. As such, the cerebellar COM tracking loop used in this model contained a 100 ms transport delay. However, it should be pointed out that the cerebellum is often assumed to be able to handle these delays quite well, effectively eliminating the effect of the delay. Miall [1993] and Massaquoi [1996] have shown that the cerebellum can be modelled as a Smith predictor to account for the long time delays [Miall et al., 1993, Massaquoi and Slotine, 1996]. A Smith predictor is a control tool often used in controlling telerobotics that incorporates a model of the system dynamics at the remote controlling end of the time delay (in this case, the cerebellum). The system dynamics are then used to predict the result of the commanded control after the known time delay. Knowing the dynamics and the time delay allows the Smith predictor to virtually eliminate (or at least significantly reduce) the effect of the delay [Smith, 1959]. For simplicity, the model assumed for

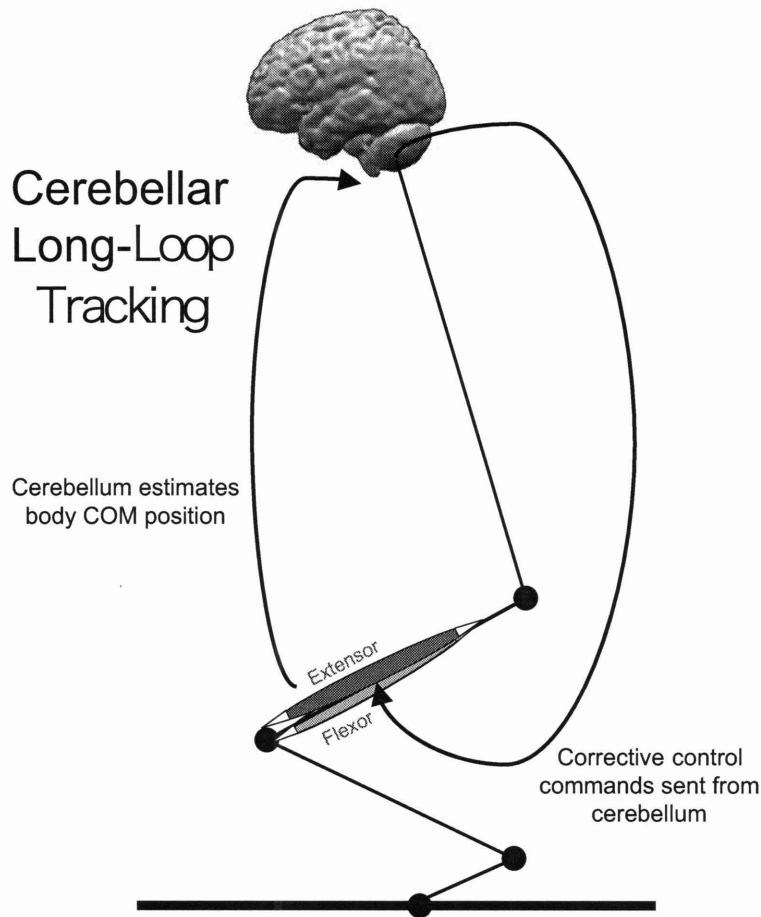


Figure 5-8: Stick-figure model illustrating the cerebellar long-loop COM tracking feedback.

this research did not include any time delay compensations such as a Smith predictor, so the full 100 ms delay was included in the cerebellar feedback loop.

The long-loop cerebellar tracking controller took the following form:

$$u_{corr} = K_c \Delta \theta_{body} \quad (5.6)$$

where u_{corr} are the correction commands assumed to be commanded by the cerebellum, $\Delta \theta_{body}$ is the angular deviation of the body's center of mass from a straight forward trajectory and K_c is the cerebellar control gain matrix that maps the angular deviation to appropriate joints to correct the perceived error. The reference

trajectory is then modified by the cerebellar tracking loop as follows:

$$u = \theta_{ref} - u_{corr} \quad (5.7)$$

where u is reference trajectory modified by the cerebellar feedback.

The gain matrix used in this model was:

$$K_c = \begin{bmatrix} 0 \\ 1.6 \\ 0 \\ 2.4 \end{bmatrix} \quad (5.8)$$

Note that the gain matrix in Equation 5.8 assumed that all COM control was executed by the ankle and hip (joints 2 and 4 when counting up from the toe joint). The vector representing the position of the body's center of mass was computed as:

$$\mathbf{r}_{com} = \left(\sum_{i=1}^4 m_i \mathbf{r}_i \right) / \left(\sum_{i=1}^4 m_i \right) \quad (5.9)$$

where m_i is the mass of the i^{th} link and the position of the center of mass of the i^{th} link, \mathbf{r}_i is defined as:

$$\mathbf{r}_i = \begin{bmatrix} l_1 \cos(\theta_1) + l_2 \cos(\theta_2) + \dots + l_i \cos(\theta_i) \\ l_1 \sin(\theta_1) + l_2 \sin(\theta_2) + \dots + l_i \sin(\theta_i) \end{bmatrix} \quad (5.10)$$

where l_i is the length of the i^{th} link, l_c is the distance from the i^{th} joint to the center of mass of the i^{th} link and θ_i is the i^{th} joint angle.

The previous section described a feedback control loop assumed to be executed through the cerebellum. However, much of simple human motion control (*i.e.* reflexes) is known to be executed via spinal feedback loops. The following section describes how a spinal feedback loop (using Golgi tendon organs) could provide adjustable force control.

5.2.2 Golgi Tendon Organ Feedback

Given that one of the key observations from Chapter 4 was that subjects reduced the maximum force exerted when performing push-offs, a natural mechanism causing force reduction is desired. The Golgi tendon organs (GTO), located at the muscle-bone interface of each muscle, is responsible for sensing muscle stress. The stress signal is relayed to the spinal cord and used to limit the amount of muscle force commanded to each muscle in order to prevent injury. The force limiting effect is accomplished by the GTO inhibiting the active muscle and activating its opposing muscle to effectively limit the torque applied to each joint [Houk and Rymer, 1981, Nichols and Houk, 1976]. Figure 5-9 illustrates this GTO feedback loop on the stick figure originally presented in Figure 5-2.

While the GTO model provides a natural means of moderating the joint torque at each joint, it also provides an inherent time delay due to the spinal signal transmission delay (approximately 35 ms in each direction). Setting a low GTO threshold for a joint would inhibit a particular joint until the joint torque falls below the set threshold. Then, after 35 ms, the GTO reactivates the joint, causing a small spike in activation. Specifically, the effect of the GTO force regulation takes the following form:

$$u_\alpha = -b[-\tau_{thresh} + \tau_{GTO}(t - \Delta t)]_+ + u \quad (5.11)$$

$$u_{joint} = u_\alpha(t - \Delta t) \quad (5.12)$$

where u_{joint} is the reference trajectory modified by both the cerebellar and spinal (GTO) feedback loops, u is the corrected reference trajectory from the cerebellar feedback (Equation 5.7), Δt is the one-way spinal transmission delay (35 ms), τ_{thresh} is the GTO torque threshold, τ_{GTO} is the joint torque sensed by the GTO, b is the GTO gain and

$$[x]_+ = \max(0, x) \quad (5.13)$$

Both the cerebellar and spinal feedback loops described above provide key control structure to the model being proposed, especially when combined with the realistic

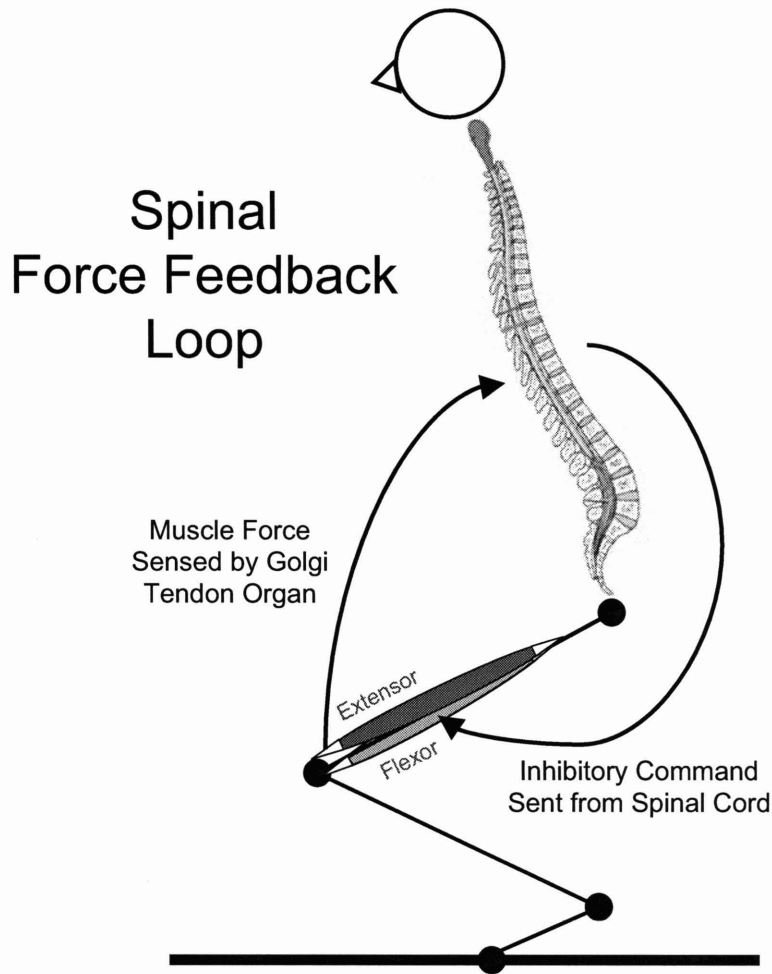


Figure 5-9: Stick figure model illustrating the Golgi tendon organ spinal feedback loop.

time delays described above. However, in addition to loop delays, the dynamics associated with the chemical and mechanical activation of muscles must be incorporated in order to provide a good representation of muscle / joint motion generation resulting from neural commands.

5.2.3 Excitation / Contraction Coupling

An important effect of human motion stems from the dynamics of muscle excitation and contraction. Both the chemical excitation and the mechanical contraction of the muscles to generate joint torques in reality does not happen instantaneously.

Instead, [Winters and Stark, 1987] showed that both these effects can be modelled using simple, linear, low-pass filters. Figure 5-10 illustrates the linear excitation / contraction coupling proposed by [Winters and Stark, 1987] and used in the model presented herein.

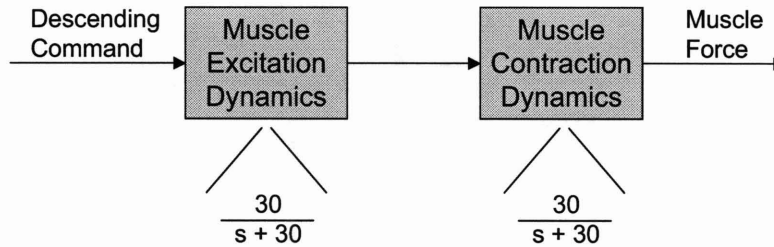


Figure 5-10: Control block diagram illustrating the linear excitation / contraction dynamics assumed for the push-off model (as described in [Winters and Stark, 1987]).

5.3 Adaptation Model

After incorporating the above-mentioned components, the new control block diagram can be found in Figure 5-11.

By scaling the GTO gains for all joints (keeping the ratios of GTO gains the same among joints so that only one parameter is tuned), the model is shown in Figure 5-12. Note the striking similarities not only in shape, but also in absolute force maximum and contact time with the sensor. By choosing an appropriate GTO gain scale factor (TG), both the early, non-adapted behaviour can be recovered in addition to the force profiles that characterize well-adapted subjects.

The base GTO gain matrix was chosen to be

$$b_{base} = \begin{bmatrix} 0.880 & 0 & 0 & 0 \\ 0 & 0.312 & 0 & 0 \\ 0 & 0 & 0.160 & 0 \\ 0 & 0 & 0 & 0.280 \end{bmatrix} \quad (5.14)$$

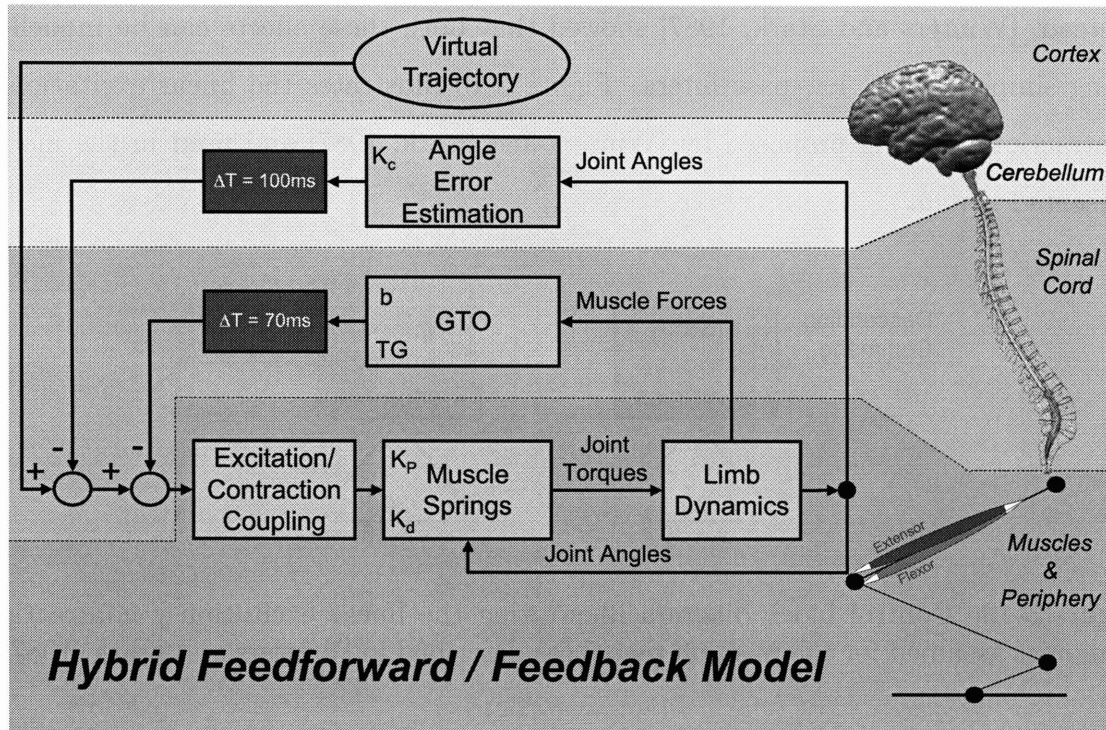


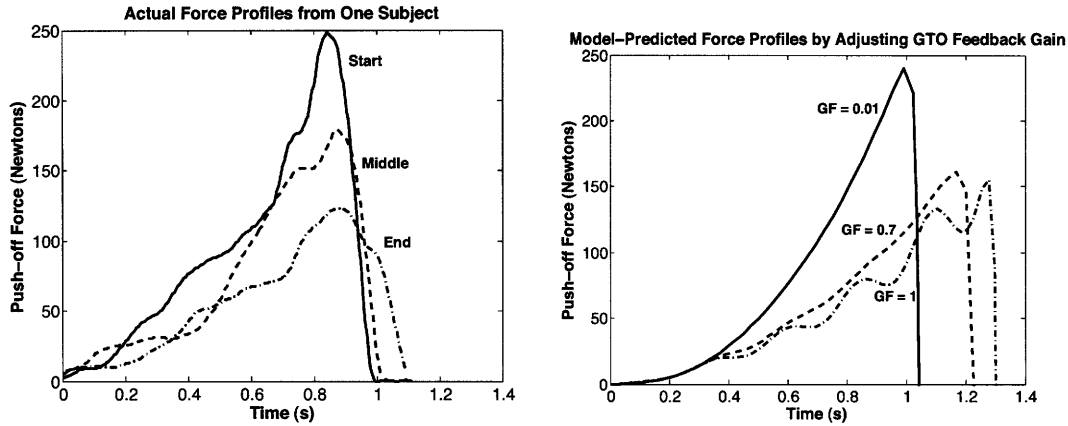
Figure 5-11: Control block diagram incorporating GTO feedback, long-loop tracking control and the excitation / contraction coupling.

and the scaled GTO gain matrix was

$$b = TG b_{base} \quad (5.15)$$

where TG is the scale factor that, when varied, reproduces the observed adaptation as depicted in Figure 5-12.

At the beginning of this chapter, it was postulated that a benefit to reducing the push-off force was that it leads to longer sensor contact times. Having foot contact with the sensor longer allows more time for the cerebellar center of mass tracking loop (see Figure 5-8) to correct these errors. This effect was demonstrated in simulation. Figure 5-13 illustrates how as the GTO gain increases (by increasing TG), the contact time increases and the targeting error decreases. The targeting error was computed assuming that the target was 4 meters away from the body at the time of the push-off. The angular error, $\Delta\theta_{body}$ from Equation 5.6 was used to compute the targeting error



(a) Representative force profiles for one subject (b) Plot of model-predicted force profiles by repeated here from Figure 5-1 for comparison. adjusting the GTO force threshold.

Figure 5-12: Plots comparing the actual experimental data (on the left) with the model predictions (on the right). The different adaptation levels are selected through modification of only one variable: The GTO force feedback gain.

in centimeters as:

$$X_{err} = 400 \tan(\Delta\theta_{body}) \quad (5.16)$$

5.4 Discussion

5.4.1 Hybrid Feedforward / Feedback Model Performance

The proposed model in Section 5.3 requires only one parameter to be tuned to predict both unadapted and adapted behaviours. This single parameter (*i.e.*, the scale factor multiplying all joint GTO gains) also holds physical relevance to the differences between gravitational environments. One of the key differences between 1-G and microgravity locomotion is the presence or absence of gravitational torques being constantly required to hold one's body up in the gravitational field. This constant force background requires high enough joint torques (and thus low force feedback gains) be permitted to prevent the body from collapsing when standing up. However, these same joint torques would not be appropriate for the low-force, delicate motions required in microgravity.

The model proposed above is a hybrid feedforward / feedback model, providing

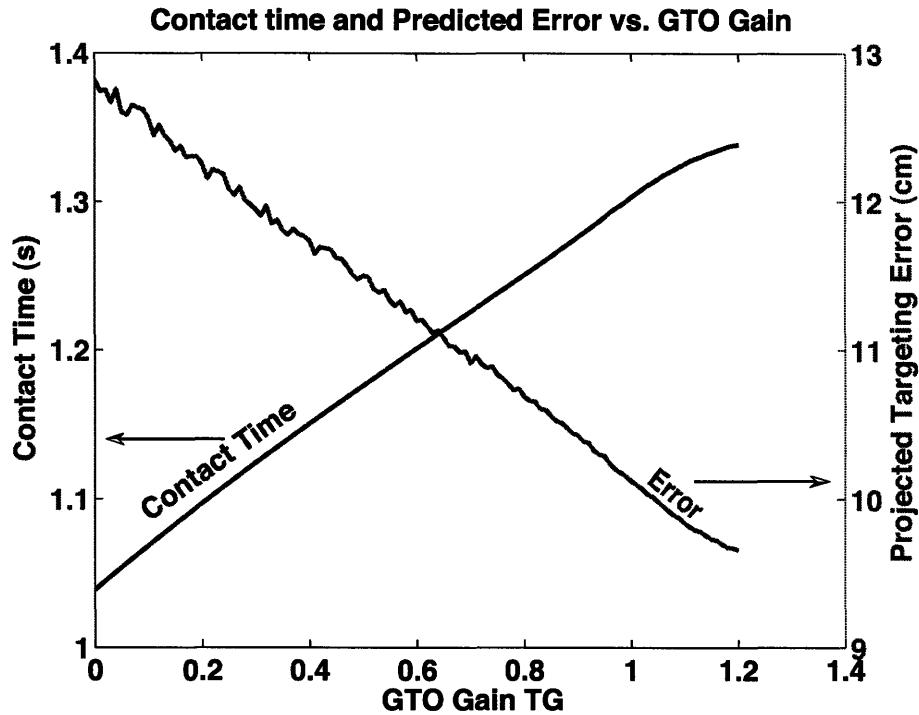


Figure 5-13: Plot illustrating the increase in contact time and the decrease in targeting error as the GTO force feedback gain is increased (simulating increasing adaptation to a microgravity environment).

natural robustness. The multi-peaked force profiles are generated by the natural time delays that arise from signal transmission times in the human body and not from arbitrarily chosen joint firing delays. Furthermore, lower force push-offs can be generated by simply increasing the GTO force feedback gains (via the TG parameter).

Decreasing the force application has other benefits aside from those noted above. [Schmidt et al., 1979, Todorov, 2002] have shown using EMG measurements that the variability of muscle force increases as the muscle force increases. The Bayesian optimization approach to motor coordination [Kording and Wolpert, 2004, Ferguson et al., 2004a] suggests that humans choose control strategies that minimize the targeting error variance of the task. Thus, if lower muscle forces (and hence, lower joint torques) reduce the error variance of the force (joint torque) application, it seems reasonable that humans would choose the lowest force they can while still being able to accomplish the task.

5.4.2 Limitations of the Proposed Model

The model proposed above has assumed a GTO model that is sensitive to both actively commanded and passively generated joint torques. Data presented in [Houk and Henneman, 1967] suggest that the GTO's actually do not respond (or respond very little) to passive forces. However, since then, others have challenged the findings of [Houk and Henneman, 1967] in [Gregory et al., 2002, Jami, 1992]. Recent research has also shown a strong link between GTO signals and the timing and control of locomotor function [Conway et al., 1987, Dietz and Duysens, 2000]. Furthermore, many prominent researchers have continued to use the GTO model presented above in recent research [He et al., 1991, Spoelstra et al., 2000].

However, while the model results presented above indicate that force control most likely plays a key role in human locomotor adaptation to different gravitational environments, an important question that has not been answered by this research is where exactly does this force control take place. In an effort to develop the simplest possible model that could predict the observed adaptation results, I assumed simple spinal force feedback, however, this need not be the case.

Research has shown that GTO force signals reach the cerebellum and cortex [Konorski, 1970, MacKay and Murphy, 1974]. Thus, it is conceivable that the force control model proposed in this chapter may actually be executed via long-loop (either cerebellar or even trans-cortical) control. Figure 5-14 compares the model results obtained by increasing the force loop delay to 100 ms, to reflect moving the force control from the spinal loop to the cerebellar loop.

The results in Figure 5-14 indicate that moving the control from the spinal loop to the cerebellar loop has very little effect on the maximum push-off force, the contact time or even the multi-peaked force profile prediction. This apparent insensitivity to the location of the force control suggests that while force control is a likely candidate for predicting locomotor control adaptation, I cannot use the modelling results in this chapter to suggest exactly where the control takes place. In Chapter 6, suggestions are made regarding future experiments that could be conducted to provide insight

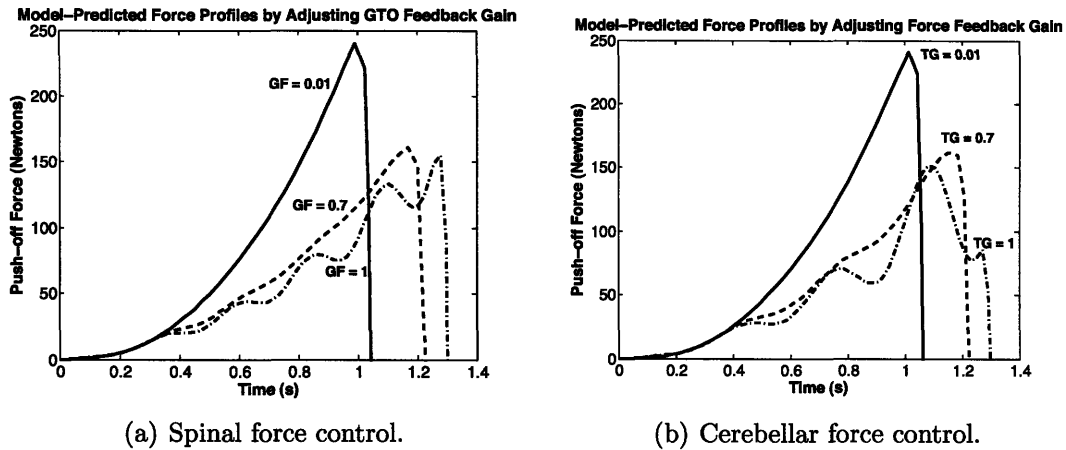


Figure 5-14: Plots comparing spinal force control versus cerebellar force control. The results were obtained by simply increasing the loop delay from 70 ms (spinal) to 100 ms (cerebellar).

into where this force control might be located.

The muscle model assumed in this research was linear, following Equation 5.1. A possibly more physiologically accurate muscle model would have the muscle stiffness increase with the activation level. As such, one could propose a muscle model similar to Equation 5.1 but where:

$$K_p(u) = K_0 + K_1u \quad (5.17)$$

where u is the output of the excitation / contraction filters (see Figure 5-10) and K_0 and K_1 are constants. Since the model in Equation 5.1 assumed $K_1 = 0$, it is possible that non-zero values for K_1 would produce a greater force as the muscle activation increased.

The kinematics produced by the model show the motions being dominated by ankle and toe motions. While a similar trend was also observed during the experiments, the knees tended to flex more during the experiments than predicted by the model. In the future, when the joint angles can be analyzed more reliably, actual kinematic data will be compared with the model results. A possible modification to the model could be to increase the knee motion to better match the observed body motions. However, without reliable joint angle data, this type of comparison and subsequent model modification is not possible at the time of this writing.

5.4.3 Other Feedback Loops to Consider

The long-loop cerebellar control law expressed in Equation 5.6 assumes no velocity feedback. It is quite possible that the long-loop control could provide some velocity feedback using visual inputs or possibly vestibular cues [Young, 1995]. A possible extension to this model could be to include a body angle rate feedback to improve the error-correcting feedback as the contact time increases.

Another important feedback mechanism that has not been considered as part of this modelling effort is the role tactile feedback might play in guiding the subject's applied force direction during the push-offs. Tactile sensations in the foot and ankle are likely to be transmitted to the cerebellum or even the cortex to enhance the feedback control.

Chapter 6

Conclusions and Recommendations

6.1 Thesis Summary

This dissertation has presented a comprehensive research effort to identify, quantify and model the key aspects of human adaptation to different gravitational and dynamic environments. The hypotheses that drove this research were as follows:

1. Kinetic data from a force / moment sensor and kinematic joint angle data can be combined in a dynamic filter to produce accurate, reliable estimates of whole body motions during adaptation experiments. Using the combined kinetic and kinematic data, metrics can be defined that illustrate control strategy adaptation to different gravitational and dynamic environments.
2. Given exposure to a particular gravity environment, humans will retain the adapted locomotor control strategies for multiple weeks of constant exposure to a different gravity environment, providing evidence of *multi-adaptation*
3. A single adaptation mechanism governs human locomotor control strategies across a spectrum of gravity environments in a manner similar to that predicted by either Bayesian optimization; or the virtual trajectory hypotheses or a combination of the two.

The first part of this research program was to design a reliable and accurate 6-axis force / moment sensor for use in human motion experiments. The ultimate application

of the force-moment sensors was for use during the Microgravity Investigation of Crew Reactions in 0-G (MICRO-G) International Space Station (ISS) experiment. The force-moment sensor design was based on a spaceflight-proven design (EDLS - Enhanced Dynamic Load Sensors) that accurately and reliably measures forces and moments in changing gravitational environments. New on-board electronics made the MICRO-G sensors modular, self-contained and easy to relocate, thus minimizing the crew time required to use them on-orbit. Furthermore, the MICRO-G sensors were designed to be used underwater in addition to on-orbit to provide crucial feedback to astronauts training for the space missions underwater in the Neutral Buoyancy Lab (NBL). Enhanced real-time feedback features of the MICRO-G sensors will engage astronauts during the MICRO-G ISS experiment and will hopefully lead to improved adaptation performance. The development of the MICRO-G sensors contributed to testing Hypothesis #1.

A suite of analysis tools were created to aid in the analysis of the kinetic (forces and moments) and kinematic (joint angles) measurements. In addition to a Kalman filter to estimate the motion of the subjects' center of mass motions, a novel joint torque estimator was also developed. The torque estimator combined an unscented Kalman filter with a non-linear least squares estimator. The results of the torque estimator development showed that reliable joint control torque estimates could be obtained using the estimator developed as part of this research, even for multi-joint systems where the joint torque observability matrix was not full rank. Furthermore, the joint torque estimator was shown to provide a simple way to include other body measurements such as accelerometers to improve the estimation accuracy.

The estimator development described above demonstrated the superior filter performance that can be achieved by combining both kinetic and kinematic data together. The force and moment measurements provide acceleration information, but no position information, while the joint angle measurements provide position information, but only limited velocity and acceleration information. By including force / moment data into human motion experiments, outcomes from these experiments can be obtained with greater reliability than using either kinematic or kinetic measure-

ments alone. The design of unique estimators to measure and record human motion adaptation further supported Hypothesis #1.

Experiments were conducted on a 1-G air-bearing floor microgravity simulator and underwater to provide contrasting dynamic and gravitational environments. Subjects performed leg push-offs and hand landings to demonstrate their control strategies as they adapted. Forces and moments from the push-offs and landings were recorded using the MICR0-G 6-axis force-moment sensors. Joint angles were measured using a kinematic video analysis system.

A set of experiment support equipment was designed and built to support the human motion experiments. A near-frictionless air-bearing floor was constructed using an industrial air-pallet and a Unistrut sensor mounting frame and air-hose support mast. The air-bearing floor provided simulated weightlessness in one plane (parallel to the floor) with a coefficient of kinetic friction of only 0.004 (or about that of a professional speed skater). The Unistrut sensor mounting frame was also designed to be assembled at the bottom of a swimming pool to support the underwater experiments. The new MICR0-G sensors (designed to be waterproof up to 10 meters underwater) and special underwater video camera housings were used to collect data during the underwater experiments.

Three experiments were conducted using a single group of repeated subjects. The first experiment was conducted on the air-bearing floor. Subjects performed a series of foot push-offs and hand landings, followed by hand push-offs and foot landings. During this experiment, the force / moment measurements indicated clear (and statistically significant) adaptation to a planar microgravity environment. The peak foot push-off force reduced and the sensor contact time increased as the subjects adapted. This observation, along with the development of the MICR0-G sensors and the associated data analysis software proves Hypothesis #1 (that human motion adaptation can be observed) to be true.

Another interesting observation made during the first experiment was the fact that after a short directed break, subjects' adaptation rate increased significantly. This result may be compatible with other research that has demonstrated the improved

learning performance of motor skills after a break, however, further experimental testing would be required to verify this learning effect.

In the second experiment, subjects placed a hoop on a post to force their motions (also conducted on the air-bearing floor) to be as accurate as possible. This added complexity caused most subjects to make distinct changes in how they controlled their bodies. As the adaptation progressed, the axial push-off force changed from being a smooth, single-peaked bell-shaped curve to a flatter, multi-peaked, wider and shorter force profile.

Another key observation from the second experiment was that most subjects retained their adapted control strategy from the first experiment even though 3 weeks had passed between the first and second experiment. This was evidenced by similar peak push-off forces and sensor contact times as those measured at the end of the first experiment. This observation provided proof that dual adaptation (the ability to retain multiple control strategies) likely was being exhibited, suggesting that Hypothesis #2 may be true. More experiments in partial gravity environments with variable exposure times would be required to completely test Hypothesis #2, however, the dual-adaptation result found in this research is promising.

The third experiment was conducted underwater. In this setting, subjects performed straight push-offs and landings in the same manner as in the first experiment. Due to the water drag, the peak push-off force and sensor contact time measurements taken underwater looked similar in magnitude and overall shape to those measured early in the the first experiment (when the subjects had not yet adapted to the air-bearing floor dynamics). Most importantly, the characteristic multi-peaked force profiles did not appear underwater. This result suggested that precise control strategies developed for underwater motions do not exactly replicated the control strategies required for true microgravity motions.

To explain the change in peak force, the force shape and the sensor contact time, a dynamic model was constructed to simulate the push-off motions. It was found that a hybrid feedforward / feedback control model including Golgi tendon organ force feedback, a cerebellar tracking loop and simple, spring-link muscles, along with rep-

representative signal propagation delays was able to reproduce similar force and contact time measurements as those measured during the experiments. A single parameter, the GTO force feedback gain, governed how far along in the adaptation process the subjects were, which fits well into a Bayesian optimization approach to motor control. For early floor experiments, GTO gains must be set low so that the force feedback is shut off to reproduce the experimental results for novice subjects. For the highly accurate, well-adapted subjects, multi-peaked force profiles with similar maximum push-off force and sensor contact times could be reproduced using high GTO gains that limit the torque at each joint. Simulations also demonstrated that the increase in contact time gained by increasing the force feedback gain resulted in better performance, measured by a predicted landing error.

In order to reproduce the shapes of the underwater force profiles, the GTO gains needed to be set so low that the force feedback was basically not activated. This result is not surprising given the force required to ensure the subject reaches the target sensor before becoming completely arrested by the water drag. However, this result indicated that while an underwater environment can be an extremely useful training tool to familiarize astronauts with the statics and situational awareness of a three-dimensional, weightless environment, the motor control strategies developed during underwater training will most likely not be appropriate for use in microgravity due to the vastly different dynamics of water versus air. The ability of the chosen model to predict the key adaptation metrics across both the adaptation process and into the underwater experiments proves Hypothesis #3 (that a single adaptation mechanism governs the adaptation across a spectrum of gravitational and dynamic environments) to be true. However, an open area of research remains that is determining exactly where the apparent force feedback control resides (*i.e.*, spinal or cerebellar feedback).

6.2 Contributions

While conducting the research program described in this dissertation, some key contributions were made to the areas of smart sensor design, non-linear estimation (data

fusion) and human motor control and modelling. The following five contributions resulting from this research are listed below:

1. Designed a robust 6-axis, wireless force / moment sensor for use in human motion experiments in 1-G, underwater and on-orbit.
2. Developed two non-linear estimators that combine force / moment measurements with joint angle measurements to obtain an accurate representation of the human motion dynamics.
3. Designed and built the infrastructure to support frictionless floor and underwater human adaptation experiments using low-cost, COTS materials.
4. Identified the key adaptation metrics that describe human motion adaptation to different dynamic and gravitational environments.
5. Demonstrated how a simple, but physiologically plausible dynamic and biological model can predict human motor control adaptation across a spectrum of gravitational and dynamic environments.

6.3 Recommendations

The results of this research program have led to several recommendations pertaining to experimental measurement, estimation and crew training techniques for space missions. This section summarizes these recommendations.

As stated in Section 3.3, a force / moment sensor can add important acceleration information to any human motion or robotic analysis study. Using the filters developed in Chapter 3, kinetic and kinematic data can be fused to create accurate representations of dynamic motions.

One of the motivations of this research program was to identify and model the primary metrics describing adaptation to a spectrum of dynamic environments in order to target training procedures and countermeasures to accelerate the adaptation. Given that it was found that a simple force feedback gains (wherever located)

predicted well-adapted microgravity control strategies, training procedures and countermeasures that target these feedback gains should be effective. Since it was shown that underwater motions required vastly different control strategies than those appropriate for a simulated planar microgravity environment, a key recommendation from this research is that underwater training not be used as a means of familiarizing astronauts with microgravity dynamics. Instead, only spatial orientation and static familiarization exercises should be performed underwater.

Training astronauts on air-bearing floors or in parabolic flight provides the best exposure to true microgravity dynamics, even if only for brief periods of time. However, training in such environments must consist of many simple and repeated trials (such as the push-offs and landings studied in this work) to give time for the subjects to properly adapt. The results from the air-bearing floor experiments presented in this dissertation indicate that adaptation can occur in as little as one hour of relatively constant exposure to a new environment. Furthermore, the adapted control strategies were shown to be retained for at least three weeks.

Preparing astronauts for arrival to either the Moon, Mars or returning to Earth following a lengthy period in microgravity should include exercises that encourage the force feedback gains to decrease. Currently, astronauts frequently use resistive training devices on the International Space Station to retain and rebuild muscle and bone mass. These types of resistive training exercises could be modified to include a performance measure providing feedback to the astronauts. The MICR0-G sensors, with their LED force display (see Chapter 2), could be used for this purpose. For instance, astronauts could be instructed to perform resistive exercises (including stand-up motions and jumps) while standing on the MICR0-G sensors. Higher and higher force targets could be set as the days get closer to their landing date. Using the MICR0-G graphical user interface, astronauts would be able to monitor the accuracy of their landings in terms of off-axis forces that could cause falls and other injuries at their planetary destination.

In addition to providing new training techniques and in-flight countermeasures, another useful tool (often requested by astronauts) is a diagnostic tool to inform them

how far along they are in their control adaptation to a particular environment. If, upon arriving on Mars for instance, the crew needed to choose one crewmember to perform a complicated, potentially dangerous construction task. Exercises such as those described above could be performed while being monitored by kinetic (forces / moments) and kinematic (joint angles) measurements. Using the metrics and data analyses presented in this dissertation, crewmembers could evaluate not only how far along they are in their adaptation, but it could also point out areas in which they need to focus their adaptation exercises. Based on this information, decisions can be made regarding whether or not certain control tasks should be attempted based on the state of the crewmembers' adapted control strategies.

6.4 Future Work

As outlined in Chapter 2, the ultimate setting for this research program is during long duration spaceflight on the International Space Station (ISS). The work presented in this dissertation represents only the ground studies for the much larger ISS experiment. While this study only considers short term adaptation, the MICRO-G ISS experiment will have the opportunity to monitor and quantify astronaut adaptation across an entire space station increment (approximately 6 months).

However, while the ISS experiment is the ultimate goal of this research program, there is still much that can and should be done to prepare for deployment on the ISS. As of this writing, the experiments described in this dissertation are being repeated during parabolic flight. In parabolic flight, subjects are exposed to approximately 25 seconds of weightlessness that is almost identical to that experienced by astronauts in-orbit. These experiments should be able to answer critical questions about the applicability of air-bearing floor exposure to the true, three-dimensional weightless environment during parabolic flight. In much the same way that key differences were noted between the underwater environment and the air-bearing floor environment, we must understand what (if any) significant differences exist between parabolic flight and air-bearing floor experiments. While air-bearing floors provide a nearly friction-

less surface, there will always be more friction than that found during parabolic flight. Does the small amount of friction provide a crutch that subjects use to help them move? How does the planar motion restriction of an air-bearing floor affect the control strategy adaptation? Performing experiments in parabolic flight should provide insight into these questions.

The underwater experiments conducted as part of this research program showed that the control strategy used by subjects underwater varied greatly to that which was appropriate on the air-bearing floor. It is possible, however, that if the motions were smaller, over shorter distances, the viscosity effect of the water might be minimized to the point where its impact is negligible. To test this theory, experiments could be conducted underwater and on the air-bearing floor whereby subjects perform low-velocity motions over short ($< 1\text{ m}$) distances. While the experiments presented in this thesis focussed on microgravity adaptation, the relative force magnitudes presented in Figure 4-16 indicate that an underwater environment might be a good simulator for partial gravity environments. The new, waterproof MICR0-G sensors could provide valuable data about the applicability of underwater training to partial gravity locomotion.

The adaptation model presented in this dissertation is based on GTO force feedback with a simple feedforward descending commands. While this model provided similar results to those observed during the experiments, no attempt was made to verify the true biological structure of the control architecture. One important question that arose from the model discussion of Chapter 5, was the physical location of the apparent force feedback. Future experiments could be planned to pin point not only what the key sources of adaptation are (*i.e.*, proprioceptive feedback, visual feedback, vestibular feedback, or some combination), but what kind of loop is being implemented to control the motions.

Studies using cerebellar patients could begin to answer questions regarding the role of the cerebellum in such adaptation. If cerebellar patients show similar adaptation trends and characteristics as the subjects did in the studies presented in this thesis, it could provide evidence supporting spinal feedback. Simple studies could be conducted

whereby subjects are asked to close their eyes prior to the push-off motion. Doing so would isolate the effect of visual feedback on the push-off task. Future studies could also involve EMG measurements to monitor exactly what commands are being transmitted to the muscles and how they are being mediated by the GTO, cerebellum or otherwise.

In order to be able to make strong statements regarding the applicability of this research to a *spectrum of gravitational environments*, more research focussed on partial gravity adaptation is required. Obviously, the push-off and landing motions conducted in this study are unique only to a microgravity situation. However, jumping in altered gravity environments should provide similar metrics (*i.e.*, maximum force, contact time and a characteristic force profile) and could characterize adaptation. The results of this study could then illuminate countermeasures that could be done of the surface of the moon or Mars that would prepare astronauts for the next part of their exploration mission.

The future of space exploration will require humans venture beyond Earth's orbit to different planets, each with its own dynamic and/or gravitational environment. While humans have demonstrated over and over their ability to adapt their bodies to new environments, we cannot afford to conduct space exploration missions without first understanding what kinds of adaptation will be required and how it can be accelerated to prevent mission-threatening injuries. This research program has provided both scientific insight and enabling technologies targeting how humans adapt to different dynamic and gravitational environments and how the adaptation process can be reliably monitored and evaluated.

Appendix A

Individual Subject Data

The following plots illustrate the individual data from each subject that was analyzed to support this research (10 subjects for Experiments 1 and 2 and 2 subjects for Experiment 3). Maximum force and contact time data are presented for each phase and subphase where results in Chapter 4 were presented.

Max Push-Off Force

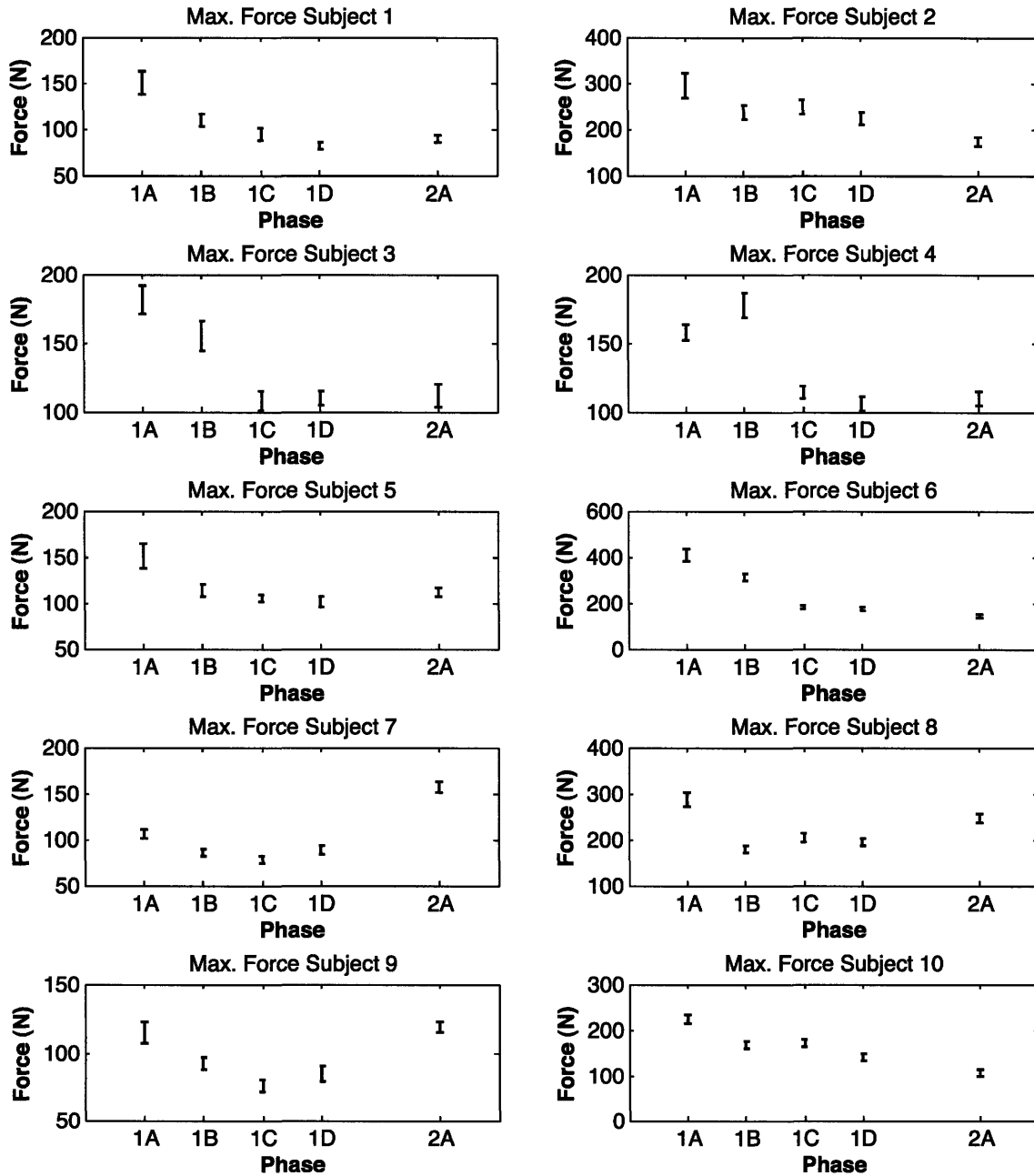


Figure A-1: All analyzed subjects maximum push-off force for Experiments 1 and 2.

Max. Force Across Break

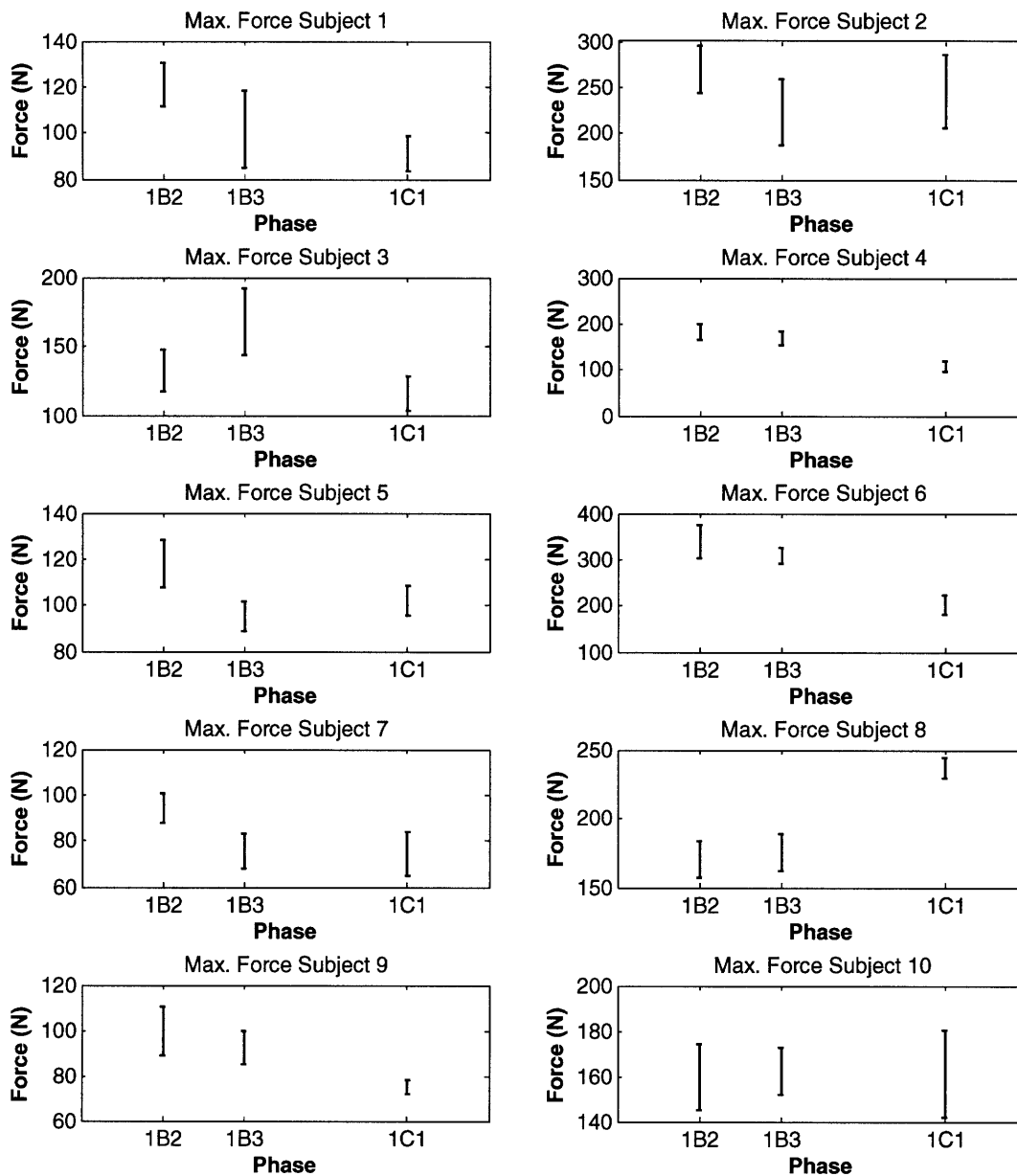


Figure A-2: All analyzed subjects maximum push-off force across a break.

Contact Time

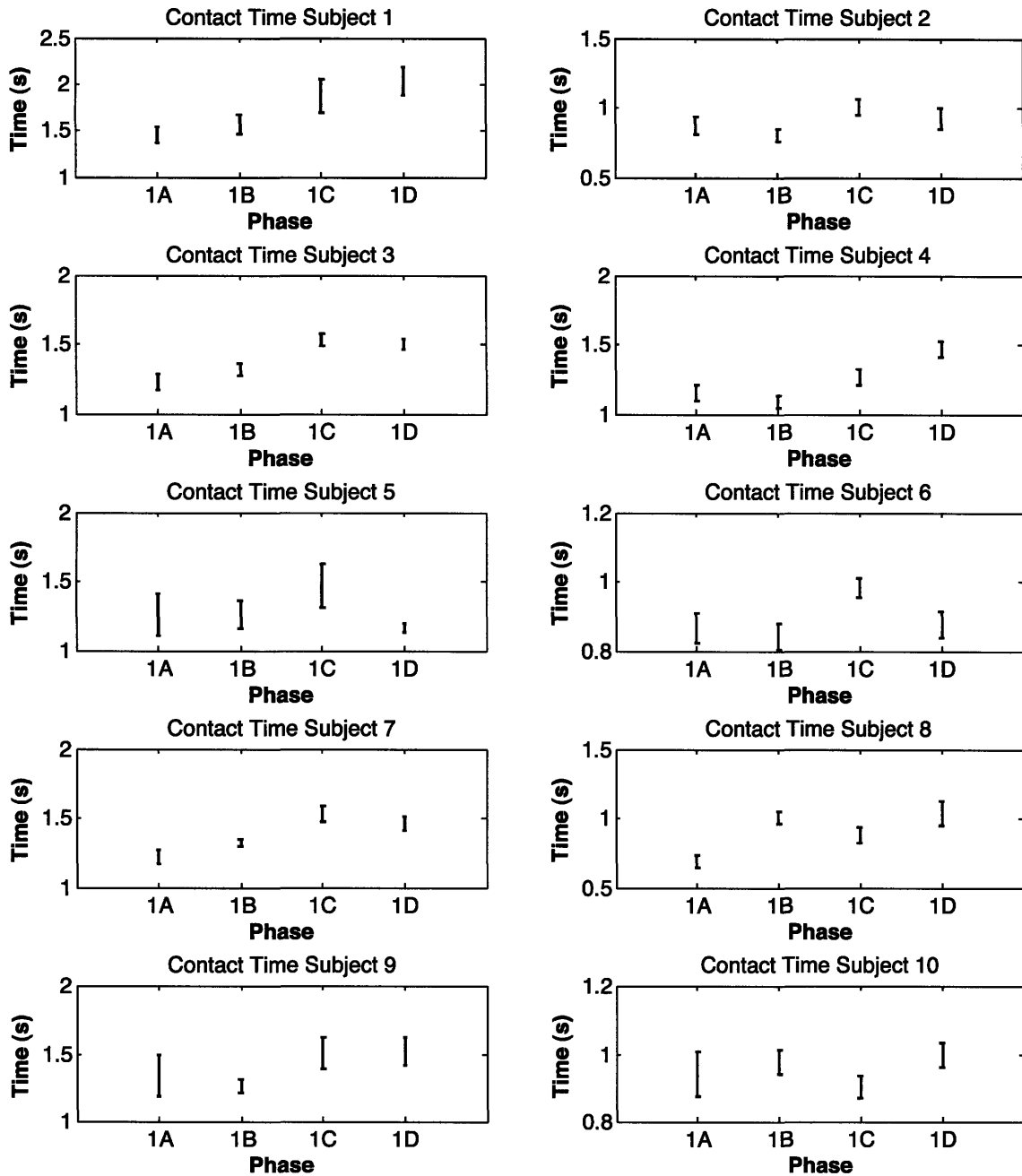


Figure A-3: All analyzed subjects contact time for Experiment 1.

Max. Push-Off Force Exp. 1 vs. Exp. 3

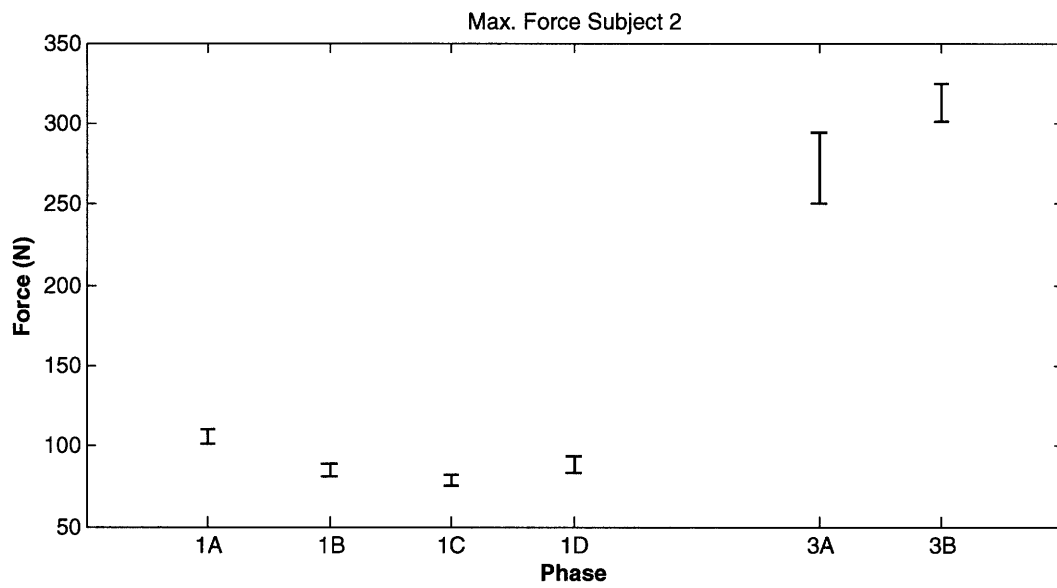
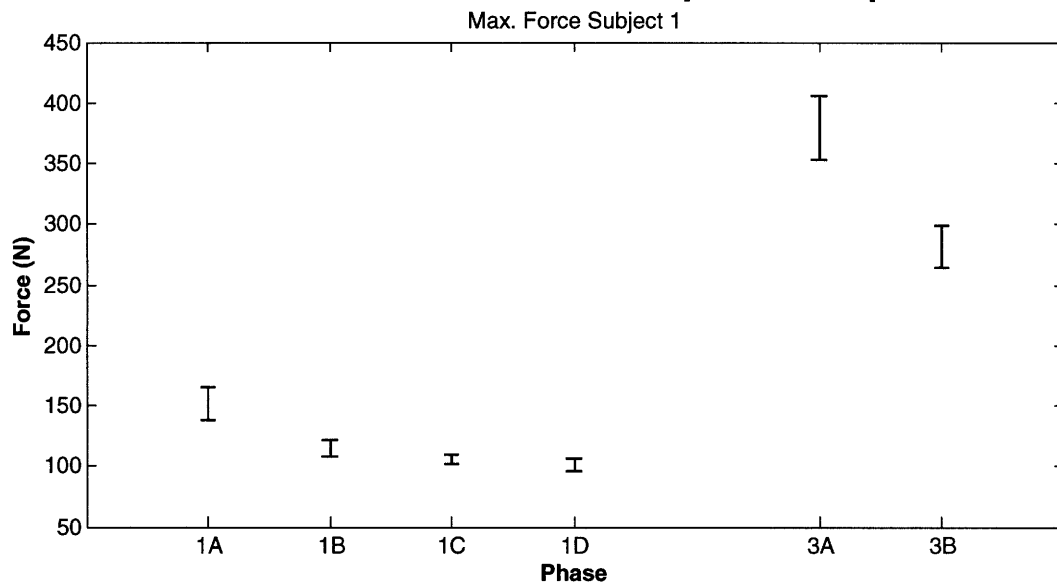


Figure A-4: All analyzed subjects maximum push-off force for Experiments 1 and 3.

Contact Time Exp. 1 vs. Exp. 3

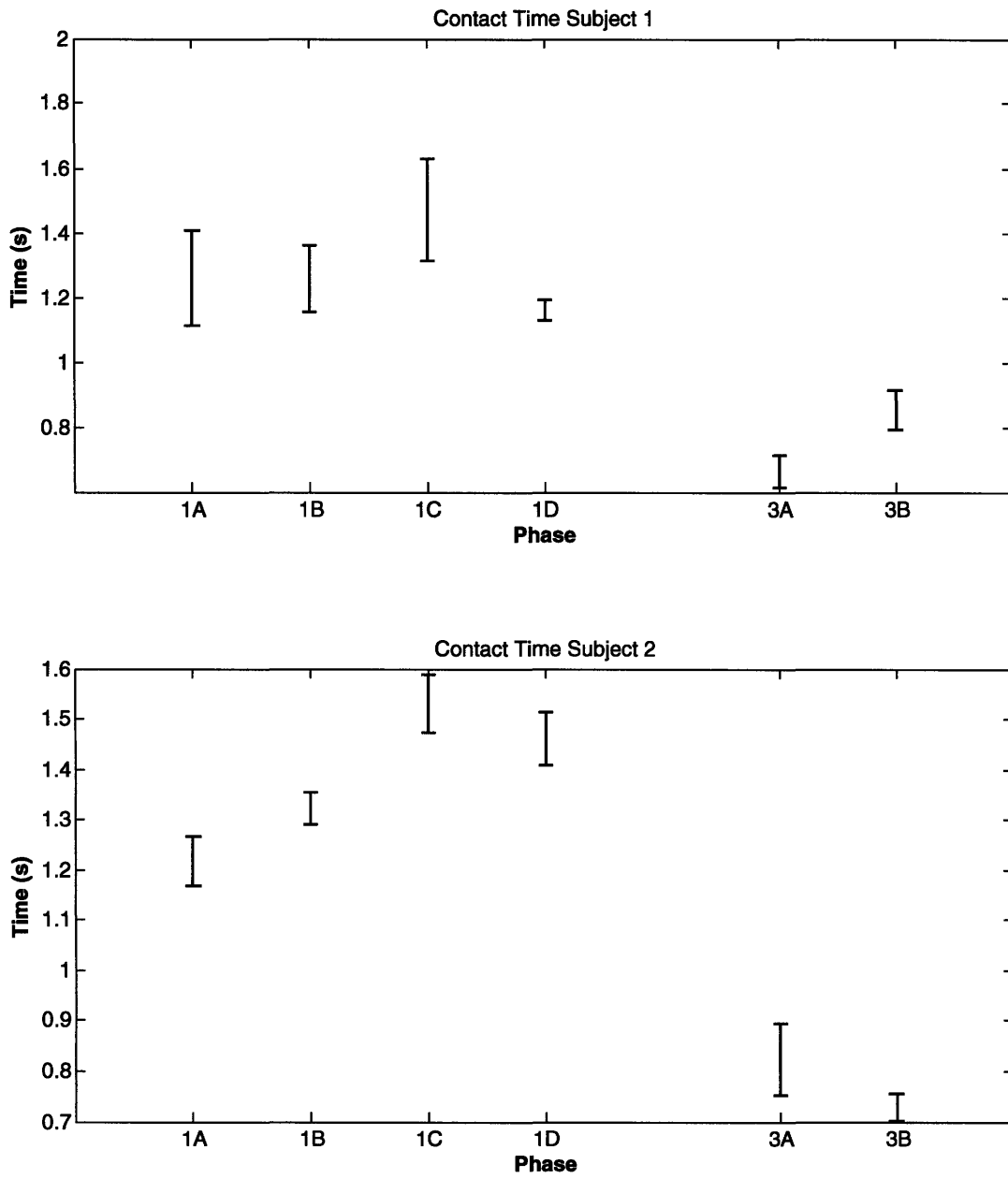


Figure A-5: All analyzed subjects contact time for Experiments 1 and 3.

Appendix B

Nonlinear Least Squares Algorithm Development

The nonlinear least squares estimator begins with the assumption that some prior knowledge of the state vector exists. Let this prior state estimate be X_0 , with associated covariance matrix, P_0 . The covariance matrix is analogous to the measurement variance matrix R defined in conjunction with Equation 3.30. In most cases, the prior state estimate, X_0 is simply a guess and P_0 represents the confidence in the initial guess (again expressed as σ^2 quantities).

The goal of the estimator is to find the best state estimate, X , that forms the best balance of previous knowledge with the new measurements. Mathematically, this is equivalent to finding X that minimizes the following cost function, J :

$$J = (X - X_0)^T P_0^{-1} (X - X_0) + (y - h(X))^T R^{-1} (y - h(X)) \quad (\text{B.1})$$

Assuming that $h(X)$ can be differentiated, the first variation of J is found to be:

$$\frac{\partial J}{\partial X} = (X - X_0)^T P_0^{-1} + (y - h(X))^T R^{-1} \left(0 - \frac{\partial h(X)}{\partial X} \right) \quad (\text{B.2})$$

The optimization problem is solved when the first variation is zero (*i.e.*, at the

minimum). Let

$$H_x = \left. \frac{\partial h(X)}{\partial X} \right|_x \quad (\text{B.3})$$

and

$$G(X) = \left. \frac{\partial J}{\partial X} \right|_x = (X - X_0)^T P_0^{-1} - (y - h(X))^T R^{-1} H_x \quad (\text{B.4})$$

Then, solving:

$$G(X) = 0 \quad (\text{B.5})$$

will provide the best estimate of the state vector X . Due to its nonlinearity, solving Equation B.4 requires the use of an iterative algorithm, such as the Newton-Raphson method.

The Newton-Raphson iterative method uses a Taylor series expansion representation of a nonlinear function to solve it. Let $f(x)$ be some nonlinear function of x . The Taylor series of f expanded about some operating point, x_0 is:

$$f(x_0 + \Delta x) = f(x_0) + \left. \frac{df(x)}{dx} \right|_{x_0} \Delta x + \left. \frac{d^2 f(x)}{dx^2} \right|_{x_0} \frac{(\Delta x)^2}{2!} + \dots \quad (\text{B.6})$$

Truncating the series after the second term, we have:

$$f(x_0 + \Delta x) \approx f(x_0) + \left. \frac{df(x)}{dx} \right|_{x_0} \Delta x \quad (\text{B.7})$$

Assume that Δx is the amount that x_0 must be adjusted in order to make $f(x_0 + \Delta x)$ zero. Solving for Δx (and setting $f(x_0 + \Delta x) = 0$):

$$\Delta x = - \frac{f(x_0)}{\left. \frac{df(x)}{dx} \right|_{x_0}} \quad (\text{B.8})$$

Thus, the new guess for the solution to $f(x) = 0$ is:

$$x_1 = x_0 + \Delta x \quad (\text{B.9})$$

The new solution of x_1 is then used to re-compute Δx from Equation B.8 and the iteration continues until the magnitude Δx falls below some pre-defined tolerance.

Applying the Newton-Raphson solution method to the solution of $G = 0$, at every step, the modification to the state vector is computed as:

$$\Delta X = \frac{G(X_0)}{\left. \frac{dG(X)}{dX} \right|_{X_0}} \quad (\text{B.10})$$

Differentiating Equation B.4:

$$\frac{dG(X)}{dX} = P_0^{-1} - H_x^T R^{-1} H_x = P_1^{-1} \quad (\text{B.11})$$

where P_1^{-1} has been defined for convenience. Thus, following Equation B.10 the update at every iteration step of the nonlinear least squares estimator becomes:

$$X_1 = X_0 - P_1 G(X_0) \quad (\text{B.12})$$

In summary, the computational steps of the nonlinear least squares estimator are as follows:

1. Guess the state, X_0 .
2. Compute $h(X_0)$ and H_{X_0} .
3. Compute P_1 using Equation B.11. Note that regardless of the iteration step, the P_0 in Equation B.11 always refers to the covariance matrix of the original state estimate and not the previously computed P_1 .
4. Compute G at the current state estimate using Equation B.4.
5. Compute the new state estimate using Equation B.12.
6. If the state is changing less than some pre-defined tolerance, stop. Otherwise, use the new state and repeat back to step 2.

Appendix C

Unscented Kalman Filter Development

The following equations were taken directly from reference [Wan and van der Merwe, 2001]. Throughout, the subscript k denotes the filter time-step.

The Unscented Kalman Filter (UKF) begins by calculating the set of sigma points as follows:

$$\chi_{k-1} = \begin{bmatrix} \hat{\mathbf{x}}_{k-1} & \hat{\mathbf{x}}_{k-1} + \gamma\sqrt{P_{k-1}} & \hat{\mathbf{x}}_{k-1} - \gamma\sqrt{P_{k-1}} \end{bmatrix} \quad (\text{C.1})$$

where $\hat{\mathbf{x}}_{k-1}$ and P_{k-1} are the previous state estimate and covariance matrix respectively and γ is a pre-defined constant that determines the filter accuracy.

The time update of the UKF proceeds as follows:

$$\chi_k^* = \Phi(\chi_{k-1}, \mathbf{u}_{k-1}) \quad (\text{C.2})$$

where Φ represents the nonlinear system dynamics and \mathbf{u} is the vector of control inputs. Using the propagated sigma points, the propagated state and covariance matrices are computed as:

$$\mathbf{x}_k^- = \sum_{i=0}^{2L} W_i^{(m)} \chi_{i,k}^* \quad (\text{C.3})$$

$$P_k^- = \sum_{i=0}^{2L} W_i^{(c)} [\chi_{i,k}^* - \mathbf{x}_k^-] [\chi_{i,k}^* - \mathbf{x}_k^-]^T + Q \quad (\text{C.4})$$

where the minus superscript denotes a quantity prior to being corrected by the measurement update, L is the dimension of the state vector, Q is the process noise covariance matrix and $W_i^{(m)}$ and $W_i^{(c)}$ are known as the unscented transformation weights. The weights are computed as:

$$W_0^{(m)} = \frac{\lambda}{(L + \lambda)} \quad (\text{C.5})$$

$$W_0^{(c)} = \frac{\lambda}{(L + \lambda)} + (1 - \alpha^2 + \beta) \quad (\text{C.6})$$

$$W_i^{(m)} = W_i^{(c)} = \frac{1}{2(L + \lambda)}, \quad i = 1, \dots, 2L. \quad (\text{C.7})$$

where λ , α and β are chosen in a similar fashion to γ to determine filter accuracy.

With the propagated state and covariance estimates, the sigma points are now redrawn:

$$\chi_k = \begin{bmatrix} \hat{\mathbf{x}}_k^- & \hat{\mathbf{x}}_k^- + \gamma\sqrt{P_k^-} & \hat{\mathbf{x}}_k^- - \gamma\sqrt{P_k^-} \end{bmatrix} \quad (\text{C.8})$$

$$Y_k = h(\chi_k) \quad (\text{C.9})$$

$$\hat{\mathbf{y}}_k^- = \sum_{i=0}^{2L} W_i^{(m)} Y_{i,k} \quad (\text{C.10})$$

The measurement update equations are:

$$P_{\tilde{\mathbf{y}}_k \tilde{\mathbf{y}}_k} = \sum_{i=0}^{2L} W_i^{(c)} [Y_{i,k} - \hat{\mathbf{y}}_k^-] [Y_{i,k} - \hat{\mathbf{y}}_k^-]^T + R \quad (\text{C.11})$$

$$P_{\mathbf{x}_k \mathbf{y}_k} = \sum_{i=0}^{2L} W_i^{(c)} [\chi_{i,k} - \hat{\mathbf{x}}_k^-] [Y_{i,k} - \hat{\mathbf{y}}_k^-]^T \quad (\text{C.12})$$

$$\kappa_k = P_{\mathbf{x}_k \mathbf{y}_k} P_{\tilde{\mathbf{y}}_k \tilde{\mathbf{y}}_k}^{-1} \quad (\text{C.13})$$

$$\hat{\mathbf{x}}_k = \hat{\mathbf{x}}_k^- + \kappa_k (\mathbf{y}_k - \hat{\mathbf{y}}_k^-) \quad (\text{C.14})$$

$$P_k = P_k^- - \kappa_k P_{\tilde{\mathbf{y}}_k \tilde{\mathbf{y}}_k} \kappa_k^T \quad (\text{C.15})$$

Appendix D

Sensor Calibration

D.1 Introduction

The goal when calibrating a 6-axis force sensor using 6 sensor voltages is to determine a calibration matrix C such that

$$\mathbf{F} = C\mathbf{y} \tag{D.1}$$

where \mathbf{y} is a vector of six sensor readings (from the six load cells inside the sensor) and

$$\mathbf{F} = \begin{bmatrix} \mathbf{F}_x \\ \mathbf{F}_y \\ \mathbf{F}_z \\ \mathbf{M}_x \\ \mathbf{M}_y \\ \mathbf{M}_z \end{bmatrix} \tag{D.2}$$

where $\begin{bmatrix} \mathbf{F}_x & \mathbf{F}_y & \mathbf{F}_z \end{bmatrix}^T$ is the three-dimensional vector of forces and $\begin{bmatrix} \mathbf{M}_x & \mathbf{M}_y & \mathbf{M}_z \end{bmatrix}^T$ is the three-dimensional vector of moments. Given the dimensions of Equation D.1, the calibration matrix C is a 6x6 matrix containing 36 unknown elements.

Prior to the EDLS experiment, the sensors were calibrated and the calibration procedure was documented in [Amir, 1998]. Since the MICR0-G sensor flexure design is based on that of the sensors used for the EDLS experiment, the EDLS calibration

procedure was used as a starting point when developing the MICR0-G calibration procedure.

It was found that the EDLS calibration procedure lacked an important aspect that prevented accurate and repeatable calibration of the sensors. This report outlines the deficiencies of the EDLS calibration procedure and what was done to improve upon it for the MICR0-G sensor calibration procedure. This report also serves to point out important design considerations for future MICR0-G sensors that could improve the calibration further.

D.2 The EDLS Calibration Procedures

The EDLS calibration procedures used an aluminum fixture that was attached to the sensor to facilitate load application in many different axes. Data collected using this fixture were then used to compute the calibration matrix, C , in Equation D.1. The following sections describe the EDLS calibration fixture and the EDLS calibration algorithm.

D.2.1 EDLS Calibration Fixture

An aluminum plate and “L” shaped hanger were built to permit loading of the EDLS sensors during calibration. The calibration fixture mounted to an EDLS sensor mounted to the lab wall is pictured in Figure D-1.

The EDLS calibration fixture was designed to be mounted directly to the load-cell flexures. Given its “L” design, only two different loading scenarios could be applied without having to rotate the sensor and/or disassemble the fixture to rotate the “L”. As described below in Section D.3.1, re-assembly and removal of the sensor top plate causes unknown loads to be imparted internally into the sensor top plate that alter the calibration by changing the voltage reading when no load is applied to the sensors.

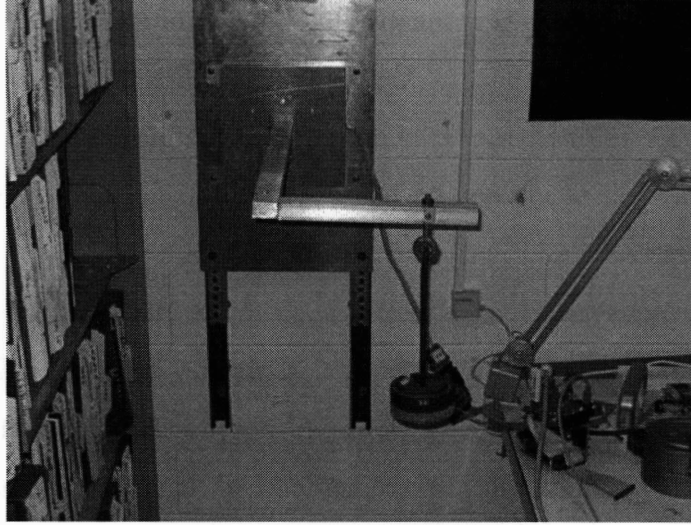


Figure D-1: Photo showing the calibration fixture used for the EDLS calibration.

D.2.2 EDLS Calibration Algorithm

The EDLS calibration procedure begins by collecting n sets of sensor voltage readings paired with known loads applied to the sensor using the fixture pictured in Figure D-1. Since there are six load cells, a single sensor response from an applied load consists of six individual voltage readings. The data collected in this manner can be expressed as:

$$\bar{\mathbf{F}} = C\bar{\mathbf{y}} \quad (\text{D.3})$$

where $\bar{\mathbf{F}}$ is a $6 \times n$ matrix of known applied loads (3-axis forces and 3-axis moments) and $\bar{\mathbf{y}}$ is a $6 \times n$ matrix of corresponding sensor responses. Right-multiplying the left and right side of Equation D.3 by $\bar{\mathbf{y}}^T$ results in:

$$\bar{\mathbf{F}}\bar{\mathbf{y}}^T = C\bar{\mathbf{y}}\bar{\mathbf{y}}^T \quad (\text{D.4})$$

Using Equation D.4, the calibration matrix, C , can then be solved as:

$$C = \bar{\mathbf{F}}\bar{\mathbf{y}}^T (\bar{\mathbf{y}}\bar{\mathbf{y}}^T)^{-1} \quad (\text{D.5})$$

Note that the quantity $\bar{\mathbf{y}}^T (\bar{\mathbf{y}}\bar{\mathbf{y}}^T)^{-1}$ is commonly known as the *pseudoinverse* of $\bar{\mathbf{y}}$. In general, if $\bar{\mathbf{y}}$ has dimensions $m \times n$, the pseudoinverse only exists if $\text{rank}(\bar{\mathbf{y}}) = n$. In

the case of sensor calibration, this means that the set of known loads applied to the sensor must span the entire space to make all six load axes (three forces and three moments) *observable*. For instance, if none of the applied loads contain a force in the x direction, the calibration cannot contain any information in that direction and thus, the pseudoinverse would not exist.

Calibrating the sensors using Equation D.5 only works if all six load cells read 0 Volts when no load is applied to the sensor. This can be seen in Equation D.1 by noting that if $\mathbf{y} = \mathbf{0}$, then $\mathbf{F} = \mathbf{0}$, which may not be the case if there are residual voltage readings. Certainly, the electronics can be tuned such that virtually any loading configuration reports 0 Volts on all load cells, however, creating a “no load scenario” in a 1-G lab is extremely difficult without disassembling the sensor and calibration fixture thereby changing the loading behavior and tainting the calibration.

D.3 The MICR0-G Calibration Procedure

To improve upon the EDLS calibration, two aspects of the calibration were reconsidered: (A) the calibration fixture and (B) the calibration algorithm. Both improvements are discussed here.

D.3.1 The MICR0-G Calibration Fixture

Since neither the EDLS nor the MICR0-G sensors are made of one solid piece of aluminum through the flexures and top plate, some hysteresis is expected. This hysteresis is due to minor slipping of the screw points connecting the flexures to the sensor housing and the flexures to the top plate. While in use, hysteresis is easy to compensate for by “zeroing” the sensor¹. However, during calibration, hysteresis can cause the zero-load sensor reading to change dramatically and can lead to inaccurate calibration results. Thus, a calibration fixture and mounting system was required that eliminated major sensor handling during the calibration procedure.

¹“Zeroing” the sensor means recording the current reading and arbitrarily calling it zero by subtracting the current sensor readings off of all subsequent readings. In commercial scales, this is sometimes referred to as a *tare* operation.

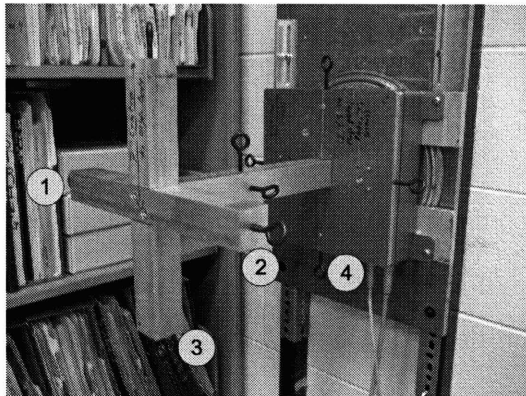
Another way in which the zero-load sensor readings can change is by removing and re-attaching the sensor top plate. Since the top plate is attached to the sensor flexures at more than one point, internal stresses are carried by the flexures and the top-plate assembly when the screws are tightened and these stresses are not necessarily the same each time the top plate is replaced. Furthermore, when the top plate is installed, these internal loads may cause the loading pattern to change slightly than if the loads were applied directly to the flexures themselves. Thus, the new calibration fixture needed to attach to the sensor top plate (and not the flexures themselves) and not require repositioning during the calibration procedure.

The new MICR0-G calibration fixture is pictured in Figure D-2. The new fixture design permits loading in all sensor axes without requiring removal and repositioning of the sensor top plate or the calibration fixture. Furthermore, the MICR0-G calibration fixture affixes directly to the sensor top plate so that the sensor is in a similar configuration during calibration as it will be during its actual use. All forces and moments except F_x can be applied with the sensor mounted on the wall. F_x application requires the sensor to be unmounted from the wall and placed on a flat surface such as a lab bench (pictured in Figure D-2(b)).

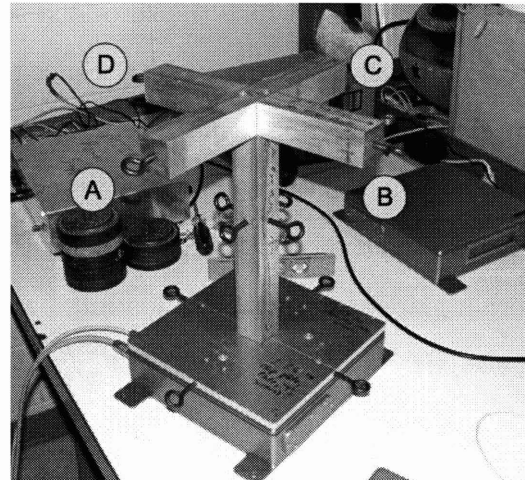
Once the calibration fixture is mounted to the sensor, the sensor is mounted to a turntable on the wall. The turn table permits easy sensor rotation to different loading orientations, thus minimizing the possibility that the sensor will be jarred and the zero-load sensor readings changed. Each loading orientation points a different axis direction towards the floor and hence, puts it in the load path. Figure D-3 illustrates the coordinate system used for reporting forces and moments².

In each orientation, four different weight application points (indicated with numbers in Figure D-2(a) and letters in Figure D-2(b)) were used to apply different known combinations of forces and moments to the sensor. The calibration fixture itself plus the sensor top plate weighs 54.49 Newtons and the hanger used to place the calibra-

²Note that the MICR0-G sensors report forces *applied* to the sensor as opposed to those *reacted* by the sensor. Thus, a weight hanging off the sensor in the positive direction of an axis will be reported as a positive force in that direction. The moments are reported in the same manner, using the right-hand rule. Figure D-3 illustrates the axis system for the MICR0-G sensors.



(a) Photo showing the calibration fixture mounted to the sensor. The numbers 1 through 4 indicate the different loading positions on the calibration fixture. The hook positions do not rotate with the sensor, so hook # 3 is always the lowest hook. The round plate behind the sensor facilitates easy sensor rotation.



(b) Photo showing the calibration fixture mounted to the sensor with the sensor on a flat table. This loading orientation is required to apply x forces. The four hooks, denoted A, B, C and D are used to apply combined forces and moments.

Figure D-2: Photos showing the sensor with calibration fixture attached.

tion weights weighs 4.31 Newtons. The long axial member of the calibration fixture is offset 30.48 centimeters while the short cross pieces each are offset 17.78 centimeters. The downward moment resulting from hanging the calibration fixture and empty weight hanger off of the sensor is 9.17 Newton-meters. The moments are assumed to be taken about a point at the center on the surface of the sensor top plate³. Using the axis system defined in Figure D-3 combined with the load location designations in Figure D-2, Table D.3.1 describes the applied loads for each sensor orientation in addition to the load offsets applied by the calibration fixture itself.

A calibration program for the MICRO-G sensors was written to streamline the data collection process and reduce tedious data entry errors. The program (found on each sensor in the `/root/new_cal/calibration/` directory) can be run in one of two different modes: *Simple* or *Advanced*.

In *Simple* mode, the sensor is assumed to be setup as documented in Figure D-2.

³Hooks located on the calibration fixture base plate (denoted hook #4 in each orientation) are assumed to be at the zero moment point even though they are technically raised 3 mm. This assumption does not noticeably affect the calibration accuracy and permits pure force loading without requiring disassembly of the sensor or calibration fixture during calibration.

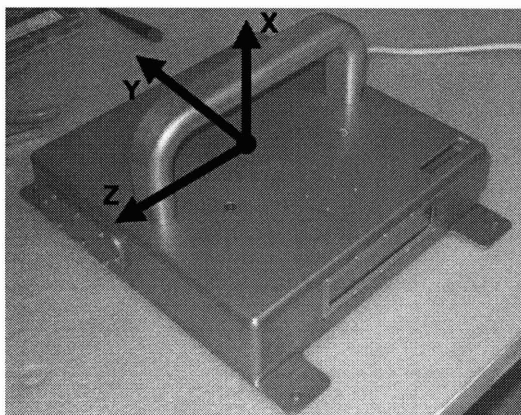


Figure D-3: An annotated MICR0-G sensor photo illustrating the axis convention.

The user is prompted for an orientation number and a hook number (or letter as is case for orientation #5). The program asks the user what his/her unit preference is for force application (the options are kilograms, grams, Newtons, pounds or ounces) and then prompts the user for the first weight to be applied to the weight hanger. The program automatically computes the force and moment caused by the added weight and the weight of the sensor. The sensor is sampled 200 times over the space of three seconds and average readings for the six load cells are obtained in A/D counts. The data is then converted into SI units from whatever the user chose at the beginning and recorded to a Matlab file. The user continues adding or removing weight from the hanger until they choose to stop. The data file can then be downloaded from the sensor via FTP to another computer with Matlab where the calibration matrix is computed using the algorithm outlined in Section D.3.2.

In *Advanced* mode, the user has much more freedom to load the sensor in any way he/she wishes. The user is prompted for both the mass units (kilograms, grams, Newtons, pounds or ounces) and the length units (meters, centimeters, yards, feet or inches). If the user wishes he/she can enter constant force or moment offsets that would compensate for a calibration fixture being used. Then, during the calibration, the user is prompted for the entire three-element force vector and three-element moment vector being applied to the sensor (if the user entered any offsets, they would be automatically added here). In this mode, the user must compute the forces and moments (in what ever units they selected) based on the geometry of their setup and

Ori. #	Grav. Dir.	Hook #	Applied Loads	Fixture Force (N)	Fixture Moment (Nm)
1	-z	1	$-F_x, +M_x, +M_y$	$[0, 0, -58.8]^T$	$[0.7665, 9.170, 0]^T$
1	-z	2	$-F_x, -M_x, +M_y$	$[0, 0, -58.8]^T$	$[-0.7665, 9.170, 0]^T$
1	-z	3	$-F_x, +M_y$	$[0, 0, -58.8]^T$	$[0, 9.170, 0]^T$
1	-z	4	$-F_x$	$[0, 0, -58.8]^T$	$[0, 7.856, 0]^T$
2	+y	1	$+F_y, +M_x, +M_z$	$[0, 58.8, 0]^T$	$[0.7665, 0, 9.170]^T$
2	+y	2	$+F_y, -M_x, +M_z$	$[0, 58.8, 0]^T$	$[-0.7665, 0, 9.170]^T$
2	+y	3	$+F_y, +M_z$	$[0, 58.8, 0]^T$	$[0, 0, 9.170]^T$
2	+y	4	$+F_y$	$[0, 58.8, 0]^T$	$[0, 0, 7.856]^T$
3	+z	1	$+F_x, +M_x, -M_y$	$[0, 0, 58.8]^T$	$[0.7665, -9.170, 0]^T$
3	+z	2	$+F_x, -M_x, -M_y$	$[0, 0, 58.8]^T$	$[-0.7665, -9.170, 0]^T$
3	+z	3	$+F_x, -M_y$	$[0, 0, 58.8]^T$	$[0, -9.170, 0]^T$
3	+z	4	$+F_x$	$[0, 0, 58.8]^T$	$[0, -7.856, 0]^T$
4	-y	1	$-F_y, +M_x, -M_z$	$[0, -58.8, 0]^T$	$[0.7665, 0, -9.170]^T$
4	-y	2	$-F_y, -M_x, -M_z$	$[0, -58.8, 0]^T$	$[-0.7665, 0, -9.170]^T$
4	-y	3	$-F_y, -M_z$	$[0, -58.8, 0]^T$	$[0, 0, -9.170]^T$
4	-y	4	$-F_y$	$[0, -58.8, 0]^T$	$[0, 0, -7.856]^T$
5	-x	A	$-F_x, +M_x$	$[-58.8, 0, 0]^T$	$[0, 0, 0.7665]^T$
5	-x	B	$-F_x, -M_y$	$[-58.8, 0, 0]^T$	$[0, -0.7665, 0]^T$
5	-x	C	$-F_x, -M_x$	$[-58.8, 0, 0]^T$	$[0, 0, -0.7665]^T$
5	-x	D	$-F_x, +M_y$	$[-58.8, 0, 0]^T$	$[0, 0.7665, 0]^T$
5	-x	E	$-F_x$	$[-54.5, 0, 0]^T$	$[0, 0, 0]^T$

Table D.1: Loading directions and fixture/hanger offsets for each sensor orientation and loading hook. The first column is the orientation number used as a reference. The second column lists the axis pointed down in the direction of the gravity vector in the given orientation. The third column lists the hook numbers denoted in Figure D-2(a). The fourth column lists the force and moment directions that can be applied in the given orientation and hook number. Finally, the last two columns display the force and moment load offset caused by the calibration fixture itself and the weight hanger, if applicable. Note that the last loading scenario (Orientation 5, hook E) does not actually use a hook since weights are placed directly on top of the calibration fixture (as seen in Figure D-2(b)).

the sensor axis system. As in *Simple* mode, the data is converted into SI units prior to being recorded to the data file (thus ensuring that the calibration matrix is always computed in SI units).

D.3.2 MICR0-G Calibration Algorithm

When the MICR0-G sensors are in use, they can be zeroed to eliminate any residual load cause by thermal deformations, internal loading due to mounting stresses or restraint installation. In this manner, we enforce the voltage readings to be zero when zero load is being applied (or asserted when the zero command is sent), as seen in Equation D.6 below:

$$\mathbf{F} = C(\mathbf{y} - \mathbf{y}_z) \quad (\text{D.6})$$

where \mathbf{y}_z is a vector of 6 sensor voltages recorded when the zero command was sent. Using Equation D.6, forces and moments *relative* to the user-defined zero point can be reported.

However, during calibration, absolute forces, moments and voltage readings must be used to keep all measurements consistent across each loading configuration. It is thus not possible to simply subtract off an arbitrary zero load unless it is truly an absolute zero load (which can only be attained in 1-G by disassembling the sensor and introducing unknown internal loads). Therefore, when calibrating the sensor, one must determine the load cell voltage readings at zero load in addition to solving for the full calibration matrix.

Taking the zero load offset into account, Equation D.1 is re-written as:

$$\mathbf{F} = C\mathbf{y} + \mathbf{J} \quad (\text{D.7})$$

where \mathbf{J} represents the force offset when all load cells read 0 Volts. Re-arranging Equation D.7 to solve for \mathbf{y} ,

$$\begin{aligned} \mathbf{y} &= C^{-1}\mathbf{F} - C^{-1}\mathbf{J} \\ &= D\mathbf{F} + \mathbf{B} \end{aligned} \quad (\text{D.8})$$

where

$$D = C^{-1} \quad (\text{D.9})$$

and

$$\mathbf{B} = -D\mathbf{J} \quad (\text{D.10})$$

The calibration problem is then re-cast as solving for D and \mathbf{B} . The calibration matrix can then be found by simply inverting D as per Equation D.9⁴.

⁴We can be certain that D is invertible because its inverse, C , must be invertible. If C were not invertible, it would mean that it would have a rank less than 6, implying that at least 2 of the 6 load cells measured exactly the same quantity. If this were true, then the calibration would not be possible since we require 6 independent measures to estimate 6 quantities (3 forces and 3 moments). So, if D were found to be singular, it would point to a sensor design error, which we know is not the case.

Equation D.8 can now be regarded as the measurement equation for a conventional least squares estimator. Since Equation D.8 is linear, it can be re-written as:

$$\mathbf{Y} = H\mathbf{X} \quad (\text{D.11})$$

where \mathbf{Y} is a $6n \times 1$ vector of all sensor voltage vectors stacked one on top of the other, \mathbf{X} is a 42×1 element column vector comprised of the 36 elements in D and the 6 elements of \mathbf{B} and H is the $6n \times 42$ measurement matrix defined as:

$$H = \left[\begin{array}{cccccc|cccccc} \mathbf{F}_1^T & \mathbf{0} & \mathbf{0} & \mathbf{0} & \mathbf{0} & \mathbf{0} & 1 & 0 & 0 & 0 & 0 & 0 \\ \mathbf{0} & \mathbf{F}_1^T & \mathbf{0} & \mathbf{0} & \mathbf{0} & \mathbf{0} & 0 & 1 & 0 & 0 & 0 & 0 \\ \mathbf{0} & \mathbf{0} & \mathbf{F}_1^T & \mathbf{0} & \mathbf{0} & \mathbf{0} & 0 & 0 & 1 & 0 & 0 & 0 \\ \mathbf{0} & \mathbf{0} & \mathbf{0} & \mathbf{F}_1^T & \mathbf{0} & \mathbf{0} & 0 & 0 & 0 & 1 & 0 & 0 \\ \mathbf{0} & \mathbf{0} & \mathbf{0} & \mathbf{0} & \mathbf{F}_1^T & \mathbf{0} & 0 & 0 & 0 & 0 & 1 & 0 \\ \mathbf{0} & \mathbf{0} & \mathbf{0} & \mathbf{0} & \mathbf{0} & \mathbf{F}_1^T & 0 & 0 & 0 & 0 & 0 & 1 \\ \vdots & \vdots & \vdots & \vdots & \vdots & \vdots & \vdots & \vdots & \vdots & \vdots & \vdots & \vdots \\ \hline \mathbf{F}_n^T & \mathbf{0} & \mathbf{0} & \mathbf{0} & \mathbf{0} & \mathbf{0} & 1 & 0 & 0 & 0 & 0 & 0 \\ \mathbf{0} & \mathbf{F}_n^T & \mathbf{0} & \mathbf{0} & \mathbf{0} & \mathbf{0} & 0 & 1 & 0 & 0 & 0 & 0 \\ \mathbf{0} & \mathbf{0} & \mathbf{F}_n^T & \mathbf{0} & \mathbf{0} & \mathbf{0} & 0 & 0 & 1 & 0 & 0 & 0 \\ \mathbf{0} & \mathbf{0} & \mathbf{0} & \mathbf{F}_n^T & \mathbf{0} & \mathbf{0} & 0 & 0 & 0 & 1 & 0 & 0 \\ \mathbf{0} & \mathbf{0} & \mathbf{0} & \mathbf{0} & \mathbf{F}_n^T & \mathbf{0} & 0 & 0 & 0 & 0 & 1 & 0 \\ \mathbf{0} & \mathbf{0} & \mathbf{0} & \mathbf{0} & \mathbf{0} & \mathbf{F}_n^T & 0 & 0 & 0 & 0 & 0 & 1 \end{array} \right] \quad (\text{D.12})$$

where \mathbf{F}_i is the i^{th} known load (forces and moments) applied to the sensor.

After forming H as per Equation D.12 and stacking the measurements to form \mathbf{Y} , an estimate of the state vector, \mathbf{X} , can be solved as:

$$\hat{\mathbf{X}} = \left[(H^T H)^{-1} H^T \right] \mathbf{Y} \quad (\text{D.13})$$

Notice the similarities between Equation D.5 and Equation D.13. Indeed, Equation D.13 is simply the pseudoinverse solution of Equation D.11. However, in the case

of Equation D.13 the state vector, \mathbf{X} contains both the (inverse of the) calibration matrix as well as the zero load voltage offsets.

It is important to remember that while this new calibration algorithm estimates both the calibration matrix, C , as well as the zero load voltage offsets, \mathbf{B} , the calibration matrix is the only quantity that is actually used during operation of the sensor. The purpose of estimating \mathbf{B} was to ensure that constant offsets in the measured voltages were treated as such and were not erroneously incorporated into the C matrix (as would have been the case when calibrating using Equation D.5).

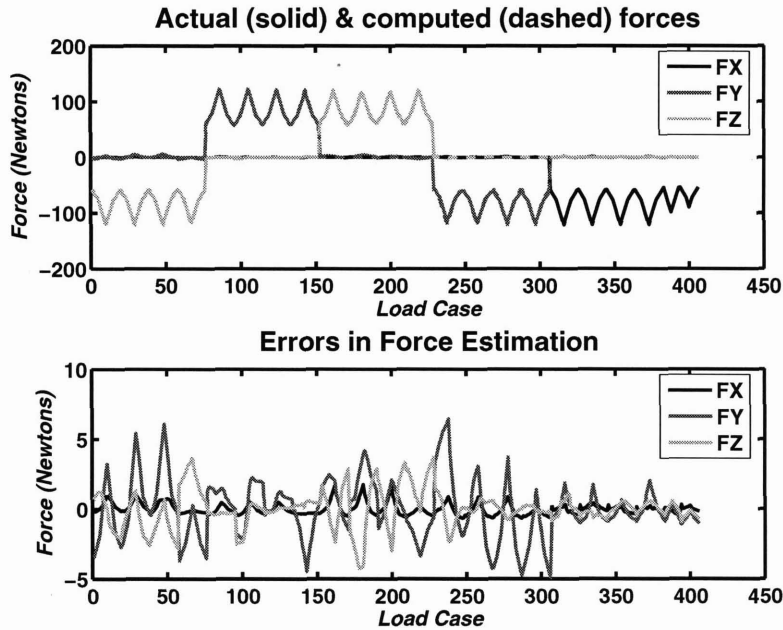
D.4 Calibration Results

Using the techniques outlined in Section D.3, the 4 prototype MICR0-G sensors were calibrated. For each loading case, 14 pounds were incrementally loaded and unloaded. The load increments went: 0, 1, 2, 3, 4, 6, 8, 10, 12, 14, 12, 10, 8, 6, 4, 3, 2, 1 and 0 pounds. Recording both the loading and unloading response ensured that if there was any hysteresis, it would be obvious when looking at the data and furthermore, the estimator would be able to approximately average it out when computing the calibration matrix and the zero load voltage offsets.

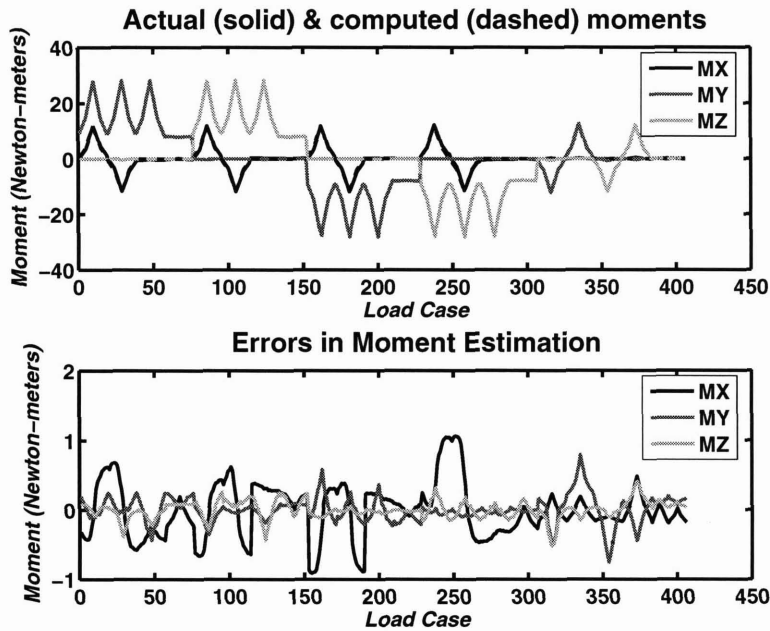
Figures D-4(a) and D-4(b) show the actual and predicted loads (using the computed calibration matrix) for each of the approximately 400 load cases applied to sensor #001 during the calibration. The calibration matrices computed for all four prototype MICR0-G sensors as well as calibration plots for sensors 002 through 004, can be found in Section D.6.

Due to the nature of the load cell placement inside the sensors, the estimation error is different for each loading axis. Since most motions will result in mainly F_x forces (see Figure D-3 for the sensor axes definitions), it was important that this axis be as accurate as possible. The results in Figure D-4(a) indicate the error in F_x forces is less than 0.4%. While the error in the other axes is larger, the error in the other force axes is less than 4% and the errors in M_y and M_z is less than 5%.

The error in M_x was larger than expected (ranging from -20% to +20% across each



(a) Forces.



(b) Moments.

Figure D-4: Plots illustrating the force/moment estimation accuracy using the computed calibration matrix for sensor #001. In the top plots, the actual loads are represented by solid lines and the computed forces using the calibration matrix are represented by dashed lines (difficult to see because they lie almost directly on top of the actual loads). The bottom plots show the error between the actual and computed loads. The load cases presented are those used to compute the calibration matrix.

loading and unloading profile), however given the expected plane of most motions, we are unlikely to see much M_x motions anyway. The high error in M_x is most likely due to hysteresis in the sensor flexures. Given the structure of the flexures, applying moments in the M_x direction could be causing significant flexure motion since they are the least stiff in the M_x direction. This motion could be causing wires and rubber sealant to rub and stick against the sensor top plate and/or the sensor housing, leading to increased hysteresis. Section D.5 briefly addresses some potential design changes that could eliminate or reduce the hysteresis observed on the prototype MICR0-G sensors.

D.5 Recommended MICR0-G Design Modifications

The prototype MICR0-G sensors are the first attempt at re-designing the EDLS sensors to be not only self-contained from a data collection and computation perspective, but also waterproof. The purpose of building four prototype sensors prior to the design and assembly of the final flight sensors was to identify areas of the design that required further consideration and address the issues.

From a calibration perspective, the sensors must respond linearly to six-axis forces and moments in order to obtain an accurate calibration matrix. Thus, eliminating or at least reducing hysteresis is extremely important. The hysteresis observed during calibration is most likely resulting from one of three sources:

1. Wires rubbing and being dragged across the sensor housing, top plate and the flexures themselves.
2. Waterproofing sealant (RTV) rubbing against the flexures and the top plate.
3. The flexures shifting slightly at their interface with the sensor housing and the top plate.

The following suggestions may improve the sensor performance with respect to hysteresis.

D.5.1 Wiring modifications

The wiring beneath the top plate of the prototype sensors uses low-gauge (large thickness) wire. Using a higher gauge (thinner) wire would reduce the wire stiffness and perhaps allow the wire to move more easily when the flexures deflect.

Furthermore, the wires are currently attached to the flexures at multiple points that require the wires run through holes drilled into the flexures. If the strain gauge terminal blocks could be located at one location on the edge of each flexure, it would minimize the amount of wire/flexure interference.

D.5.2 Flexure interfaces

The current flexure design leaves very little clearance for wires or connector bulkheads. As a result, the top plate often contacts the wires or RTV under the top plate. While there will be no need to waterproof the flight sensors, contact between the wires and the top plate needs to be eliminated.

For the prototype sensors, washers were added between the tops of the flexures and the underside of the top plate to allow approximately 2 mm of extra clearance. For the flight version, this extra clearance should be built into the flexures themselves to eliminate any contact.

To reduce the slipping between the bottom of the flexures and the sensor housing, the flexures could be bonded at that interface. However, this would prevent the flexures from being removed at a later date, so the strain gauges would need to be extensively tested prior to installation.

D.6 Calibration Matrices

The following matrices take voltages represented in A/D counts and convert them into Newtons and Newton-meters. The A/D gain settings for the Diamond Systems analog to digital card and the custom analog electronics are:

Parameter Name	Parameter Value	Description
dsccb.boardtype	DSC_DMM16AT	The type of A/D board
dsccb.base_address	0x300	Hex address of the A/D board
dsccb.int_level	7	Interrupt level (not used)
output_b	0x12	Output byte sent to custom gain chips
output_port_num	0	I/O port connected to custom gain chips
dscadsettings.range	RANGE_10	Full A/D voltage range
dscadsettings.polarity	0	Input polarity set to bipolar
dscadsettings.gain	GAIN_2	Gain set in A/D board
dscadsettings.load_cal	0	Do not load board calibration settings
dscadsettings.current_channel	0	Initializes calibration settings for channel 0
dscadscan.low_channel	0	Start scanning channel 0
dscadscan.high_channel	5	Stop scanning at channel 5
dscadscan.gain	GAIN_2	Same gain setting as above

Table D.2: A/D settings.

D.6.1 Prototype Sensor #001

$$C_1 = \begin{bmatrix} -0.0000216984 & 0.0084895031 & -0.0000115749 & 0.0085619945 & 0.0000431785 & 0.0086481744 \\ 0.0006025493 & -0.0001167517 & 0.0076689957 & 0.0006582371 & -0.0080913390 & -0.0008273385 \\ -0.0090193502 & -0.0003179082 & 0.0046984422 & 0.0000294005 & 0.0048390911 & 0.0002157437 \\ -0.0003485699 & -0.0000783892 & -0.0004847471 & -0.0000906915 & -0.0003965285 & -0.0000706237 \\ -0.0001472502 & -0.0000161133 & 0.0000853340 & 0.0005931973 & 0.0000690629 & -0.0006550543 \\ 0.0000075041 & -0.0006905108 & -0.0001521711 & 0.0003535649 & 0.0001474188 & 0.0004023532 \end{bmatrix} \quad (D.14)$$

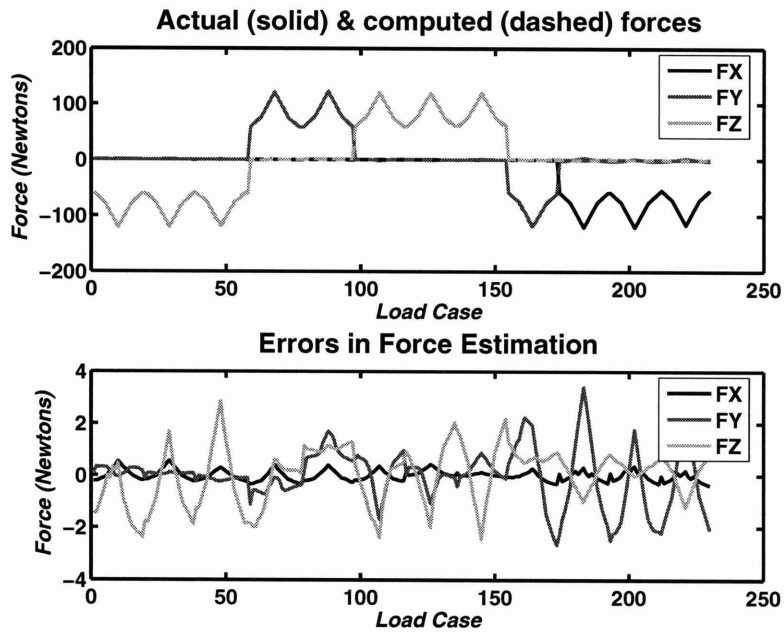
The calibration plots for sensor #001 can be found in Figure D-4 in the text above.

D.6.2 Prototype Sensor #002

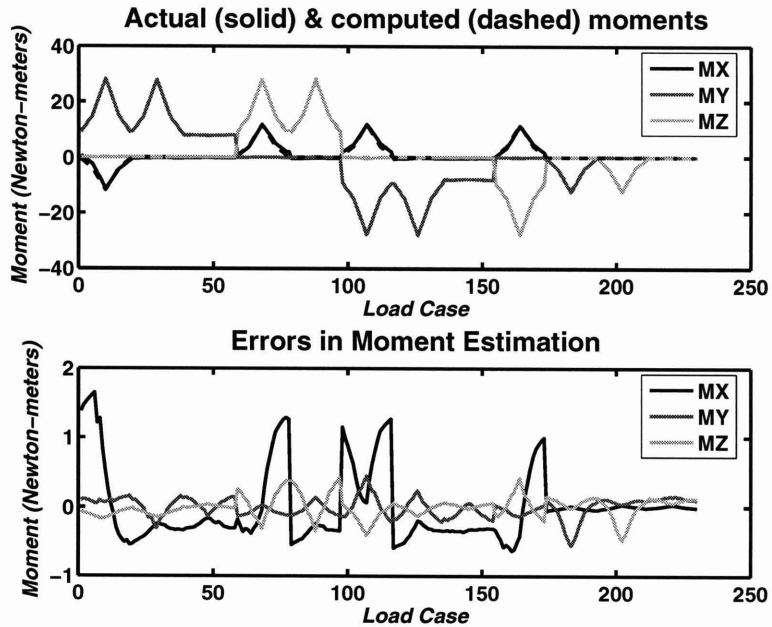
$$C_2 = \begin{bmatrix} 0.0000141084 & 0.0085520905 & 0.0000371611 & 0.0083969635 & -0.0000227753 & 0.0084143917 \\ -0.0001688378 & -0.0009971730 & 0.0077516978 & -0.0000073196 & -0.0076023317 & -0.0011921684 \\ -0.0088426547 & -0.0001694749 & 0.0048270936 & 0.0004717752 & 0.0042064050 & 0.0005586754 \\ -0.0003360284 & -0.0000293623 & -0.0003436577 & -0.0000406958 & -0.0003702159 & -0.0000335772 \\ -0.0001563840 & -0.0000609335 & 0.0000284698 & 0.0006074274 & 0.0001330830 & -0.0006199893 \\ 0.0000172802 & -0.0006609557 & -0.0000887184 & 0.0003443302 & 0.0000869794 & 0.0003560197 \end{bmatrix} \quad (D.15)$$

D.6.3 Prototype Sensor #003

$$C_3 = \begin{bmatrix} -0.00001467334 & -0.00847730937 & -0.00003251323 & 0.00852200777 & 0.00012002389 & -0.00872109419 \\ 0.00835710977 & -0.00080496070 & -0.00006745167 & -0.00000302958 & -0.00831406680 & 0.00042846016 \\ 0.00504757923 & -0.00009955634 & -0.00962916429 & -0.00058600896 & 0.00511339364 & -0.00044683191 \\ -0.00036424107 & 0.00003836038 & -0.00035586670 & -0.00002978317 & -0.00036966981 & 0.00003692176 \\ 0.00011108033 & -0.00061089651 & -0.00016031569 & -0.00003244859 & 0.00006201269 & 0.00063834609 \\ -0.00015562547 & -0.00032504833 & 0.00004301222 & -0.00068796542 & 0.00012876181 & -0.00034993788 \end{bmatrix} \quad (D.16)$$

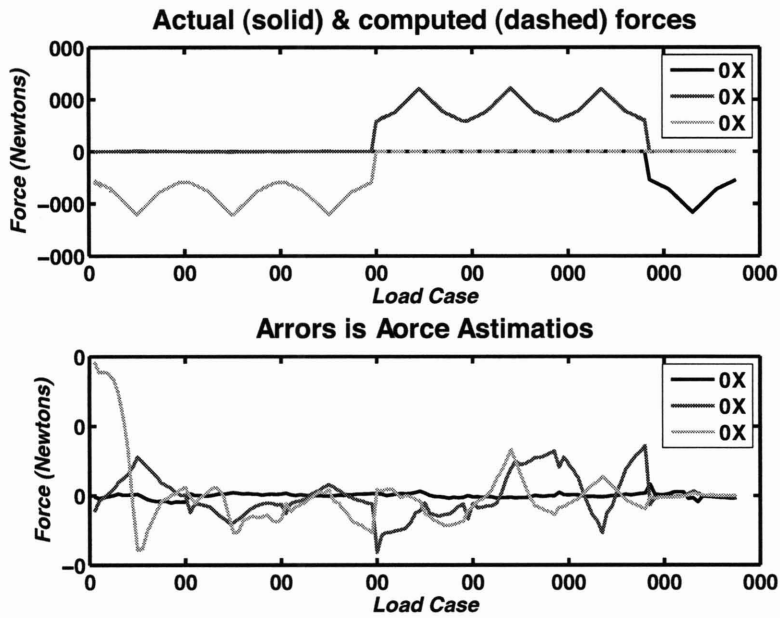


(a) Forces.

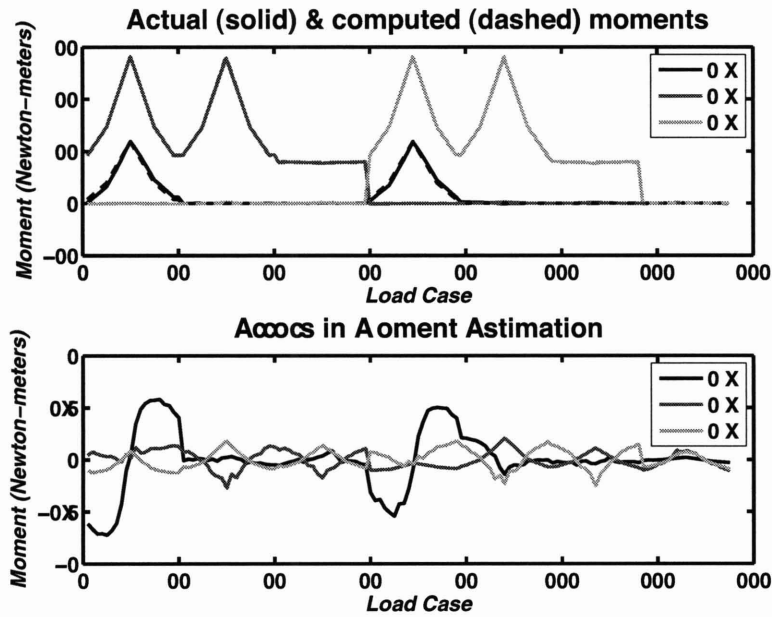


(b) Moments.

Figure D-5: Calibration plots for sensor #002.



(a) Forces.

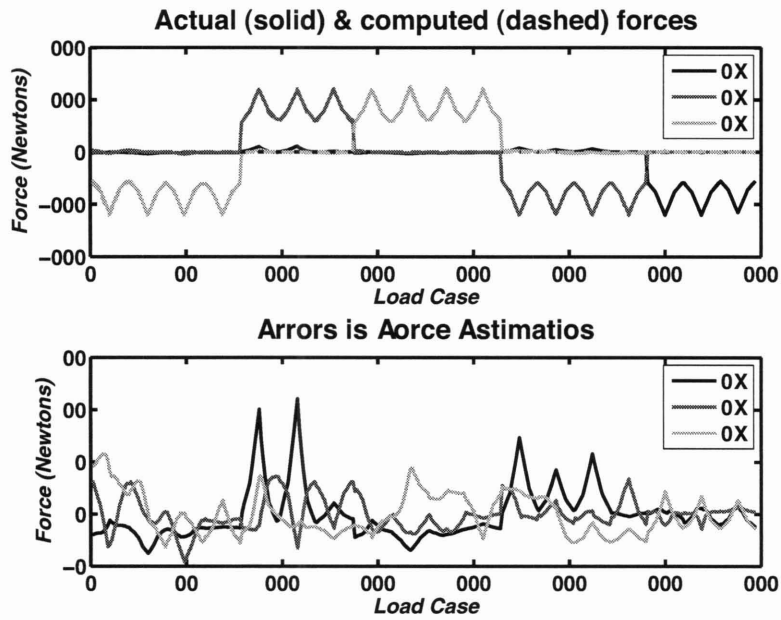


(b) Moments.

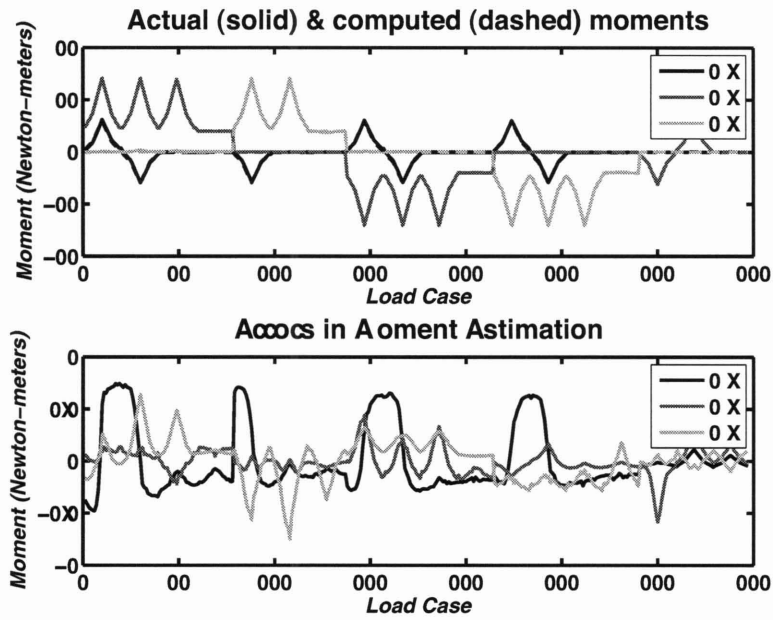
Figure D-6: Calibration plots for sensor #003.

D.6.4 Prototype Sensor #004

$$C_4 = \begin{bmatrix} -0.00008048375 & 0.00819636008 & -0.00015244259 & 0.00851280846 & 0.00007782692 & 0.00852475708 \\ 0.00015213001 & -0.00010635899 & -0.00792844719 & -0.00052983055 & 0.00793701088 & 0.00066019270 \\ -0.00908357556 & -0.00082495205 & 0.00472303546 & -0.00015229516 & 0.00463149406 & -0.00004294007 \\ -0.00041169206 & -0.00004361794 & -0.00044582678 & -0.00005705005 & -0.00043984572 & -0.00006025895 \\ -0.00013264883 & -0.00001132286 & 0.00007767362 & 0.00062453337 & 0.00006423120 & -0.00063867292 \\ 0.00000168341 & 0.00071152284 & 0.00017128729 & -0.00038377011 & -0.00016939755 & -0.00041403830 \end{bmatrix} \quad (\text{D.17})$$



(a) Forces.



(b) Moments.

Figure D-7: Calibration plots for sensor #004.

Appendix E

Hoop Game Design

This appendix describes the design of the hoop game used in Experiment 2 (see Chapter 4). The hoop game was fabricated out of a copper pipe, some copper wire, and an electronics box containing an LED, a push-button, a 5 Volt buzzer and associated electronic components. The physical hoop game equipment can be found in Figure E-1 while the electrical schematic for the hoop game electronics can be found in Figure E-2.

The hoop cables are plugged into the connector marked “Hoop”. The post cable is connected to the connector marked “Rod”. If the hoop contacts the copper part of the post, the JK flip-flop (see Figure E-2) latches and activates the buzzer and the LED. The buzzer and LED can be reset by pressing the red reset button, located on top of the game electronics box. The latching behaviour was required to ensure that the test director could detect a very brief contact between the post and the hoop. A small low pass filter was added to prevent electrical noise from tripping the circuit.

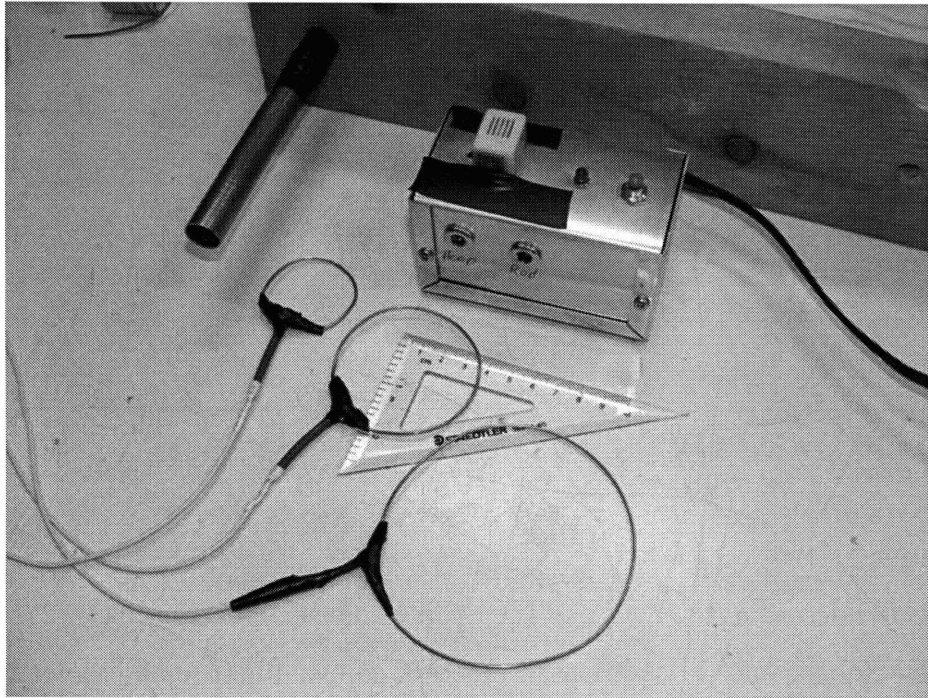


Figure E-1: The hoop game equipment including the post, the electronics box and the three hoops sized 10 cm, 6 cm and 4 cm.

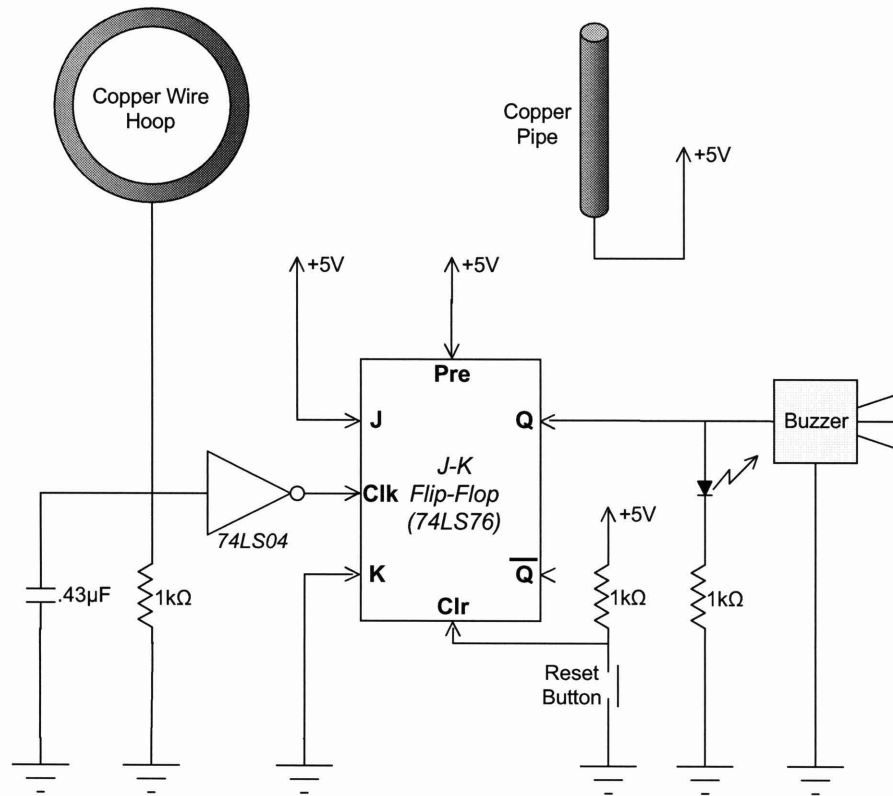


Figure E-2: Electronic schematic for the hoop game.

Appendix F

Sensor Operating Procedures

F.1 Theory of Operation

F.1.1 Overview

The purpose of the MICR0-G sensors (one of which is pictured in Figure F-1) is to measure 6-axis forces and moments (3-axis forces and 3-axis moments). Software has been written to autonomously collect the force and moment data on the sensors. A completely separate piece of software runs on a separate computer, is used to view the force / moment data in real-time as well as send simple commands to the sensor (such as the “zero” (tare) command).

The sensors can each be configured as hand-holds, foot restraints or plain touch pads. Three aluminum hand-holds from the EDLS sensors can be mounted directly to the top plates of the sensors.

F.1.2 Electrical

Electrically, the sensors have two primary connections: (A) Power and (B) Ethernet (data). Both connectors are found on one side of the sensor. The power connector contains 6 pins and the ethernet connector contains 10 pins. To mate each connector, simply push the connector into the socket until a “click” is heard. To remove a connector, pull on the connector housing to release the latch. A slight “pop” sound

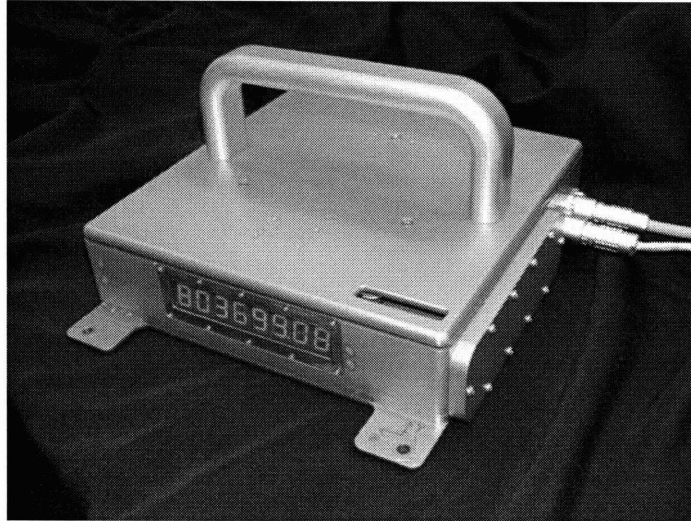


Figure F-1: One of 4 MICR0-G sensors.

will be heard as the connector releases from the sensor (due to the fact that the connectors are water-tight).

A single power supply box provides power to all 4 sensors. The power supply box (pictured in Figure F-2) has 4 power output jacks. Each output jack is identical, so it can be used to power any of the sensors. There is a single switch on the power supply box that activates and deactivates all power jacks at once. It is important that this switch is used to turn the sensors on and off (and not simply plugging the sensors into a live jack) because the sensors themselves do not have an on/off switch. Powering the sensors without the use of a switch will result in improper operation of the sensors and possible damage to the sensor electronics.

F.1.3 Software

The MICR0-G sensors each run a fully-functional version of Slackware Linux (version 6.0) with the standard Linux kernel (version 2.4.26). Upon boot-up, the sensors must be logged into in order to start the software, make software changes or shutdown. All sensors must be logged into with username `root` and password `microg` (all case sensitive). The operating system has built-in network security, so a secure shell (SSH) must be used to log into the sensors.



Figure F-2: The 4-port MICRO-G power supply.

ATTENTION: It is extremely important that the sensors are NEVER turned off without sending the appropriate shutdown commands (see Section F.2.4). Doing so could result in substantial data loss, but would most definitely result in a lengthy (*i*. 10 minutes) restart procedure. This is because the disk must be re-checked following a restart if the sensor was not properly shutdown. Since the hard drive has a capacity of 60 GB, this disk check takes a VERY long time.

Each sensor has its own IP address. This is how the sensors are communicated with in most circumstances. Sensor #1 has address 192.168.1.11, Sensor #2 has address 192.168.1.12, Sensor #3 has address 192.168.1.13 and Sensor #4 has address 192.168.1.14. One might recognize these addresses as those reserved for “private networks”. Indeed, this is true. The sensors are designed to communicate on their own private and isolated network from the rest of the world-wide internet. These settings can be changed in the future if the need arises (*i.e.*, to permit the sensors to be accessed from anywhere in the world).

Nominally, the sensors communicate through a *router*. While any router will work, a wireless router is useful because:

1. Wireless routers typically have 4 wired ports on them which can accept wired connections from all 4 sensors at once.

2. With all 4 sensors plugged into the wireless router, a laptop equipped with a wireless network adapter can communicate with all 4 sensors.
3. The sensors are equipped with wireless network adapters that could allow them to communicate with the wireless router. Currently, this method of communication is not reliable since the wireless adapter on each sensor is encased in a solid metal box (acting like a very effective Faraday cage).

The wireless router has an IP address of 192.168.1.1. Figure F-3 shows a picture of the Linksys router used for these experiments.



Figure F-3: The Linksys wireless router.

To permit communications between the sensors and the laptop (or laptops) monitoring their data, all must be on the private network. To accomplish this, each sensor and laptop must set their gateway to be 192.168.1.1 and have an IP address that is 192.168.1.xxx. The Apple operating system (OSX at the time this document was written) has an option from the “apple” menu to choose a “network location”. A location named “microg” has been created on both laptops used to communicate with the sensors that sets up the appropriate IP address and gateway.

When the sensor initially boots up, the data collection software will not be running. The Linux operating system will be running, but no forces will be recorded.

When the software is running properly, the clock on the side of the window will illuminate and count upwards.

The sensor software (started using the commands in Section F.2.2 establishes a primitive telnet server. It is through this telnet server that the sensor broadcasts its data to be displayed on the GUI, running on a laptop. Once the sensor software has been started, the only way to stop it cleanly is to telnet into the server and send the SHUTDOWN command. Do not confuse logging into the sensor using SSH and telnetting into the sensor *server*. As long as the Linux operating system is running, one can always SSH into the sensor. However, one can only telnet into the MICR0-G *server* if the MICR0-G server software is running. The MICR0-G server software is started by logging into the sensor (using SSH) and starting the MICR0-G server program.

Note: It is important to understand that while this data is being transmitted to the MICR0-G GUI on the laptop at 10Hz, the actual data (stored at 250 Hz) is being stored on the sensors themselves.

Once the MICR0-G server has been started, data collection can begin. When data is being collected, X, Y and Z forces and moments (6 measurements in total) are recorded at 250 Hz. Each measurement has associated with it a time. The time is the Linux system time, expressed as the number of seconds since the epoch (January 1, 1970). The 6 least significant digits plus two digits to the right of the decimal point are displays on the digital clock at the side of the sensor when the sensor software is running. This clock display serves two purposes:

1. Video cameras can see this time and it can be used to synchronize force data with video kinematic data.
2. The test director can record the time displayed on the side of the sensor at each motion. Special Matlab software (written specifically for this task) is then used to locate the “event” closest to the time recorded by the test director.

Unfortunately, two of the 2 sensors (possibly more) have faulty CMOS batteries, meaning that the onboard computer does not remember the time after a power-down. Thus, after each start-up, the date and time needs to be set using the Linux `date`

command. After each sensor has been powered up that is going to be used for a particular experiment and all dates are checked and possibly reset, the clocks need to be synchronized to ensure consistent data between all sensors and video cameras. The time synchronization is accomplished by the Network Time Protocol (NTP). Section F.2 provides more detail on how to set the sensor time and how to synchronize the clocks across all sensors.

The sensors only collect data when someone or something is applying a force greater than 1 Newton to the sensor top plate. This force could result from contact with the sensor or from thermal fluctuations on the sensor top plate. For this reason, one should not leave the sensor software running unattended for an extended period of time (*i.e.*, hours or days). Eventually, the sensors will need to be re-zeroed (using the MICR0-G GUI) due to thermal loads.

F.2 Detailed Instructions

F.2.1 Setup

1. Make sure power supply box is OFF (switch is in lower position and red light is OFF).
2. Plug all sensor power cables into the power supply box and into the power jacks on the side of the sensor. The power jack is the 6-pin connector located closest to the corner of the sensor. When plugging the power cable into the sensor, be sure you hear a “click” to verify it is latched.
3. Plug the 10-pin ethernet cables into the sensors immediately beside the power cable. Again, be sure to hear a click to confirm that the cable is fully seated in the connector.
4. Plug in the black DC power cable to the wireless router into the mains.
5. Plug all ethernet cables from the sensors into the YELLOW ports of the wireless router. The ethernet connector on the sensor is immediately beside the power

connector. Again, make sure you hear a “click” when inserting the connector onto the sensor.

6. Switch the power supply on using the switch at the front of the power supply box.

F.2.2 Sensor Software Startup

1. Open a terminal window on the laptop.
2. Set the laptop to the “microg” location using the Apple menu at the top left.
3. Ensure that the laptop is connected to the “microg” wireless access point by clicking on the wireless icon in the upper right toolbar.
4. Verify connection with the router by typing: `ping 192.168.1.1 <enter>`. The router should respond to the ping and the program should give you the response times. To stop pinging, press `CTRL-c`.
5. Connect to Sensor #1 by typing: `ssh -lroot 192.168.1.11 <enter>`. Password: `microg`
6. Change directories to the sensor execution directory by typing `cd microg_server/exec <enter>`.
7. Start the data collection software by typing `./microg_server -dfilename` where *filename* is the name of the data file the sensor should save the data to.
8. Open up a new terminal window `<apple>-n` and repeat Steps 5 to 7 for each powered up sensor. Sensor #2 has address `192.168.1.12`, Sensor #3 has address `192.168.1.13` and Sensor #4 has address `192.168.1.14`
9. Start the MICRO-G GUI software by clicking on it in the “dock”.
10. Click “OK” when it says it can’t find any servers.
11. Select from the drop-down menu: File → Connect.

12. Type in the IP Address for the first sensor. In the Port window, type 9000. Click “OK”.
13. Select from the drop-down menu: Server → Scan.
14. Repeat Steps 11 to 13 for each sensor started in Step 8.

F.2.3 Restarting Sensor Software for a New Subject

1. Quit the MICR0-G GUI by pressing `<apple>-q`.
2. Open a new terminal window on the laptop.
3. Log into the sensor software by typing `telnet ip-address 9000 <enter>` where *ip-address* is the address of the sensor.
4. You should see a message telling you what your “escape” character is. Type `SHUTDOWN <enter>`.
5. In the terminal window where you started the sensor software after ssh’ing into the sensor, you should have your prompt returned to you.
6. Repeat Steps 3 to 5 for each sensor.
7. You can now re-start the software (if you wish) using a new filename by starting at Step 7 in Section F.2.2.

F.2.4 Powering Down the Sensors

1. Follow the steps in Section F.2.3 but without restarting the software.
2. In the terminal window for each sensor (*i.e.*, the window where you started the `microg_server` program), type `shutdown -h now <enter>`.
3. Wait at least 30 seconds (VERY IMPORTANT!!!) and then flip the switch on the power supply.

Appendix G

Data Analysis Software

```
function analyze_data_new()

% Constants
rad2deg = 180/pi;
deg2rad = pi/180;
pounds2kg = 0.45359237;

% Load the supplemental data collected in the lab book
% The file supplemental_data.m must exist in the subject's data directory
clear error_code
supplemental_data;

% Get the rotation matrix for the current sensor configuration
fm_rot_mat = get_force_rot_mat(sensor_config);

% Parse force data
% This will parse the raw sensor data and ask the user for the contact
% start and stop times. It will also save the individual events into
% separate .mat files
force_filenames = load_all_data(push_off_sensor_filename, push_off_sensor_number, supp_data);

% Check to see if the current subject already as a saved data file
% If it does, load it. If it doesn't, then create the structure
if check_for_file('saved_subject_data.mat')
    disp('This subject has been analyzed in the past, so loading past analysis data.');
```

```
    load saved_subject_data.mat
else
    % We know that this will always be overwritten, so set the time vector
    % just to start the structure
    disp('Creating the subject_data structure since this is the first analysis run for this subject');
    subject_data(1).time_vec = 0;
end

% Check to see if we haven't yet checked the contact data
load(force_filenames{1});
if ~exist('bad_data')
    disp('We have not checked the force data yet, so checking now.');
```

```
    check_comp_contact;
else
    disp('Data already checked, so we do not have to check it again.');
```

```

end

% Loop through the number of runs to perform the analysis
for i = runs_to_analyze
    % Get the subject's body parameters from the inertia program
    if (limb_code(i) == 1)
        [robo, num_links, full_body_mass, cart_mass] = get_subject_leg_parameters(inertial_parameters_filename, g, subject_mass_pounds*pounds2kg);
    else
        disp('Error! You need to define the arm model first!');
    end

    % Save the robo object into the subject_data structure
    subject_data(i).robo = robo;

    % Setup the torque estimation parameters into the workspace
    % and compute the torque estimation weighting matrices
    torque_estimator_parameters;
    [R, Qk, P0] = get_estim_params(num_links, time_step, angle_meas_noise, force_meas_noise, accel_proc_noise, jerk_proc_noise, init_ang_err, init_rate_err);

    % Load the force data
    load(force_filenames{i});

    % Only proceed if the data is good
    if ~bad_data

        % Save the flag for good / bad data in the subject_data structure
        subject_data(i).bad_data = bad_data;

        % Rotate the forces and moments to match the body frame
        [forces, moments] = rotate_forces_moments(forces, moments, fm_rot_mat);

        % Set the time vec to be based on the forces first
        time_vec = get_6_lsd(force_time_vec);

        if angle_data_available(i)
            disp('Loading the angle data')
            % Load the angle data
            [angle_time, angles] = interpret_angle_data(angle_filename{i,1}, limb_code(i));

            % Even up the time traces
            disp('Making the forces, moments and angles even')
            [time_vec, data_mat] = even_time_trace(time_step, [force_time_vec, forces, moments], [angle_time, angles]);

            % Parse the even data
            [data_mat_length, data_mat_width] = size(data_mat);
            forces = data_mat(:,1:3);
            moments = data_mat(:,4:6);
            angles = data_mat(:,7:data_mat_width);
        else
            % If the angle data is not available, just save an empty matrix as
            % a placeholder
            disp('Not using angle data for this analysis run')
            angles = [];
        end

        % Trim data down to contact time only
        % The contact start and stop times are defined in the force .mat file
        [time_vec, data_mat] = trim_time_data(time_vec, [forces, moments, angles], get_6_lsd(contact_start_time), get_6_lsd(contact_end_time));

        % Re-parse this data matrix again
        [data_mat_length, data_mat_width] = size(data_mat);

```

```

forces = data_mat(:,1:3);
moments = data_mat(:,4:6);
if angle_data_available(i)
    angles = data_mat(:,7:data_mat_width);
else
    angles = [];
end

% Subtract off any force offsets
if offset_present
    force_off = forces(length(forces),:);
    moment_off = moments(length(moments),:);

    for mmm = 1:length(forces)
        forces(mmm,:) = forces(mmm,:) - force_off;
        moments(mmm,:) = moments(mmm,:) - moment_off;
    end
end

% Apply the friction model to the forces to obtain "real" forces
forces_raw = forces;
forces = floor_friction_model(forces, (full_body_mass + cart_mass));

% Save the forces, moments and angles into the subject data structure
subject_data(i).forces_raw = forces_raw;
subject_data(i).forces = forces;
subject_data(i).moments = moments;
subject_data(i).angles = angles; % If no angle data is available, this will be empty

% Normalize the time vector
abs_start_time = time_vec(1);
time_vec = time_vec - abs_start_time;

% Compute the contact time
contact_time = time_vec(length(time_vec));

% Save the time data
subject_data(i).abs_start_time = abs_start_time;
subject_data(i).time_vec = time_vec;
subject_data(i).contact_time = contact_time;

% Save the game results data if there are any
if (exist('error_code') == 1)
    if (error_code(i) > 200)
        subject_data(i).game_failed = 1;
    else
        subject_data(i).game_failed = 0;
    end
else
    subject_data(i).game_failed = 0;
end

% Obtain the normal force and the direction vectors
[normal_force_vec, dir_vecs] = compute_norm_force(forces, force_mask(i,:));

% Save the simple force analysis
subject_data(i).normal_force_vec = normal_force_vec;
subject_data(i).max_force = max(normal_force_vec);
subject_data(i).mean_force = mean(normal_force_vec);
subject_data(i).median_force = median(normal_force_vec);
subject_data(i).std_force = std(normal_force_vec);

```

```

subject_data(i).dir_vecs = dir_vecs;

% Compute some stats on the force direction
if (length(dir_vecs) > 0)
    for ijk = 1:length(dir_vecs)
        if (norm(dir_vecs(1,ijk)) > 0)
            dir_angle(ijk) = atan2(dir_vecs(2,ijk), dir_vecs(1,ijk))*rad2deg + 90;
        else
            dir_angle(ijk) = 0;
        end
    end
else
    dir_angle = 0;
end

% Save the analysis on the force direction
subject_data(i).force_dir_angle = dir_angle;
subject_data(i).max_force_dir_angle = max(abs(dir_angle));
subject_data(i).sum_dir_angle = sum(dir_angle);
subject_data(i).mean_dir_angle = mean(dir_angle);
subject_data(i).var_dir_angle = var(dir_angle);

% Work out the body com motion based on forces only (open loop)
disp('Integrating Motion Equations based on force data only')
% Determine guesses for the initial body position
if angle_data_available(i)
    init_com_pos_guess = compute_com_body(angles(1,:), robo);
    init_com_vel_guess = compute_com_body_vel(angles(1,:), init_jr_est.*ones(1, num_links), robo);
else
    init_com_pos_guess = init_com_est(i,:);
    init_com_vel_guess = init_com_vel_est(i,:);
end
[com_pos_fonly, com_vel_fonly, body_ang_fonly, euler_rates_fonly] = estimate_com_trajectory_fonly(robo, init_com_pos_guess,
init_com_vel_guess, forces(:,1:2), time_step);

% Save the data into the subject data structure array
subject_data(i).com_pos_fonly = com_pos_fonly;
subject_data(i).com_vel_fonly = com_vel_fonly;
subject_data(i).body_ang_fonly = body_ang_fonly;
subject_data(i).euler_rates_fonly = euler_rates_fonly;

% Compute and save the total body angle change (min to max)
body_angle_change_fonly = max(body_ang_fonly) - min(body_ang_fonly);
subject_data(i).body_angle_change_fonly = body_angle_change_fonly;

% Compute the departure variables
departure_vel_fonly = norm(com_vel_fonly(length(com_vel_fonly),:));
departure_angle_fonly = atan2(-com_vel_fonly(length(com_vel_fonly),1), com_vel_fonly(length(com_vel_fonly),2));
departure_rotation_rate_fonly = euler_rates_fonly(length(euler_rates_fonly));
departure_body_ang_fonly = body_ang_fonly(length(body_ang_fonly));

% Save the departure variables
subject_data(i).departure_vel_fonly = departure_vel_fonly;
subject_data(i).departure_angle_fonly = departure_angle_fonly;
subject_data(i).departure_rotation_rate_fonly = departure_rotation_rate_fonly;
subject_data(i).departure_body_ang_fonly = departure_body_ang_fonly;

% Compute the estimated com targetting error
departure_vel_vec_fonly = com_vel_fonly(length(com_vel_fonly),:);
departure_pos_fonly = com_pos_fonly(length(com_pos_fonly),:);
landing_distance_fonly = rig_length - 0.5;

```

```

land_err_fonly = compute_landing_error(departure_vel_vec_fonly, departure_pos_fonly, rig_length);

% Save the landing error
subject_data(i).land_err_fonly = land_err_fonly;

% Compute the energy based on the velocity of the center of mass
disp('Computing the linear and rotational pushoff energy for forces only');
% Linear
linear_pushoff_energy_fonly = (1/2)*(cart_mass + full_body_mass)*departure_vel_fonly^2;

% Save the linear pushoff energy
subject_data(i).linear_pushoff_energy_fonly = linear_pushoff_energy_fonly;

if angle_data_available(i)
    % Work out the body com motion computed directly from the angles (no
    % forces)
    for abc = 1:length(angles)
        com_pos_aonly(abc,:) = compute_com_body(angles(abc,:), robo);
    end

    % Save the data into the subject data structure array
    subject_data(i).com_pos_aonly = com_pos_aonly;
end

if angle_data_available(i)
    % Estimate the body com motion
    if (recompute_com_motion(i) || ~isfield(subject_data(i), 'com_pos') || (length(subject_data(i).com_pos) == 0))
        disp('Integrating Motion Equations based on force and angle data')
        % Integrate Equations of Motion
        init_joint_angle_rates = init_jr_est.*ones(1, num_links);
        init_joint_angle_errors = init_ja_err.*ones(1, num_links);
        init_joint_angle_rate_errors = init_jr_err.*ones(1, num_links);
        joint_angle_meas_err = ja_meas_err.*ones(1, num_links);
        force_errors = f_err.*ones(1,2);
        [com_pos, com_vel, body_ang, euler_rates, P_store] = estimate_com_trajectory(robo, angles, init_joint_angle_rates, init_joint_angle_errors, init

    % Save the data into the subject data structure array
    subject_data(i).com_pos = com_pos;
    subject_data(i).com_vel = com_vel;
    subject_data(i).body_ang = body_ang;
    subject_data(i).euler_rates = euler_rates;
    else
        disp('Loading Motion data from a previous solve')
        % Load the data from the saved structure array
        com_pos = subject_data(i).com_pos;
        com_vel = subject_data(i).com_vel;
        body_ang = subject_data(i).body_ang;
        euler_rates = subject_data(i).euler_rates;
    end

    % Compute the departure variables
    departure_vel = norm(com_vel(length(com_vel),:));
    departure_angle = atan2(-com_vel(length(com_vel),1), com_vel(length(com_vel),2));
    departure_rotation_rate = euler_rates(length(euler_rates));
    departure_body_ang = body_ang(length(body_ang));

    % Save the departure variables
    subject_data(i).departure_vel = departure_vel;
    subject_data(i).departure_angle = departure_angle;
    subject_data(i).departure_rotation_rate = departure_rotation_rate;

```

```

subject_data(i).departure_body_ang = departure_body_ang;

% Compute the estimated com targetting error
departure_vel_vec = com_vel(length(com_vel),:);
departure_pos = com_pos(length(com_pos),:);
landing_distance = rig_length - 0.5;
land_err = compute_landing_error(departure_vel_vec, departure_pos, rig_length);

% Save the landing error
subject_data(i).land_err = land_err;

% Compute the energy based on the velocity of the center of mass
disp('Computing the linear and rotational pushoff energy');
% Linear
linear_pushoff_energy = (1/2)*(cart_mass + full_body_mass)*departure_vel^2;
% Rotational
rotational_pushoff_energy = (1/2)*euler_rates(length(euler_rates))^2*compute_body_inertia(angles(length(angles),:), robo);

% Save the linear and rotational pushoff energy
subject_data(i).linear_pushoff_energy = linear_pushoff_energy;
subject_data(i).rotational_pushoff_energy = rotational_pushoff_energy;

% Compute the progression of the body moment of inertia
if (recompute_body_I(i) || ~isfield(subject_data(i), 'body_I_observed') || (length(subject_data(i).body_I_observed) == 0))
    disp('Computing inertias based on observed angles');
    body_I_observed = [];
    for jjj = 1:length(angles)
        body_I_observed(jjj,1) = compute_body_inertia(angles(jjj,:), robo);
    end

% Compute the percent change in body inertia
body_inertia_change = ((body_I_observed(length(body_I_observed)) - body_I_observed(1))/body_I_observed(1))*100;

% Save the observed body com pos and inertia
subject_data(i).body_I_observed = body_I_observed;
subject_data(i).body_inertia_change = body_inertia_change;
else
% Load data from a previous solve
disp('Loading body inertias from a past analysis run');
body_I_observed = subject_data(i).body_I_observed;
body_inertia_change = subject_data(i).body_inertia_change;
end

% Estimate the joint torques
if (torque_estimator_on(i) || ~isfield(subject_data(i), 'est_torques') || (length(subject_data(i).est_torques) == 0))
    disp('Estimating the joint torques')
% Filter the data
filter_order = 2;
force_fc = 40; % Hz
moment_fc = 40; % Hz
angle_fc = 5; % Hz
f_forces = lpfilt(forces, time_step, force_fc, filter_order);
f_moments = lpfilt(moments, time_step, moment_fc, filter_order);
f_angles = lpfilt(angles, time_step, angle_fc, filter_order);

% Save the filtered forces and angles
subject_data(i).f_forces = f_forces;
subject_data(i).f_moments = f_moments;
subject_data(i).f_angles = f_angles;

% Form the measurement matrix

```



```

meas_store = [f_angles'; -f_forces'];

% Setup the initial conditions
init_cond_vec = [meas_store(1:num_links,1); zeros(num_links*2,1)];

% Figure out if we need to run the ukf
if (ukf_on(i))
    ukf_estim_flag = 1;
else
    if ~isfield(subject_data(i), 'filter_est_states')
        ukf_estim_flag = 1;
    else
        ukf_estim_flag = 0;
    end
end

% Estimate the torques
[est_torques, filter_est_states] = torque_estimator(meas_store, init_cond_vec, R, Qk, PO, time_step, robo, ukf_estim_flag);

% Save the outputs
subject_data(i).est_torques = est_torques;
if (ukf_estim_flag == 1)
    subject_data(i).filter_est_states = filter_est_states;
end

else
    % Load the data from the last saved
    disp('Loading the joint torques from a previous run')
    est_torques = subject_data(i).est_torques;
    filter_est_states = subject_data(i).filter_est_states;
end

% Compute the work done by each joint
disp('Computing the joint work');
joint_work = get_joint_work(est_torques, filter_est_states);
total_joint_work = sum(joint_work);

% Save the joint work variables
subject_data(i).joint_work = joint_work;
subject_data(i).total_joint_work = total_joint_work;

% Compute the internal limb energy expended
if (recompute_limb_energy(i) || ~isfield(subject_data(i), 'limb_energy') || (length(subject_data(i).limb_energy) == 0))
    disp('Computing the limb energy');
    limb_energy = get_limb_energy(filter_est_states, robo);

    % Save the limb energy data
    subject_data(i).limb_energy = limb_energy;
else
    % Load past limb energy data
    disp('Loading limb energy data from a previous analysis run');
    limb_energy = subject_data(i).limb_energy;
end

end

else
    disp('Skipping this data because it was bad from the sensors.')
end

end

% Save the subject data into a file
% This will overwrite the current file
save saved_subject_data.mat subject_data

```

```

%%%%%%%%%%%%%%%%%%%%%%%%%%%%%%%%%%%%%%%%%%%%%%%%%%%%%%%%%%%%%%%%%%%%%%%%
function [pos_est, vel_est, ang_est, w_est, P_store] = estimate_com_trajectory(robo, angles, init_joint_angle_rates, init_joint_angle_errors,
init_joint_angle_rate_errors, joint_angle_meas_err, forces, force_errors, base_R, time_step)

% Make the inputs what we think they should be
angles = force_column(angles);
force_errors = force_column(force_errors);

% Setup initial conditions
init_pos = compute_com_body(angles(1,:), robo);
init_vel = compute_com_body_vel(angles(1,:), init_joint_angle_rates, robo);

% Vectorize the quantities
F = [-forces];
init_X = [init_pos; init_vel];

% Compute the symbolic R and P matrices
R_sym = get_symbolic_R(robo);
P_sym = get_symbolic_P(robo);

% Form the angular error variance vector
angle_var = joint_angle_meas_err.^2;

% Form the initial P matrix
P_init = eval_P(P_sym, angles(1,:), init_joint_angle_rates, init_joint_angle_errors.^2, init_joint_angle_rate_errors.^2);

% Get the initial body mass parameters
m = get_body_mass(robo);

% Form the continuous Q matrix
w_pos = zeros(2,1);
w_vel = force_errors./m;
w_vec = [w_pos; w_vel];
Q = diag(diag(w_vec*w_vec'));

% Compute the measured body positions from the joint angles
for i = 1:length(angles)
    meas_pos(:,i) = [compute_com_body(angles(i,:), robo)];
end

% Form the measurement matrix
H = [eye(2), zeros(2)];

% Start the filter
disp('filter')
X = init_X
P = P_init;
for i = 1:length(angles)
    % Measurement update
    R = eval_R(R_sym, angles(i,:), angle_var) + base_R;
    K = P*H'*inv(H*P*H' + R);
    X = X + K*(meas_pos(:,i) - H*X);
    P = (eye(size(P)) - K*H)*P*(eye(size(P)) - K*H)' + K*R*K';

    % Store the state estimate and covariance
    state_store(:,i) = X;
    P_store(:,i) = diag(P);
end

```

```

    % Time update
    [A, B] = get_lin_force_dyn(X, m);
    [Phi, Bk, Qk] = get_discrete_dyn(A, Q, B, time_step);
    X = propagate_com_motion_rk(X, time_step, F(i,:)', m);
    P = Phi*P*Phi' + Qk;
end

% Assign the estimated quantities
pos_est = state_store(1:2,:);
vel_est = state_store(3:4,:);
ang_est = zeros(1,length(state_store));
w_est = zeros(1,length(state_store));

for i = 1:length(angles)
    body_roll_angle = 0;
    quat_true(:,i) = get_quat_from_pos([pos_est(i,:), 0]', body_roll_angle);
    Rott = quat2R(quat_true(:,i));
    ang_est(i) = acos(Rott(1,1));
    w_est(i) = get_planar_rate_from_carts(pos_est(i,:), vel_est(i,:));
end

%%%%%%%%%%%%%%%%%%%%%%%%%%%%%%%%%%%%%%%%%%%%%%%%%%%%%%%%%%%%%%%%%%%%%%%%

function new_state = propagate_state_rk(X, time_step, ctrl_torques_in, robo)

% Determine the number of links
num_links = length(X)/3;

% Parse state vector
pos_vec = X(1:num_links);
vel_vec = X((num_links + 1):(num_links*2));
acc_vec = X((2*num_links + 1):(num_links*3));

% Create a "small state vector"
small_state = [pos_vec; vel_vec];

% Compute the derivatives using the current state vector
k1 = time_step*state_derivs_own(0, small_state, robo, ctrl_torques_in);
k2 = time_step*state_derivs_own(time_step/2, (small_state + k1./2), robo, ctrl_torques_in);
k3 = time_step*state_derivs_own(time_step/2, (small_state + k2./2), robo, ctrl_torques_in);
k4 = time_step*state_derivs_own(time_step, (small_state + k3), robo, ctrl_torques_in);

% Do the Fourth Order Runge-Kutta propagation
new_small_state = small_state + (1/6).*(k1 + 2.*k2 + 2.*k3 + k4);

% Compute the accelerations now
state_deriv = state_derivs_own(time_step, new_small_state, robo, ctrl_torques_in);

% Pull out accelerations
new_acc_vec = state_deriv((num_links + 1):(num_links*2));

% Form the output
new_state = [new_small_state; new_acc_vec];

%%%%%%%%%%%%%%%%%%%%%%%%%%%%%%%%%%%%%%%%%%%%%%%%%%%%%%%%%%%%%%%%%%%%%%%%

function [est_torques, filter_est_states] = torque_estimator(meas_store, init_cond_vec, R, Qk, P0, time_step, robo, ukf_on)

% Determine some parameters
L = length(init_cond_vec);

```

```

num_links = length(init_cond_vec)/3;
kappa = 0;
alpha = 0.1;
beta = 2;
lambda = (alpha^2)*(L + kappa) - L;
gamma = sqrt(L + lambda);

% Extract the inertia vector from the robot object
links_cell = robo.link;
I = [];
for i = 1:num_links
    this_link = links_cell{i, 1};
    I_t = this_link.I;
    I(i) = I_t(3,3);
end

% Store the init_conds as the first estimate
filter_est_states = init_cond_vec;

% Assume that the initial control torques are zero to start
ctrl_torques = zeros(num_links, 1);

% Store these initial control torques as the first torque estimate
est_torques = ctrl_torques;

% Set the optimization options
options = optimset('TolFun', 0.000001');

% Pull out the angle data from the measurement vector
angle_data = meas_store(1:num_links, 1:length(meas_store)-1);

% Set the f_forces variable
% The forces used to be filtered here but not anymore
f_forces = meas_store((num_links + 1):(num_links + 2), :);

% Form the new matrix of measurements
meas_filt_interp = [angle_data; f_forces(:, 1:length(f_forces)-1)];

% Get the m state
m = get_m(angle_data, time_step);

% Save the original m for possible measurement use
m_orig = m;

% Compute the symbolic H matrix
H_sym = get_sym_H(robo);
H_full_sym = get_sym_H_full(robo);

% Figure out the number of steps
num_steps = length(meas_filt_interp);

% Start the estimation
max_repeats = 1;
max_diff_tol = 0.01;
max_diff = 10;
num_repeats = 0;
est_torques = zeros(num_links, num_steps);
while ((max_diff > max_diff_tol) & (num_repeats < max_repeats))
    % Set the number of repeats
    num_repeats = num_repeats + 1;

```

```

% Initialize the state estimate and covariance matrix
X_filter = init_cond_vec;
P = P0;

% Save the old estimated torques
t_old = est_torques;

for i = 2:num_steps
    % Display a progress message
    disp(sprintf('Computing estimation step %d of %d in iteration %d of a max of %d.\n', i, num_steps, num_repeats, max_repeats));

    % Figure out the control torques
    % NOTE: These control torques can be stored at time i and directly
    % compared with the actual_control_torques matrix at the same time i
    % In other words, these torques should actually be used to go from the
    % state at time i-1 to the state i.
    nls_pos_meas = m_orig(1:num_links,i);
    nls_frc_meas = f_forces(:,i);
    nls_meas = [nls_pos_meas; nls_frc_meas];
    nls_guess_state = m(:,i);
    nls_guess_state(2*num_links+1:3*num_links) = zeros(num_links, 1);

    disp(sprintf('Solving for acceleration states.\n'));
    [ctrl_torques, nls_X] = nls_torque_est(nls_meas, H_sym, nls_guess_state, robo, R);

    disp(sprintf('Solving for all states.\n'));
    [ctrl_torques, nls_X, P_nls_out] = nls_torque_est_full(nls_meas, H_full_sym, [nls_guess_state(1:num_links*2); nls_X], robo, R);

    % Store these control torques
    %ctrl_torques
    est_torques(:,i) = ctrl_torques;

    if ukf_on
        % Run the Unscented Kalman Filter (UKF)
        % NOTE: When I do the update here, I shouldn't use the torque that I
        % just computed. That torque should have been used to propagate the
        % previous state to this one!

        disp(sprintf('Doing the UKF.\n'));
        % Do the UKF time update
        [chi, X_filter, P, Y, y] = ukf_time_update(X_filter, P, (Qk + P_nls_out.*time_step), gamma, L, lambda, alpha, beta, robo, time_step, ctrl_torques);

        % Do the UKF measurement update
        [X_filter, P] = ukf_meas_update(X_filter, P, meas_filt_interp(:,i), y, chi, Y, R, lambda, L, alpha, beta);

        % Store the new state estimate
        filter_est_states(:,i) = X_filter;
    else
        filter_est_states(:,i) = m(:,i);
    end
end

% Set the m state to run the simulation again
m = filter_est_states;

% Save the filter progression
prog_est_states(:,num_repeats) = filter_est_states;
prog_est_torques(:,num_repeats) = est_torques;

% Find out how much these torques have changed since the last iteration
t_diff = est_torques - t_old;

```

```

    % Determine the magnitude of the difference in the computed torques
    for nor_cnt = 1:num_links
        norm_vec(nor_cnt) = norm(t_diff(nor_cnt,:));
    end
    max_diff = max(norm_vec);
end

% Add one entry to the end of the estimated torques and states
est_torques = [est_torques, est_torques(:,length(est_torques))];
filter_est_states = [filter_est_states, filter_est_states(:,length(filter_est_states))];

%%%%%%%%%%%%%%%%%%%%%%%%%%%%%%%%%%%%%%%%%%%%%%%%%%%%%%%%%%%%%%%%%%%%%%%%

function [X_new, P_new] = ukf_meas_update(X, P, meas, y, chi, Y, R, lambda, L, alpha, beta)

% Compute the measurement updated covariance matrix
Pyy_sum = 0;
Pxy_sum = 0;
for j = 0:(2*L)
    % Compute the weights
    if (j == 0)
        Wc = lambda/(L + lambda) + (1 - alpha^2 + beta);
    else
        Wc = 1/(2*(L + lambda));
    end

    % Add to the weighted sums
    Pyy_sum = Pyy_sum + Wc*( Y(:,(j+1)) - y )*( Y(:,(j+1)) - y )';
    Pxy_sum = Pxy_sum + Wc*( chi(:,(j+1)) - X )*( Y(:,(j+1)) - y )';
end
Pyy = Pyy_sum + R;
Pxy = Pxy_sum;

% Compute the gain
ukf_gain = Pxy*inv(Pyy);

% Do the state measurement update
X = X + ukf_gain*(meas - y);

% Do the covariance matrix update
P = P - ukf_gain*Pyy*ukf_gain';

% Assign the outputs
X_new = X;
P_new = P;

%%%%%%%%%%%%%%%%%%%%%%%%%%%%%%%%%%%%%%%%%%%%%%%%%%%%%%%%%%%%%%%%%%%%%%%%

function [chi_new, x_new, P_new, Y_predict, y_predict] = ukf_time_update(X, P, Qk, gamma, L, lambda, alpha, beta, robo, update_period, ctrl_torques)

% Get the matrix square root of the covariance matrix
sqP = sqrtm(P);

% Calculate sigma points
state_mat = [];
for j = 1:L
    state_mat(:,j) = X;
end

```

```

chi = [X, (state_mat + gamma*sqP), (state_mat - gamma*sqP)];

% Propagate the chi matrix
chi_prop = [];
for j = 1:(2*L + 1)
    chi_prop(:,j) = propagate_state_rk(chi(:,j), update_period, ctrl_torques, robo);
end
chi = chi_prop;

% Do the weighted sums to complete the time update
% Do x_hat first
x_sum = 0;
for j = 0:(2*L)
    % Compute the weights
    if (j == 0)
        Wm = lambda/(L + lambda);
    else
        Wm = 1/(2*(L + lambda));
    end

    % Add to the weighted sum
    x_sum = x_sum + Wm*chi(:,j+1);
end
X = x_sum;

% Now do P
P_sum = 0;
for j = 0:(2*L)
    % Compute the weights
    if (j == 0)
        Wc = lambda/(L + lambda) + (1 - alpha^2 + beta);
    else
        Wc = 1/(2*(L + lambda));
    end

    % Add to the weighted sum
    P_sum = P_sum + Wc*( chi(:,(j+1)) - X )*( chi(:,(j+1)) - X )';
end
P = P_sum + Qk;

% Get the matrix square root of the new covariance matrix
sqP = sqrtm(P);

% Redraw sigma points
state_mat = [];
for j = 1:L
    state_mat(:,j) = X;
end
chi = [X, (state_mat + gamma*sqP), (state_mat - gamma*sqP)];

% Compute the predicted measurements based on the current chi matrix
% First, compute the Y matrix
Y = [];
for j = 1:(2*L + 1)
    Y(:,j) = get_meas(chi(:,j), robo);
end

% Now, do a weighted sum to get the actual predicted measurements
y_sum = 0;
for j = 0:(2*L)
    % Compute the weights
    if (j == 0)

```

```

        Wm = lambda/(L + lambda);
    else
        Wm = 1/(2*(L + lambda));
    end

    % Add to the weighted sum
    y_sum = y_sum + Wm*Y(:,(j+1));
end
y = y_sum;

% Assign final values
chi_new = chi;
x_new = X;
P_new = P;
y_predict = y;
Y_predict = Y;

%%%%%%%%%%%%%%%%%%%%%%%%%%%%%%%%%%%%%%%%%%%%%%%%%%%%%%%%%%%%%%%%%%%%%%%%

function [mean_vec, median_vec, var_vec, std_vec, index_vec] = window_stats(data, window_size, real_data_locs)

% Put data into column format
[data, flopped] = force_column(data);

% Check to see if window_size is an appropriate size
if (window_size > length(data))
    disp('Error! Window size too big!');
    return
end
full_data_size = length(data);

% Initialize the output vectors
mean_vec = [];
median_vec = [];
var_vec = [];
std_vec = [];
index_vec = [];

% Initialize the window counter
jj = 1;

% Initialize the beginning and end of the window
window_start = 1;
window_end = window_size;

while (window_end <= full_data_size)
    % Compute the stats for each column
    [rows, cols] = size(data);
    for i = 1:cols
        mean_num = mean(data(window_start:window_end,i));
        median_num = median(data(window_start:window_end,i));
        var_num = var(data(window_start:window_end,i));
        std_num = std(data(window_start:window_end,i));
    end

    % Figure out where on the plot these stats should be placed
    stats_location = window_size*(jj-1) + window_size/2;

    % Put everything into the output vectors
    mean_vec = [mean_vec; mean_num];
    median_vec = [median_vec; median_num];

```



```
var_vec = [var_vec; var_num];
std_vec = [std_vec; std_num];
index_vec = [index_vec; stats_location];

% Increment the window counter
jj = jj + 1;

% Set the new window_end
window_end = window_size*jj;

% Set the new window_start
window_start = window_end - window_size + 1;
end
```


Appendix H

Human Subject Use Documentation

H.1 Informed Consent Form

CONSENT TO PARTICIPATE IN NON-BIOMEDICAL RESEARCH

Microgravity Investigations of Crew Reaction in 0-G – Underwater (MICR0-G – UW)

You are asked to participate in a research study conducted by Professor Dava Newman, PhD and Philip Ferguson, SM, from the department of Aeronautics and Astronautics at the Massachusetts Institute of Technology (M.I.T.). You have been asked to participate in this study because you have been identified as a SCUBA certified member of the MIT community who might be interested in such a research program. If you agree to take part in this study, you will be one of about 10 to 20 other subjects. You should read the information below, and ask questions about anything you do not understand, before deciding whether or not to participate.

• PARTICIPATION AND WITHDRAWAL

Your participation in this study is completely voluntary and you are free to choose whether to be in it or not. If you choose to be in this study, you may subsequently withdraw from it at any time without penalty or consequences of any kind. The investigator may withdraw you from this research if circumstances arise which warrant doing so.

If at any time during this study, any investigator feels that your safety is at risk, the investigators may terminate your participation in this study.

• PURPOSE OF THE STUDY

The purpose of this study is to identify the control strategies used by humans to move their body from one location to another in the absence of gravity. Future space exploration missions will require astronauts to spend long periods of time in a microgravity environment and then be expected to perform tasks in full or partial gravity. Understanding the mechanisms by which humans adapt their control strategies to differing gravity environments may lead to the development of new astronaut countermeasures. These countermeasures would be designed to accelerate astronauts' adaptation to a new gravity environment and reduce the risk of injuries associated with falls.

When weighted properly underwater, humans experience a weightless sensation similar to that experienced by astronauts in space. Humans can also experience a similar weightlessness feeling when rolling on a smooth floor in one plane. Thus, this experiment will be carried out both underwater and rolling on a smooth floor to simulate a zero-gravity, space environment.

This study will be paired with another separate study (COUHES #2718) which investigates control strategies adopted during parabolic flight on NASA's KC-135 microgravity aircraft. Control strategies from the underwater experiments and the KC-

135 experiments will be compared and techniques for underwater adaptation will be evaluated based on subjects performance.

• **PROCEDURES**

If you volunteer to participate in this study, we would ask you to do the following things:

For subjects participating in the 1-G “rolling” portion of the study:

Preparation:

- You will lie on a rolling platform, similar to a “mechanic’s creeper” and will be lightly strapped down
- You will be instructed where the sensors are that you will be interacting with

Acclimation:

- You will be given the opportunity to move yourself around using your arms and legs to push and pull yourself around while you get used to moving on the rolling platform

Experiment:

- You will be asked to move your body along a small course made up of 3-4 sensors. You will use the sensors as restraints to pull and push yourself from one sensor to the next.
- The course will be repeated approximately 5 – 10 times.
- After completion of the course trials, you will be asked to perform a series of prescribed body motions including push-offs and landings.

For subjects participating in the underwater portion of the study:

Preparation:

- You will be briefed on all risks associated with SCUBA diving
- The investigators will review emergency procedures
- You will don a SCUBA mask, weight belt, ankle weights and small inflatable snorkeling vest
- You will put a SCUBA regulator in your mouth from a tank sitting on the pool deck (this setup is known as a “hookah”)
- You will next enter the water with 2 investigators. The investigators will work with you to adjust the weights on the weight belt and on your ankles to make you neutrally buoyant (neutrally buoyant means that you neither sink nor float).

Acclimation:

- You will be given the opportunity to swim at the bottom of the pool while using the hookah.
- You will be given as much time as you need to feel comfortable with ear equalization and breathing using the hookah.

Experiment:

- You will be asked to move your body along a small course made up of 3-4 sensors. You will use the sensors as restraints to pull and push yourself from one sensor to the next.
- The course will be repeated approximately 5 – 10 times.
- After completion of the course trials, you will be asked to perform a series of prescribed body motions including body twists, limb extensions and push-offs and landings.

All experiment operations will take place at either the Alumni pool or the Z-center pool at MIT. The entire experiment will take approximately 2 hours to complete.

• **POTENTIAL RISKS AND DISCOMFORTS**

The only risks involved in this study are those associated with SCUBA diving in shallow (less than 15 feet) of water. There are no risks or discomforts associated with the sensor hardware.

In any SCUBA diving environment, divers are exposed to risks and discomforts relating to pressure differentials. Subjects may feel discomfort when descending due to blockages in their inner ears. In extreme conditions, subjects may rupture an eardrum if the blockage is severe.

When working underwater, there is always a risk of drowning if subjects inhale sufficient amounts of water.

While this study will be carried out in less than 15 feet of water, there is still a small risk of subjects incurring over-expansion injuries. These can occur if a subject is breathing regulated (high pressure) air underwater, holds his/her breath and quickly swims to the surface.

As a safety precaution, two fully trained SCUBA divers will accompany the subject during the experiment. Each SCUBA diver will have a spare breathing regulator and will be ready to assist the subject in the event of an emergency.

If at any time during the study any investigator feels that the subject has become uncomfortable underwater to the point where the subject's safety is in jeopardy, the investigators may terminate the subject's participation in this study.

For subjects performing only the 1-G "rolling" study, there are no inherent risks.

• **POTENTIAL BENEFITS**

Other than accumulating SCUBA experience, subjects are NOT anticipated to benefit directly from participating in this study.

Understanding the control strategies of astronauts is central to the development of countermeasures that will allow humans to conduct extended space exploration missions. This study is designed to reveal the typical control strategies that humans adopt in a 0-G setting and will hopefully lead to new countermeasure development.

- **PAYMENT FOR PARTICIPATION**

Subjects will NOT be paid for participating in this study.

- **CONFIDENTIALITY**

Any information that is obtained in connection with this study and that can be identified with you will remain confidential and will be disclosed only with your permission or as required by law.

Video taping will be only used to back out joint angles. Several video cameras will record the subject's motions and custom software will be used to extract the joint angles. If possible, the cameras will be setup to exclude the subjects' faces from the video. Furthermore, all subjects will be wearing SCUBA masks and regulators, so subject recognition will be extremely difficult, even if video cameras happen to capture subjects faces. In the event that a subject is recognizable, the video will be altered to obscure the identity. The anonymity of the subjects will be fully preserved.

Following the experiment, force and joint angle data will be stored on lab hard drives and on CD/DVD's. All video from which subjects can be recognized will be destroyed.

- **IDENTIFICATION OF INVESTIGATORS**

If you have any questions or concerns about the research, please feel free to contact:

Principal Investigator: Professor Dava Newman
dnewman@mit.edu
617-258-8799

Co-Investigator: Philip Ferguson
philf@mit.edu
617-253-5487

- **EMERGENCY CARE AND COMPENSATION FOR INJURY**

In the unlikely event of physical injury resulting from participation in this research you may receive medical treatment from the M.I.T. Medical Department, including emergency treatment and follow-up care as needed. Your insurance carrier may be billed for the cost of such treatment. M.I.T. does not provide any other form of compensation for injury. Moreover, in either providing or making such medical care available it does not imply the injury is the fault of the investigator. Further information may be obtained by calling the MIT Insurance and Legal Affairs Office at 1-617-253 2822.

- **RIGHTS OF RESEARCH SUBJECTS**

You are not waiving any legal claims, rights or remedies because of your participation in this research study. If you feel you have been treated unfairly, or you have questions regarding your rights as a research subject, you may contact the Chairman of the Committee on the Use of Humans as Experimental Subjects, M.I.T., Room E32-335, 77 Massachusetts Ave, Cambridge, MA 02139, phone 1-617-253 6787.

SIGNATURE OF RESEARCH SUBJECT OR LEGAL REPRESENTATIVE

I understand the procedures described above. My questions have been answered to my satisfaction, and I agree to participate in this study. I have been given a copy of this form.

Name of Subject

Name of Legal Representative (if applicable)

Signature of Subject or Legal Representative

Date

SIGNATURE OF INVESTIGATOR

In my judgment the subject is voluntarily and knowingly giving informed consent and possesses the legal capacity to give informed consent to participate in this research study.

Signature of Investigator

Date

H.2 Underwater Subject Selection Questionnaire

Subject Selection Questionnaire
For
Microgravity Investigations of Crew Reaction in 0-G – Underwater

Please answer all questions.

1. Are you SCUBA Certified (circle one)? YES NO
2. When was your last dive? _____
3. Have you consumed any alcohol in the last 24 hours (circle one)? YES NO
If so, please indicate how much: _____
4. Have you consumed drugs of any kind (i.e. muscle relaxants, decongestants, pain relievers or other prescription, over the counter or illicit drugs) in the last 24 hours (circle one)? YES NO
If so, please indicate what kind of drugs: _____
5. Are you comfortable using SCUBA equipment (circle one)? YES NO
6. Are you aware of the over-expansion risks associated with SCUBA diving (circle one)? YES NO
7. Do you consider yourself to be a competent swimmer (circle one)? YES NO
8. Have you had a head cold within the past week (circle one)? YES NO
9. Are you capable of equalizing your ears (circle one)? YES NO
10. In the event of an emergency in 15 feet of water where you cannot inhale, please describe what actions you would take:

Bibliography

David L. Akin. Quantifying human performance in space operations. Technical Report SSL 23-86, Massachusetts Institute of Technology, 1986.

Amir R. Amir. Design and development of advanced load sensors for the international space station. Engineer's thesis, Massachusetts Institute of Technology, September 1998.

Amir R. Amir and Dava J. Newman. Research into the effects of astronaut motion on the spacecraft: A review. *Acta Astronautica*, 47(12):859–869, June 2000.

Amir R. Amir, Guido Baroni, Alessandra Pedrocchi, Dava J. Newman, Giancarlo Ferrigno, and Antonio Pedotti. Measuring astronaut performance on the iss: Advanced kinematic and kinetic instrumentation. *IEEE Transactions on Instrumentation and Measurement*, 50(5):1450–1455, October 2001.

H. Asada and J. J. E. Slotine. *Robot Analysis and Control*. J. Wiley, New York, N.Y., 1986.

Christopher G. Atkeson and John M. Hollerbach. Kinematic features of unrestrained vertical arm movements. *Journal of Neurophysiology*, 5(9):2318–2330, September 1985.

G. Baroni, G. Ferrigno, M. Rabuffetti, A. Pedotti, and J. Massion. Long-term adaptation of postural control in microgravity. *Experimental Brain Research*, 128(3):410–416, 1999.

- Guido Baroni, Alessandra Pedrocchi, Giancarlo Ferrigno, Jean Massion, and Antonio Pedotti. Static and dynamic postural control in long-term microgravity: evidence of a dual adaptation. *Journal of Applied Physiology*, 90:205–215, August 2001a.
- Guido Baroni, Alessandra Pedrocchi, Giancarlo Ferrigno, Jean Massion, and Antonio Pedotti. Motor coordination in weightlessness conditions revealed by long-term microgravity adaptation. *Acta Astronautica*, 49(3-10):199–213, 2001b.
- J.L. Barron, D.J. Fleet, S.S. Beauchemin, and T. A Burkitt. Performance of optical flow techniques. *CVPR*, 92:236–242, 1992.
- Thomas J. Beck, Christopher B. Ruff, Karen E. Warden, William W. Scott Jr., and Gopala U. Rao. Predicting femoral neck strength from bone mineral data - a structural approach. *Investigative Radiology*, 25(1):6–18, January 1990.
- G. Bergmann, F. Graichen, and A. Rohlmann. Is staircase walking a risk for the fixation of hip implants? *Journal of Biomechanics*, 28(5):535–553, 1995.
- E. Bizzi, N. Hogan, F. A. Mussa-Ivaldi, and S. Giszter. *Movement Control*, chapter 1 - Does the nervous system use equilibrium-point control to guide single and multiple joint movements?, pages 1–11. Cambridge University Press, Cambridge, 1994.
- Emilio Bizzi, William Chapple, and Neville Hogan. Mechanical properties of muscles - Implications for motor control. *Trends in Neurosciences*, 5(11):395–398, November 1982.
- J. J. Bloomberg and A. P. Mulavara. Changes in walking strategies after spaceflight. *IEEE Engineering in Medicine and Biology Magazine*, 22(2):58–62, March-April 2003.
- Jacob J. Bloomberg, Ajitkumar Mulavara, and Helen S. Cohen. Developing sensorimotor countermeasures to mitigate postflight locomotor dysfunction. *Journal of the American Institute of Aeronautics and Astronautics*, (AIAA 2001-4941), 2001.

- Otmar Bock, Ian P. Howard, Kenneth E. Money, and Karin E. Arnold. Accuracy of Aimed Arm Movements in Changed Gravity. *Aviation, Space, and Environmental Medicine*, 63:994–998, 1992.
- A. Brubakk. Man in extreme environments. *Aviation, Space, and Environmental Medicine*, 71:A126–A130, September 2000.
- George W. Bush. American Presidential Address announcing new space initiative, January 2004.
- Christopher E. Carr. *The bioenergetics of walking and running in spacesuits*. PhD thesis, Massachusetts Institute of Technology, Cambridge, MA, 2005.
- G. A. Cavagna and R. Margaria. Mechanics of walking. *Journal of Applied Physiology*, 21(1):271–278, 1966.
- G. Clément and F. Lestienne. Adaptive modifications of postural attitude in conditions of weightlessness. *Experimental Brain Research*, 72:381–389, 1988.
- B. A. Conway, H. Hultborn, and O. Kiehn. Proprioceptive input resets central locomotor rhythm in the spinal cat. *Experimental Brain Research*, 68(3):643–656, 1987.
- P. I. Corke. A robotics toolbox for MATLAB. *IEEE Robotics and Automation magazine*, 30(1):24–32, March 1996.
- J.J. de Koning, G. de Groot, and G.J. van Ingen Schenau. Ice friction during speed skating. *Journal of Biomechanics*, 25(6):565–571, June 1992.
- Douglas DeCarlo and Dimitris Metaxas. Optical flow constraints on deformable models with applications to face tracking. *International Journal of Computer Vision*, 38(2):99–127, 2000.
- Paul DeVita and Tibor Hortobagyi. Obesity is not associated with increased knee joint torque and power during level walking. *Journal of Biomechanics*, 36(13):1355–1362, March 2003.

- Volker Dietz and Jacques Duysens. Significance of load receptor input during locomotion: a review. *Gait and Posture*, 11(2):102–110, April 2000.
- A. G. Feldman. *Movement Control*, chapter 9 - Open Peer Commentaries - Fundamentals of motor control, kinesthesia and spinal neurons: In search of a theory, pages 133–135. Cambridge University Press, Cambridge, 1994.
- P. A. Ferguson, D. J. Newman, M. Tryfonidis, and C. S. Poon. Reconsidering Bayesian optimization of visuomotor performance revealed in microgravity. 2004a.
- Philip Ferguson and Dava Newman. Dynamic joint torque estimation using force-plate and joint angle data. *Submitted to Journal of Biomechanics*, 2006.
- Philip Ferguson, Charles Coleman, and Dava Newman. Characterization of human locomotor control strategies and adaptation across a spectrum of gravitational environments. In *Proceedings of the 55th International Astronautical Congress*, Vancouver, BC Canada, October 2004b. IAF.
- G. Ferrigno, G. Baroni, and A. Pedotti. Methodological and technological implications of quantitative human movement analysis in long term space flights. *Journal of Biomechanics*, 32:431–436, 1999.
- Robert H. Fitts, Danny R. Riley, and Jeffrey J. Widrick. Physiology of a microgravity environment - Invited review: Microgravity and skeletal muscle. *Journal of Applied Physiology*, 89:823–839, 2000.
- T. Flash. The control of hand equilibrium trajectories in multi-joint arm movements. *Biological Cybernetics*, 57:257–274, 1987.
- Tamar Flash and Neville Hogan. The coordination of arm movements: An experimentally confirmed mathematical model. *Journal of Neuroscience*, 5(7):1688–1703, July 1985.
- Tamar Flash, Neville Hogan, and Magnus J. E. Richardson. Optimization principles in motor control. In M. A. Arbib, editor, *The Handbook of Brain Theory and Neural Networks*, chapter 1, pages 827–831. MIT Press, 2003.

- R. A. Fox, N. G. Daunton, and M. L. Corcoran. Study of adaptation to altered gravity through systems analysis of motor control. *Advanced Space Research*, 22(2):245–253, 1998.
- Arthur Gelb, Joseph F. Kasper, Raymond A. Nash, Charles F. Price, and Arthur A. Sutherland. *Applied Optimal Estimation*. The MIT Press, Cambridge, MA, 1999.
- Siome Goldenstein, Christian Vogler, and Dimitris N. Metaxas. Statistical cue integration in DAG deformable models. *IEEE Transactions on Pattern Analysis and Machine Intelligence*, 25(7):801–813, 2003.
- Hiroaki Gomi and Mitsuo Kawato. Equilibrium point control hypothesis examined by measured arm stiffness during multijoint movement. *Science*, 272:117–120, April 1996.
- J. E. Gregory, C. L. Broukett, D. L. Morgan, N. P. Whitehead, and U. Proske. Effect of eccentric muscle contractions on Golgi tendon organ responses to passive and active tension in the cat. *Journal of Physiology*, 538(1):209–218, 2002.
- Paul L. Gribble, David J. Ostry, Vittorio Sanguineti, and Rafael Laboissiere. Are complex control signals required for human arm movement? *Journal of Neurophysiology*, 79:1409–1424, 1998.
- Z. Hasan. Optimized movement trajectories and joint stiffness in unperturbed, inertially loaded movements. *Biological Cybernetics*, 53:373–382, 1986.
- Jiping He, William S. Levine, and Gerald E. Loeb. Feedback gains for correcting small perturbations to standing posture. *IEEE Transactions on Automatic Control*, 36(3):322–332, 1991.
- Thomas Heldt, Eun B. Shim, Roger K. Hamm, and Roger G. Mark. Computational modeling of cardiovascular response to orthostatic stress. *Journal of Applied Physiology*, 92:1239–1254, November 2002.

- W. A. Hodge, K. L. Carlson, R. S. Fijan, R. G. Burgess, P. O. Riley, W. H. Harris, and R. W. Mann. Contact pressures from an instrumented hip endoprosthesis. *Journal of Bone and Joint Surgery*, 71-A(9):1378–1386, 1989.
- James C. Houk and Elwook Henneman. Responses of golgi tendon organs to active contractions of the soleus muscle of the cat. *Journal of Neurophysiology*, 30(3): 466–481, 1967.
- James C. Houk, Jay T. Buckingham, and Andrew G. Barto. Models of the cerebellum and motor learning. *Behavioural Brain Science*, 19:368–383, 1996.
- J.C. Houk and W.Z. Rymer. *Handbook of physiology*, chapter Section 1, The nervous system; Volume 2, Motor control; Part 1, Neural control of muscle length and tension, pages 257–323. American Physiological Society, 1981.
- Jonathan P. How. Inertial navigation and estimation class notes 16.984. MIT. 2002.
- Lena Jami. Golgi tendon organs in mammalian skeletal muscle: Functional properties and central actions. *Physiological Reviews*, 72(3):623–666, 1992.
- Simon J. Julier and Jeffrey K. Uhlmann. Unscented Filtering and Nonlinear Estimation. *Proceedings of the IEEE*, 92(3):401–411, March 2004.
- Masazumi Katayama and Mitsuo Kawato. Virtual trajectory and stiffness ellipse during multijoint arm movement predicted by neural inverse models. *Biological Cybernetics*, 69:353–362, 1993.
- Mitsuo Kawato and Hiroaki Gomi. The cerebellum and VOR/OKR learning models. *Trends in Neurosciences*, 15(11):445–453, 1992.
- Mary E. Kieza, William F. Readdy, Richard Williams, Guy Fogleman, and Jeffrey R. Davis. Bioastronautics Critical Path Roadmap (BCPR). Technical Report JSC-62577, NASA, Johnson Space Center, Houston, Texas, 2004.
- J. Konorski. The problem of the peripheral control of skilled movements. *International Journal of Neuroscience*, 1:39–50, 1970.

- Konrad P. Kording and Daniel M. Wolpert. Bayesian integration in sensorimotor learning. *Nature*, 427:244–247, January 2004.
- J. R. Lackner and P. DiZio. Motor function in microgravity: movement in weightlessness. *Current Opinion in Neurobiology*, 6:744–750, 1996.
- James R. Lackner and Paul DiZio. Gravitoinertial force background level affects adaptation to coriolis force perturbations of reaching movements. *Journal of Neurophysiology*, 80:546–553, 1998.
- James R. Lackner and Paul DiZio. Rapid adaptation to coriolis force perturbations of arm trajectory. *Journal of Neurophysiology*, 72(1):299–313, July 1994.
- James R. Lackner and Paul DiZio. Human orientation and movement control in weightless and artificial gravity environments. *Experimental Brain Research*, 130:2–26, May 1999.
- Corinna E. Lathan and Gilles Clément. *Fundamentals of Space Life Sciences*, chapter 5 - Response of the neurovestibular system to spaceflight, pages 65–82. Krieger Publishing Company, Malabar, Florida, 1997.
- Charles S. Layne, Ajitkumar P. Mulavara, P. Vernon McDonald, Casey J. Pruett, Innessa B. Kozlovskaya, and Jacob J. Bloomberg. Effect of long-duration spaceflight on postural control during self-generated perturbations. *Journal of Applied Physiology*, 90:997–1006, 2001.
- Guangjun Liu, Karl Iagnemma, Steven Dubowsky, and Guillaume Morel. A base force/torque sensor approach to robot manipulator inertial parameter estimation. In *The Proceedings of the IEEE International Conference on Robotics and Automation*. IEEE, 1998.
- W. A. MacKay and J. T. Murphy. Responses of interpositus neurons to passive muscle stretch. *Journal of Neurophysiology*, 37(6):1410–1423, 1974.

- Steve G. Massaquoi and Jean-Jacques E. Slotine. The intermediate cerebellum may function as a wave-variable processor. *Neuroscience Letters*, (215):60–64, July 1996.
- J. Massion, K. Popov, J.-C. Fabre, P. Rage, and V. Gurfinkel. Is the erect posture in microgravity based on the control of trunk orientation or center of mass position? *Experimental Brain Research*, 114:384–389, 1997.
- Jean Massion, Bernard Amblard, Christine Assaiante, Laurence Mouchnino, and Sylvie Vernazza. Body orientation and control of coordinated movements in microgravity. *Brain Research Reviews*, 28:83–91, 1998.
- Joseph McIntyre and Emilio Bizzi. Servo hypotheses for the biological control of movement. *Journal of Motor Behavior*, 25(3):193–202, 1993.
- Thomas A. McMahon. *Muscles, reflexes and locomotion*. Princeton University Press, Princeton, New Jersey, 1984.
- Dimitris N. Metaxas. *Physics-based deformable models: Applications to computer vision, graphics and medical imaging*. Springer, 1996.
- R. C. Miall, D. J. Weir, D. M. Wolpert, and J. F. Stein. Is the cerebellum a Smith predictor? *Journal of Motor Behavior*, 25(3):203–216, 1993.
- Guillaume Morel and Steven Dubowsky. The precise control of manipulators with joint friction: A base force/torque sensor method. In *Proceedings of the 1996 IEEE International Conference on Robotics and Automation*, Minneapolis, MN, April 1996.
- Guillaume Morel, Karl Iagnemma, and Steven Dubowsky. The precise control of manipulators with high joint-friction using base force/torque sensing. *Automatica: The Journal of the International Federation of Automatic Control*, 36(7):931–941, 2000.
- F. A. Mussa-Ivaldi, N. Hogan, and E. Bizzi. Neural, mechanical, and geometric factors subserving arm posture in humans. *Journal of Neuroscience*, 5(10):2732–2743, October 1985.

- Akinori Nagano, Yusuke Ishige, and Senshi Fukashiro. Comparison of new approaches to estimate mechanical output of individual joints in vertical jumps. *Journal of Biomechanics*, 31(17):951–955, June 1998.
- D. Newman, S. Beck, A. Amir, G. Baroni, G. Ferrigno, and A. Pedotti. Measuring astronaut performance in microgravity: Loads and modeling. In *Proceedings of the First Biennial Space Biomedical Investigators' Workshop*, League City, TX, January 1999.
- D. J. Newman. *Human locomotion and energetics in simulated partial gravity*. PhD thesis, Massachusetts Institute of Technology, Cambridge, MA, June 1992.
- D. J. Newman and R. H. Wu. Astronaut adaptation across the spectrum of gravity. In *Proceedings of the 13th Humans in Space Symposium*, Santorini, Greece, May 2000.
- D. J. Newman, A. R. Amir, and S. M. Beck. Astronaut-induced disturbances to the microgravity environment of the mir space station. *Journal of Spacecraft and Rockets*, 38(4):578–583, August 2001.
- Dava J. Newman. Microgravity Investigations of Crew Reactions in 0-G MICR0-G Experiment Document. Technical Report LS-20459A, NASA, 2005.
- Dava J. Newman and D.K. Jackson. *Neural Control of Posture and Movement*, chapter 20, pages 282–291. Springer-Verlag, 2000.
- Dava J. Newman and Corinna E. Lathan. Memory processes and motor control in extreme environments. *IEEE Transactions on Systems, Man, and Cybernetics - Part C: Applications and Reviews*, 29(3):387–394, August 1999.
- Dava J. Newman and Grant Schaffner. Skeletal consequences of spaceflight. September 2003.
- Dava J. Newman, Jessica Marquez, and K. Sienko. Neurovestibular adaptation to weightlessness. 2003.

- T. R. Nichols and J. C. Houk. Improvement in linearity and regulation of stiffness that results from actions of stretch reflex. *Journal of Neurophysiology*, 39(1):119–142, 1976.
- G. Niemeyer and J. J. E. Slotine. Performance in adaptive manipulator control. *International Journal of Robotics Research*, 10(2):149–161, April 1991.
- Charles M. Oman. Motion sickness: a synthesis and evaluation of the sensory conflict theory. *Canadian Journal of Physiology and Pharmacology*, 68:294–303, 1988.
- Charles M. Oman. Human visual orientation in weightlessness. In *Proceedings of the York Conference 2001: Levels of Perception*, Man Vehicle Laboratory, Massachusetts Institute of Technology, Cambridge, MA 02139, 2001.
- Alessandra Pedrocchi, Antonio Pedotti, Guido Baroni, Jean Massion, and Giancarlo Ferrigno. Inverse dynamic investigation of voluntary trunk movements in weightlessness: a new microgravity-specific strategy. *Journal of Biomechanics*, 36:1691–1700, 2003.
- Alessandra Pedrocchi, Guido Baroni, Antonio Pedotti, Jean Massion, and Giancarlo Ferrigno. Inverse dynamic investigation of voluntary leg lateral movements in weightlessness: a new microgravity-specific strategy. *Journal of Biomechanics*, 38(4):769–777, 2005.
- D. M. Ray. Partial gravity simulation using a pneumatic actuator with closed loop mechanical amplification. Master’s thesis, University of Houston, 1993.
- Carrie A. Roller, Helen S. Cohen, Kay T. Kimball, and Jacob J. Bloomberg. Variable practice with lenses improves visuo-motor plasticity. *Cognitive Brain Research*, 12: 341–352, 2001.
- Carrie A. Roller, Helen S. Cohen, Kay T. Kimball, and Jacob J. Bloomberg. Effects of normal aging on visuo-motor plasticity. *Neurobiology of Aging*, 23:117–123, 2002.

- Grant Schaffner. *Assessment of hip fracture in astronauts exposed to long-term weightlessness*. PhD thesis, Massachusetts Institute of Technology, Cambridge, MA, August 1999.
- R. A. Schmidt, H. Zalaznik, B. Hawkins, J. S. Frank, and J. T. Quinn. Motor-output variability; a theory for the accuracy of rapid motor acts. *Psychol. Rev.*, 86:415 – 445, 1979.
- Nicolas Schweighofer, Michael A. Arbib, and Mitsuo Kawato. Role of the cerebellum in reaching movements in humans. I. Distributed inverse dynamics control. *European Journal of Neuroscience*, 10:86–94, July 1998a.
- Nicolas Schweighofer, Jacob Spoelstra, Michael A. Arbib, and Mitsuo Kawato. Role of the cerebellum in reaching movements in humans. II. A neural model of the intermediate cerebellum. *European Journal of Neuroscience*, 10:95–105, July 1998b.
- Rachael D. Seidler. Multiple motor learning experiences enhance motor adaptability. *Journal of Cognitive Neuroscience*, 16(1):65–73, 2004.
- Reza Shadmehr and Henry H. Holcomb. Neural correlates of motor memory consolidation. *Science*, 277:821 – 825, August 1997.
- Mark Shelhamer and Richard Clendaniel. Context-specific Adaptation of Saccade Gain. *Experimental Brain Research*, 146:441–450, 2002.
- Mark Shelhamer, Grace C. Y. Peng, Stefano Ramat, and Vivek Patel. Context-specific adaptation of the gain of the oculomotor response to lateral translation using roll and pitch head tilts as contexts. *Experimental Brain Research*, 146:388–393, 2002.
- Mark Shelhamer, Richard A. Clendaniel, and Dale C. Roberts. Context-specific adaptation of saccade gain in parabolic flight. *Journal of Vestibular Research*, 12:211–221, 2003.
- Jean-Jacques E. Slotine and Weiping Li. *Applied nonlinear control*. Number 0-13-040890-5. Prentice-Hall, Upper Saddle River, New Jersey, 07458, 1991.

- O. J. Smith. A controller to overcome dead time. *ISA Journal*, 6(2):28–33, 1959.
- Jacob Spoelstra, Nicolas Schweighofer, and Michael A. Arbib. Cerebellar learning of accurate predictive control for fast-reaching movements. *Biological Cybernetics*, 82: 321–333, 2000.
- Jack W. Stuster. Bold endeavors: Behavioral lessons from polar and space exploration. *Gravitational and Space Biology Bulletin*, 13(2), June 2000.
- E. Todorov. Cosine tuning minimizes motor errors. *Neural Comput.*, 14:1233 – 1260, 2002.
- Michail Tryfonidis. *Robust Adaptive Control Modeling of Human Arm Movements subject to Altered Gravity and Mechanical Loads*. PhD thesis, Massachusetts Institute of Technology, May 1999.
- Michail Tryfonidis, Philip Ferguson, and Dava Newman. A Bayesian optimization approach to human arm control modelling in 1-G and microgravity. 2004.
- E. A. Wan and R. van der Merwe. *Kalman filtering and neural networks*, chapter 7 - The Unsecented Kalman Filter, pages 221–280. Wiley Publishing, 2001.
- Leslie A. Wickman and Bernadette Luna. Locomotion while load-carrying in reduced gravities. *Aviation, Space, and Environmental Medicine*, 67(10):940–946, October 1996.
- J. M. Winters and L. Stark. Muscle models: What is gained and what is lost by varying model complexity? *Biological Cybernetics*, 55:403–420, 1987.
- M. R. Yeadon. The simulation of aerial movement - II. A mathematical inertial model of the human body. *Journal of Biomechanics*, 23(1):67–74, February 1990.
- L. R. Young. The coding of velocity and direction of self-rotation in response to visual and vestibular clues. In *The proceedings of the 1995 Neurology of Human Spatial Orientation Workshop*, Ibiza, Spain, May 1995.

- Laurence R. Young, Charles M. Oman, Daniel Merfeld, Douglas Watt, Serge Roy, Carlo DeLuca, David Balkwill, Jock Christie, Nicolas Groleau, D. Keoki Jackson, Glenn Law, Sherry Modestino, and William Mayer. Spatial orientation and posture during and following weightlessness: Human experiments on Spacelab life sciences. *Journal of Vestibular Research*, 3:231–239, 1993.
- Li-Qun Zhang, Gordon Nuber, Jesse Butler, Mark Bowen, and Willian Z. Rymer. In vivo human knee joint dynamic properties as functions of muscle contraction and joint position. *Journal of Biomechanics*, 31:71–76, 1998.
- R. Zhang, N. Paragios, and D. Metaxas. Implicit representations towards recovery and reconstruction of motion layers. In *Proceedings of the IEEE Workshop on Variational, Geometric and Level Set Methods in Computer Vision*, 2003.
- Z. Zhang. Flexible camera calibration by viewing a plane from unkown orientations. In *The Proceedings of the Seventh IEEE International Conference on Computer Vision*, pages 666–673, 1999.

Index

- Mir*, 28
- 3D, 43
- acceleration information, 52, 67, 136, 140
- accelerometer measurements, 78
- adaptation, 24, 32, 98, 99, 113, 135, 137
 - dual adaptation, 29, 81, 92, 101, 138
- adaptation model, 127
- adaptive control, 28
- AeroGo, 82
- air=bearing floor, 82
- air bearing floor, 25, 30, 48, 82, 87, 93,
 - 99, 101, 137, 141, 142
- Alumni Pool, 42
- Alumni pool, 84
- Ampro, 38
- Arcom, 37
- arm control, 27
- astronaut data, 108
- astronaut training, 96
- backplane, 38
- backup, 43
- bathing suit, 96
- battery, 40
- Bayesian optimization, 26, 28, 130, 135, 139
- body center of mass, 53, 55, 123
- body shape, 118
- bone decalcification, 23
- Brandeis University, 27
- break effect, 101, 137
- buoyancy compensator, 96
- buzzer, 94
- calibration matrix, 157
- camera, 43
- cardiovascular de-conditioning, 23
- centripetal torques, 63
- cerebellar control, 122, 138
- cerebellum, 29, 143
- clock board, 34, 38, 39
- coefficient of friction, 82, 137
- contact time, 103, 108, 113, 122, 127, 137
- contrast hypothesis test, 100
- contributions, 139
- coordinate system, 161
- copper, 92
- Coriolis matrix, 63
- Coriolis torques, 63
- COUHES, 81
- countermeasures, 31, 141, 144

course traverse, 88
 covariance bound, 60
 covariance matrix, 151
 CPU, 37
 Critical Design Review, 35

 dampers, 115
 damping to ground, 116
 data analysis, 187
 deformable models, 43
 deleted subjects, 99
 derived quantities, 92
 diagnostics, 141
 Diamond Systems, 37
 differentiation, 51, 60, 61, 64, 67
 directly measured quantities, 91
 disorientation, 23
 disturbances, 33
 DMM-16-AT, 37
 DWL-122, *see* wireless
 dynamic filter, 55, 135
 dynamics, 58, 61, 63, 67
 dynamic state estimator, 65

 EDLS, 33, 136, 157
 EDLS calibration fixture, 158
 electrical tape, 94
 EMG, 144
 Epoch, 39
 equilibrium position, 115
 Equinox, 98

 error correction, 121, 139
 ESM, 33
 excitation / contraction coupling, 126
 experiment document, 47
 experiment protocol, 84
 experiment sessions
 prescribed motion sessions, 46
 regular daily activities sessions, 46
 extended Kalman filter, 68
 extreme environments, 23

 feedback, 41
 feedforward, 121, 143
 fin, 96
 flowchart, 38
 force-level indicator, 41
 force feedback, 125, 138, 141, 143
 force moment sensor, 27, 30, 52, 58, 62,
 66, 78, 80, 91, 135, 137, 140
 force moment sensors, 32, 83
 force profile, 108, 127, 138
 force profiles, 104, 113
 forward kinematics, 54
 frame, 44
 friction torques, 63, 77

 Gaussian noise, 57
 Gaussian white noise, 66
 gender effect, 99
 general linear model, 99, 103
 Golgi tendon organ, 125, 138, 143

ground reaction forces, 62
 hard drive, 37
 hip fatigue, 85
 hip joint, 61
 hookah, 96
 hoop game, 92, 138
 human motion experiments, 61, 81, 113, 135, 140
 hybrid model, 129, 138
 hydrodynamics, 103
 hypotheses, 25, 135
 hypothesis, 32
 hysteresis, 160, 167, 169
 increment, 46
 inertial torques, 63
 inertia matrix, 63, 77
 information content, 52, 66
 informed consent, 87, 93, 96
 initial push-off conditions, 86, 90
 integration, 52
 internal sensor stress, 161
 interview, 85
 inverse dynamics, 61
 inverse kinematics, 56
 ISS, 23, 25, 31, 36, 46, 82, 136, 142
 Jacobian, 62
 joint accelerations, 61
 joint activation, 119
 joint angles, 43
 joint control torques, 61, 64, 118, 136
 joint friction matrix, 63
 Kalman filter, 30, 53, 57, 65, 68, 136
 measurement update step, 59
 propagation step, 59
 kinematic data, 135
 kinematics, 43, 60, 62, 118
 kinetic data, 113, 135
 kinetics, 60, 62, 118
 lead shot, 96
 least squares estimator, 66
 LED, 41, 94
 Linux, 38
 locomotor adaptation, 81
 locomotor control strategy, 87, 103, 138
 locomotor skills, 25, 26, 82, 135
 low-pass filter, 51
 Lyapunov stability analysis, 117
 manipulandum, 61
 Mars, 23
 mask, 96
 Matlab, 41, 77, 163
 maximum force, 99, 103, 108, 113, 127, 137
 measurement equation, 57
 measurement variance matrix, 56, 66, 151
 memory stick, 43
 metrics, 51, 91, 98, 135, 140

MICR0-G, 25, 30, 31, 82, 136, 141, 142, 157
 MICR0-G calibration fixture, 160
 MICR0-G sensors
 concept prototype, 34
 flight sensors, 36, 43
 prototype sensors, 34
 Mir, 33
 modelling, 113
 Moon, 23
 moonwalker, 27
 motor learning, 29
 muscle activation, 119
 muscle atrophy, 23
 muscle dynamics, 126
 muscles, 115
 muscle stiffness, 121
 NASA, 96
 neuro-muscular system, 121
 neutral buoyancy, 96
 Neutral Buoyancy Lab, 136
 Newton's laws, 53, 58
 Newton-Raphson, 152
 non-linear least squares estimator, 136
 nonlinear least squares estimator, 66, 151
 NTP, 40
 observability, 66, 67, 77, 160
 optical flow, 43
 parabolic flight, 99, 141
 partial gravity, 144
 passive muscle force, 131
 Payload Systems, 34
 PC/104, 37
 PCMCIA, 38, 42, 43
 phase table, 97
 pilot studies, 84
 pixel, 44
 planar model, 54
 planar motion, 77, 87
 plasticity, 29
 POGO, 27
 predictor-corrector estimator, 65
 prescribed motion sessions, *see* experiment
 sessions
 prior information, 77
 process noise, 58, 70
 Prometheus, 37
 proportional-derivative control, 69, 115
 proprioceptive feedback, 122, 143
 pseudo-measurement, 56
 pseudoinverse, 159, 166
 quadratic trajectory, 118
 questionnaire, 96
 random noise, 70
 rank, 67, 136, 159
 rank deficient, 78
 rats, 28
 reference trajectory, 116, 117, 125

regular daily activities sessions, *see* experiment sessions
 repeated measures, 99, 102
 resistive training, 141
 restraints, 36
 rigid body model, 54, 115
 robot, 62, 80
 robotics toolbox, 77
 robustness, 130
 rotation room, 27
 running, 110, 114
 SCUBA, 42, 84, 87, 96
 sensor mounting frame, 83, 97
 shadows, 44
 single parameter, 113
 singularities, 56
 Slackware, *see* Linux
 Smith predictor, 122
 snorkel, 96
 software
 client software, 41
 sensor software, 38
 spatial orientation, 141
 speed skating, 82
 springs, 114
 state transition matrix, 59
 state variable, 68
 state vector, 54, 65
 statics, 62
 statistical results, 106
 strain gauge, 61, 170
 strain gauges, 34, 38
 stratum, 40
 subject instructions, 90, 95
 swimming, 97
 synchronization, 40
 SYSTAT, 100
 tactile cue, 91
 tactile feedback, 133
 targeting error, 128
 tare, 160
 Taylor series, 57
 Taylor series expansion, 152
 telnet, 38
 test director, 94
 thread, 38
 threshold, 125
 time delay, 121
 toe flick, 120
 training, 141
 transport delay, 122, 125
 underwater, 25, 27, 30, 82, 83, 96, 102, 137, 138, 140, 143
 unscented Kalman filter, 68, 136, 155
 USB, 40, 43
 variational calculus, 56
 velocity feedback, 133
 vestibular conditioning, 23
 vestibular feedback, 143

vestibular system, 133
VGA, 37, 42
video, 27, 28, 32, 34, 43, 53, 61, 64, 65,
84, 91, 98, 137
vinyl bump, 85
virtual work, 63
viscosity, 84
visual feedback, 143
VOR, 28, 29

walking, 110
waterproof, 42
weight belt, 96
wet-suit, 96
wireless, 34, 40, 41, 43